



AN EVALUATION OF AFT-END IGNITION FOR SOLID PROPELLANT ROCKET MOTORS

by

J. D. Kilgroe, R. E. Fitch, and J. L. Guenther

prepared for

NATIONAL AERONAUTICS AND SPACE ADMINISTRATION

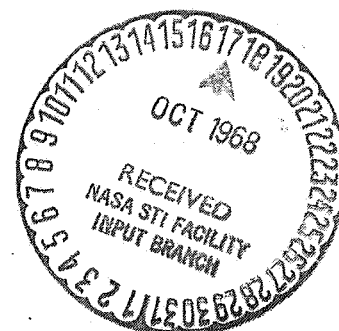
CONTRACT NAS 3-10297

N 68-35729	
(ACCESSION NUMBER)	(THRU)
291	1
(PAGES)	(CODE)
CR-72447	38
(NASA CR OR TMX OR AD NUMBER)	(CATEGORY)

GPO PRICE \$ _____
CSFTI PRICE(S) \$ _____

Hard copy (HC) ☒
Microfiche (MF) ☐

ff 653 July 65



NOTICE

This report was prepared as an account of Government sponsored work. Neither the United States, nor the National Aeronautics and Space Administration (NASA), nor any person acting on behalf of NASA:

- A.) Makes any warranty or representation, expressed or implied, with respect to the accuracy, completeness, or usefulness of the information contained in this report, or that the use of any information, apparatus, method, or process disclosed in this report may not infringe privately owned rights; or
- B.) Assumes any liabilities with respect to the use of, or for damages resulting from the use of any information, apparatus, method or process disclosed in this report.

As used above, "person acting on behalf of NASA" includes any employee or contractor of NASA, or employee of such contractor, to the extent that such employee or contractor of NASA, or employee of such contractor prepares, disseminates or provides access to any information pursuant to his employment or contract with NASA, or his employment with such contractor.

Requests for copies of this report should be referred to

National Aeronautics and Space Administration
Office of Scientific and Technical Information
Attention: AFSS-A
Washington, D. C. 20546

NASA CR-72447
CETEC 2008-FR
00037

FINAL REPORT

AN EVALUATION OF AFT-END IGNITION FOR
SOLID PROPELLANT ROCKET MOTORS

by

J. D. Kilgroe, R. E. Fitch, and J. L. Guenther

prepared for

NATIONAL AERONAUTICS AND SPACE ADMINISTRATION

September, 1968

CONTRACT NAS 3-10297

Technical Management
NASA Lewis Research Center
Cleveland, Ohio
H. Bankaitis

CONSOLIDATED ENGINEERING TECHNOLOGY CORPORATION
188 Whisman Road
Mountain View, California 94040

FOREWORD

The authors wish to acknowledge the work of individuals who contributed significantly to the technical aspects of the program. Thanks go to Mr. R. Parthasarathy for his work in development of the analytical blockage and jet penetration models, Professor W. L. Chow for conceptual work on the analytical blockage model, and Dr. R. Anderson for contributions in fundamental ignition theory.

Major contributions were made in the experimental phases of the program by Atlantic Research Corporation personnel who conducted the detailed design, experiment fabrication and test activities. The authors thank Mr. J. Elliot and Mr. R. Gurtler for project management and engineering, Mr. E. Hancock for test motor and igniter design, and Mr. R. Naismith and Mr. J. Wertz for instrumentation, testing and data reduction.

ABSTRACT

A program for the evaluation of aft-end ignition of solid propellant rocket motors was conducted to determine the igniter design and placement parameters which give adequate ignition characteristics while avoiding motor overpressurization. Nine instrumented solid rocket motor aft-end ignition tests were performed. The results demonstrated that, by correct design and placement of the fixed aft-end igniter, satisfactory ignition times can be achieved without overpressurization. However, nozzle pressure oscillations, which arise from interaction of the igniter and motor flows, were found to present a serious problem which remains to be solved. An analytical model was developed which predicts the igniter parameters which avoid overpressurization.

TABLE OF CONTENTS

<u>Title</u>	<u>Page</u>
I. SUMMARY	I-1
II. INTRODUCTION	II-1
III. TECHNICAL ACTIVITIES	III- 1
A. ANALYTICAL MODELS	III- 2
1. Penetration, Ignition and Flame Propagation	III- 8
2. Blockage.	III-20
a. Background	III-20
B. EXPERIMENT DESIGN AND FABRICATION. . .	III-37
1. Experiment Conceptual Design	III-37
2. Main Motor Design and Fabrication	III-38
a. Grain Design and Ballistic Performance	III-38
b. Main Motor Assembly Description	III-43
3. Igniter Assembly Design and Fabrication . .	III-43
a. Grain Design and Ballistic Performance .	III-43
b. Pyrogen Assembly Description.	III-45
4. Propellant Processing and Non-Destructive Testing	III-48
a. Main Motor	III-48
b. Igniter.	III-50
5. Instrumentation and Test Equipment	III-50
a. Main Motor Assembly.	III-50
b. Igniter Assembly	III-53
c. Pyrogen Holding Assembly and Aligning Device.	III-53
d. Thrust Stand	III-53
e. Data Acquisition Equipment	III-57
f. Motion and Still Picture Photography. . .	III-57

<u>Title</u>	<u>Page</u>
C. TESTING	III- 58
1. Test Procedure	III- 61
2. Special Problems	III- 69
3. Data Reduction	III- 70
4. Test Results	III- 71
a. Ignition Transient and Early Steady State Operation	III- 74
b. Late Steady State Operation and Igniter Tail-Off	III- 94
D. DATA EVALUATION AND CORRELATION	III-104
1. Penetration, Ignition and Flame Propagation	III-104
a. Jet Penetration	III-105
b. Ignition and Flame Propagation	III-113
2. Nozzle Flow Interactions	III-129
a. Flow Field Characteristics	III-133
b. Prediction of Motor Nozzle Blockage . .	III-148
c. Motor Overpressures	III-154
d. Thrust Modifications	III-163
e. Nozzle Pressure Oscillations and Pressure Distribution	III-170
f. Slip Surface, Bow Shock Location and Sonic Surface	III-185
g. Nozzle Side Forces	III-196
IV. CONCLUSIONS AND RECOMMENDATIONS	IV-1
REFERENCES	R-1

<u>Title</u>	<u>Page</u>
APPENDICES	
A. BLOCKAGE MODEL	A-1
B. PENETRATION MODEL	B-1
C. MOTOR BALLISTIC COMPUTER DATA	C-1
D. SUPPLEMENTAL TEST DATA	D-1
E. THROAT AREA AND OVERPRESSURIZATION CALCULATIONS	E-1

LIST OF ILLUSTRATIONS

<u>Figure No.</u>		<u>Page</u>
III-1.	Igniter Jet Penetration Modes	III- 4
III-2.	Blocked Nozzle Flow Interactions	III- 6
III-3.	Unblocked Nozzle Flow Interactions	III- 7
III-4.	Aft-end Igniter Heat Transfer Correlations	III-10
III-5.	Effects of Igniter Design Parameters on Motor Propellant Grain Average Heat Flux	III-12
III-6.	Motor Pressure Transients for Various Igniter Configurations.	III-14
III-7.	Geometrical Epsilon Star Relationship.	III-15
III-8.	Jet Penetration Model Schematics	III-17
III-9.	Counter-flowing Free Stream Bow Shock Stand-off Distances	III-24
III-10.	Compressed Air Overpressurization Test Apparatus	III-27
III-11.	Igniter and Booster Nozzle Geometries	III-28
III-12.	Effects of Igniter Pressure and Position on Booster Pressure	III-29
III-13.	Analytical Blockage Model Control Volume	III-32
III-14.	Comparison of the Analytical Blockage Model with Salmi's Experimental Data	III-35
III-15.	Analytical Model Parametric Data	III-36
III-16.	Test Motor Assembly.	III-39
III-17.	Motor Pressure Versus Burn Time	III-42

<u>Figure No.</u>		<u>Page</u>
III-18	Theoretical and Actual Igniter Pressure-Time Curves	III- 46
III-19	Igniter Assembly	III- 47
III-20	Bottom Fill Casting Set-Up	III- 49
III-21	Thermocouple and Tripwire Instrumentation Locations	III- 51
III-22	Eroding Thermocouple	III- 52
III-23	Nozzle Pressure Tap Locations	III- 54
III-24	Igniter Motor Instrumentation Schematic	III- 55
III-25	Igniter Aligning Fixture	III- 56
III-26	Test Camera Locations	III- 59
III-27	Prefire Test Assembly, Test 1	III- 63
III-28	Postfire Test Assembly, Test 1	III- 64
III-29	Post Igniter and Motor Nozzle Close-ups, Test 1	III- 65
III-30	Prefire Test Assembly, Test 7	III- 66
III-31	Typical Igniter and Motor Pressure Traces	III- 73
III-32	Test 3, Ignition Transient, Thermocouple and Tripwire Data	III- 75
III-33	Test 9, Ignition Transient, Thermocouple and Tripwire Data	III- 77
III-34	Test 3, Ignition Transient Principle Pressure and Thrust Data	III- 79
III-35	Test 9, Ignition Transient Principle Pressure and Thrust Data	III- 82

<u>Figure No.</u>	<u>Page</u>
III-36.	Test 3 Ignition Transient Nozzle Pressure Data . III- 83
III-37.	Test 9 Ignition Transient Nozzle Pressure Data . III- 85
III-38.	Test 3 Ignition Transient Motor Chamber Data . . III- 87
III-39.	Test 9 Ignition Transient Motor Chamber Data . . III- 89
III-40.	Test 3 Igniter Tail-off, Principle Pressure and Thrust Data. III- 95
III-41.	Test 9 Igniter Tail-off, Principle Pressure and Thrust Data. III- 97
III-42.	Test 3 Igniter Tail-off, Nozzle Pressure Data . . III- 99
III-43.	Test 9 Igniter Tail-off, Nozzle Pressure Data . . III-101
III-44.	Head-end Pressure During Ignition Transient. . . III-106
III-45.	Typical Penetration Flow Field and Pressure Distribution. III-107
III-46.	Breakwire Response Times, Test 4 III-109
III-47.	Motor Grain Thermocouple Temperatures, Test 9. III-110
III-48.	Comparison of Thermocouple Ignition Tempera- tures, Test 6 III-111
III-49.	Influence of $(w/A)_{\max}$ on Jet Penetration. III-112
III-50.	Typical Plotted Tripwire Data III-115
III-51.	Effect of ϵ^* on Flame Propagation III-117
III-52.	Flame Propagation Dependency Upon Maximum Igniter Mass Flow Parameter. III-118
III-53.	Flame Propagation Rate Correlation III-120
III-54.	Ignition Transient Data, Test 7 III-121

<u>Figure No.</u>		<u>Page</u>
III-55	Time Average Igniter Chamber Pressures	III-123
III-56	Reduced Thermocouple Data, Test 7	III-124
III-57	Reduced Thermocouple Data, Test 8	III-125
III-58	Reduced Thermocouple Data, Test 9	III-126
III-59	Thermocouple Temperature Versus Axial Location, Test 8	III-127
III-60	Ignition Transient Oscillograph Data, Test 6 . . .	III-135
III-61	Plotted Ignition Transient Pressure Data, Test 6 .	III-136
III-62	Igniter and Motor Nozzle Pressure Data for Ignition Transients, Test 7	III-138
III-63	Igniter and Motor Nozzle Pressure Data at Onset of Pressure Disturbances, Test 7	III-139
III-64	Igniter and Motor Nozzle Pressure Data During Maximum Pressure Disturbances, Test 7	III-140
III-65	Igniter and Motor Nozzle Pressure Data at Onset of Pressure Disturbances, Test 1	III-143
III-66	Igniter and Motor Nozzle Pressure Data During Maximum Pressure Disturbances, Test 1	III-144
III-67	Motor and Igniter Nozzle Pressure Data, Test 3 .	III-145
III-68	Igniter and Motor Nozzle Flow Pressure Interactions, Test 4	III-146
III-69	Comparison of Analytical Blockage Model with Experimental Data	III-149
III-70a	Effect of Pressure Integral on Unblocking Pressure Ratio	III-153
III-70b	Analytical Model Adjustment Using Experimental Pressure Integral	III-153

<u>Figure No.</u>		<u>Page</u>
III-71.	Maximum Overpressurizations	III-157
III-72.	Maximum Incremental Overpressures	III-158
III-73.	Effective Throat Areas and Incremental Overpressures, Test 3	III-160
III-74.	Effective Throat Areas and Incremental Overpressures, Test 2	III-161
III-75.	Comparison of Typical Incremental Overpressures	III-162
III-76.	Incremental Pressures versus Igniter to Motor Chamber Pressure Ratio	III-164
III-77.	Thrust and Pressure Data for Ignition Transient, Test 1	III-166
III-78.	Thrust and Pressure Data During Minimum Oscillations, Test 1	III-167
III-79.	Thrust and Pressure Data Showing Maximum Oscillations, Test 1	III-168
III-80.	Thrust and Pressure Data Showing Maximum Thrust Oscillations, Test 8	III-169
III-81.	Effect of ϵ^* on Test Motor Thrust	III-171
III-82.	Effect of ϵ^* on Thrust Amplification Coefficient	III-172
III-83.	Effect of Igniter Mass Flow Parameter and ϵ^* Upon Thrust Amplification Coefficient	III-173
III-84.	Typical Nozzle Pressure Oscillations, Test 6	III-175
III-85.	Nozzle Pressure Distribution During Typical Pressure Oscillation Cycles, Test 6	III-177
III-86.	Asymmetric Nozzle Pressures, Test 6	III-178

<u>Figure No.</u>		<u>Page</u>
III-87	Nozzle Wall Pressure Distribution, Test 1	III-180
III-88.	Nozzle Wall Pressure Distribution, Test 6	III-181
III-89.	Nozzle Wall Pressure Distribution, Test 3	III-182
III-90.	Nozzle Pressure Data At Ignition, Test 8	III-183
III-91.	Nozzle Wall Pressure Distribution, Test 8	III-184
III-92.	Nozzle Pressure Data at Onset of Pressure Disturbance, Test 8	III-186
III-93.	Nozzle Pressure Distribution During Pressure Cycle, Test 8.	III-187
III-94.	Nozzle Pressure Distribution During Pressure Cycle (cont'd), Test 8	III-188
III-95.	Typical Slip Surfaces, Test 8	III-190
III-96.	Igniter and Motor Nozzle Streamlines, Slip Surface and Sonic Surfaces, Test 8	III-191
III-97.	Bow Shock, Slip Surface and Nozzle Pressure Distribution, Test 8	III-192
III-98.	Effect of ϵ^* on Bow Shock Location, Test 8	III-194
III-99.	Effect of Igniter Flow on Bow Shock Location, Test 8	III-195
III-100.	Nozzle Pressure Distributions at Selected Times, Test 8	III-197
III-101.	Nozzle Wall Force Distribution	III-200

LIST OF TABLES

<u>Table No.</u>		<u>Page</u>
III-1.	Propellant Composition and Properties Comparison	III- 41
III-2.	Summary of Motor and Igniter Data	III- 44
III-3.	Test Plan Parameters	III- 60
III-4.	Typical Test Pressure Instrumentation	III- 67
III-5.	Thermocouple and Tripwire Instrumentation. .	III- 68
III-6.	Reduced Tripwire Data	III-114
III-7.	Characteristic Nozzle Flow Operating Modes .	III-131
III-8.	Igniter and Motor Nozzle Pressure Data, Test 7	III-141
III-9.	Reduced Nozzle and Chamber Pressure Data, Tests 2 thru 5	III-147
III-10.	Local Maximum Chamber Pressures	III-156

SYMBOLS

A	area, sq. in.
A^*	sonic throat area, sq. in.
$A_b(r)$	propellant grain surface burn area as a function of web burn back distance, sq. in.
$A_{an} = A_s$	annular area between motor nozzle and igniter lip, sq. in.
A_{ei}	igniter exit area sq. in.
A_{MN}	conical area along nozzle wall from motor throat to intersection of normal drawn from igniter lip, sq. in.
A_p	circular motor port area, sq. in.
A_{ti}	igniter throat area, sq. in.
A_{tm}	motor throat area, sq. in.
a	propellant burn rate pressure coefficient
b	mixing zone width in initial area of jet or radius in principle area of jet
b_o	initial radius of igniter jet
c^*	characteristic motor velocity, ft/sec
C_F'	95 percent of the theoretical thrust coefficient for $\gamma = 1.18$ corresponding to the test motor nozzle area ratio and chamber to atmospheric pressure ratio
c_v	specific heat at constant volume, $\frac{\text{Btu}}{\text{lb} \cdot ^\circ\text{R}}$
D	diameter, in.
D_a	inside diameter of nozzle exit cone, in.
D_b	outside diameter of nozzle exit cone, in.

D_p	diameter of motor port, in.
D_t	throat diameter, in.
D_{tm}	diameter of motor throat, in.
D_z	motor nozzle diameter at intersection of nozzle wall and normal from wall to igniter lip, in.
d	distance from the motor throat to the intersection of the normal from the igniter lip with the nozzle wall, in.
F	thrust or force, lb_F
F_1, F_2	experiment thrust measurements of main motor, lb_F
g_c	gravitational constant, $32.17 \frac{lb_m \text{ ft}}{lb_f \cdot sec^2}$
H	radius of dead end channel (motor port) in the penetration model, in.
h	heat transfer coefficient, $BTU/sec \cdot in^2 \cdot ^\circ F$
h	enthalpy, BTU/lb_m
h_{co}	chamber stagnation enthalpy, BTU/lb_m
h_{io}	igniter stagnation enthalpy, BTU/lb_m
L	length of motor nozzle from throat to exit plane, in.
ℓ/d_m	stand-off parameter, distance from model face to free-stream bow shock divided by model diameter
M	Mach number
m	mass of gas, lb_m
\dot{m}_c	mass accumulation parameter, lb_m/sec
n	propellant burn rate pressure exponent
Nu	Nusselt number

p	static pressure, psia
P	total or stagnation pressure, psia
$P_1, P_2 \dots P_{17}$	experimentally measured pressures at specific locations in the main motor, psia
$P_{18} \dots P_{22}$	experimentally measured pressures at specific locations in the igniter motor, psia
P_2/P_1	stagnation pressure ratio across a normal shock
$p_{an} = p_s$	pressure across annular area between igniter lip and nozzle motor wall, psia
p_{ei}	static pressure at igniter exit plane, psia
P_i	total pressure of igniter, psia
P_j	jet total pressure, psia
P_m	total pressure of main motor, psia
$p_{mn} = p_{ts}$	pressure distribution along conical nozzle wall section from motor throat to intersection of normal drawn from igniter lip, sq. in.
$P_{m,o}$	motor pressure without igniter flow interference, psia
$\bar{P} = (P_1 + P_5)/2$	average chamber pressure, psia
ΔP_m	incremental increase in motor chamber pressure, psia
q	heat flux, BTU/sec-in ²
q_{c+r}	convective, conductive and radiative heat flux, BTU/sec-in ²
q_r	radiative heat flux, BTU/sec-in ²
\dot{r}	propellant burn rate, in/sec
r	propellant burn back distance, in.
T	temperature, °F

$T_1, T_2 \dots$ $\dots T_{20}$	thermocouple or tripwire location or measurement at a specific location in the main motor, °F
T_c	average gas temperature in motor chamber, °F
T_{tr}	temperature of trapped atmospheric gases in main rocket chamber, °F
t	time in milliseconds unless otherwise noted
t_f	time to deactivation of final tripwire, ms.
t_i	time to deactivation of first tripwire, ms.
u_H	velocity of the reverse flow from the main motor, ft/sec
u_m	centroid velocity in the principal area of the jet, ft/sec
u_o	initial potential velocity of igniter jet, ft/sec
V_i	initial motor void volume downstream to the motor throat plane from the point of first ignition, cu. in.
V_t	total motor void volume upstream of throat plane, cu. in.
v_a	average flame spread velocity, in/sec
w	mass flow rate, lb_m/sec
w_c	mass flow rate of chamber gases, lb_m/sec
w/A	igniter mass flow parameter; mass flow rate of igniter divided by motor throat area, $lb_m/sec-in^2$
X	distance from nozzle throat along motor centerline, in.
x	distance along wall from nozzle throat break point, in. also, distance from igniter nozzle exit along centerline of dead end channel in penetration model, in.
$x' = x$	coordinate parallel to x in penetration model
y	coordinate perpendicular to x in penetration model
$y' = y - b_o$	coordinate parallel to y in the penetration model

y_1	distance to outer edge of mixing zone in penetration model
y_2	distance to inner edge of mixing zone in the initial area of the jet
$y_1' = y_1 - b_o$	distance in penetration model
$y_2' = y_2 - b_o$	distance in penetration model
$z = s$	distance from igniter lip normal to the motor nozzle exit cone, in.
$\alpha = u_H/u_o$	velocity ratio in penetration model
γ	gas specific heat ratio
$\epsilon^* = A_{an}/A_{tm}$	igniter epsilon star; annular area around igniter lip normal to main motor nozzle wall divided by motor throat area
λ	penetration model similarity parameter
η	penetration model similarity parameter
η_1	similarity parameter value at the outer edge of the mixing zone
η_2	similarity parameter value at the inner edge of the mixing zone in the initial area of the jet
θ	nozzle cone half angle
ρ	propellant density, lb _m /cu. in.

SUBSCRIPTS

c	chamber
e	nozzle exit
eff	effective
i	igniter
j	jet
k	an integer
m	motor
t	throat
tr	trapped-refers to initial gases trapped in motor chamber
*	pertaining to sonic area or conditions except when used with ϵ^*
act	actual, measured data
theo	theoretical
max	maximum
min	minimum

I. SUMMARY

A theoretical and experimental program was conducted to investigate the aft-end ignition of solid propellant rocket motors. The purpose of the program was to determine the igniter design and placement parameters necessary to achieve satisfactory ignition through adequate igniter jet penetration, while avoiding overpressurization due to aerodynamic blockage of the motor throat. Analytical models were developed, an experiment was designed and assembled, and nine test firings were conducted.

Analytical models were developed to predict aerodynamic blockage criteria and to characterize the jet flow field within the motor port as functions of igniter design and location parameters. The blockage model was completed and was found, by comparison with experimental data, to predict the igniter parameters necessary to avoid motor chamber overpressures. The jet penetration model was only partially finished during this program because of the complexity of the problem.

The test motor and pyrogen igniter designs were based upon an extensive review of previous work and the results of the analytical studies. The motor propellant formulation, grain design and nozzle configuration were similar to those in the NASA 260" solid rocket development program. The motor featured a 5" diameter nozzle throat, a 17.5° half angle conical nozzle, and a grain configuration consisting of a cylindrical port with a head-end star. The igniter was designed to enable testing of a variety of igniter chamber pressures and mass flow rates and incorporated nozzle configurations selected to promote high igniter jet penetration and fast ignition.

The detailed design, hardware procurement, motor processing and testing was conducted under subcontract by the Atlantic Research Corporation, Propulsion System Division, of Alexandria, Virginia. Instrumentation provided for each test included 20 or 21 motor and igniter pressure measurements, 10 tripwire channels to determine ignition and flame propagation across the grain surface, 8 thermocouple temperature measurements of the motor propellant grain surface, and 2 motor thrust measurements.

Two open-air igniter firings and nine fully instrumented aft-end ignition tests were satisfactorily conducted. Four of the motor firings were used to determine the effects of igniter ϵ^* (ratio between igniter-nozzle annular area and motor throat area) on the ignition transient and motor chamber overpressurizations. The remaining five tests were conducted to determine the effects of igniter mass flow parameter (igniter mass

flow rate divided by the main motor throat area - w/A) on ignition characteristics and motor flow blockage. The effects of ϵ^* and w/A changes on motor thrust level and motor nozzle pressure distributions were also investigated.

The test results confirmed that motor ignition transients are shortened, while motor overpressurization and thrust values are increased with decreasing igniter ϵ^* location and increasing igniter mass flow parameter. Ignition intervals varied from 70 milliseconds at the highest w/A to 200 milliseconds at the lowest. Motor overpressures ranged from zero at $\epsilon^* = 1.79$ to 36 percent of the design value at $\epsilon^* = 1.21$. For ϵ^* values greater than 1.5, overpressures of less than 5 percent were noted.

In addition to the expected motor thrust and pressure modifications, severe motor nozzle pressure oscillations were observed. These oscillations resulted from the unstable interaction of the igniter and main motor gas flow fields. For some tests, transient motor nozzle exit cone pressures one and one-half times greater than the motor nozzle throat pressures were recorded. In all tests except the test conducted at the highest ϵ^* location (1.79), the nozzle pressure disturbances were reflected in the motor nozzle and chamber pressures.

The motor nozzle flow interactions and nozzle blockage phenomena were characterized by four basic modes of interaction which are postulated to correspond to four separate overexpanded igniter nozzle flow regimes. These modes describe stable and unstable flow field interactions, both with and without blockage and overpressurization.

Motor flow blockage characteristics were determined primarily by the igniter ϵ^* location and the igniter jet shock structure and penetration distance. Blockage varied from complete penetration of the motor throat in the first mode to intermittent blockage with only slight perturbations of the motor nozzle throat and chamber pressures in Modes 3 and 4.

Detail test data analysis indicated that the large magnitude nozzle pressure disturbances probably resulted from unstable igniter nozzle flow separation rather than an inherently unstable character of the interacting igniter and main motor flows. However, it is postulated that, when the igniter operated in an unstable flow regime, both the igniter nozzle flow and mixing process perturbations were mutually exciting.

The time dependent distribution of motor nozzle pressures indicated that the motor nozzle oscillations were lateral, longitudinal and/or rotational

in character. With one exception, the motor nozzle pressure taps were located in a single axial plane. However, the one motor exit cone tap which was located 90° from the others indicated considerable asymmetry in the nozzle pressure distributions, during the periods of nozzle pressure oscillation. More complete characterization of the oscillatory flow fields will require further tests.

Major conclusions resulting from the study were:

- (a) Aft-end igniters can be designed and located in a fixed position in the main motor exit cone in a manner which precludes overpressurization and achieves satisfactory ignition.
- (b) The analytical blockage model developed during the program predicts the igniter parameters necessary to avoid overpressures.
- (c) The motor chamber overpressures and thrust levels increase with increasing igniter mass flow parameter and decreasing ϵ^* .
- (d) Large magnitude pressure oscillations in the motor nozzle exit cone present serious design problems and must be resolved.
- (e) The motor nozzle oscillations are asymmetrical in nature, and are caused by unstable igniter operation and by interaction of the igniter jet with the main motor flow.
- (f) Additional testing is required, with a more comprehensive instrumentation distribution, to solve the nozzle pressure oscillation problem.

II. INTRODUCTION

The ignition of solid propellant rocket motors has been performed, in the past, almost exclusively by head-end mounted pyrotechnic and pyrogen igniters. Although head-end igniters have proved satisfactory in most cases, aft-end pyrogen igniters have inherent characteristics which makes them superior for many applications. The primary advantage stems from the separation of the ignition system from the main motor. By this separation, the reliability of the ignition system may be increased by the employment of redundancy and design conservatism to a degree unobtainable with head-end igniters. Auxiliary advantages include increased design flexibility for other systems in the motor head-end (such as termination systems) and the reduction in stage weight by elimination of a built-in ignition system for that stage.

The fluid dynamical flow phenomena peculiar to aft-end ignition present design problems which are not encountered in head-end ignition. Two major problems which may arise from improper design and location of the aft-end igniter are: (1) possible long ignition intervals resulting from low penetration of the igniter jet into the motor port and subsequent slow flame propagation rates into the head-end and (2) main motor overpressurizations resulting from aerodynamic blockage of the main motor throat by the igniter jet.

Earlier work^(1, 2, 3) has demonstrated that aft-end igniters can be designed and placed within the exit cone of the main motor so that satisfactory ignition is achieved. Overpressurizations were avoided in these tests by ejection of the igniter rocket motor before main chamber pressure was reached. The only solid propellant motor aft-end ignition tests in which the igniter was retained in position after full motor ignition clearly demonstrated that serious overpressures can occur.⁽⁴⁾

The difficulties of ejecting the igniter system of a large pad launched solid booster, such as the 260" solid motor, are obvious. It would be easier to allow the launch vehicle to rise off a fixed position igniter; however, overpressurizations from a fixed aft-end igniter could result in catastrophic failure of the launch vehicle. Aft-end ignition technology studies have consequently been undertaken to develop fixed position igniter design parameters which will enable satisfactory ignition while avoiding overpressurization. Recent experimental studies at NASA-Lewis⁽⁵⁾ using compressed air in model motor and igniter systems have indicated that overpressures can be avoided by proper placement of the igniter and by correct

selection of igniter design parameters relative to the main motor. However, these same results have not been demonstrated in the ignition of actual solid propellant motors.

The program reported on herein was funded to investigate the conditions under which the satisfactory aft-end ignition of actual solid propellant motors could be obtained. To achieve these objectives, the program encompassed theoretical and experimental studies which included testing of nine instrumented solid rocket motors with axially aligned aft-end igniters, and the analysis and correlation of data therefrom. The detail design, fabrication and testing activities were performed under sub-contract to CETEC by the Atlantic Research Corporation, Alexandria, Virginia.

III. TECHNICAL ACTIVITIES

The purpose of the Aft-End Ignition Program was to accomplish, through a combined theoretical and experimental study, the following objectives:

- (1) Determination of the aft-end ignition parameters which produce satisfactory motor ignition with minimum overpressurization and igniter size.
- (2) Determination of the extent of the igniter motor aerodynamic interference with the main motor nozzle flow.
- (3) Determination of the effect of the igniter motor on the main motor thrust.

The above objectives were to be achieved by employing an aft-end igniter motor which was fixed in a given position for the duration of each test.

The program was conducted through a series of technical work tasks, as follows:

- (1) Development of analytical models of the jet penetration (ignition), and the nozzle flow field interactions which produce blockage and chamber overpressurization.
- (2) Experiment conceptual design and establishment of design criteria which would result in a safe, reliable test system, provide for maximum igniter flexibility, and feature the extensive instrumentation required to measure the necessary ignition and flow field phenomena.
- (3) Design, procurement, and manufacture of the test motors and pyrogens.
- (4) Testing and data reduction for 2 open air igniter tests and 9 motor ignition tests. The latter included 4 tests for the determination of igniter placement effects and 5 tests for the determination of igniter mass flow and nozzle expansion characteristics.

- (5) Data evaluation and correlation and comparison of test results with the analytical models to establish aft-end ignition design criteria applicable to the 260" solid propellant motors.

Items 3 and 4, the design, manufacture, testing and data reduction, were performed for CETEC under subcontract by Atlantic Research Corporation, Alexandria, Virginia.

The results of the program technical activities are discussed in detail in the following subsections.

A. ANALYTICAL MODELS

Visualization of the phenomena of aft-end ignition may be aided by the use of a descriptive model developed during this program and previous experimental and theoretical studies. The sequence of events described by this model begins when the rocket igniter discharges a jet of hot gases forward through the nozzle of the main motor. As the igniter jet penetrates into the motor cavity, it gradually decays, expands and finally at some point becomes attached to the port walls. The penetration depth depends upon the constraining solid boundaries and the igniter and main motor design parameters which determine the jet characteristics. In cases where the jet does not completely penetrate to the main motor head-end, the expanded jet blocks the port and acts as a piston to entrap and compress the cold air initially contained within the motor port. This entrapment of cold gases in the motor port results in the formation of a stagnation zone or region which is compressed with increasing motor chamber pressure.

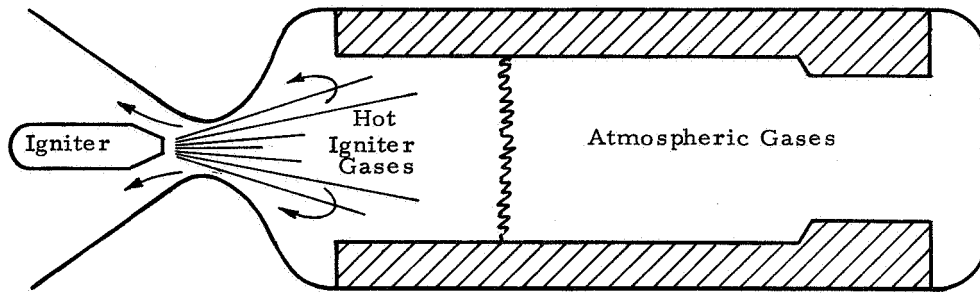
Equilibrium is established when the motor discharge rate balances the igniter jet mass flow rate. The position of the stagnation region is stable as long as the igniter mass flow rate remains constant and no propellant ignition occurs. For complete penetration, the stagnation region can be visualized as being at the motor head-end. However, in most applications, the jet has been observed to penetrate approximately 70 percent of the total motor length. Aft of the stagnation zone, the igniter gases flow in a core toward the stagnation region. As they approach the stagnation region they are reversed and flow in an annular area around the incoming jet, along the port walls and out the motor nozzle. In the area aft of the stagnation zone, the ignition process is similar to that of a head-end igniter.

First ignition occurs within the aft region at the point of maximum heat transfer and progresses aft and forward until the entire grain surface is ignited. The aft section is ignited much faster by virtue of its exposure to the full igniter convective heat flux and after first ignition, the motor combustion products. Ignition propagation into the head-end is much slower. As time progresses the ignition boundary defined by the stagnation plane propagates toward the head end of the motor. A major driving energy for the ignition propagation into the stagnation region is the radiative heat flux from the body of hot gases in the aft-end of the motor. Other important contributions are provided by conductive and convective heat fluxes on newly exposed surface areas resulting from (1) movement of the stagnation plane forward during build-up in motor chamber pressure and (2) localized penetration of the hot gases into the cold stagnation zone resulting from the turbulent mixing processes within the stagnation region.

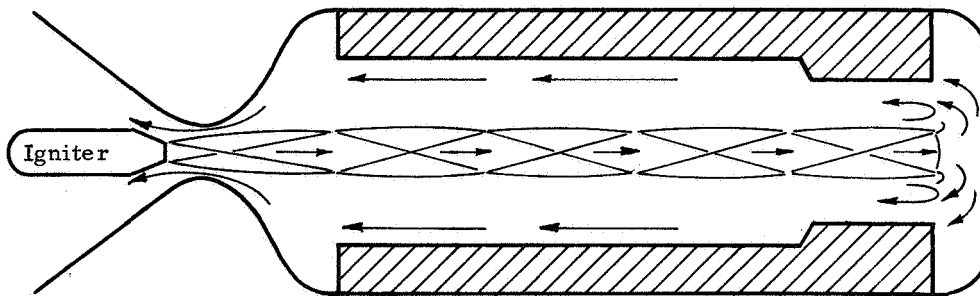
This ignition model reveals the importance of jet penetration and possible formation of a stagnation region in determining the character of aft-end ignition. Since the stagnation zone limits the fraction of propellant surface exposed to igniter convective heat flux, the existence and position of the stagnation plane and the degree of motor throat blockage have a profound effect on characteristic ignition items. High penetrations coupled with partial blockage of the motor throat during a considerable portion of the ignition interval give characteristic motor ignition transient times comparable or superior to those observed in head-end ignition. Low penetrations with slow ignition front propagation rates yield longer ignition transients with relatively large pressure rise times.

The two extreme flow situations for an aft-end igniter are represented by the two models shown in figure III-1. In figure III-1a, the condition of the exhaust from the igniter motor is such that the igniter gases expand to contact the propellant surface, block the flow port and act as a piston to compress the atmospheric gases in the chamber. This results in low penetration and subsequent delays in the ignition propagation into and along the non-penetrated region. Figure III-1b depicts the case of high penetration.

In addition to the igniter heat transfer effects upon ignition and flame propagation, the igniter jet also provides a partial blockage of the main motor throat which enhances the rate of pressure rise within the main motor chamber. If the igniter is properly located within the main motor exit cone, the igniter jet will be disorged by the main motor prior to achievement of full design chamber pressure; however, if the igniter is



a. Slight Penetration



b. Full Penetration

Figure III-1 Igniter Penetration Modes

positioned too close to the motor nozzle throat plane, the igniter jet will cause partial aerodynamic blockage of the main motor throat and will result in an undesirable elevation of the motor chamber pressure.

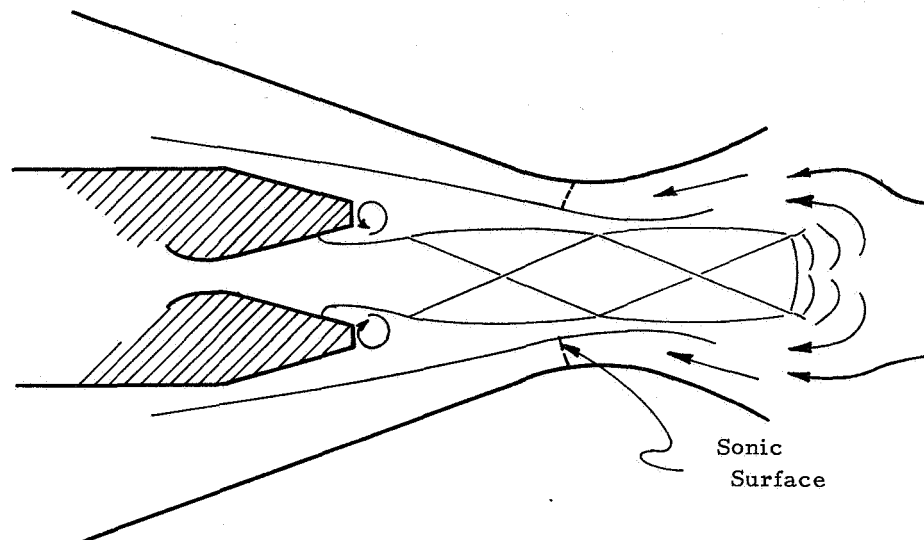
Figure III-2a presents the flow patterns which are believed to exist during the early ignition transient period when the igniter jet penetrates the main motor throat plane. The igniter jet dissipation is characterized by oblique shocks and turbulent mixing zones. The penetration at any given time is dependent upon the relative strength of the igniter to main motor flows, the igniter and motor geometries, and the conditions at the igniter nozzle exit which determine the induced igniter jet shock structure.

The flow field which is postulated to exist at motor steady state operating conditions, and which corresponds to aerodynamic blockage of the main motor throat by the igniter jet, is presented in figure III-2b. In this case, a strong shock exists within the igniter jet either within the igniter exit cone or externally in the jet flow field. Downstream of the shock, the jet flow is decelerated by the adverse pressure gradient and by viscous mixing until it terminates at the slip surface interface between the igniter jet and main motor flow fields.

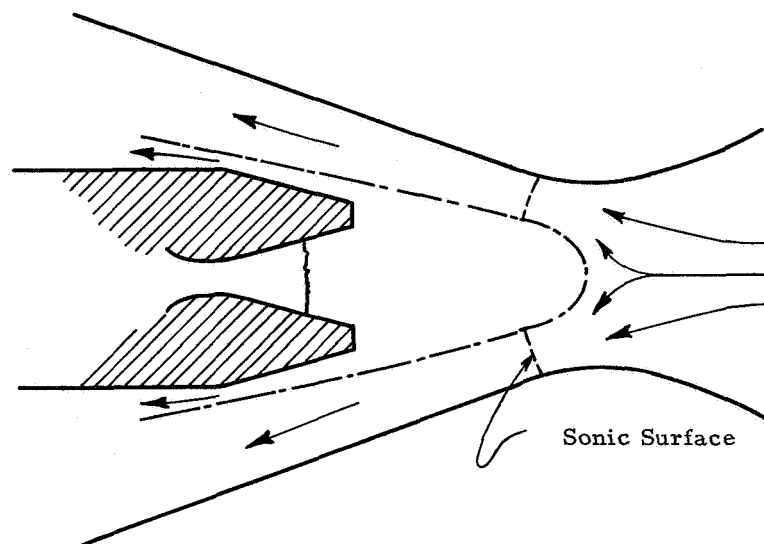
Figure III-3a and III-3b present the conditions which are believed to exist for the case of unblocked main motor flow. As in the previous case, a strong shock exists within the igniter jet. The downstream flow is dissipated by turbulent mixing interactions and opposed jet momentum transfer; however, the igniter jet body does not penetrate to the main motor throat and the main motor flow transitions normally to supersonic conditions. The igniter jet shock may occur either outside of the igniter nozzle exit cone (III-3a) or inside the nozzle exit cone (III-3b).

The main motor flow is reduced to subsonic conditions by a bow shock produced by the effective blunt body simulated by the igniter flow and is accelerated and again transitions to supersonic flow at some point downstream. It should be emphasized that the flow fields resulting from these interactions are highly complex and include regions of inviscid and strongly viscous flows, as well as mixed subsonic-supersonic flow regions.

These are the most significant phenomena which are believed to best describe aft-end ignition. The work of other investigators from which the preceding concepts were derived are summarized in the following sections along with analytical models developed during this program.



a. Weak Shock Configuration



b. Strong Shock Configuration

Figure III-2. Blocked Nozzle Flow Interactions

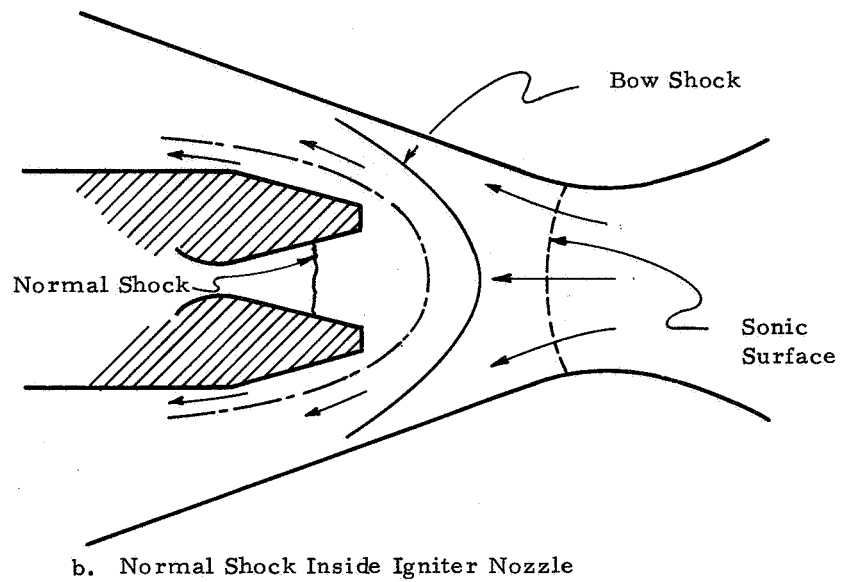
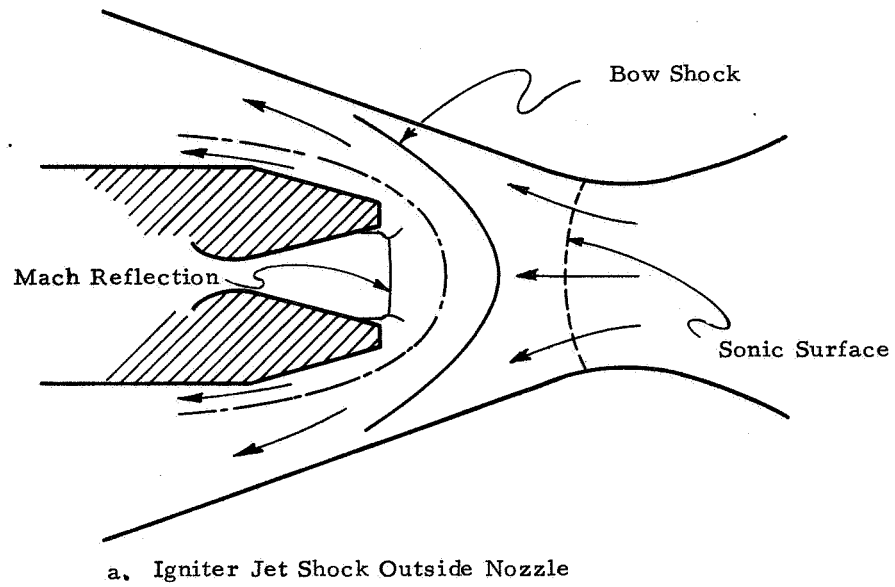


Figure III-3. Unblocked Nozzle Flow Interactions

1. Jet Penetration and the Ignition Transient

a. Background

Sufficient data to provide an accurate prediction of the aft-end igniter jet penetration and the subsequent ignition transient have not previously been generated. Aft-end igniter ignition transient prediction depends upon determination of (1) jet penetration and location of the stagnation zone, (2) initial heat input into the propellant grain prior to first ignition, (3) the percentage of motor throat blockage by the igniter jet as a function of time during the ignition transient, (4) flame propagation rates both upstream and downstream from the first ignition point, and (5) the chamber filling transient after complete ignition of the entire surface.

Early work in characterization of aft-end ignition was conducted at UTC⁽¹⁾ in tests using large thin web solid propellant test motors. These tests were made for various igniter configurations and positions, and for different motor or grain length-to-diameter ratios and characteristic chamber lengths (L^*). It was found that the relationship between igniter mass flow rate, motor port diameter and motor ignition for aft-end mounted pyrogens is quite similar to that of the head-end mounted pyrogen igniters. A major difference noted was that the igniter gases did not penetrate to the head-end of the motor being ignited, but formed a stagnation plane or zone within the main motor port cavity. The best penetration was obtained with supersonic igniters expanded to near optimum conditions. The underexpanded subsonic igniter jets did not penetrate far into the motor port but expanded, blocked the motor port and prevented further penetration. Flame propagation into the region ahead of the stagnation region was slow, and for tests with sonic igniter nozzles and motors with high port length-to-diameter ratios (L/D) a significant time increase in ignition interval was noted. The essential elements of the qualitative penetration and ignition model, presented in the previous section and developed in reference 1, were based upon these data.

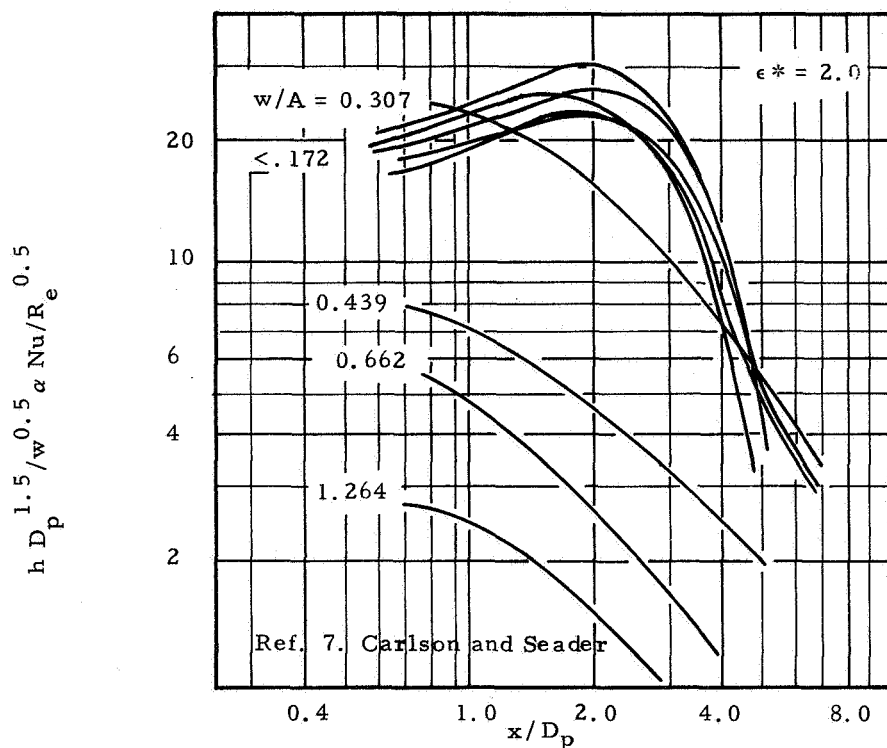
Because supersonic igniters provide the best penetration and are normally used for most practical applications, the aft-end igniter discussions which follow will pertain only to supersonic igniters operating at near optimum expansion unless otherwise noted.

Plumley,⁽⁵⁾ developed an analytical model for predicting the degree of penetration and head-end motor pressure prior to first ignition. His model, which is based upon mass and momentum balances for the igniter and main motor, assumes that one-dimensional isentropic flow

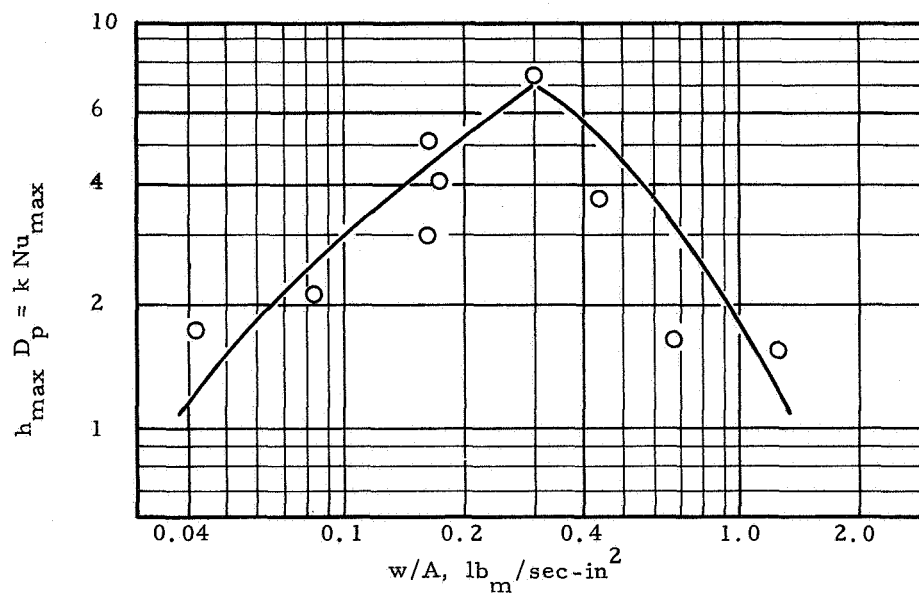
relationships are valid and that no mixing occurs between the igniter gases and the cool air trapped within the motor port. Bretting and Niessen,⁽⁶⁾ who conducted igniter firings into clear Plexiglas motors, confirmed the existence of the stagnation zone and reported that Plumley's analysis predicted the location of the stagnation zone in their tests to approximately 10% of the actual values. Carlson and Seader⁽⁷⁾ performed an experimental study of the heat transfer characteristics of hot gas igniters and concluded that Plumley's analysis predicted head-end pressure, and hence penetration, only moderately well for the data obtained in their study. Failure of the model to predict accurately the location of the stagnation zone was probably due to limitations imposed by the simplifying assumptions used in formulation of the model. Major effects not accounted for in the model included mixing between the igniter gases and cold chamber gases, energy losses due to viscous dissipation and heat transfer, and reduction of the effective flow areas in the nozzle throat due to the mixing zone between the incoming and out flowing jets.

Several investigators^(7, 8, 9, 10) have studied heat transfer from aft-end hot gas or solid propellant igniters. Carlson and Seader⁽⁷⁾ found that for cylindrical port motors the length-dependent convective heat transfer rates can be correlated using classical non-dimensional parameters. These correlations are valid only for supersonic igniters operating over a given range of the igniter mass flow parameters (w/A). The maximum value of w/A in cylindrical port motors for which their correlations were valid was $0.3 \text{ lbm/in}^2\text{-sec}$. For values of w/A greater than 0.3, the length dependency of the correlations no longer remained valid but were reduced as w/A was increased. This phenomena is illustrated in figure III-4a, which depicts the parameter $hD^{1.5}/w_i^{0.5}$ vs. X/D as a function of w/A . The manner in which the profiles decay as w/A increases indicates a reduction in both penetration depth and magnitude of heat transfer coefficient. This dual reduction is believed to be a result of interference and dissipation mechanisms between the incoming igniter jet and returning wall or port flow.

Several sources have reported that maximum penetration and minimum ignition delay is achieved for a value of $w/A = 0.3 \text{ lb/sec-in}^2$. This is supported by heat transfer data from reference 7 as illustrated in figure III-4. Here the maximum heat transfer coefficients, multiplied by the model port diameter, are plotted against igniter mass flow parameter. The diameter heat transfer coefficient maximizes for values of w/A of approximately 0.3 lbm/sec-in^2 . Wrubel and Carlson⁽⁹⁾ reported that maximum heat transfer and penetration are also obtained



a. Aft-end Heat Transfer Data for Nitrogen



b. Replotted Maximum Heat Transfer Data

Figure III-4. Aft-End Igniter Heat Transfer Correlations

for starport grains for values of w/A in the neighborhood of $0.3 \text{ lbm/in}^2\text{-sec}$. However, they reported that for conocyl port geometries the "optimum heat transfer was obtained---with the nozzle choking parameter $w/A = 0.47 \text{ lb/sec-in}^2$ under proper expansion conditions."

In pyrogen igniter heat transfer studies using an instrumented copper duct Mullis⁽⁸⁾ and Kilgroe⁽¹⁰⁾ reported that actual pyrogen igniter convective heat transfer was in essential agreement with the results of Carlson and Seader over the range of parameters tested. However, aft-end data were not collected over a sufficiently wide range of variables to provide fully meaningful correlations.

Little data have been obtained on flame propagation into the head end of aft-end ignited solid propellant motors. In an investigation of ignition and flame propagation in solid propellant motors Jensen and Cose, et. al.,⁽¹¹⁾ found that the propagation rates were a strong function of the igniter design; specifically, the igniter nozzle mass flux and the igniter nozzle configuration (expansion ratio).

It was found that time for ignition at a given point could be related to the average incident heat flux at that point. First ignition was achieved at or near the point of highest heat flux and propagated in either direction at rates dependent on the previous heat flux-time history. While the ignition propagation could be correlated with the prior heat flux input, no correlation for the heat flux input as a function of time and location on the motor grain surface was found in terms of the igniter mass flow and nozzle configuration. This resulted from the unknown relationships between igniter and main motor transient flow fields and the igniter and main motor design and positioning parameters.

In reference 12, it was found that for sonic nozzle igniter motors the penetration was slight. A five-fold increase in igniter mass flux did not appreciably improve ignition delay times. Supersonic igniter nozzles optimally expanded to atmospheric pressure indicated considerably higher penetration and flame propagation rates. Average heat flux data over the interval to first ignition, which is directly related to the rate of flame propagation, is presented in figure III-5 for various igniter mass fluxes and nozzle configurations. The highest heat fluxes which correspond to the highest flame propagation rates occur for the supersonic igniter with the highest mass flux.

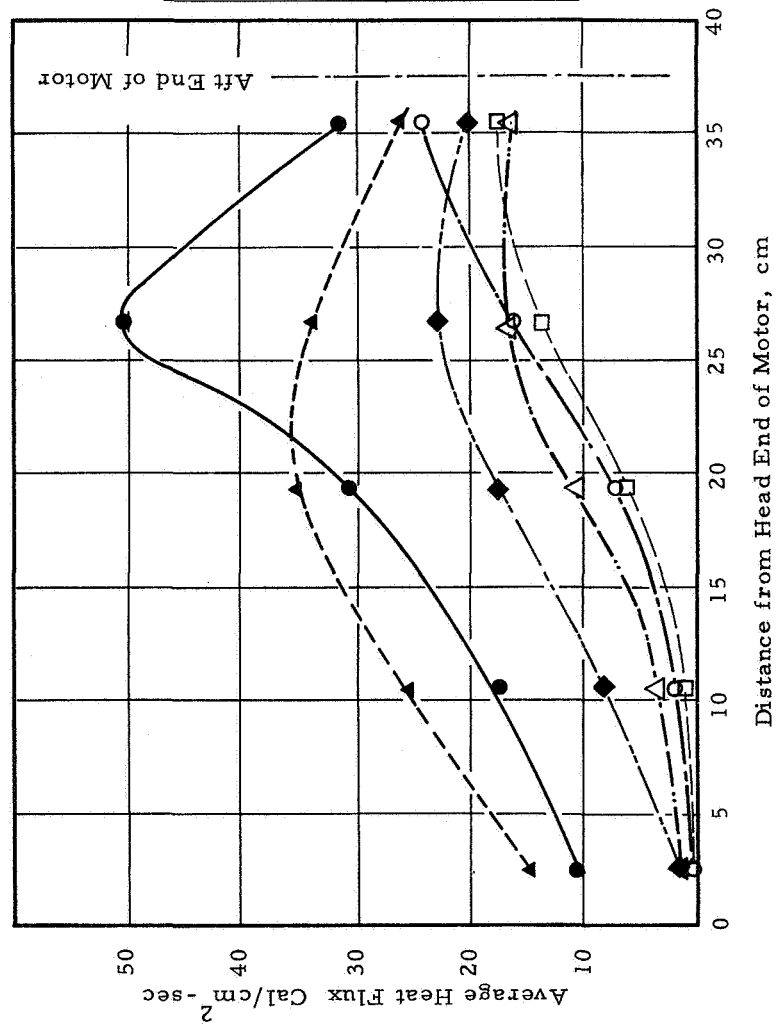


Figure III-5. Effects of Igniter Design Parameters on Motor Propellant Grain Average Heat Flux

Figure III-6 presents motor chamber pressure ignition transients for similar igniter configurations, compared with head-end igniters. High igniter mass fluxes, coupled with supersonic exhaust, provide ignition intervals which are of the same order as head-end igniters, and which are less, by a factor of four to five, than those from aft-end sonic nozzle igniters.

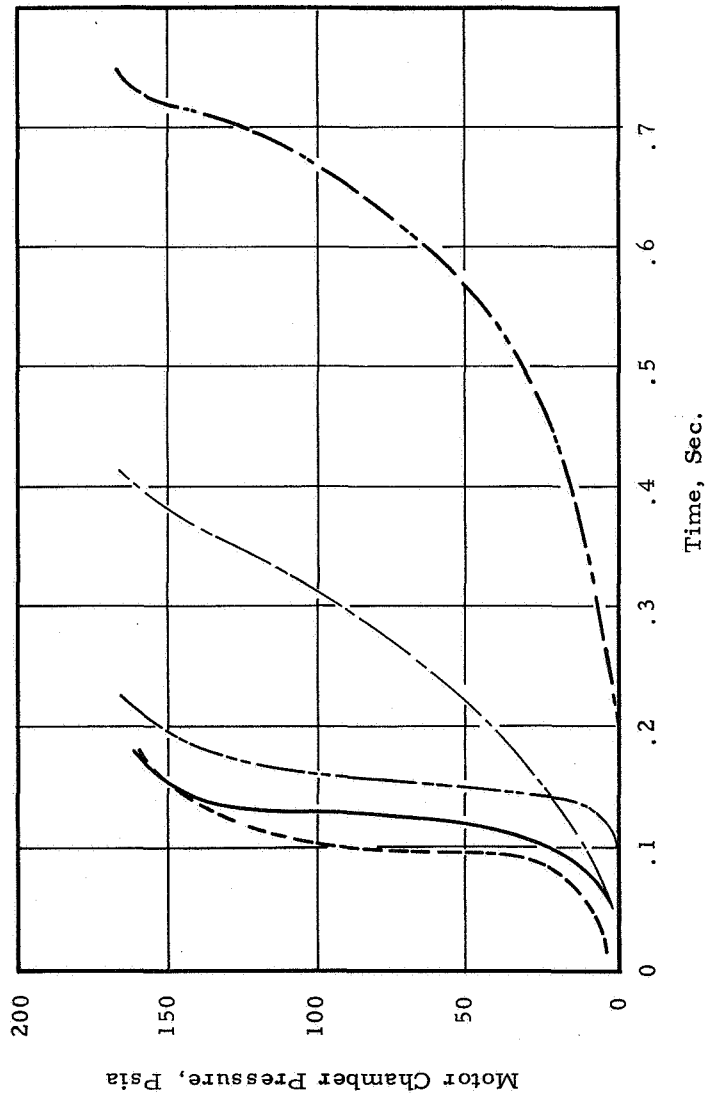
Another important aspect of the aft-end ignition transient is the reduction of the main motor throat effective flow area by the penetrating igniter jet. The principle affect of this penetration is the influence upon the motor pressure time history and resulting modifications of the jet and internal motor flow field. A parameter which has been used to experimentally characterize the geometrical effects of the relationship between the igniter and main motor nozzle is the epsilon star (ϵ^*) parameter. This is defined as the ratio of annular area between the igniter and main nozzle to the motor throat area (see figure III-7).

To avoid overpressurization of the main motor the value of ϵ^* must be greater than one, i. e., the annular area around the igniter must be greater than the motor throat area. The importance of ϵ^* in determining the pressure transient for a given igniter-motor combination stems from the axial shift in the pressure and heat transfer profiles, and the change in degree of igniter jet penetration of the motor throat during the ignition transient (and hence pressurization rates) which accompany the axial movement of the igniter with varying ϵ^* .

b. Jet Penetration Model

Ignition and flame propagation in aft-end ignited solid propellant motors is strongly dependent upon igniter jet penetration and the associated heat transfer characteristics of the counter-flowing gas field within the motor port. Methods of predicting jet penetration and subsequent heat transfer are currently limited to an analytical model⁽⁵⁾ which at best provides a qualitative description of penetration, and empirical data which give length dependent heat transfer correlations for some typical motor configurations^(7, 9).

Work was begun during this program to develop an analytical model to describe the dynamic flow field within the motor port in the time interval before first ignition of the solid propellant grain. The intent of the



	Placement	Igniter Mass Flux $G/cm^2 \cdot sec$	P_i Psia	Nozzle
---	Aft-end	1.55	1500	Supersonic
----	Head-end	1.46	500	Sonic
---	Aft-end	1.85	500	Supersonic
----	Aft-end	2.53	500	Sonic
---	Head-end	1.64	500	Sonic

Figure III-6. Motor Pressure Transients for Various Igniter Configurations

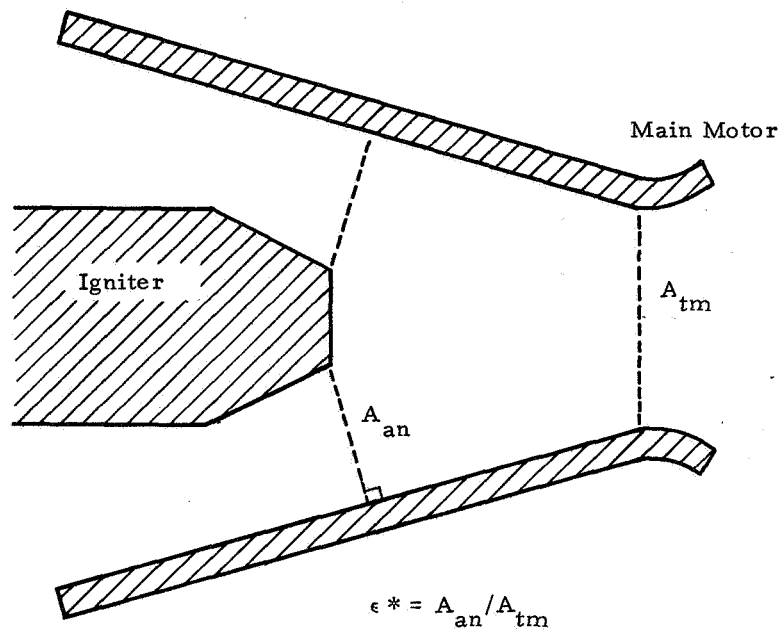


Figure III-7. Geometrical Epsilon Star Relationship

model was to characterize the jet penetration, motor throat blockage and counterflowing igniter gas field along the cylindrical port propellant grain wall prior to ignition. With analytical data on the effective velocity field within the port, and by use of experimental heat transfer data, it may be possible to analytically describe and predict, by classical methods, the convective heat transfer and subsequent flame propagation.

Due to the complexity of this model, the computer program for solution of the model was not completed during the current program. Work completed on the model is described in the following section and in Appendix B.

The jet penetration model is based upon the assumption that the general interactions between the penetrating jet and counterflowing wall stream are similar to those described by Abramovich⁽¹³⁾. However, the current solution is for compressible flow and is concerned at present only with the turbulent mixing region aft of the cross section where flow reversal mechanisms predominate.

A simplified diagram of the propagation of a turbulent jet into a dead-end channel is shown in Figure III-8. Here it is assumed that the motor port corresponds to the longitudinal section of a channel with a height or diameter $2H$. The igniter jet of initial diameter $2b_0$ and constant exit velocity U_0 is discharged into the channel at the open end. As the jet moves downstream from the igniter exit in section 1, the thickness, b , of the zone in which the jet mixes with the surrounding fluid, is enlarged and the constant velocity potential core in the jet is narrowed and ultimately dissipates completely. This is called the initial area of the jet. The region beyond this point, in which the axial velocity u_m drops as the distance from the initial region increases, is called the principal region of the jet. At a certain section 3, the jet begins to turn and the direction of the flow is reversed. Between section 3 and the stagnation zone in the motor head-end, a flow reversal region exists. An analysis of the flow reversal in this region was not incorporated in the analytical model developed in this program; however, it may be possible to approximate the flow in this region by using potential flow theory and conformal mapping.⁽¹⁴⁾

Between the lateral boundary of the jet and the channel wall a region of back flow exists with an average wall flow velocity at any axial location given by u_H .

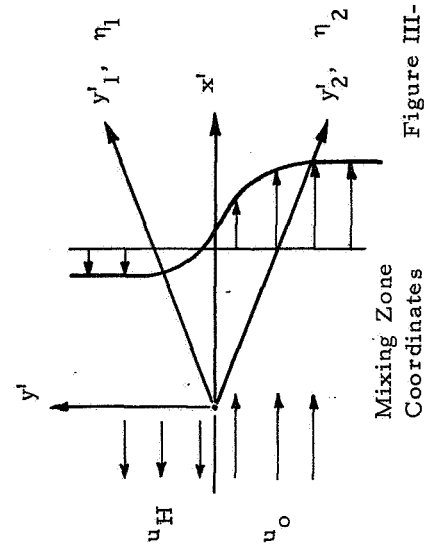
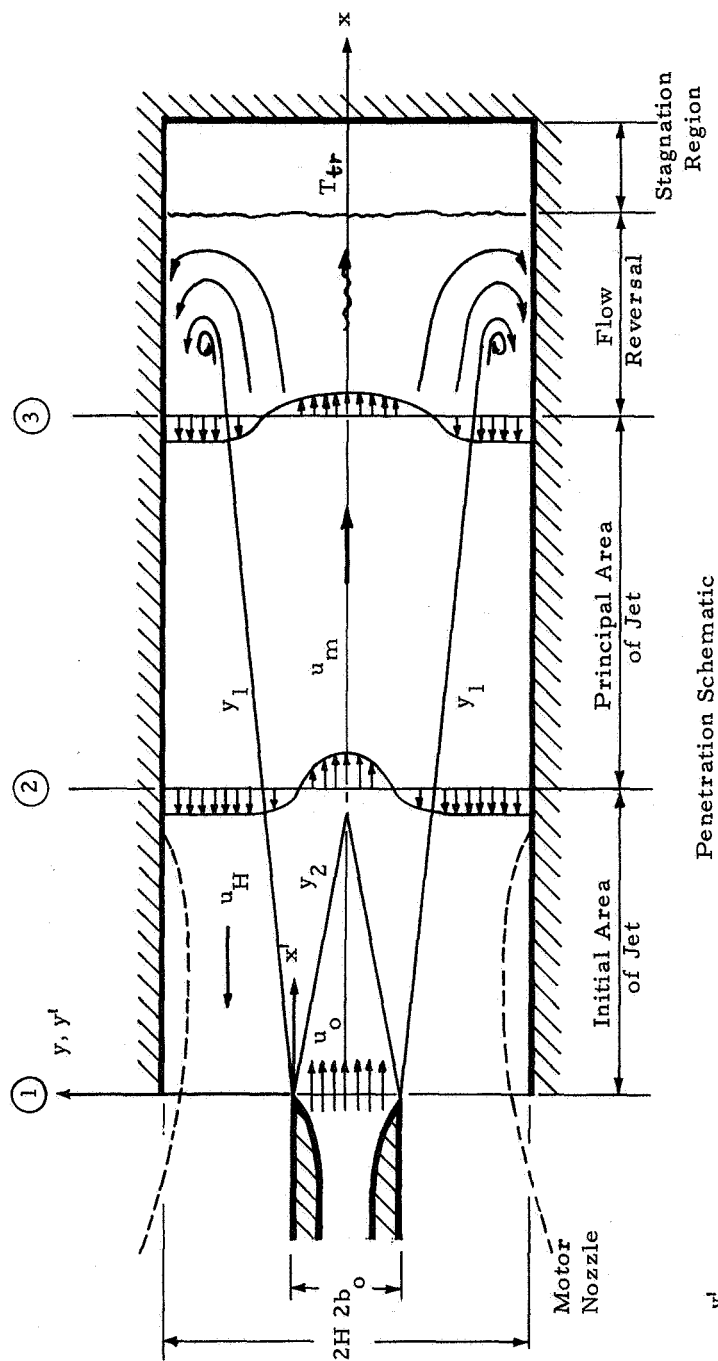


Figure III-8. Jet Penetration Model Schematics

In an actual motor the average wall flow velocity will be modified by the area ratio effect of the motor throat between sections (2) and (1). In the test motor design, the actual port-to-throat area ratio is in the neighborhood of 1.8. It is therefore assumed for the current model that the increased wall velocity will have negligible effect upon the mixing zone profile, and area ratio change may be neglected.

The basic coordinate system is taken with the positive x-axis along the centerline of the igniter and motor chamber with the origin at the igniter exit plane. A schematic of the principle coordinate systems are also presented in figure III-8.

The mathematical model is developed in two interdependent parts. In the first part, the average time dependent properties and their rate of change in the motor chamber are calculated on an inviscid basis by application of the one-dimensional forms of the conservation equations of mass, energy and momentum, the equation of state, and by use of a mass accumulation parameter (\dot{m}_c). In the second part, steady state flow field quantities are found by substitution of a motor-to-igniter velocity ratio ($\alpha = U_H/U_O$) and the motor mass accumulation factor (\dot{m}_c) into the equations describing the viscous turbulent flow field in the initial and principle areas of the jet. Solutions from the two parts are compared and corrections are made in the assumed values of α and \dot{m}_c .

Chamber Parameters

Relationships between the basic fluid properties in the chamber are derived by use of the one-dimensional forms of the equations of conservation of mass, momentum and energy and the equation of state. However, one additional equation is needed to determine a unique solution for this system of equations. In the current form of the program this is provided by use of a mass accumulation term (\dot{m}_c) which, in essence, specifies the instantaneous rate of chamber pressure increase for any set of input conditions. Use of this mass accumulation parameter in effect linearizes the penetration model so that the flow field may be solved independently of the average chamber parameters. This was done to reduce the problem of simultaneously solving both the flow field and chamber equations to obtain meaningful solutions for checkout of the total program. Once the flow field model has been verified, a relationship from the flow field, which provides the final equation for a unique solution of the chamber parameters, can be provided.

Basic assumptions which were used in formulating the equations describing the chamber outlet properties were:

- (1) Conservation equations taken on the control volume can be expressed in basic one-dimensional form.
- (2) Heat lost to the surroundings can be neglected.
- (3) Original gas forward within the chamber of the motor throat is initially at atmospheric conditions, is completely trapped by the incoming igniter gases and does not mix with the hot igniter gases.

Although it was assumed that no heat was lost to the chamber walls, the incorporation of the energy equation was necessary because of the mass accumulation within the chamber.

Motor Chamber Flow Field

In order to define the motor chamber flow field, it is necessary to analytically construct the velocity field induced by the jet in the dead-end channel and to determine the coordinates of the characteristic sections including the end of the initial area of the jet, the beginning of the jet reverse flow and the mixing zone boundaries. The solution to this problem will only be summarized in this section. The basic equations used in the solution appear in Appendix B.

Integral forms of the mass and momentum equations in the initial and principal area of the jet are expressed in terms of dimensionless parameters. These non-dimensional parameters represent the geometrical constants, the non-dimensionalized coordinate system and the physical properties within the flow field as shown in figure III-8. The unknowns are the local density and velocity and the mixing zone profile.

In the initial area of the jet, the mixing zone profile coordinates are determined by solution of the axi-symmetric compressible viscous boundary layer equations of continuity and momentum. The energy equation is satisfied since energy losses to the surroundings are assumed negligible. The mass and momentum equations are transformed to the incompressible plane by Howarth's⁽¹⁵⁾ transformation. By use of Prandtl's⁽¹⁶⁾ compressible jet spread parameter, the transformed equations are reduced to a single third order differential equation. This equation is solved by Tollmein's⁽¹⁸⁾ method with the constants of

integration being found by use of the boundary conditions. The resulting solution gives the mixing zone profile in terms of the local velocity and density. The number of independent variables is further reduced by using the equation of state and assuming that the pressure is constant in any plane normal to the motor centerline. The density profile is related to the enthalpy profile, which is, in turn, related to the velocity profile by means of the Crocco⁽¹⁶⁾ integral relation.

In the principle area of the jet, the velocity profile is expressed by an empirical formulation and by assuming that the stagnation enthalpy is constant along the jet centerline. As before, the stagnation enthalpy is related by the Crocco integral to the density profile.

The solution of the mixing zone profile and relationships between the velocity and density profiles in the initial and primary regions of the jet are substituted into the integral momentum and mass equations for the respective regions, which are integrated to obtain equations giving an algebraic solution of the flow field.

There is a major difficulty apparent in the current model. Results of the computer analysis show that solutions to the flow field equations are limited to values of α greater than -0.2088. Flow field equation solutions over the range of possible mass accumulation parameters will not be found within the range of α 's permitted by the conservation equations. It is possible that this discrepancy results from the use of a particular solution of the jet profile used in the initial area of the jet. The method initially used, which employed Tollmein's solution of the boundary layer equations and incorporated a jet spread parameter, has been shown to be applicable to parallel flowing jets. It is possible that it is not applicable to counter-flowing jets. To further investigate this possibility, an analysis using the velocity profile based upon an integral approach as formulated by Abramovich⁽¹³⁾ was made. Preliminary hand calculations using Abramovich's method indicated that the velocity ratio has a lower bound with a value in the neighborhood of -0.2 to -0.3. If correct, these results appear to indicate that the previous methods might still provide satisfactory results for analysis of counter flowing streams. This postulation, however, must be verified by further analytical work and comparison with experimental data.

2. Throat Blockage

a. Background

In the past, aft-end ignition of large solid motors has been accomplished by mounting pyrogen igniter units of considerable size

in the exit cone of the main motor a short distance downstream of the main motor throat plane. Overpressurizations have been prevented by ejection of the igniter at some time after ignition has occurred, but before the full chamber pressure has been reached,^(1,2,3) More recent cold flow studies have indicated that overpressurizations can be prevented by proper design and location of the igniter obviating the necessity of complicated igniter ejection system.⁽⁵⁾ However, these results have not been verified by firings using solid propellant motors and fixed aft-end igniters.

It should be noted that overpressurization and nozzle flow blockage are not always synonymous. Nozzle blockage occurs when, for a given set of igniter and main motor flow rate and pressure conditions, the motor throat is physically obstructed by the igniter jet or is caused to separate abnormally at the motor throat plane. Overpressurization results from blockage only when the required flow cannot be accommodated by the modified throat area except at a chamber pressure which is higher than the normal operating pressure required to pass the flow from the fully burning grain surface area. Thus overpressures are defined herein as a condition of elevated pressure which occurs in conjunction with flow blockage only after normal steady state burning conditions are achieved within the solid propellant motor.

The axial placement of the aft-end igniters in large solid motors as a means to avoid motor overpressurization was first studied at UTC⁽¹⁾. As a result of this work, the parameter ϵ^* (ratio between the annular area formed by the nozzle wall and the igniter exit plane, and the motor throat area) was formulated to be an effective parameter for description of the overpressurizing potential of a given geometric arrangement. Based on test data, it was postulated that the annular area to main motor throat area (ϵ^*) be greater than approximately 1.1 to avoid overpressurization.

In later work conducted at AFRPL⁽⁶⁾, it was observed that overpressures were possible with ϵ^* locations as high as 1.4, indicating that the main motor flow does not choke-off the igniter flow, for all cases, where the theoretical flow area (ϵ^*) is greater than unity. At times the igniter motor continues to operate after significant flow from the main motor is encountered, and although ϵ^* may be greater than 1.0, the interaction between the main flow and igniter flow can be of such severity as to impose

a virtual gas dynamic throat on the main stream of less area than that of the motor physical nozzle throat, causing sizeable overpressures. Consequently, the intricate characteristics of the two counter flowing streams must be analyzed in sufficient depth to accurately assess the significance of the various interactions.

The fluid dynamics of a supersonic jet exhausting into a counter-flowing stream has received limited attention. Due to the complexity of the supersonic jet mixing problem, a clear analytical solution does not exist and only a few experimental results are available. Mainly, the experimental results on these types of flow fields have been performed on re-entry configurations to evaluate schemes for modifications of the plasma sheath surrounding the blunt bodies or to determine the effect of retrorockets on the aerodynamic characteristics of re-entry bodies.

Work by Romeo and Starrett⁽¹⁹⁾ on the effects of a forward-facing jet on the bow shock of a blunt body indicates that when a supersonic jet is exhausted into a counterflowing supersonic stream, two basic flow configurations may exist. These experimentally observed flow patterns are characterized by either strong or weak bow shock interactions.

In the case of the strong shock configurations typified by figure III-3, two strong shocks exist in the flow, the first reducing the main-stream flow to subsonic flow. The second shock exists near or within the igniter nozzle reducing the igniter flow to subsonic values.

For the other flow configurations, which is similar to that depicted in figure III-2a, considerable energy transfer occurs in oblique shock interactions and in the jet mixing region of the jet which is terminated at the igniter slip surface. This is called the weak shock interaction. For some configurations tested by Romeo and Starrett⁽¹⁹⁾ the stand-off distance for the weak shock was sometimes found to be eight times higher than the standoff distance for the strong double shock pattern. Obviously, the weak shock configuration must be avoided in aft-end igniter design as it would probably result in penetration of the main motor throat plane and main motor overpressurization.

For the strong shock solution, (Figure III-2), the stagnation pressures in the subsonic mixing zones downstream of the main motor shock and downstream (with respect to the igniter) of the igniter must be equal. These stagnation pressures are determined by the main motor and igniter motor stagnation pressures and by the Mach number at which both jet and mainstream shocks exist.

Similarly, the stagnation pressures at the slip surface interface between the igniter and main motor flows in the weak interaction configuration must also be equal. However, since the proper conditions for shock total pressure losses do not exist in the igniter jet, the required total pressure losses must be achieved through a series of oblique shocks and viscous erosion, leading to high penetration distances.

Figure III-9 constructed from data from reference 19, shows the regimes of strong and weak shock interaction for two forward facing air jet models operating in a Mach six free stream. These data which are for conical and contoured model nozzle configurations show the main stream bow-shock stand-off distance normalized by the model diameter (ℓ/dm) versus the jet to main-stream total pressure ratio (P_j/P_∞). Both models were constructed with model to jet diameter ratios of 1:12, identical throat and exit areas, and operated at a nominal jet exit Mach number of 6.4.

The contoured nozzle displays higher main-stream shock-displacement distances over a wider range of total pressure ratios. For total pressure ratios greater than

$$\frac{P_j}{P_\infty} = \frac{\left(\frac{P_2}{P_1}\right)_\infty^{M=6.0}}{\left(\frac{P_2}{P_1}\right)_j^{M=6.4}} = 1.31,$$

it is postulated that stagnation pressure losses in the jet occur outside the model nozzle. Since the diverging jet flow in the conical nozzle is underexpanded for $P_j/P_\infty > 1.3$, it readily expands outside the nozzle to the Mach number ∞ at which the stagnation pressure adjustments across the jet and main-stream bow-shock may equalize. In the case of the contoured nozzle, the underexpanded jet which emerges in parallel flow from the nozzle exit cone apparently does not expand to a sufficiently high Mach number to accommodate a shock of the required strength, but, instead goes through a series of oblique shocks and viscous mixing before sufficient erosion of jet momentum.

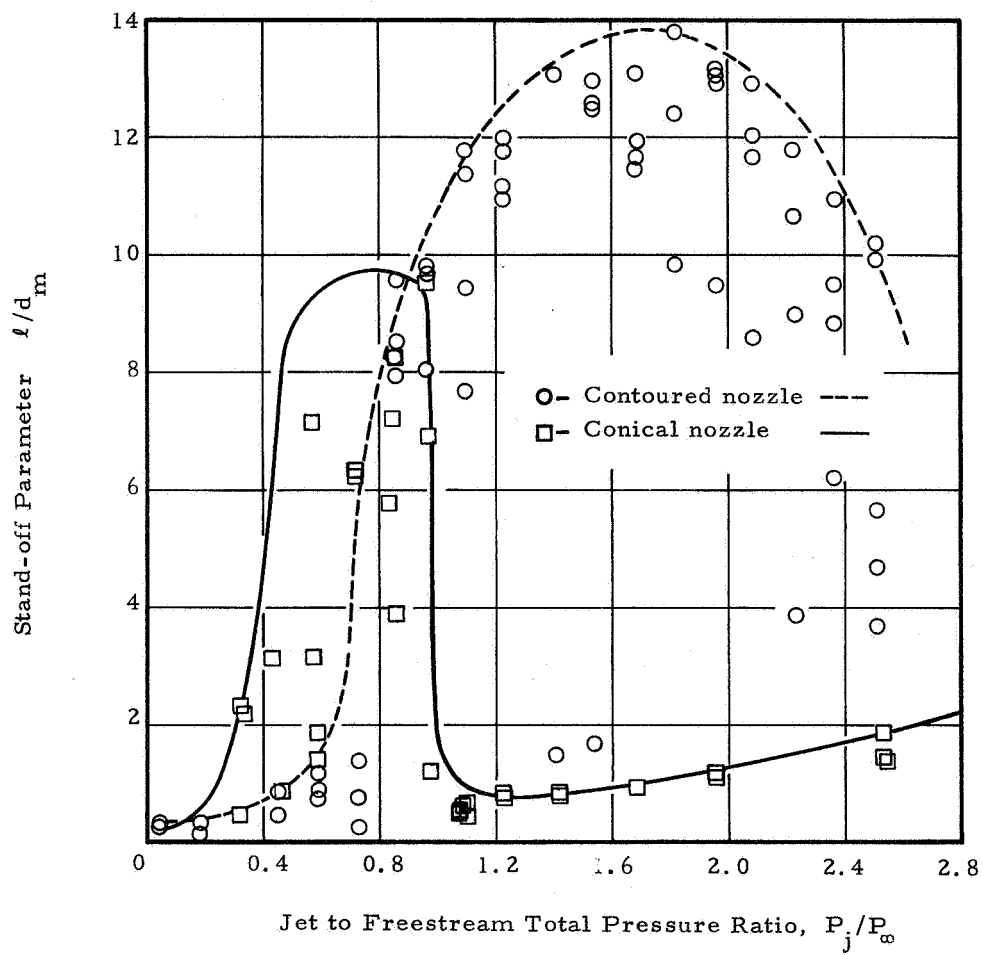


Figure III-9. Counter-Flowing Free Stream Bow Shock Stand-off Distances

For jet to main-stream stagnation ratios less than 1.31, the jet either separates from the exit cone in response to the adverse pressure gradient or goes through a normal shock pressure adjustment within the model nozzle exit cone. Differences in the stand-off distances over this range of pressure ratios result from response of the two different nozzle configurations to the effective model nozzle pressure ratio.

These data indicate that to prevent large jet penetrations during full motor flow condition, the igniter nozzle should be conical and the igniter-to-motor chamber pressure ratio and back pressure conditions should be large enough to assure operation in the strong shock interaction regime.

Salmi⁽⁵⁾ at NASA-Lewis conducted an experimental program to study throat blockage effects upon combustion chamber pressure. These tests were made in a Lewis Propulsion Systems Laboratory altitude chamber and used a 1/14.2 scale model to simulate the configuration used in the NASA 260-inch diameter solid rocket motor program. The igniter and solid propellant motor gases were simulated with compressed air. Five different model configurations were used to investigate the effects of various igniter design parameters.

The results of the study indicated that igniter interference could cause large overpressures in the booster rocket combustion chamber. The magnitude of the interference effect of the simulated igniter was dependent on the igniter position, diameter, ratio of igniter-to-booster total pressure, and weight flow. At low igniter-to-booster chamber pressures, which correspond to the condition where the booster rocket is at its design chamber pressure, the interference effect varied greatly with igniter position. Increases of up to 60 percent in the booster chamber pressure, which were dependent upon igniter geometry, were noted when the igniter was positioned 0.2 booster diameters downstream of the booster nozzle throat (X/D_{tm}). At a station corresponding to 0.6 diameters, the interference effects were generally negligible.

At high igniter-to-booster pressure ratios, which reflect low booster chamber pressures during the initial ignition phase, the booster chamber pressure was greatly increased by the igniter jet, as desired for rapid ignition. However, at these pressure ratios, the position of the ignition rocket in the booster nozzle had little effect on booster overpressure.

A schematic of the igniter and booster model test setup used in Salmi's experiments is shown in figure III-10. To simulate the effect of gas generation from the burning solid propellant booster grain, the inner surface of the booster model grain was constructed of perforated steel. The perforated area was about 65 percent of the booster-nozzle throat area. The pressure across the simulated grain was maintained at a value such that the orifices in the grain remained choked at all times. In this manner, the mass rate of flow into the booster model remained independent of igniter position or mass flow effects. The igniter and booster nozzle geometries used are shown in figures III-11.

In general, increases in the booster rocket chamber pressure were displayed at increasingly higher igniter-rocket position parameters (X/D_{tm}) as the ratio of igniter to booster total chamber pressures was increased. Little or no blockage was found for no igniter flow if sufficient nozzle flow area was available for the motor flow, ($\epsilon^* \geq 1.0$). Overpressures in the booster chamber pressure for the cases without igniter flow begins at position parameter locations which correspond closely to values of $\epsilon^* = 1.0$.

The effect on the booster rocket chamber pressure due to the ignition rocket is shown in nondimensional form in figure III-12 for model 4. These curves are presented for selected positions of the ignition rocket in the booster nozzle as defined by X/D_{tm} and ϵ^* . They show the ratio of the incremental chamber pressure increase ΔP_m to the initial combustion chamber pressure $P_{m,0}$, as a function of the ratio of the ignition rocket total pressure P_i to the booster-rocket initial pressure.

Both the igniter position and the igniter-to-booster pressure ratio have a large effect on the degree of interference. The pressure ratio for a large booster such as the 260-inch solid rocket varies from about 67 at first ignition to about 1.67 at full booster chamber pressure. The curves in figure III-12 indicate that, in general, the interference effects decrease rapidly with decreasing pressure ratio. However, at low values of $P_i/P_{m,0}$, this trend suddenly decreased and, in some cases, was reversed at a pressure ratio of about 3.

In general, the variation of the interference effect with igniter-to-booster pressure ratio can be correlated with the flow models. At high pressure ratios, the shock recovery pressure of the expanded ignition-rocket jet is considerably higher than the booster and a pressure increase is produced in the motor chamber. When the chamber pressure is increased, the supersonic expansion of the ignition jet is limited so that its shock recovery pressure is equal to the booster chamber pressure. The flow

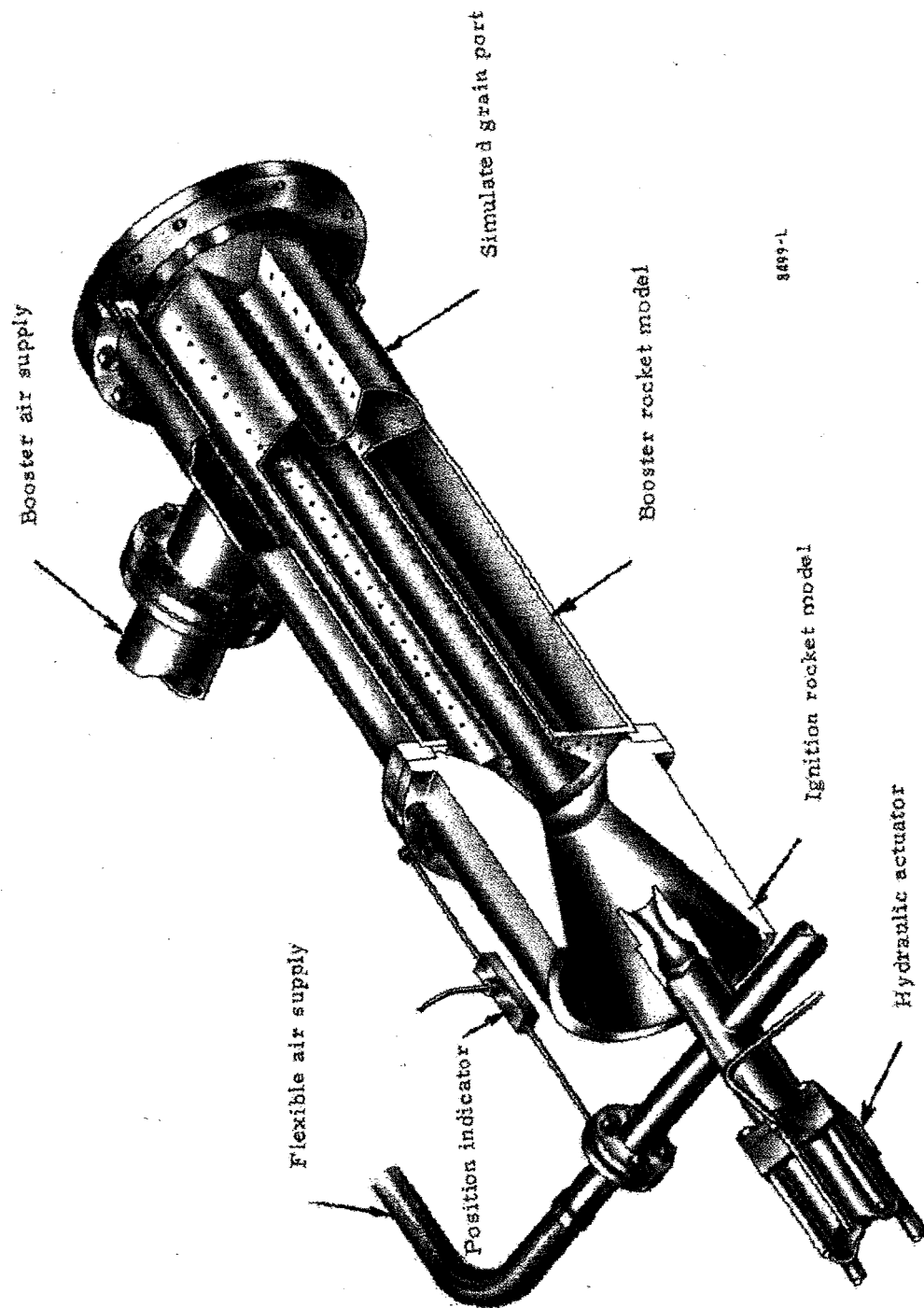
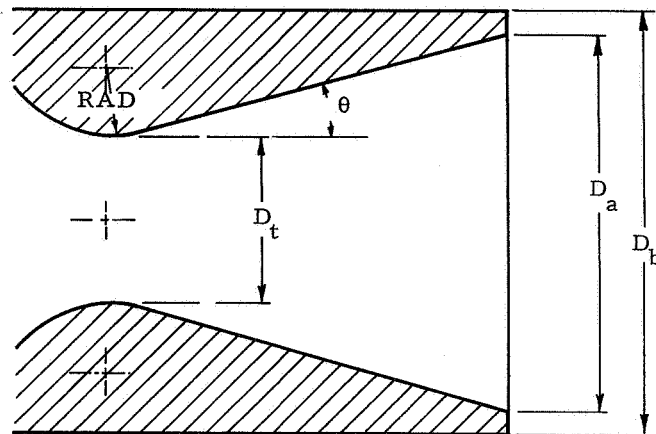


Figure III-10. Compressed-Air Overpressurization Test Apparatus



	Model	Outside Diameter, D_b , in.	Throat Diameter D_t , in.	Nozzle Exit Diameter D_a , in.	Radius, RAD in.	Nozzle Half Angle, θ , Deg.
Igniter	1	2.11	1.02	2.11	2.04	15
	2	2.85	1.02	2.11	2.04	15
	3	2.53	1.21	2.52	2.42	15
	4	2.85	1.21	2.52	2.42	15
	5	2.85	1.51	2.84	3.02	15
Booster		13.5	5.0	12.28	2.5	17.5

Figure III-11. Igniter and Booster Nozzle Geometries

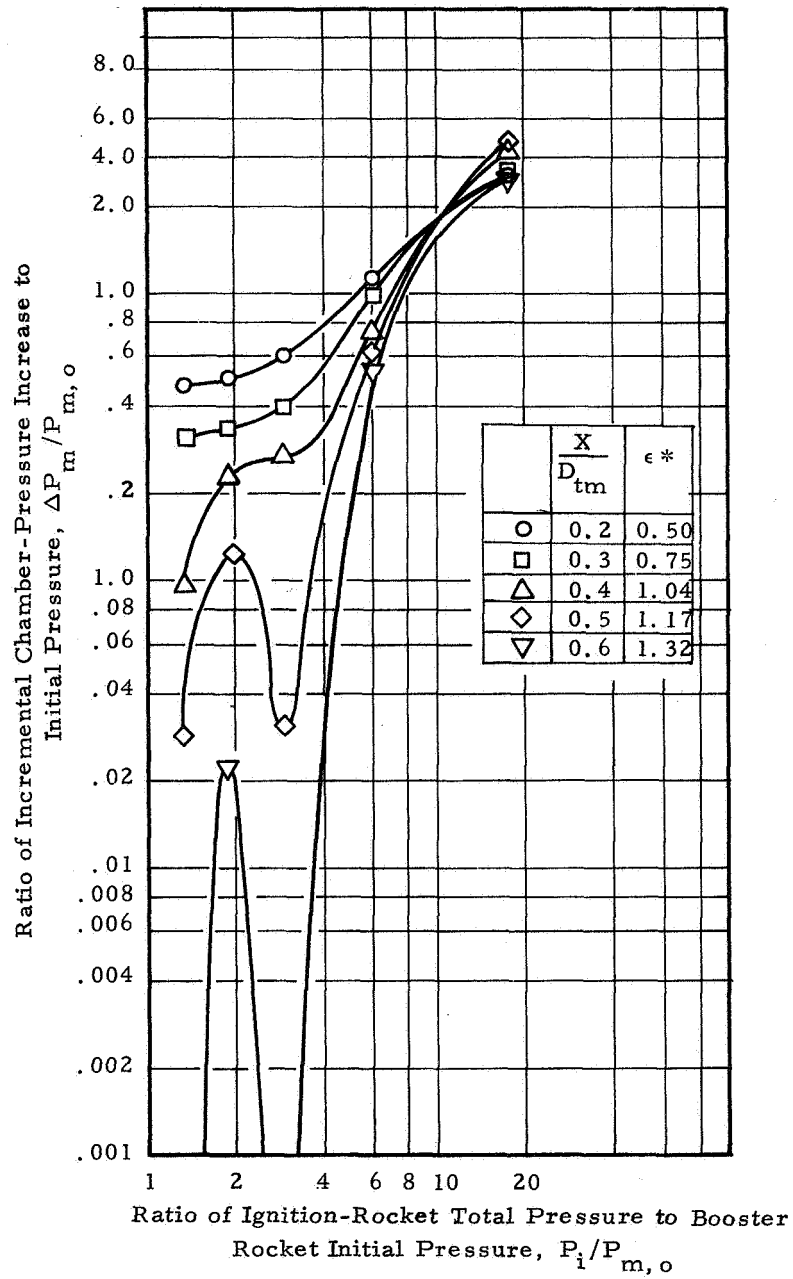


Figure III-12. Effects of Igniter Pressure and Position on Booster Pressure

phenomenon is similar to that shown in figure III-2 where the booster exhaust flow passes through the annular flow area outlined by the interface of the reversed ignition jet flow and the nozzle wall. With further increases in the booster chamber pressure, the jet flow and the jet shock wave are diminished to the point where they occur at the ignition-rocket nozzle exit or within it. At this point, the total-pressure loss of the jet becomes small with a correspondingly small variation of its external sonic flow area. The interference effect, should, therefore, exhibit small variations at low igniter-to-booster pressure ratios; however, there is evidence which indicates that this is not always the case.

Some experimental data generated in the current program indicates that a normal shock within the igniter nozzle is not always established at the proper Mach number (area ratio) such that the shock total recovery pressure of the igniter is equal to the booster total pressure. At low igniter-to-booster total pressure ratios the shock (s) must occur at a low area ratio to satisfy matching of the igniter jet shock recovery pressure and booster stagnation pressure; however, conditions do not always exist in the igniter nozzle to induce a shock at the correct location. Instead, the effective igniter nozzle back pressure may force the igniter to operate in a regime characterized by nozzle flow separation and oblique rather than normal shock interactions.

In the oblique shock case the total pressure reduction corresponds to the weak shock interactions reported by Romeo and Sterrett. For the weak (oblique) shock case, the jet penetration can exceed the strong (normal) shock jet penetration even though the igniter-to-booster total pressure ratio is less than for the strong shock. Changes in blockage mechanism from strong to weak shock interaction possibly explain the reversal observed by Salmi in incremental overpressurization as the igniter-to-booster total pressure ratio was decreased below 3.

b. Blockage Model

Following a review of applicable aft-end ignition work, analytical models were developed to predict the positioning and design parameters for fixed aft-end igniters which would avoid overpressurizations at full main motor flow.

Interpretation of the basic work of Romeo and Sterrett on counterflowing streams led to the formulation of the three simple theoretical models describing the interactions of the igniter jet with the main motor flow for both blocked and unblocked flow conditions.

These models, which were discussed more completely in previous sections, are shown schematically in figure III-2 and III-3. The first, figure III-2a, corresponds to flow patterns in which the igniter penetrates the throat plane before reversing direction. Losses in the jet are principally through viscous mixing and a series of oblique shocks. In this model, the virtual throat for the mainflow gases is formed in the annular region between the main throat wall and the igniter jet, resulting in a reduced throat area and subsequent chamber pressure increases.

The second model shown in figure III-2b also results in blockage of the main motor flow. Here the igniter jet does not penetrate into the nozzle throat plane, but the interaction between the streams produces a virtual throat for the main motor flow which is less than the design throat area. Igniter jet total pressure losses may be either through normal or oblique shock interactions.

In the third model, figures III-3a and III-3b, the igniter jet does not penetrate into the motor throat plane and the flow interactions do not provide a virtual throat area downstream of the main motor throat. The main motor flow is choked at the physical motor throat and motor chamber conditions are not influenced by the igniter and main motor flow interactions.

In the sequence of ignition events the igniter flow must at some time transition from the first into the second mode of operation and finally into the third, if the motor is to operate under unblocked conditions. The analytical model developed during the current studies is applicable to conditions described in the second model and under certain limitations, the third. By application of conditions which exist at the transition point, i.e., attainment of choked flow at the main motor throat, the minimum igniter design and placement parameters which specify conditions to avoid overpressurization, are established.

The analytical model is based upon mass and momentum balances taken on a control volume contained within the main motor nozzle exit cone. Figure III-13 shows a schematic of the control volume and the pressure and mass flow distributions used for the mass and momentum balances. Basic geometric relationships taken into consideration in

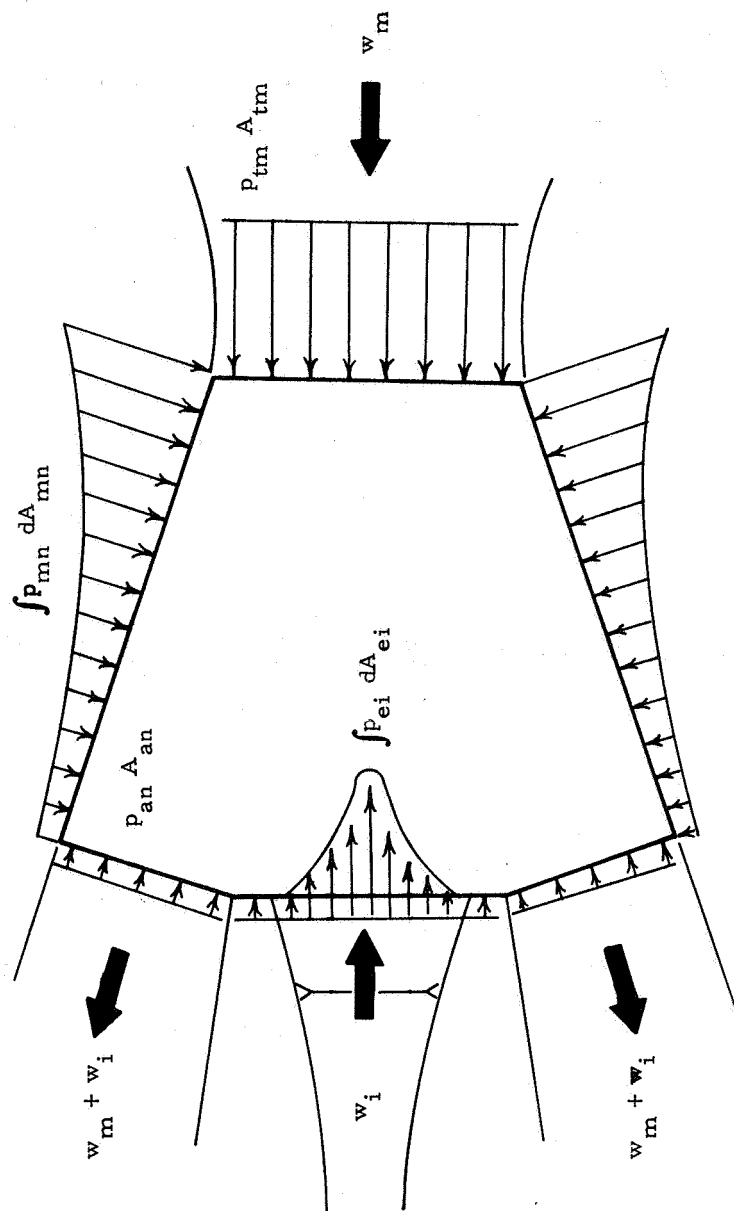


Figure III-13. Analytical Blockage Model Control Volume

the model include: main motor and igniter throat areas, igniter exit area, igniter body outside diameter at the exit plane, main motor nozzle divergence half angle and igniter to main motor ϵ^* location.

In formulating the model the following assumptions were made:

1. Motor and igniter exhaust products are assumed to exhibit perfect gas behavior. Two-phase flow, chemical reactions and viscous interactions are neglected. Consequently the flow entering and leaving the control volume may be described by isentropic flow relations.
2. Pressure forces are constant across the motor throat plane and annular flow passage around igniter body.
3. Pressure forces along the main motor exit cone assume a parabolic shape.
4. Pressure forces across the igniter exit are expressed by a polynomial.
5. Any main motor flow shocks occur at a sufficiently low Mach number so that the total pressure losses may be neglected.
6. Heat transfer effects are small in comparison with mass and momentum effects and may be neglected.
7. The respective total temperatures, gas constants, and isentropic exponents of the igniter and main motor gases are equal.
8. A normal shock occurs within the igniter nozzle exit cone or at an appropriate igniter jet area ratio in the control volume such that the igniter total pressure is equal to the motor total pressure.

Taking into consideration the preceding assumptions, the mass and momentum conservation equations were written for the defined control volume and were coded for computer solution. Solutions of the problem were obtained for a specified igniter and main motor geometry and ϵ^* location by assigning an igniter-to-main motor total pressure ratio and

by iterating on the main motor throat Mach number until the solution of the mass and momentum equations were satisfied by the assumed conditions. Alternatively, the Mach number at the throat could be assumed with iteration on the igniter-to-main motor total pressure. The basic equations used in the blockage model and detailed computer program information are presented in Appendix A.

Solutions from the blockage model computer program for an igniter (Model 1) and main motor geometry identical to that used in Salmi's experimental study are presented in figure III-14. Included for comparison are experimental data points from that study. For this configuration and pressure ratio good agreement is shown between the experimental and analytical model for ϵ^* locations greater than 1.0. Of particular interest is the point at which the main motor throat begins to be blocked by the igniter jet, i. e., the point where the Mach number first deviates from the steady state unblocked condition (1.0). Essential agreement is seen between the analytical and experimental results, both of which indicate that, for a value of $P_i/P_m = 1.84$, the igniter should be placed at an ϵ^* greater than 1.27 in order to avoid overpressurization.

Parametric curves corresponding to various values of P_i/P_m are presented in figure III-15a and the values of P_i/P_m vs ϵ^* at which unblockage first occurs, are plotted in figure III-15b. It is emphasized that these data are for the specific motor and igniter geometries and can only be applied to other igniter to main motor systems if the geometrical design ratios A_{tm}/A_{ti} , A_{tm}/A_{ei} , and D_b/D_a are comparable.

Comparison of the analytical model with experimental test data indicates that the model provides an adequate method of determining igniter design and position parameters necessary to avoid overpressurization. A discussion of the analytical model comparison with the experimental data is presented in section IIIE-2b.

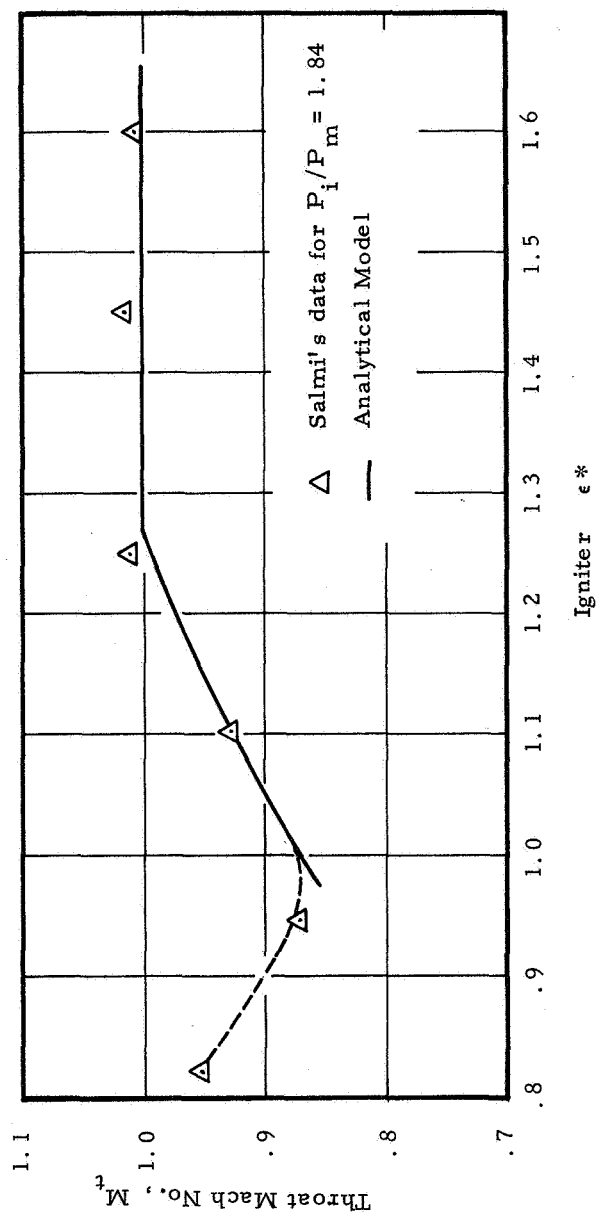


Figure III-14. Comparison of the Analytical Blockage Model with Salmi's Experimental Data

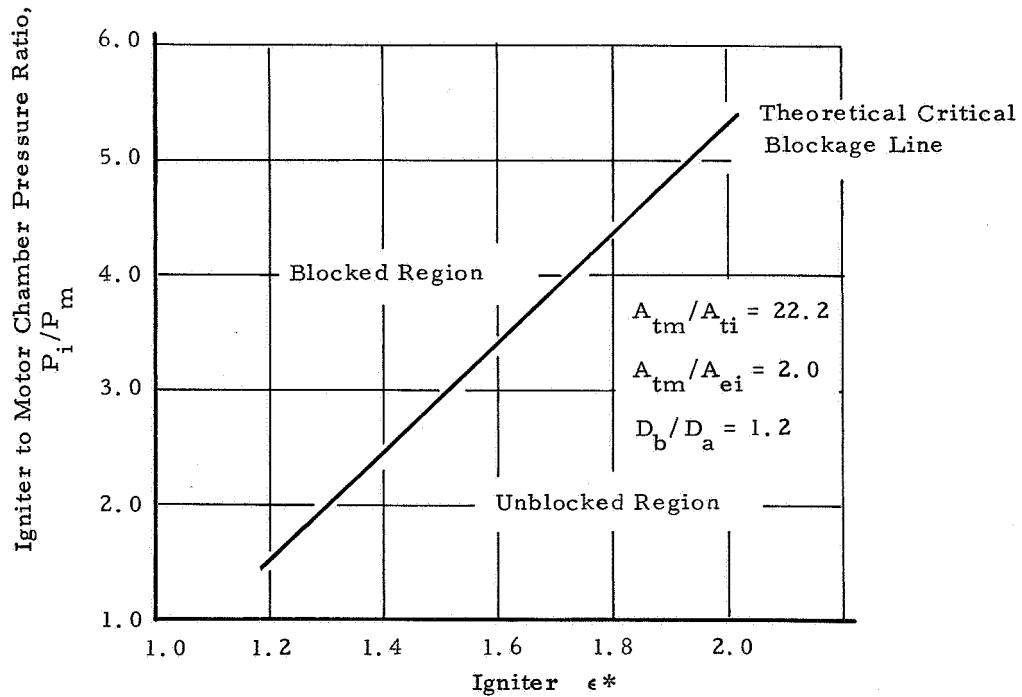
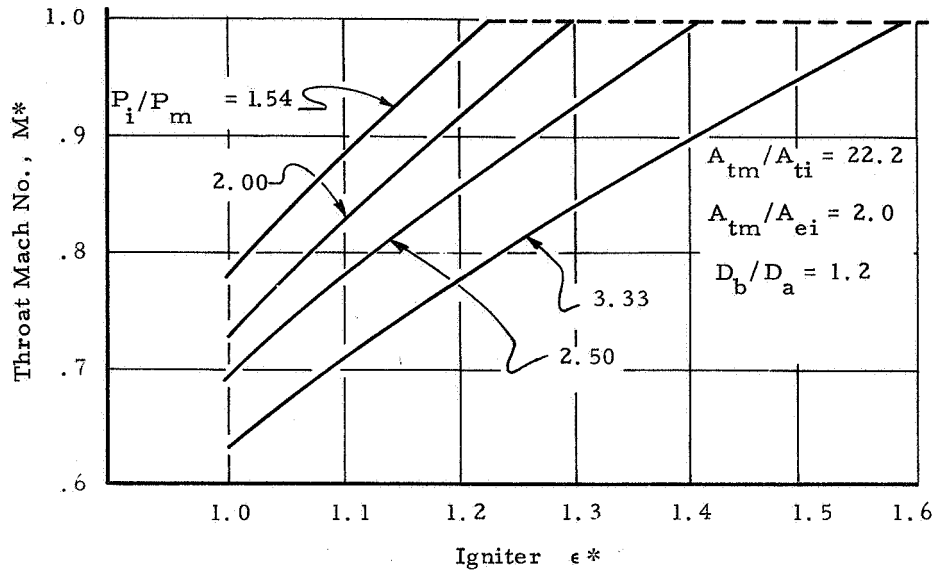


Figure III-15. Analytical Model Parametric Data

B. EXPERIMENT DESIGN AND FABRICATION

The following sections present information on:

- (1) The experiment conceptual design
- (2) Motor design and fabrication
- (3) Igniter assembly design and fabrication
- (4) Propellant processing and non-destructive testing and
- (5) Instrumentation and test equipment

1. Experiment Conceptual Design

The experiment design was based upon program requirements, a review of previous work and the analytical studies presented in section IIIA. Constraints which were placed upon the main motor design were that it (1) simulate 260 inch solid motor initial burn area conditions and utilize a similar solid propellant formulation, (2) contain a 5-inch throat diameter and 17.5° half angle conical nozzle, and, (3) operate at an average chamber pressure from 500 to 600 psia. These requirements were specified so that the experimental data would be applicable to design of a full scale 260" solid propellant motor and could be compared with previous work. (3, 5)

The thin web main motor grain was designed to satisfy the previous stated criteria and to provide a motor burn time of approximately 2.0 seconds under normal operating conditions. The igniter was designed to have an action time of approximately 1.2 seconds. This provided approximately one second of combined igniter and motor operation and one second of motor operation undisturbed by the igniter flow.

A basic objective for the igniter was the ability to vary igniter chamber pressures and mass flow ratio from test to test. This objective was achieved by use of interchangeable throat inserts and cartridge loaded grains which could be cut to specified lengths. The igniter nozzle was designed with a 17.5 degree half angle to aid in easy separation and with a sufficiently high area ratio to obtain optimum expansion at a nozzle pressure ratio of approximately 75. This latter criteria was specified to provide good initial penetration and short ignition intervals.

Experiment instrumentation was designed to obtain maximum data return, within the scope of the program, for analysis of the complex aft-end ignition phenomena. Motor bore and chamber pressure transducers were provided to study the early igniter jet penetration, the ignition transient and steady state operating conditions. Tripwire and thermocouple probes were mounted flush with the propellant surface to study

initial grain heat input, ignition and subsequent flame propagation. These data are also used to establish motor throat blockage during the ignition transient since blockage in a solid propellant motor, as calculated by the motor chamber pressure, would be indeterminate if the propellant burning surface area is unknown.

Motor and igniter nozzle pressure instrumentation was provided to establish characteristic nozzle flow interactions. Igniter chamber pressures were used to determine igniter flow condition. Thrust data was provided to investigate the effects of the aft-end igniter configurations tested upon main motor thrust.

2. Main Motor Design and Fabrication

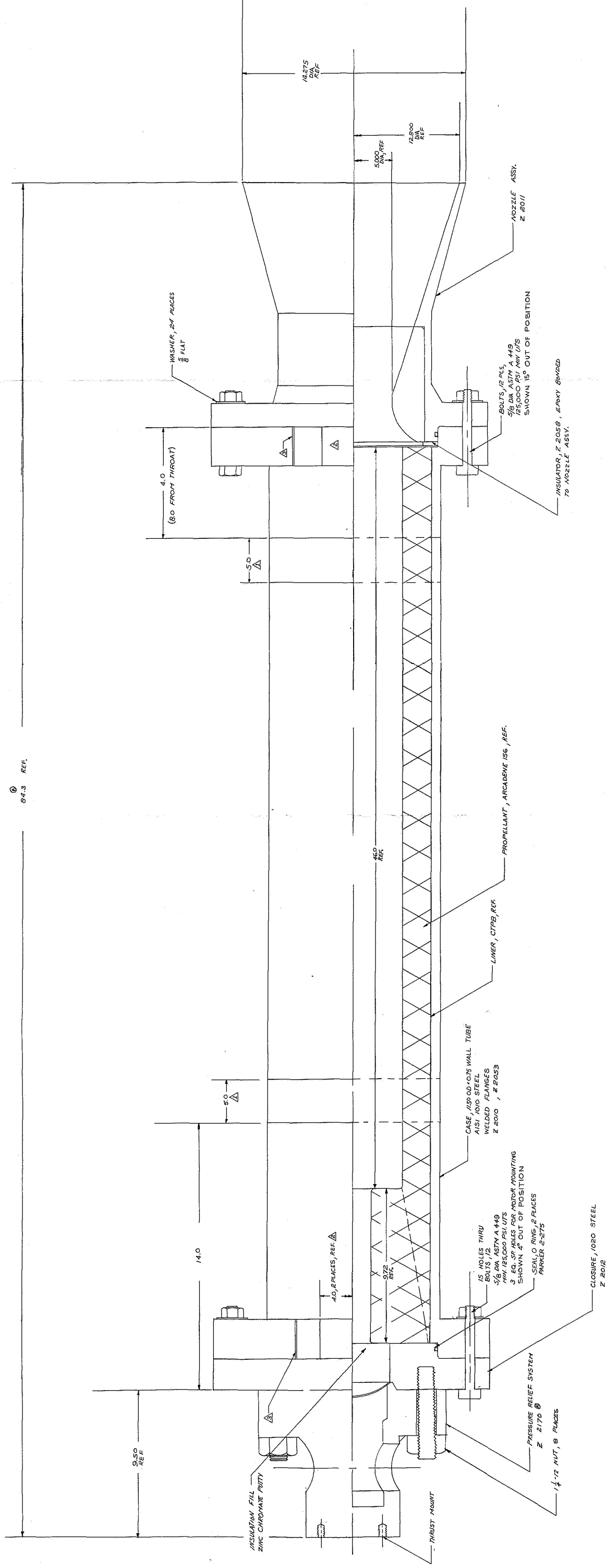
a. Grain Design and Ballistic Performance

The motor propellant grain shown in figure III-16 was designed to produce a nearly neutral pressure trace over the web action time. The grain configuration was designed to simulate the initial burning area of the 260-inch-diameter motor given in NASA Report CR-54925. However, direct scaling of the test motor grain from the full-sized 260-inch-diameter motor produced a minimum local port-to-throat ratio for the propellant of approximately 1.10. Because this value is low enough to cause erosive burning of the propellant grain, which would obscure throat blockage effects, the motor was redesigned to a minimum port-to-throat ratio of 1.80. The aft end configuration of the grain was changed from a series of tapers to a cylindrical section tapered to make correlation of theoretical and experimental data simpler.

The star section at the grain head end was changed to reflect a goal of approximately 20 percent of the total grain length in star design. This was to assure that the motor pressure-time relationship was maintained as close to neutrality as possible while still maintaining the correct ratio of cylindrical to star grain length.

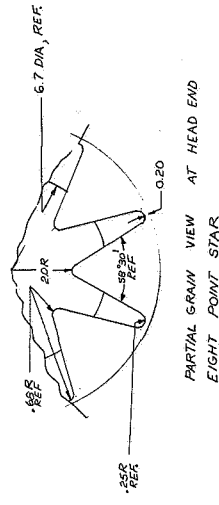
Atlantic Research Corporation's ARCADENE 156 propellant, which was used in the test motors, simulated the formulation, density and physical characteristics of the propellant grain used in the 260-inch motor. Table III-1 compares the 260-inch diameter motor formulation with ARCADENE 156.

A theoretical pressure-time plot for the motor is shown in figure III-17 and the pressure and thrust-time computer analysis (360 FORTRAN) is given in Appendix C. These computer predictions compared well with actual ballistic performance data for cases where the overpressurization effects from the igniter could be neglected.



NOTES

- △ GAGE DIA
△ FLAT SURFACE
△ ALIGNMENT GROOVE, SHOWN OFF CENTER FOR CLARITY



COMPANY <i>Mc Donnell Douglas</i> PROJECT <i>Boeing</i> DRAWING NO. <i>10-7-67</i> DATE <i>10/15/67</i>		ATLANTIC AIR RESEARCH ALEXANDRIA, VIRGINIA	
TITLE		CETEC SCALE MOTOR ASSY.	
SUBMITTER R & VE PRODUCTION PROJECT Q & A CUSTOMER		SIZE 99335	DATE DUE NO. CHG. Z 1968/4
SCALE		DRW NO.	SHEET

Figure III-16. Test Motor Assembly

Table III-1

Propellant Composition and Properties Comparison

	ANP 3254 <u>Weight Percent</u>	Test Motor ARCADENE 156 <u>Weight Percent</u>
<u>Composition</u>		
Oxidizer	69.00	68.00
Metal Fuel	15.00	16.00
Burning Rate Catalyst	0.75	2.00
Binder	15.25	14.00
<u>Propellant Properties</u>		
Burning Rate at 1000 psia, in/sec	0.8	0.86
Density, lb/in ³	0.065	0.065

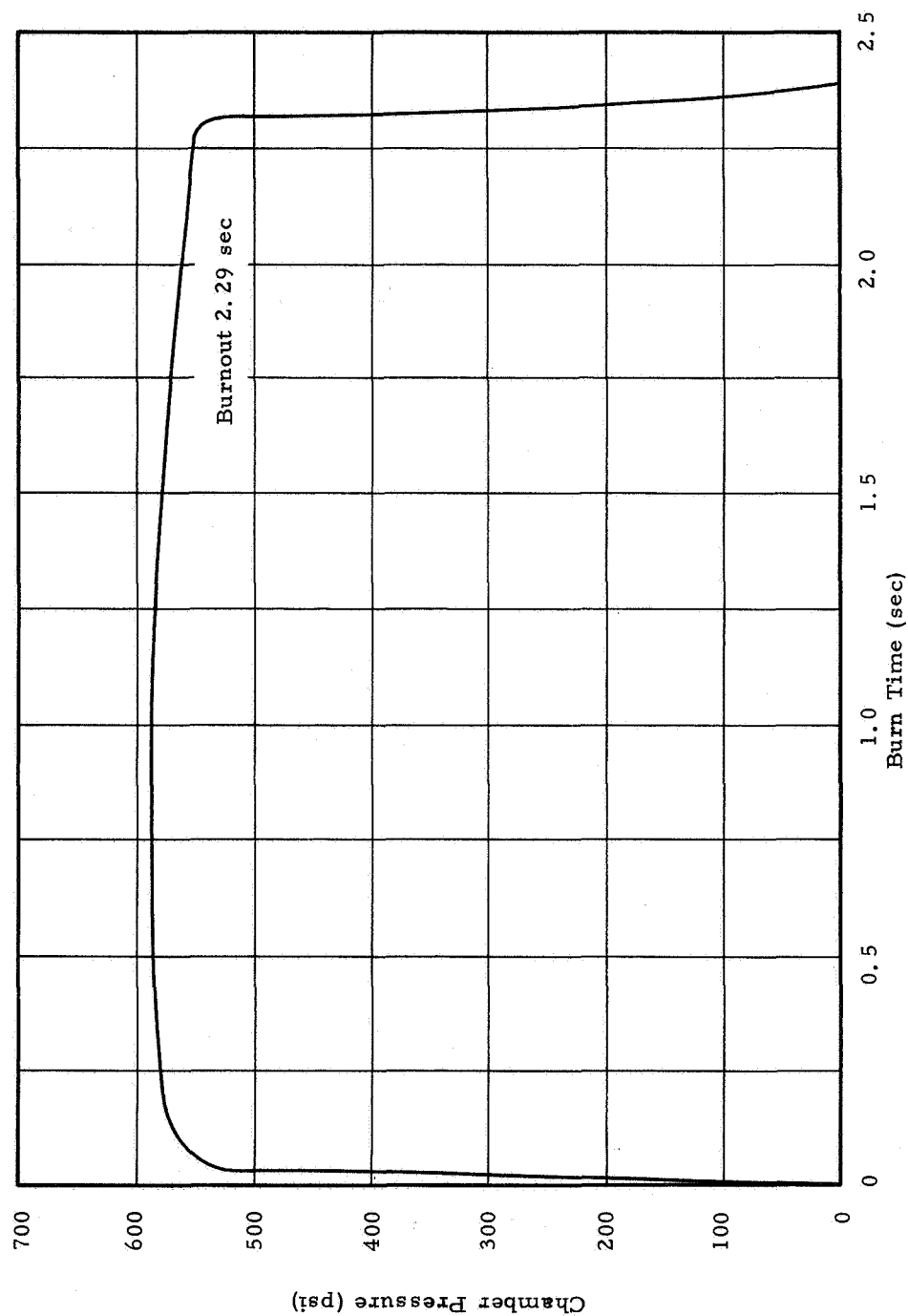


Figure III-17. Motor Pressure Versus Burn Time

b. Main Motor Assembly Description

The main motor hardware components were of heavywall construction with low operating stresses. The cylindrical portion of the motor case was fabricated from AISI 1010 steel tubing with a 11.5-inch O.D. and 0.75-inch wall thickness. Flanges for installation of the nozzle and forward closures were welded to each end.

The motor design, figure III-16, incorporated an insulated diaphragm overpressurization relief system and vent which mounted on the motor forward end centerline. The design relief pressure was approximately 2200 psig. The basic overpressurization relief system body acted as the thrust mount and was constructed so that a majority of the vented exhaust gases would be turned 90 degrees from the motor centerline to essentially null thrust and avoid direct impingement on the thrust stand. The overpressurization system was hydrostatically tested to 2000 psig prior to motor tests. A summary of motor data are shown in Table III-2.

The end closure flanges were machined from AISI 1010 steel and welded to the cylindrical portion of the case. The motor cases were hydrostatically tested to 2000 psig prior to loading to confirm the structural integrity of the design.

The nozzle closure houses a replaceable ATI graphite throat insert. A 17.5 degree half angle exit cone was machined as an integral part of the closure. Tapped holes were provided to obtain the required pressure measurements along the nozzle profile.

The replaceable graphite throat inserts were machined from 10-inch billets of ATJ graphite. These were pressed into the nozzle housing prior to drilling the instrumentation ports.

3. Igniter Assembly Design and Fabrication

a. Grain Design and Ballistic Performance

Grains for the pyrogen igniter were cast into a four-point wagonwheel configuration which provided an essentially neutral burning surface. In order to maintain a minimum cross-sectional area to be exposed to main motor exhaust gases, a high loading fraction for the igniter grain was necessary. This was found to result in erosive burning and a characteristic regressive igniter pressure trace.

Table III-2

Summary of Test Motor and Igniter Data

<u>Performance</u>	<u>Test Motor</u>	<u>Igniter^a</u>
Operating Pressure, psi	550	1500
Burn Time, sec	2.5	1.5
Grain Configuration	8-point star/circular perforation	4-point wagonwheel
Expansion Ratio	6.5	10.0
Thrust, lb	16,600	1550
 <u>Dimensions</u>		
Case Diameter, in	11.5	4.0
Grain Length, in	55.7	23.39
Nozzle Throat Diameter, in	5.0	0.884
Nozzle Type, degree conical	17-1/2	17-1/2
Motor Overall Length, in	84.3	30.3
Motor Maximum Diameter, in	16.0	7.0
Sleeve Diameter, in	--	5.0
 <u>Weights</u>		
Propellant, lb	160	9.8
Inert, lb	880	68.8
Total Weight, lb	1040	77.6

^aValues apply to full length grain.

The propellant used for the igniter was ARCADENE 131B which is similar in composition, including solids loading, to ARCADENE 156 used in the main motor. The only significant difference was in deletion of the burning rate catalyst which resulted in the lower burning rate required for the igniter.

An example of the theoretical and actual igniter pressure-time curves is shown in figure III-18. The erosive burning portion of the curve varied as a function of grain length from approximately 500 psi overpressure for the full-length grain to approximately 200 psi overpressure for the shorter grain lengths.

b. Pyrogen Assembly Description

The pyrogen igniter hardware, shown in figure III-19, consisted of an internal pressure vessel containing the grain with an integral exterior protective sleeve and aft insulator (nozzle assembly). Provisions were made for three pressure transducers in the insulator and two transducers in the igniter chamber.

The igniter case was machined from standard AISI 4130 steel tubing. The case was symmetrical with a threaded section and O-ring seal surface at each end.

The forward and aft closures were machined from 4130 steel stock. The head closure housed the electric squib and initiating charge which contained 14 grams of B-KNO₃ pellets. The initiator charge was installed prior to assembly of the case and head closure. A flange was provided for securing the igniter in the exterior sleeve for testing with the main motor.

The nozzle closure contained a graphite insert with a divergent section which was mated with a graphite ring in the phenolic aft insulator.

The nozzle inserts for the pyrogen igniter were machined from ZTA high density graphite stock and the aft insulators were machined from a molded billet of asbestos phenolic. A ring of ATJ graphite was pressed into the exit cone just downstream of the throat insert to prevent localized erosion of the phenolic insulator.

An exterior protective sleeve was machined from 5-inch-diameter steel tubing and a 7-inch-diameter support flange was welded to the forward end of the sleeve to provide for mounting the igniter on the support stand for testing. The aft end of the sleeve was mated with the phenolic insulator on the igniter.

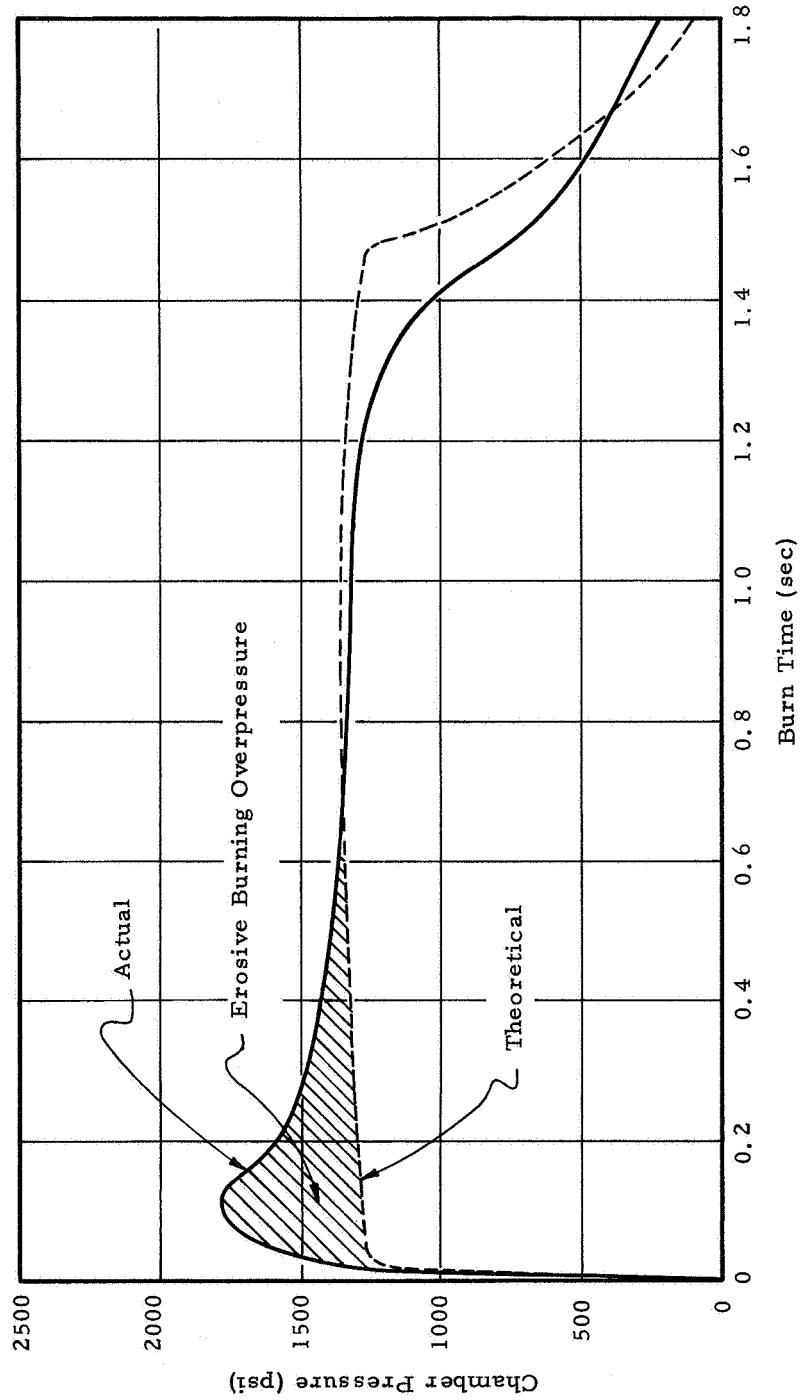


Figure III-18. Theoretical and Actual Igniter Pressure-Time Curves

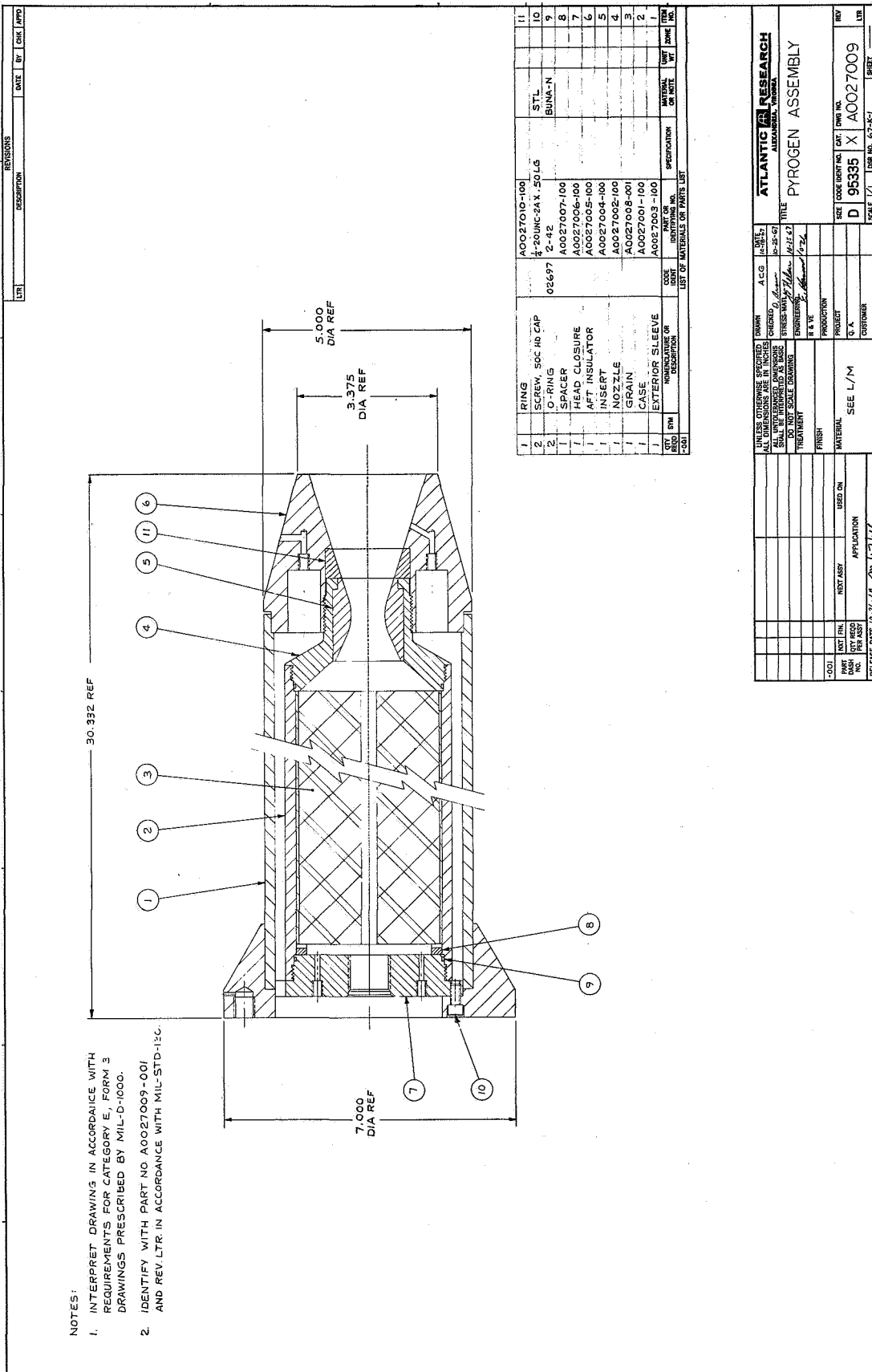


Figure III-19. Igniter Assembly

4. Propellant Processing and NonDestructive Testing

a. Main Motor

The main motor was lined with CTPB liner while the case was rotated on powered rollers. Graduated liner thickness was achieved by applying additional liner where required after a partial cure of the initial coating. After completion of liner application, the liner was cured to a thixotropic, tacky condition. Final liner cure was accomplished during propellant cure.

Propellant mixing utilized the early curative addition technique to provide lower end-of-mix viscosity and better processing characteristics. The first two mixes were made in a Day 50-gallon planetary vertical mixer. The remaining mixes were made in a Baker-Perkins 150 gallon vertical mixer. Oxidizer was added to the mix by a remote feed system utilizing a Sweco vibrating screen.

Casting was accomplished using a bottom fill casting setup as shown in figure III-20. Three bottom forming plugs shut off propellant flow from the plenum at the bottom of the motor and small overcast risers over each star point provided the necessary reservoir for cure shrinkage. The motors were cured in a forced circulation steam-heated oven.

After the motors were cooled, the two-piece mandrel was removed from the grain. First the mandrel which formed the star section of the grain was removed. Then the motor was rotated 180 degrees, and the mandrel which formed the grain cylindrical section was removed.

Processing was completed with propellant riser removal and cleaning out and trimming the instrumentation ports.

Two forms of nondestructive tests were used to inspect motor conditions. Each motor was X-rayed for deficiencies near the instrumentation port locations as well as in every star/valley at the grain forward end in accordance with MIL-STD-453.

Due to the motor case rough surface conditions, ultrasonic inspection was not as successful as would ordinarily be expected. Bond line discontinuities between liner and case were detected with a reasonable amount of confidence, but bond line deficiencies between propellant and liner were not readily apparent.

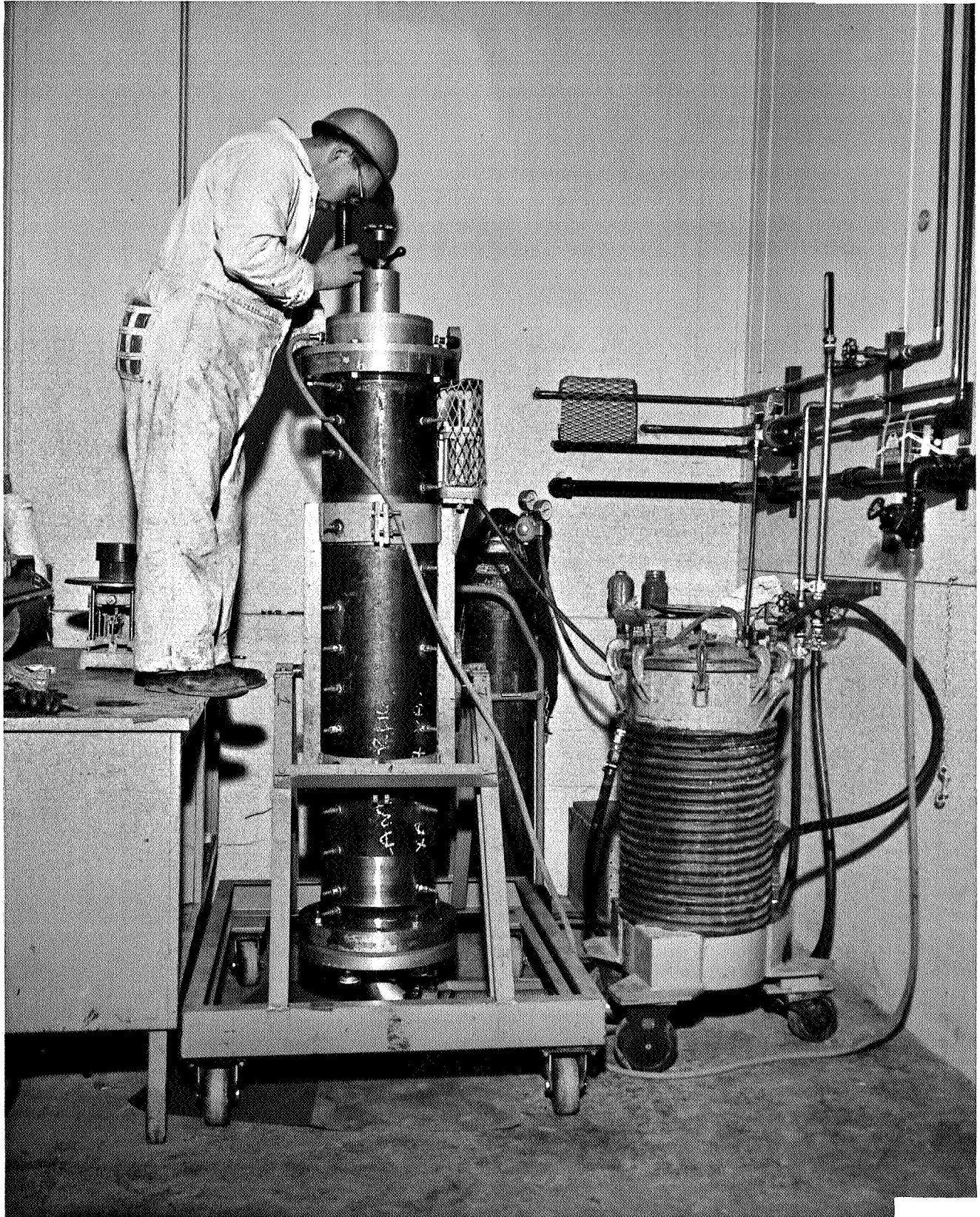


Figure III-20. Bottom Fill Casting Set-up

b. Igniter

Premolded paper-phenolic tubes sanded on the internal surfaces to remove mold glaze were coated with CTPB liner material. After a pre-cure to a tacky state, the tubes were bottom cast with the mandrel, forming the internal perforation in the grain, in place. After oven curing, the mandrel was removed, and the grains were sawed to length.

The igniter grains were subjected to a radiographic inspection in accordance with MIL-STD-453. Two rotations, 0 and 90 degrees, were inspected.

5. Instrumentation and Test Equipment

a. Main Motor Assembly

The motor case design provided for 5 pressure and 20 thermocouple or tripwire measurements as shown in figure III-21. The five pressure transducers were installed along a horizontal plane down the side of the motor. Four of these were inserted through inhibited holes in the propellant so that the pressure could be measured at the motor bore. Beginning with the second firing, copper tubes were inserted in the holes to prevent collapse during firing. The transducers were short-coupled to the case and all lines filled with low viscosity silicone grease. The fifth pressure measurement was made in the head-end gap between the end of the grain and the forward closure.

Eight Nanmac Model 521 thermocouples, shown in figure III-22, were used for each test, installed in two planes 90 degrees apart. The probes were inserted through threaded holes in the motor case and into inhibited holes in the propellant and were adjusted until they were flush with the propellant surface.

Ten tripwire assemblies were installed in the same planes as the thermocouples and were used to provide data on ignition of the propellant surface. The tripwires consisted of Pyrofuse wire mounted in the surface of a propellant plug which was bonded to a stainless steel shaft. The pyrofuse wire was placed in a recess in the propellant with the top surface of the wire flush with the propellant surface. The ends of the wire were taken from the surface plug through holes to the back of the plug where they were soldered to copper lead wires connected to an appropriate trip wire circuit and oscillograph recorder. The propellant plug was bonded to the end of a 6-inch length of stainless steel tubing with the instrumentation lead wires running through the tubing and out the other end. The tubing was filled with epoxy to provide a tight

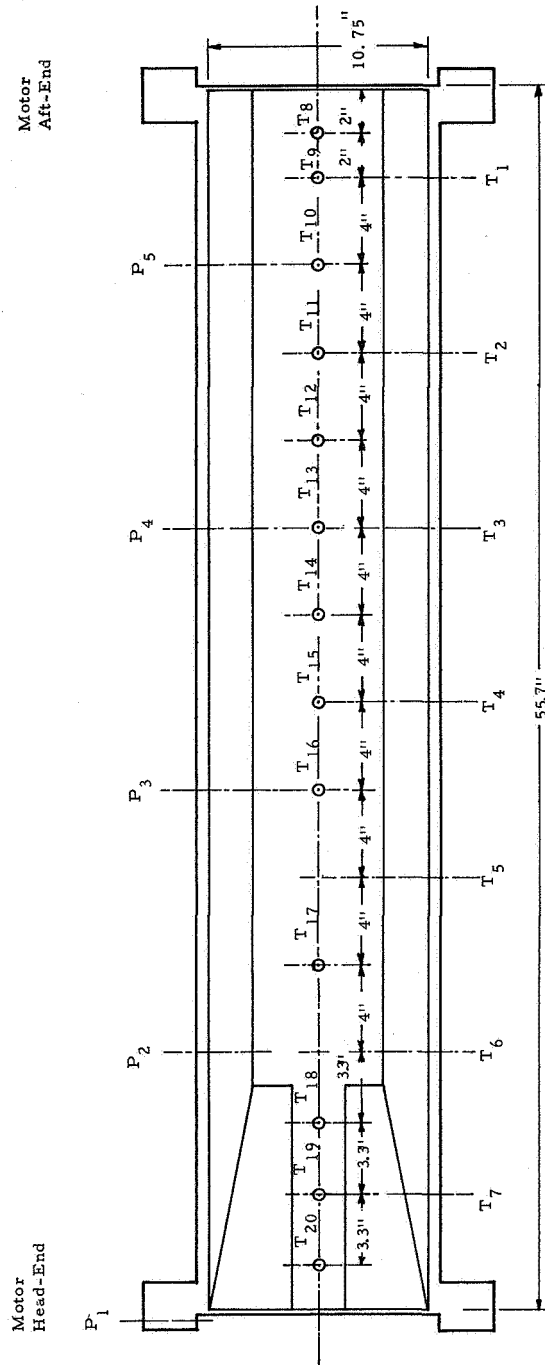


Figure III-21. Thermocouple and Tripwire Instrumentation Locations

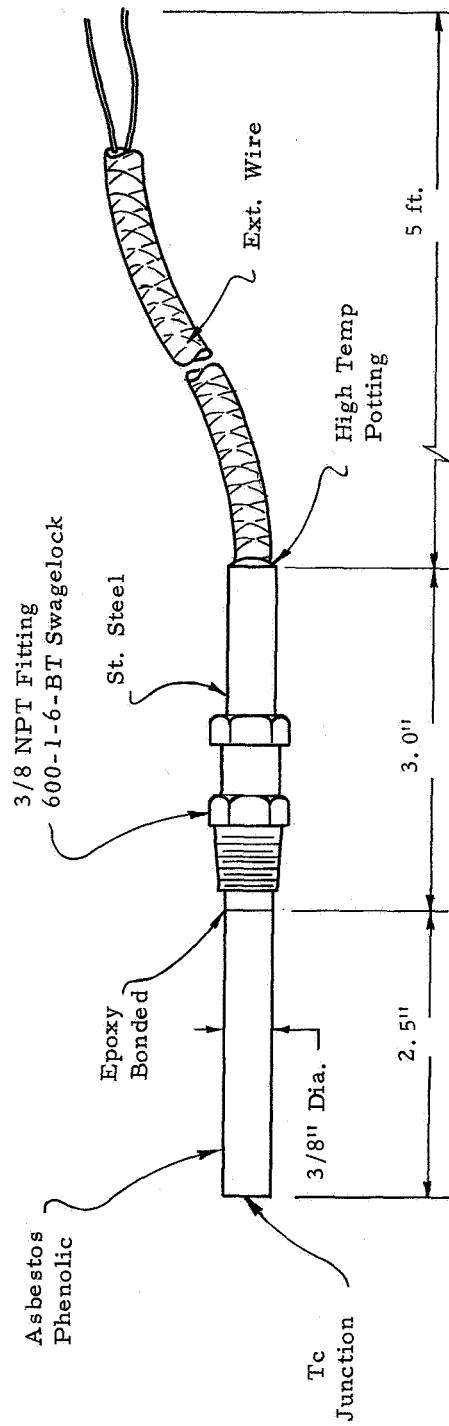


Figure III-22. Eroding Thermocouple

pressure seal. The trip wire assemblies were mounted in the motor casting wall using Swagelock thermocouple fittings and were adjusted so that the propellant plug surface was flush with the internal surface of the propellant motor grain. Ignition at a given tripwire location was assumed to occur when electrical continuity was lost.

Twelve positions were available for pressure data measurements on the nozzle. Ten were in a horizontal plane and two were in a vertical plane. The pressure taps ran from upstream of the nozzle throat to the end of the exit cone. All transducers were connected with 1/4-inch pipe filled with silicone grease. Figure III-23 shows the location and designation of nozzle pressure instrumentation.

b. Igniter Assembly

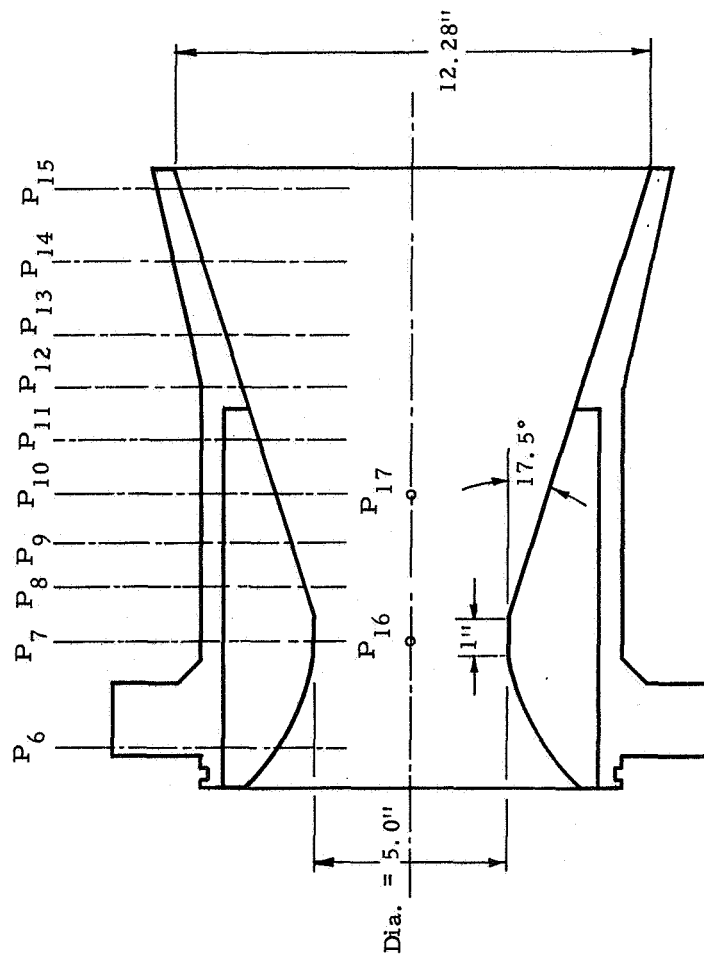
Three Dynisco PT 110 pressure transducers were installed in the phenolic insulator on the igniter to measure gas pressure inside and outside of the exit cone. Nitrogen gas was bled into the transducer cavity after firing to prevent heat soak damage to the gauge. Two additional transducers were mounted on the aft end of the pyrogen to record operating chamber pressure. Figure III-24 shows the arrangement of the igniter pressure transducers.

c. Pyrogen Holding Assembly and Aligning Device

A welded steel assembly served as the pyrogen holder. The pyrogen was mounted through the aft end flange and also through a mounting ring which clamped on to the cylindrical section. The holder was aligned with the thrust stand in such a manner leaving only longitudinal position and minor transverse adjustments to be made to establish the correct position. As an aid to alignment, a holding fixture was built which centered the pyrogen in the exit cone prior to mounting to the holder. Figure III-25 shows a picture of the motor and igniter with the aligning fixture in place.

d. Thrust Stand

All static firings were made on a modified three-component thrust stand in which side force load cells were replaced with rigid nonactive elements. Only redundant axial thrust loads were measured.



P	A/A*
6	1.59
7	1.00
8	1.16
9	1.49
10	1.86
11	2.38
12	2.97
13	3.63
14	4.60
15	5.69
16	1.00
17	1.86

Figure III-23. Nozzle Pressure Tap Locations

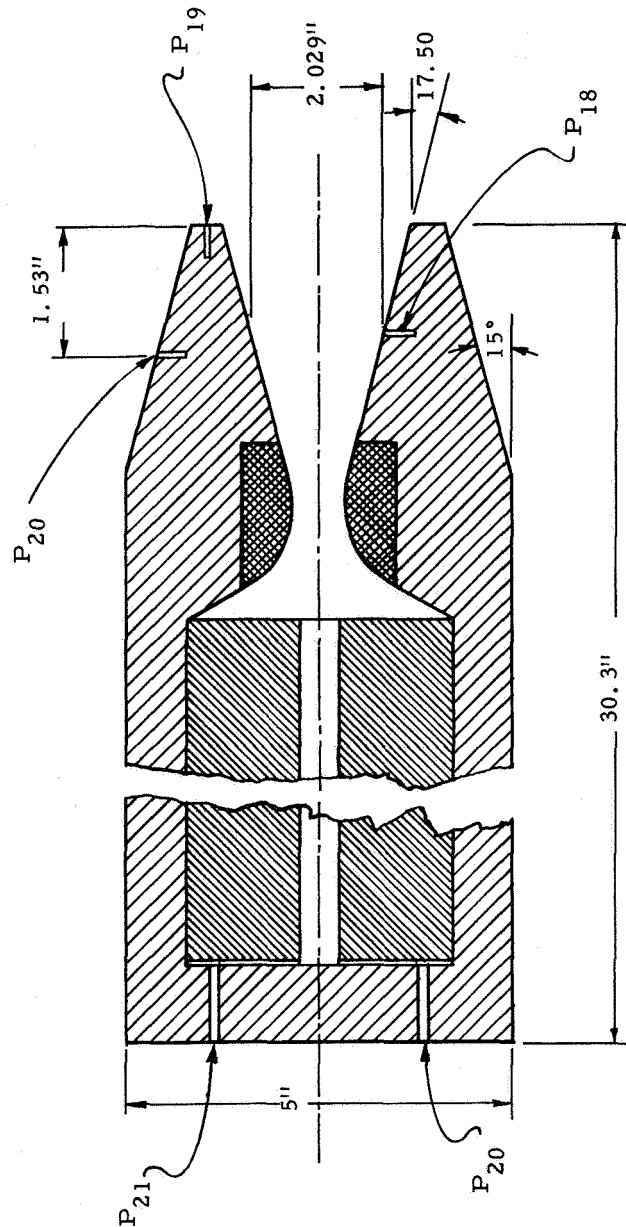


Figure III-24. Igniter Motor Instrumentation Schematic

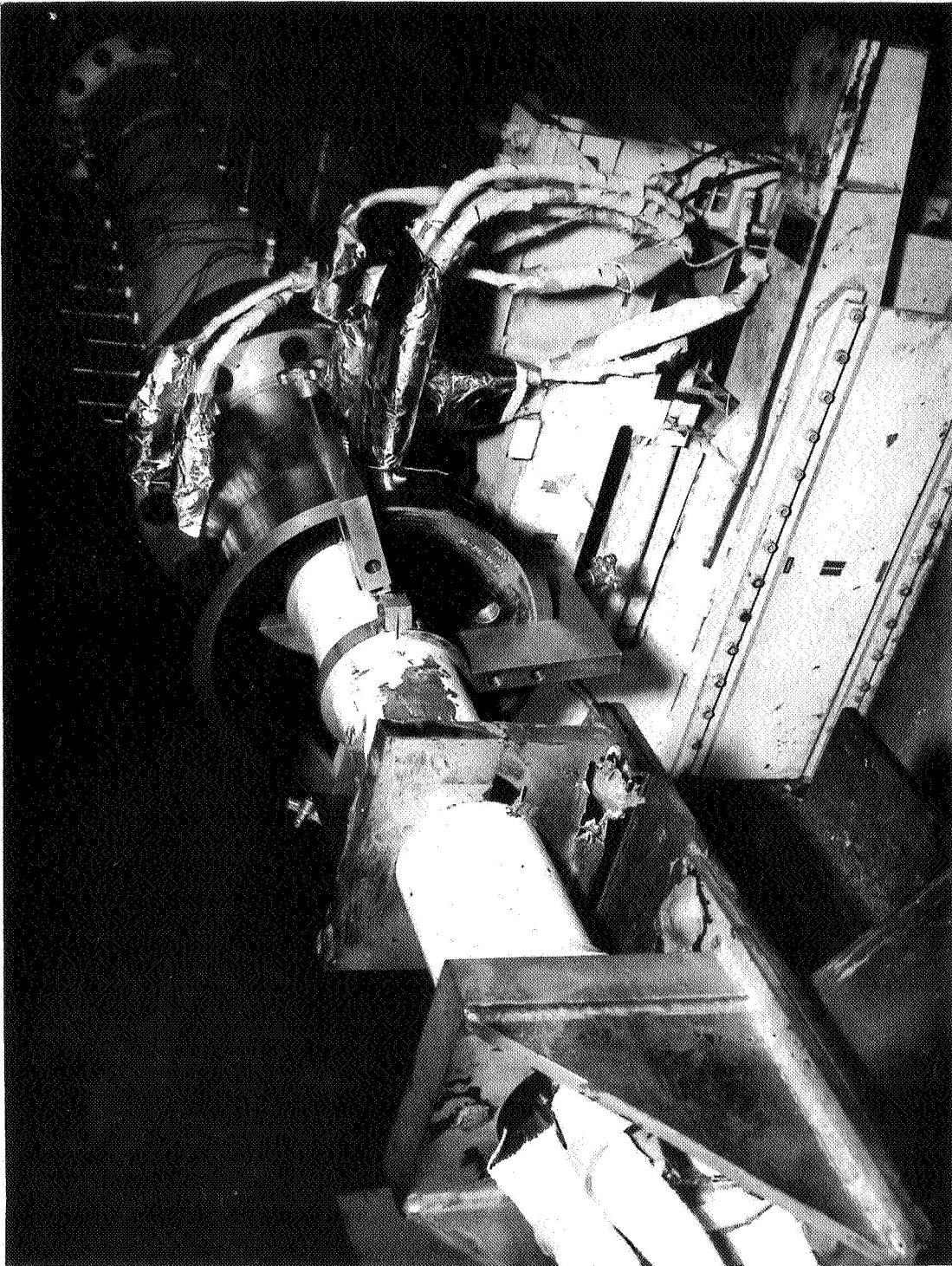


Figure III-25. Igniter Aligning Fixture

e. Data Acquisition Equipment

The signal generating system consisted of the load cells, pressure transducers and temperature sensing elements previously mentioned.

Load and pressure forces were measured by converting the deformation of mechanical elements in the transducers to electrical signals through the use of bonded strain gauge bridge powered with high quality dc power supplies.

The output from the 14 primary channels of load and pressure transducers was fed through shielded cable to chopper-stabilized dc amplifiers having a frequency response in the order of 30 kHz. At the amplifier's output, the signal is fed to CEC 5-119 recording oscillographs. For eight channels the output was paralleled to a semidigital recorder system. Integral parameters were obtained from this semidigital system; point values and time values from the analog system. In the semidigital system, the output voltage from the amplifier is converted into a series of pulses. The number of pulses per second varies from 0 with no input to 10,000 with full input. This voltage-to-frequency converter is a true integrator in that it actually follows the input signal with no averaging or sampling. It pulses when equal areas under the curve have been transversed. The pulses are then recorded on magnetic tape. Oscillations on a thrust-time signal, therefore, do not affect the accuracy of the integral measurements. On tape playback, the pulses are fed into high-speed electronic counters which count pulses over any preselected time interval. The accuracy of the counter is good to within one count.

The outputs from the other pressure transducers, the thermocouples, and tripwires were directly recorded on analog records. The analog recording of primary thrust and pressure data recorded on the semidigital system were also redundantly recorded on two Consolidated Electrodynamics Corporation 12-inch galvanometer oscillographs. A total of four CEC Type 5-119 recorders were used for each test.

f. Motion Picture and Still Photography

High-speed motion pictures of the firings were taken of 11 tests using 16 mm Fastax WFS-4 cameras with Ektachrome EFB and infrared 16 mm film. Igniter Tests 1 and 2 were photographed with one camera using EFB film and one camera using infrared film. Photography of Motor Test Number 3 used one camera with EFB film and one camera with infrared film. Motor Tests 4 through 9 were photographed using

one camera with EFB film. Average camera speed for the EFB film was 3000 frames per second at F-11 using a 25 percent neutral density filter. Average camera speed for the infrared cameras was 2000 frames per second.

Black and white still photographs were taken with a 4 X 5 press camera with electronic flash using Tri-X panchromatic film to document every pretest and post-test condition of interest in the 11 different tests. Figure III-26 shows camera locations for the various firings.

C. TESTING

The principle program objective was to determine the igniter design and positioning parameters required to provide satisfactory ignition without motor overpressurization. Consistent with this goal, a general test plan based upon the analytical and theoretical studies conducted during the early phases of the program was formulated. This plan specified the igniter mass flow parameter (w/A), the igniter to motor total pressure ratio (P_i/P_m), the main motor throat to igniter exit area ratio (A_{tm}/A_{ie}), and the igniter epsilon star (ϵ^*) position for each of nine tests.

During the test program, this plan was modified in accordance with the initial test results to provide more meaningful data for comparison with the analytical model. Table III-3 presents a summary of the significant design and test parameters for each of the nine tests.

The first four tests were conducted at constant igniter design conditions but varying ϵ^* locations to determine the effect of ϵ^* upon main motor overpressurization and ignition delay. Tests 5 through 9 were conducted at various igniter mass flow parameters and ϵ^* locations to establish the effects of other igniter design variables. All nine were conducted for a A_{tm}/A_{ie} ratio of 2. Tests 1 through 8 were with the same diameter nozzle insert so that the igniter nozzle expansion ratio was the same for each of these tests. The igniter for test number nine contained a smaller diameter throat, but the same exit plane diameter resulting in a higher nozzle expansion ratio. Igniter mass flow and chamber pressures were varied, in Tests 1 through 8, by trimming the igniter propellant cartridge to various lengths and in the case of Test 9, by changing both the igniter grain length and nozzle throat area.

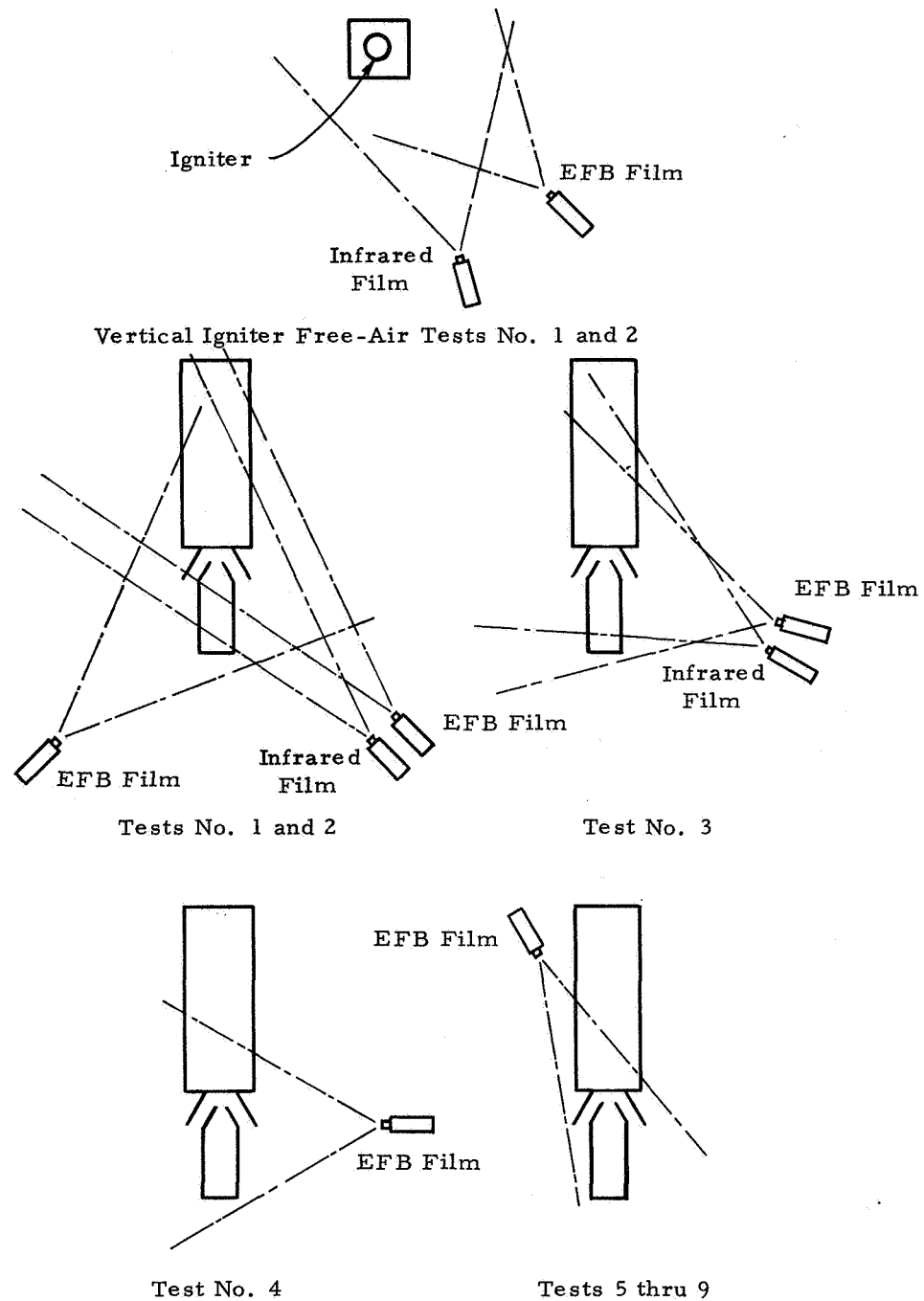


Figure III-26. Test Camera Locations

Table III-3
Test Plan Parameters

Test No.	ϵ^*	$(P_i)_{\text{design}}$ psia	$(P_i)^+$ psia	$(P_i/P_i)_{\text{design}}$	$(w/A)_{\text{design}}$ lb/sec-in ²	$(w/A)^+_{\text{max}}$ lb/sec-in ²	A_{ti} in ²
1	1.79	1375	1756	2.5	0.275	0.357	0.608
2	1.34	1375	1652	2.5	0.275	0.336	0.608
3	1.21	1375	1731	2.5	0.275	0.352	0.608
4	1.45	1375	1653	2.5	0.275	0.336	0.608
5	1.28	1100	1293	2.0	0.226	0.263	0.608
6	1.33	1100	1260	2.0	0.226	0.261	0.608
7	1.65	1650	2759	3.0	0.336	0.561	0.608
8	1.54	1650	2819	3.0	0.336	0.572	0.608
9	1.45	2250	2246	4.1	0.200	0.202	0.269

⁺Maximum experimental values

Tests 5 and 6 were conducted at low igniter mass flow parameters and igniter to booster pressure ratios while Tests 7 and 8 were conducted at relatively high w/A and P_i/P_m to study the effects of these variables. Test 9 was conducted at a high P_i/P_m and low w/A .

The test procedures, specific problems encountered, data reduction techniques and typical test data are presented in the following sections.

1. Test Procedure

Following completion of processing clean-up and non-destructive testing, the unassembled main motor components were moved to the test bay for installation and assembly. Major pre-test and post-test work performed from installation through firing and final hardware removal was accomplished in accordance with the following steps:

- (1) Place motor cylindrical section on thrust stand, close in test bay and condition to $70^{\circ}\text{F} \pm 10^{\circ}\text{F}$.
- (2) Install tripwires, thermocouple and motor chamber pressure instrumentation.
- (3) Install forward motor closure and overpressurization relief valve assembly, bolting motor to thrust adapter.
- (4) Install aft-closure (nozzle).
- (5) Leak-test motor.
- (6) Install motor nozzle instrumentation.
- (7) Hook-up main motor instrumentation, check outputs and repair as required.
- (8) Calibrate thrust.
- (9) Install preassembled igniter.
- (10) Hook-up and check-out igniter instrumentation.
- (11) Align igniter.

- (12) Remove aligning fixture, cover gauges exposed to the motor exhaust with insulation and remove test bay environmental enclosures.
- (13) Take prefire photographs.
- (14) Run pre-test electrical calibrations.
- (15) Fire motor.
- (16) Run post-test electrical calibrations.
- (17) Check igniter alignment and any test damage.
- (18) Take post-test pictures.
- (19) Disassemble motor and remove from test bay.

Photographic data showing the experiment set-up are presented in figures III-27 through III-30. In figure III-27 the overall test set-up is shown prior to the firing on Test 1. This photograph was taken with alignment fixture still in place. Also shown are the motor chamber pressure transducers on the left hand side of the motor, tripwire and thermocouple instrumentation probes along the motor top dead center, the igniter holding fixture, and the motor thrust stand. A more detailed close-up of the alignment fixture is shown in figure III-25. In the background are the insulated motor nozzle pressure transducers as well as the tripwire and thermocouple probes. Figure III-28 shows post-test damage including motor exhaust erosion of the igniter holding fixture and burn-through of the igniter instrumentation cables. Figure III-29 is a close-up showing erosion of the motor nozzle downstream of the graphite throat insert and minor damage to the external pyrogen metallic sleeve. In subsequent tests, damage to the instrumentation cables was prevented by installation of a insulated cable conduit. Erosion of the pyrogen sleeve was minimized by use of a phenolic sleeve insulator as shown in figure III-30. The erosion of the steel motor nozzle exit cone in Test 1 was attributed to impingement of the igniter bow-shock with an associated increase in local heat transfer rates. This problem was encountered only in test 1 at the highest ϵ^* location investigated. No erosion of the graphic throat inserts or steel nozzle exit cone were noted on any of the subsequent tests.

Instrumentation transducer type and range are shown in tables III-4 and III-5.

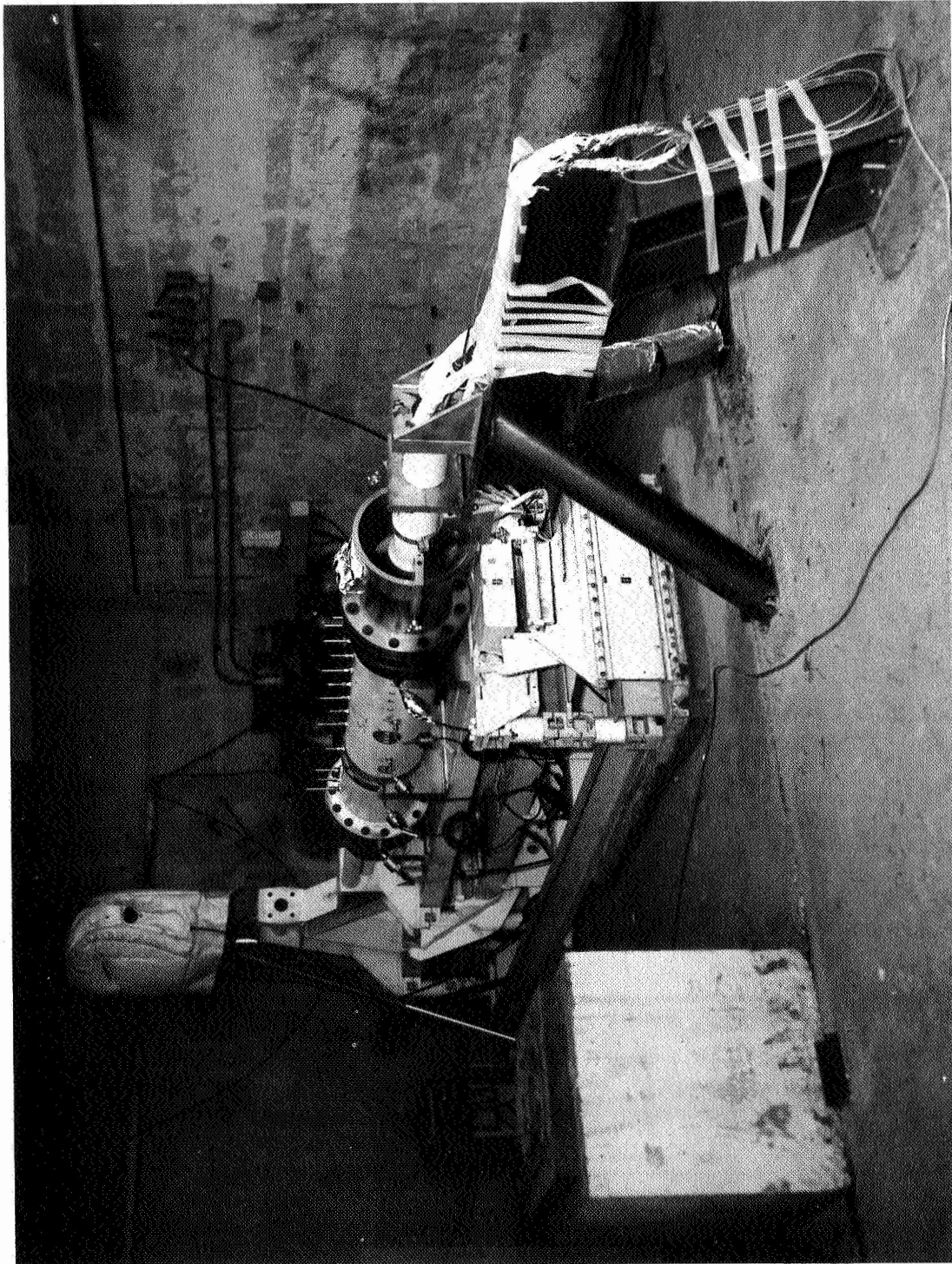


Figure III-27. Pre-fire Test Assembly, Test 1



Figure III-28. Post Fire Test Assembly, Test 1

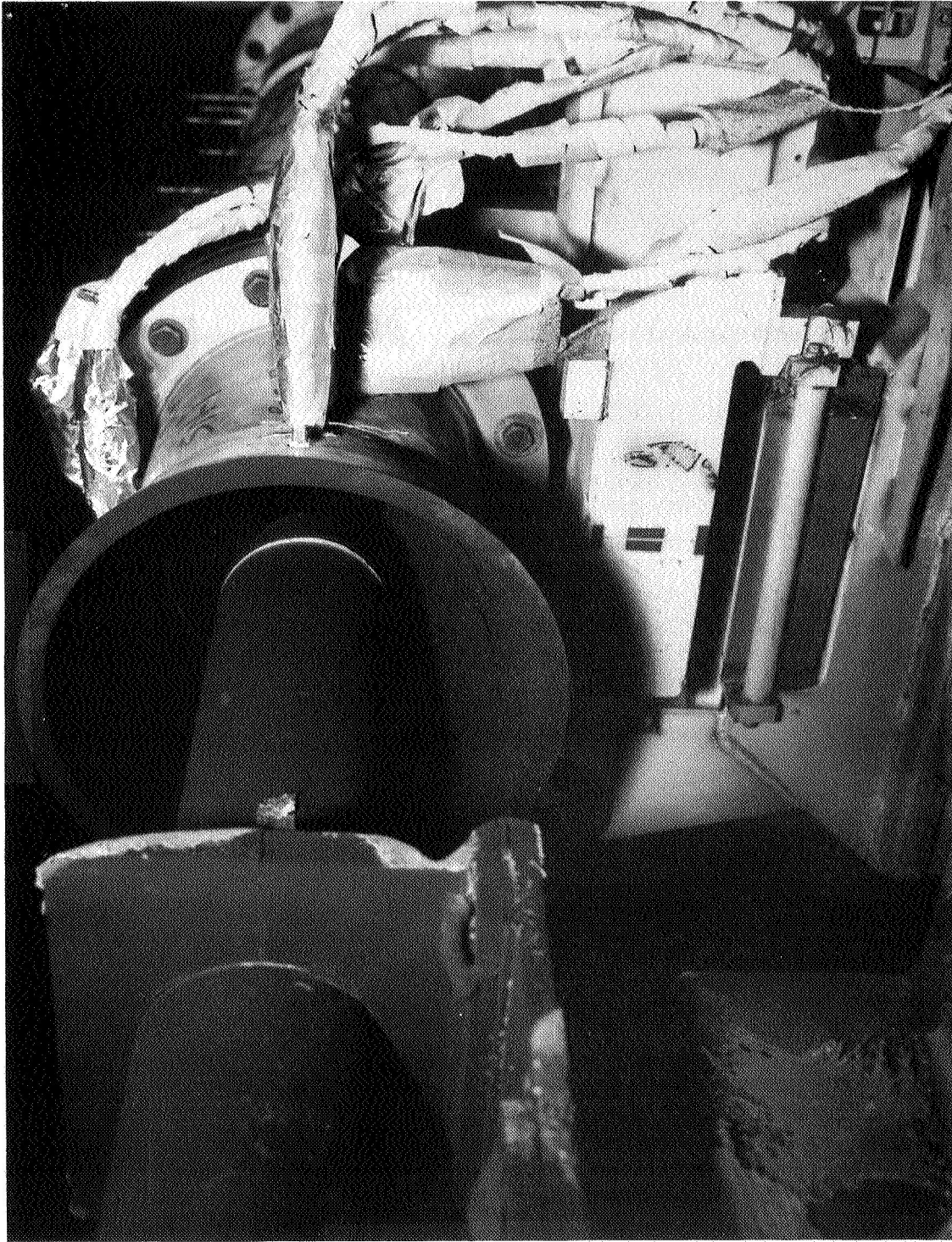


Figure III-29. Post Fire Igniter and Nozzle
Close-ups, Test 1

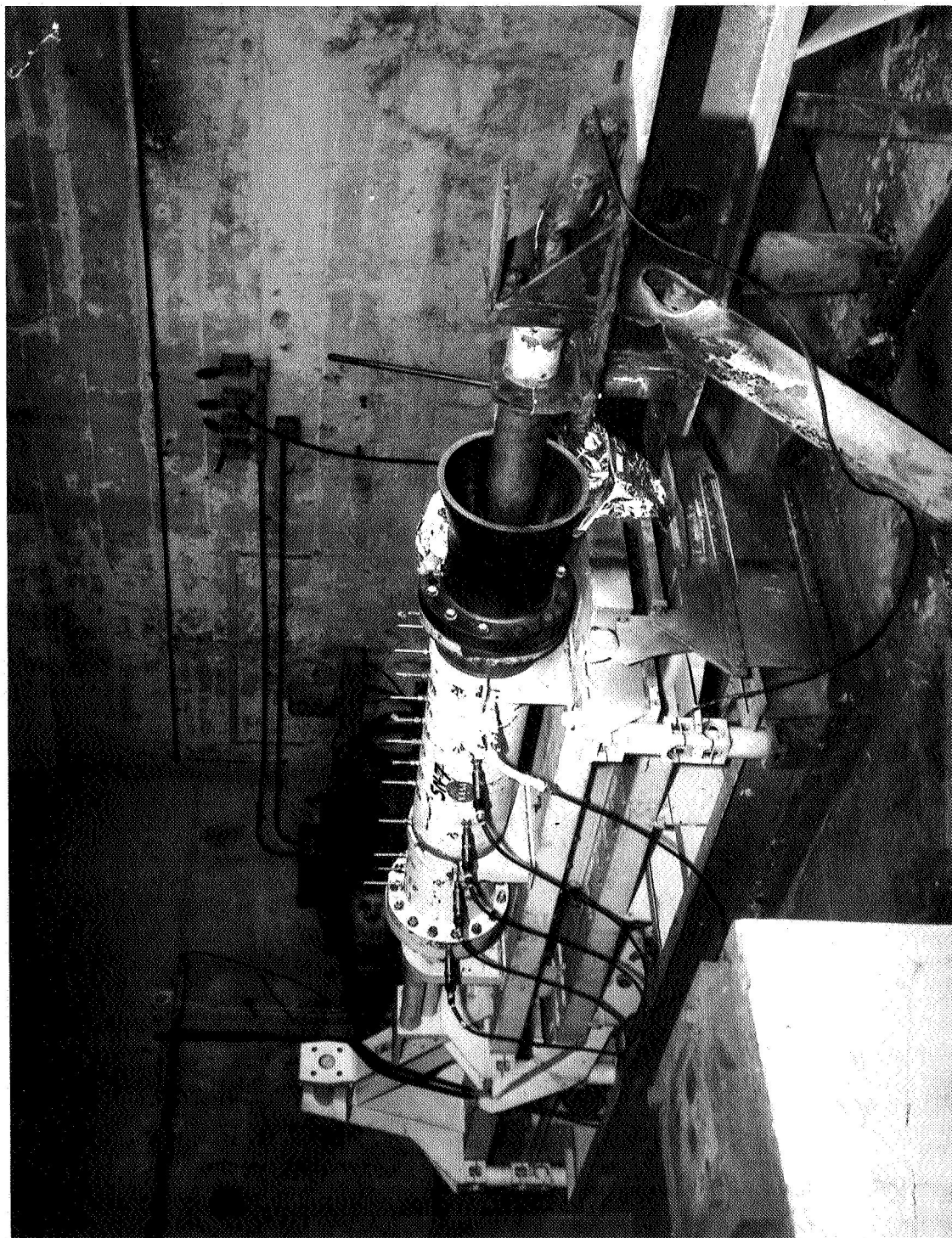


Figure III-30. Pre-Fire Test Assembly, Test 7

Table III-4

Typical Test Pressure Instrumentation

	<u>Range</u>	<u>Gage</u>	<u>S/N</u>	<u>Calibration(Physical)</u>
1	5K	BLH	31042	0-2500 psi
2	2K	BLH	34022	0-500 psi
3	2K	BLH	34137	0-500 psi
4	2K	BLH	40124	0-500 psi
5	2K	BLH	37042	0-500 psi
6	500	BLH	42949	0-500 psi
7	500	BLH	42946	0-500 psi
8	IK	Dynesco	28831	0-500 psi
9	IK	Alinco	23301	0-500 psi
10	350	BLH	43168	0-350 psi
11	350	BLH	43175	0-350 psi
12	350	BLH	37051	0-250 psi
13	350	BLH	37059	0-250 psi
14	200	BLH	38027	0-200 psi
15	OPEN			
16	IK	Dynesco	37754	0-500 psi
17	IK	Dynesco	31793	0-500 psi
18	ID	Dynesco PT110	36317	0-1000 psi
19	ID	Dynesco PT110	36319	0-500 psi
20	ID	Dynesco PT110	36321	0-1000 psi
21	5K	BLH	43458	0-3000 psi
22	5K	BLH	34360	0-3000 psi

Table III-5
Thermocouple and Tripwire Instrumentation

PARAMETERS RECORDED				
Parameter	Location ⁽¹⁾	Calibration	Resolution	Type
25 Thermocouple	T ₈	0-2500°F	5 DGT	Chromel-Alumel
26 TC1	T ₁	"	"	" "
27 TC11	T ₁₁	"	"	" "
28 TC13	T ₁₃	"	"	" "
29 TC15	T ₁₅	"	"	" "
30 TC5	T ₅	"	"	" "
31 TC6	T ₆	"	"	" "
32 TC19	T ₁₉	"	"	" "
33* Tripwire TW2	T ₂	on-off	1 ms	
34 Tripwire TW3	T ₃	"	"	
35* Tripwire TW4	T ₄	"	"	
36 Tripwire TW7	T ₇	"	"	
37 Tripwire TW9	T ₉	"	"	
38 Tripwire TW10	T ₁₀	"	"	
39 Tripwire TW12	T ₁₂	"	"	
40 Tripwire TW14	T ₁₄	"	"	
41 Tripwire TW16	T ₁₆	"	"	
42 Tripwire TW17	T ₁₇			
43 Tripwire TW18	T ₁₈	"	"	
44 Tripwire TW20	T ₂₀	"	"	

*Blanks were used for these locations because of instrumentation limitations.

2. Special Problems

Technical problems encountered during the test program were primarily associated with motor processing or test instrumentation.

Three motor castings were rejected, two because of process difficulties in casting the propellant. A third motor was rejected for a total void volume exceeding the acceptable limit. Corrective action was taken to improve the mixing and casting techniques, and with the installation of a vibrator on the casting tooling the oversized voids in the propellant were eliminated.

A major problem involving probe installation occurred on the first two motors because of difficulties in cleaning out the instrumentation holes running through the propellant grain. This resulted primarily from the fact that the holes were not square with the motor centerline. The problem was solved by using fittings in the steel case to align the hole cleanout probe and by using copper instead of teflon stiffening rods in the instrument boots during casting operations. The remaining problem was that of slight ridges and humps around some of the instrumentation ports at the grain bore. This problem was not significantly rectified and records were kept of the ridge and hump positions to assist in data analysis.

The thrust stand was excited to its natural frequency by the violent oscillations associated with igniter and motor flow interactions. Because the vibrations were sinusoidal, it was not difficult to obtain satisfactory average and point data. The average and integrals were not affected because the voltage-to-frequency system used to secure these values is a true integrator and follows the curve rather than sampling it. Some improvement in the amplitude of ringing could be made by further modifications of the thrust support structure.

The need for very high response during ignition transients and the presence of high level pressure oscillation from the nozzle pressure disturbances created a continuing problem. Several approaches were evaluated to improve transducer performance.

Beginning with the second and all subsequent firings, copper tubes were installed in the pressure port holes and through the propellant to prevent collapse or the likelihood of accumulator action (bulging of the propellant cavity). Air bubbles trapped in the silicone grease used in the pressure connections caused occasional response problems.

The most serious problem, however, occurred in the nozzle assembly pressure transducers. These suffered from a shifting base which varied from 10 percent to 60 percent after firing. Initially, the shift was thought to be caused by grease being sucked out of the pressure connections and heat affecting the sensing elements of the transducers. It was later observed, however, that the effect occurred even in those cases where grease remained in the connections after firing. The shift was then assumed to be caused by either the violent pressure oscillations present in the motors or by heating of the transducers. Any future testing must utilize transducers capable of withstanding these extreme conditions.

Although the Nanmac thermocouples used are reported to offer high response and heat transfer conditions similar to the propellant, analysis indicates that the data generated were not completely valid. It is believed that the thermocouples were either response limited over the higher temperature range or that the propellant combustion products produced an uncalibrated change in sensing element output of the higher temperature values.

Future testing should include heat flux gauges to calibrate or replace the thermocouple transducers.

3. Data Reduction

The test data were reduced to basic engineering values by application of the appropriate scale factors determined from pre-test and post-test calibration of each instrumentation transducer.

Integral and average data were calculated in the following manner:

- (1) A baseline was drawn for the thrust or pressure trace.
- (2) After the maximum thrust or pressure point was located, the 10 percent points were found on the ascending and descending portion of the curve.
- (3) The 75 percent point on the descending portion of the curve was located.
- (4) The start and stop time from the CEC K-4 computer playback was selected.
- (5) The calibration factors were then used to convert the counts to engineering units.

Point data were reduced from the analog records as follows:

- (1) A baseline was drawn for each parameter to be reduced.
- (2) A 12-inch steel rule, graduated in one hundredths of an inch, was used to measure from the baseline to the parameter in question. This was done for all parameters at the times desired.
- (3) The calibration factor was then used to convert these measurements to engineering units.

Igniter mass flow rates used in data analysis were determined by use of experimental chamber pressures, measured throat area data and theoretical thermochemical calculations for the igniter propellant in accordance with the formula:

$$w_i = \frac{P_i A_{ti} g_c}{C_i^*}$$

In the above formula C_i^* was taken to be 95% of the theoretical value.

The igniter ϵ^* location was calculated by use of the formulas:

$$Z = \frac{D_z - D_{tm}}{2 \tan \theta} + \frac{D_z - D_{bi}}{2} \tan \theta$$

$$D_z^2 = D_{bi}^2 + \epsilon^* D_{tm}^2 \cos \theta$$

where θ is the main motor exit cone half angle.

4. Test Results

Two igniter open air firings and nine aft-end motor ignition tests were conducted with satisfactory results. Significant pressure and thrust data recorded during these tests are summarized in tables D-1 and D-2 in Appendix D. A short description of the significant events observed during each of the tests is also presented in Appendix D. Tripwire and thermocouple data are presented in section IIID-1b.

Igniter operation in the two open air firings displayed a significant initial pressure peak with gradual tail-off. This resulted from erosive burning of the initial burning surface area and a slight erosion of the igniter graphite throat insert. On subsequent tests a higher grade graphite was used, eliminating the throat erosion problem. Erosive burning of the igniter grain was considered acceptable and proved beneficial since a greater range of igniter mass flow rates and chamber pressures were obtained during each run.

Operation of the igniter and motor were satisfactory in each of the combined aft-end ignition tests. Igniter action times in the neighborhood of 1.2 seconds were observed while the typical run duration for the test motors were approximately 2.0 seconds. In most cases, this provided about one second of main motor operation during igniter action and one second of operation during igniter tail-off and without igniter flow.

Figure III-31 shows typical igniter and main motor chamber pressures for two different tests. The first, Test 3, was conducted at an $\epsilon^* = 1.21$ and $w/A = 0.276$ and displayed the worst main motor overpressures of any test. The second, Test 9, ($\epsilon^* = 1.45$, $w/A = 0.202$) had the longest ignition delay and little, if any, overpressurization. The slight main motor pressure bump which occurs about the time igniter tail-off begins, as shown in Test 9, was typical of all motors except Test 3. In Test 3, the hump was somewhat obscured by the elevation in chamber pressure due to overpressure produced by aerodynamic blockage of the main motor throat. This peculiar hump-backed shape was caused by the change in motor grain burn area with time.

Maximum thrust augmentations due to positioning of the igniter in the exit cone in the neighborhood of 70 and 25 percent for tests 3 and 9, respectively, were observed. These thrust augmentations resulted from the added igniter thrust and from main motor chamber pressure and nozzle flow modifications.

Significant motor nozzle pressure oscillations were noted in each test. The existence and severity of these oscillations were found to be related to igniter ϵ^* location and mass flow rate.

To aid in understanding the analysis of test results, it is appropriate to present and discuss representative test data. The following two sections show and discuss data recorded during the two time intervals which provided information of prime interest. These time intervals are (1) the igniter and motor ignition transient and early steady state operation and (2) late igniter steady state operation and igniter tailoff. The first interval is of interest because of the ignition phenomena involved. The

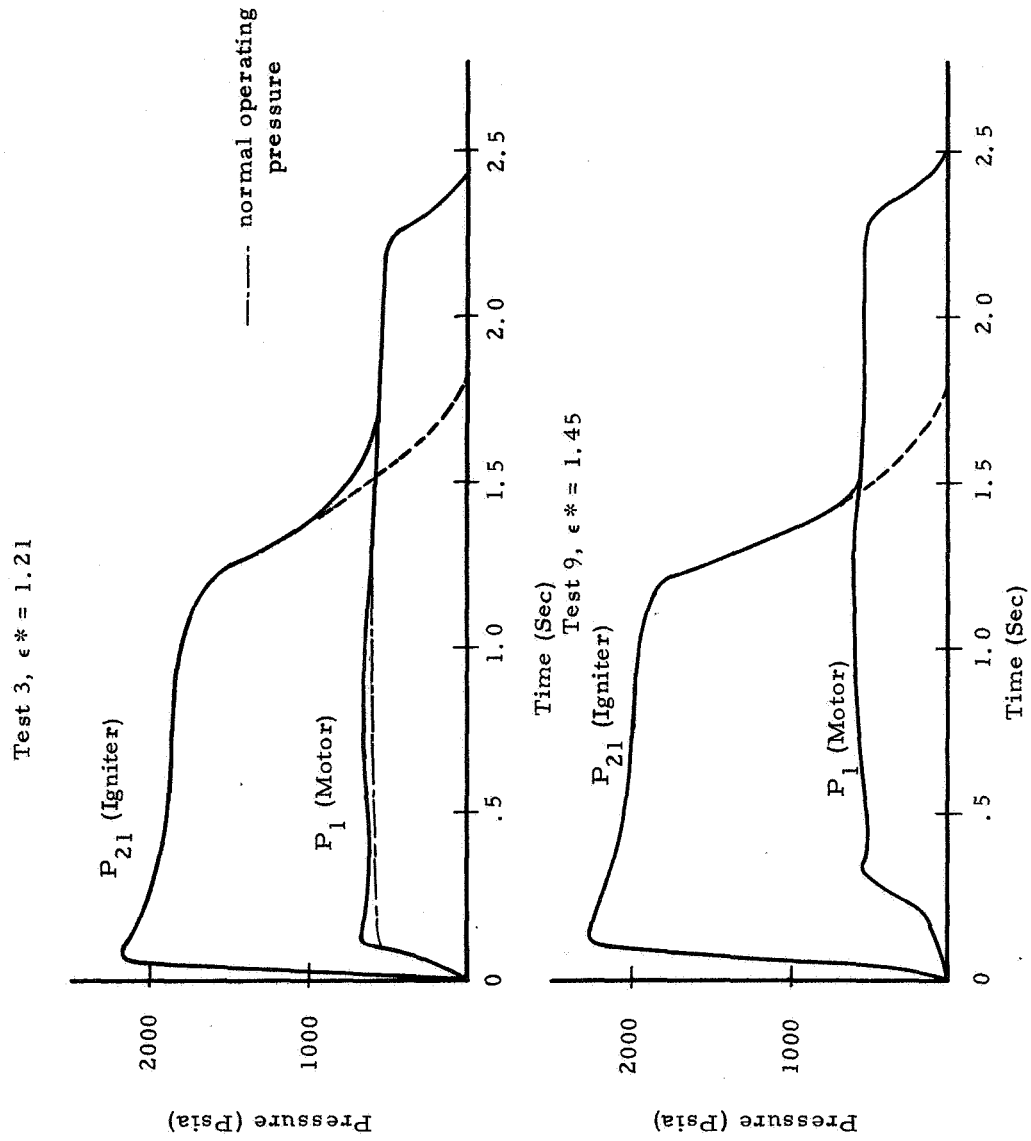


Figure III-31. Typical Igniter and Motor Pressure Traces

importance of the second interval lies in its illustration of steady state operating characteristics and the characteristics of unblocking which occurred during igniter tailoff in a majority of the tests. Since it was not possible to present data from each test, data from tests 3 and 9 were selected as illustrating some of the extremes in phenomena observed during the test series.

a. Ignition Transient and Early Steady State Operation

Oscillograph data showing the ignition transient for Tests 3 and 9 are shown in figures III-32 through III-39. In these figures time is given in milliseconds and is referenced to the ignition firing switch signal. Each trace is labeled with its location designation. Figure III-32 shows the igniter chamber pressure (P_{21}), the main motor head-end chamber pressure (P_1) and the tripwires and thermocouple data from the motor port grain area for test 3. The thermocouple and tripwires toward the top of oscillograph correspond to locations at the aft-end (igniter end) of the grain and are recorded in order of increasing distance toward the head-end. These tripwire data indicate that ignition first occurs at the aft-end of the main motor grain and progresses to the head-end. The thermocouple data confirm this observation. In general, ignition at the head-end, which is shown by the loss of the last tripwire trace, corresponds closely to the attainment of steady state chamber pressure in the main motor. This is indicative that the flame propagation rate into the head-end, and not the chamber filling rate, limits the rate at which steady state operating conditions can be reached. Similar data from Test 9 are shown in figure III-30. As indicated, the main motor pressure ignition transient was considerably longer. Although Test 9 was conducted with the igniter at a somewhat higher ϵ^* than Test 3 (1.45 vs. 1.21) the primary reason for the slow ignition transient is attributed to either the much lower igniter mass flow parameter or changed igniter nozzle expansion ratio used for Test 9.

Motor thrust, throat pressures (P_7 and P_{16}) and motor and igniter head-end pressures, are shown in figures III-34 and III-35 for Tests 3 and 9, respectively. The large pressure oscillations recorded in Test 3 at the motor nozzle pressure taps were the worst observed in any test. These oscillations are attributed to interference of the main motor flow by the igniter jet and are specially severe in this test because of the low ϵ^* and relatively high igniter mass flow parameter.

Thrust oscillations were recorded on all runs and are believed to have been produced by excitation of the natural frequency of the thrust stand. However, it is noted that the oscillations were more severe during

FOLDOUT FRAME 1

FOLDOUT FRAME 2

NASA CR-72447

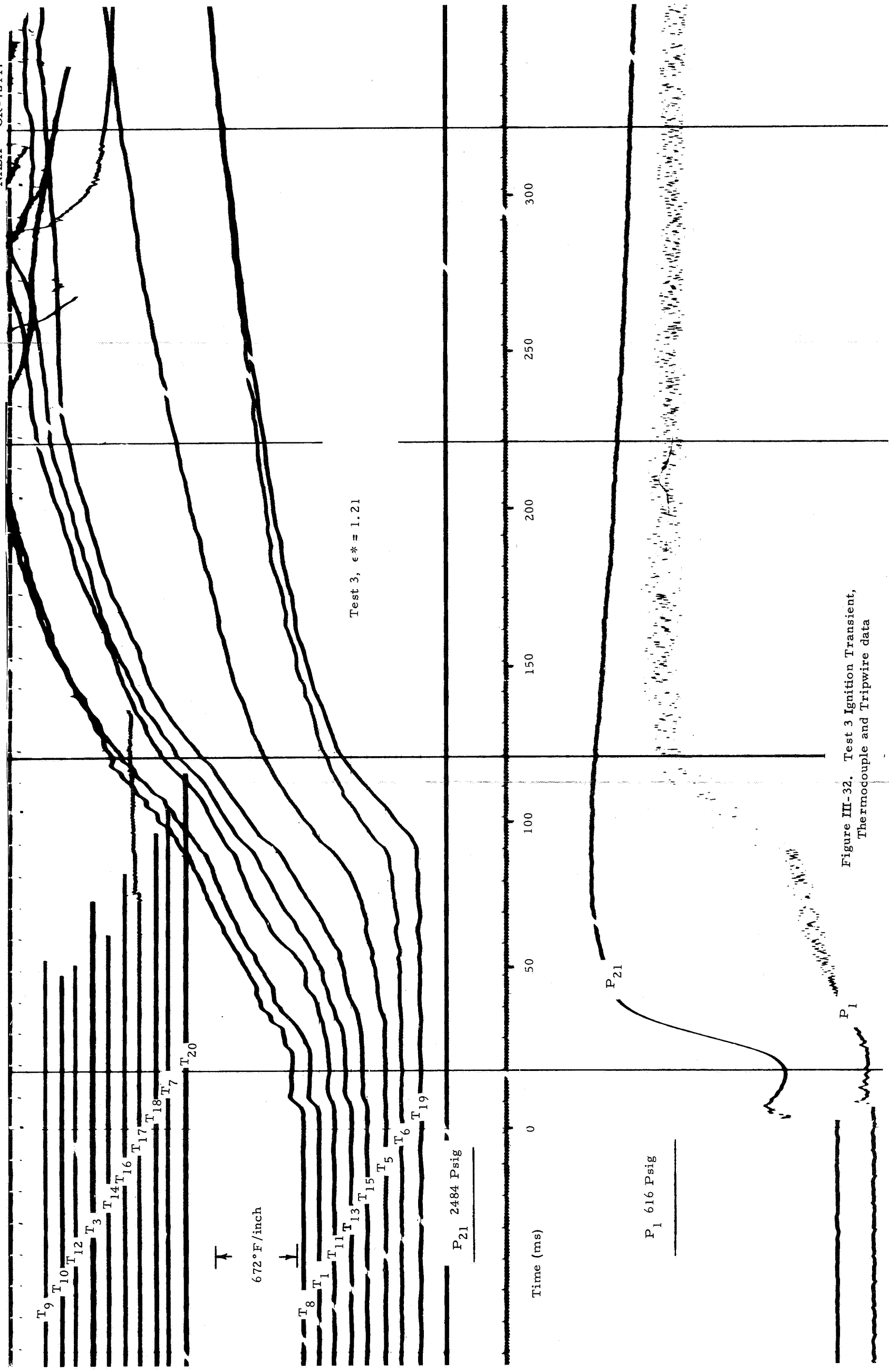


Figure III-32. Test 3 Ignition Transient, Thermocouple and Tripwire data

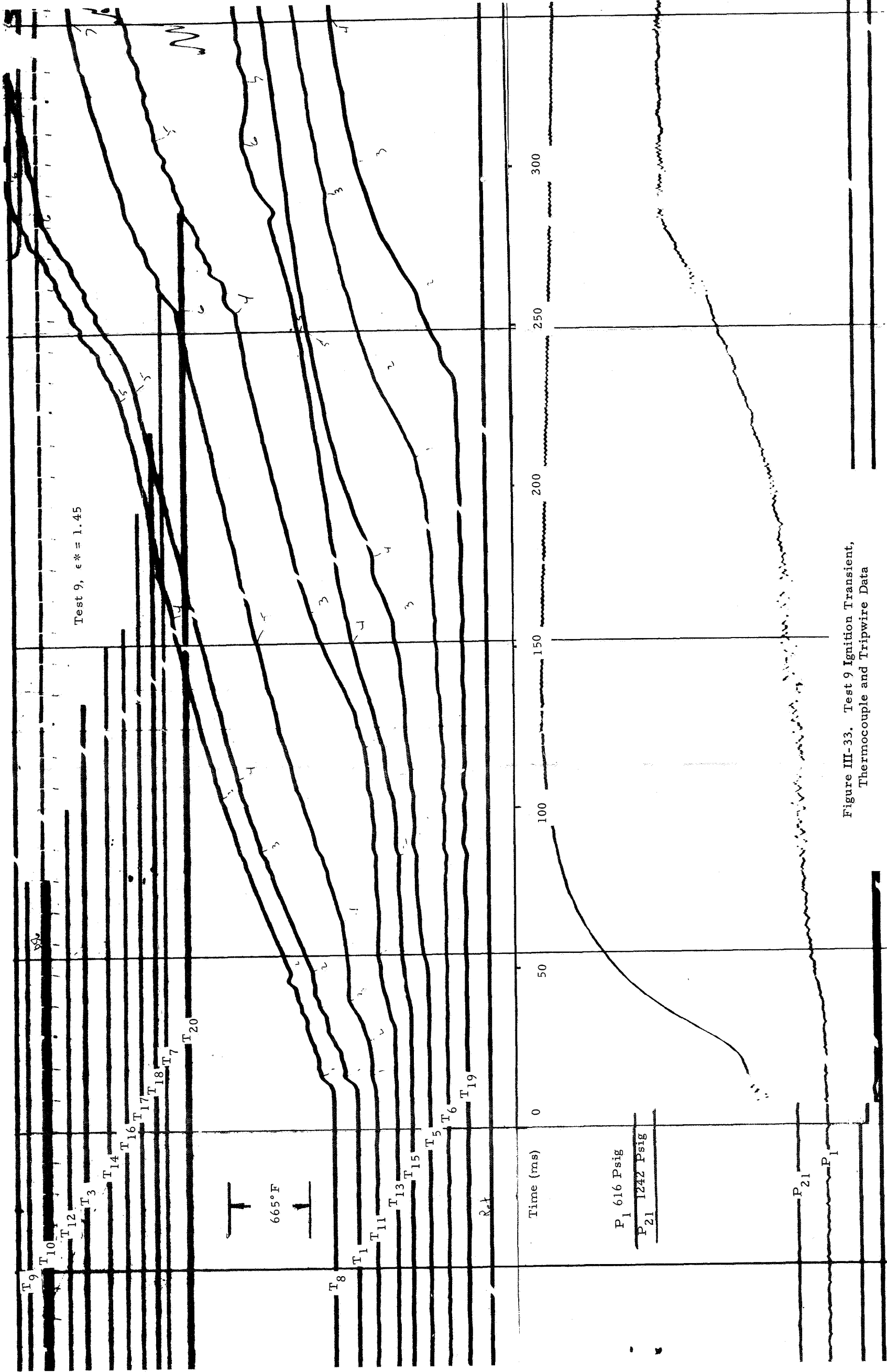


Figure III-33. Test 9 Ignition Transient, Thermocouple and Tripwire Data

PRECEDING PAGE BLANK NOT FILMED.

NASA CR-72447

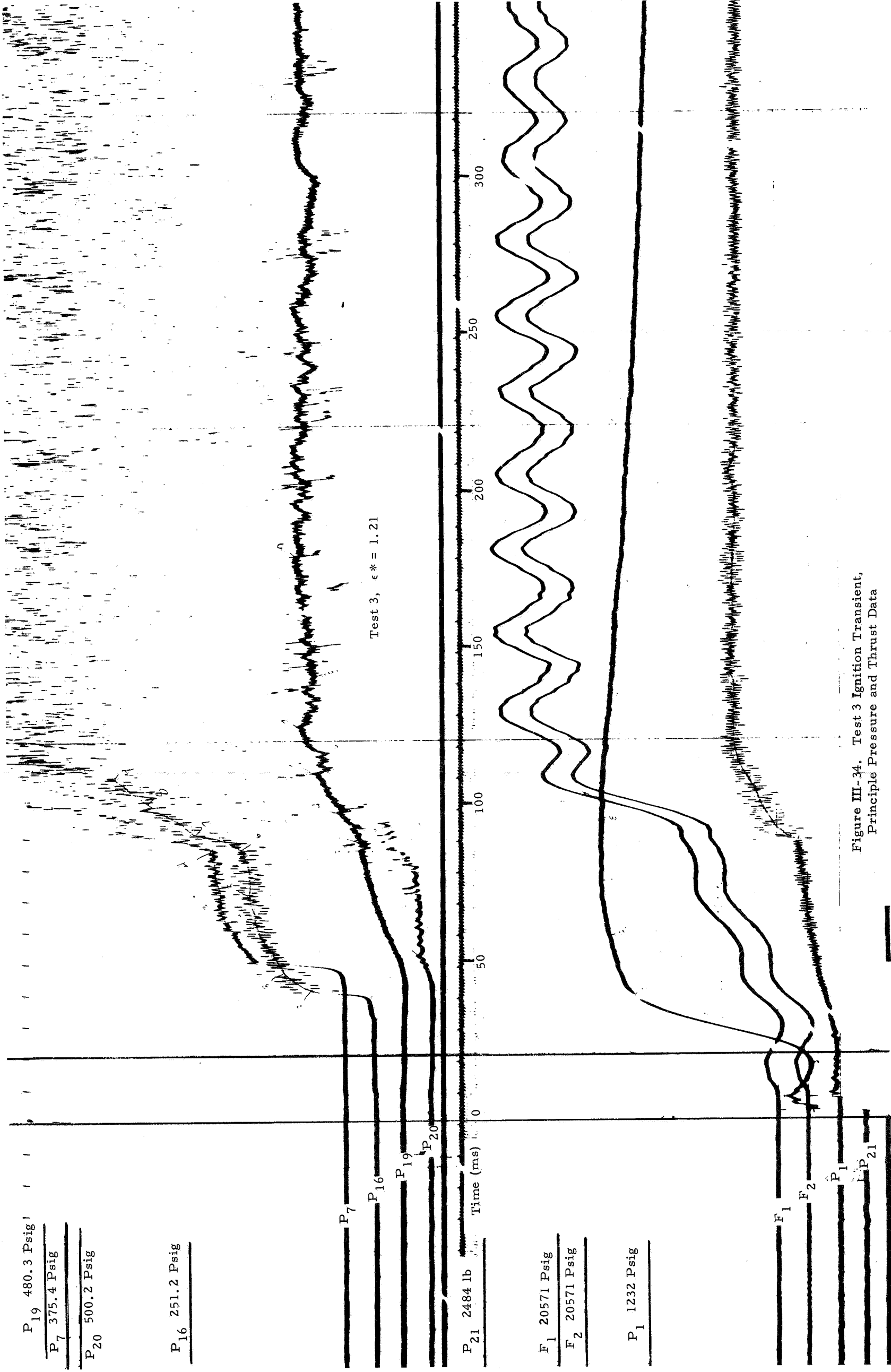
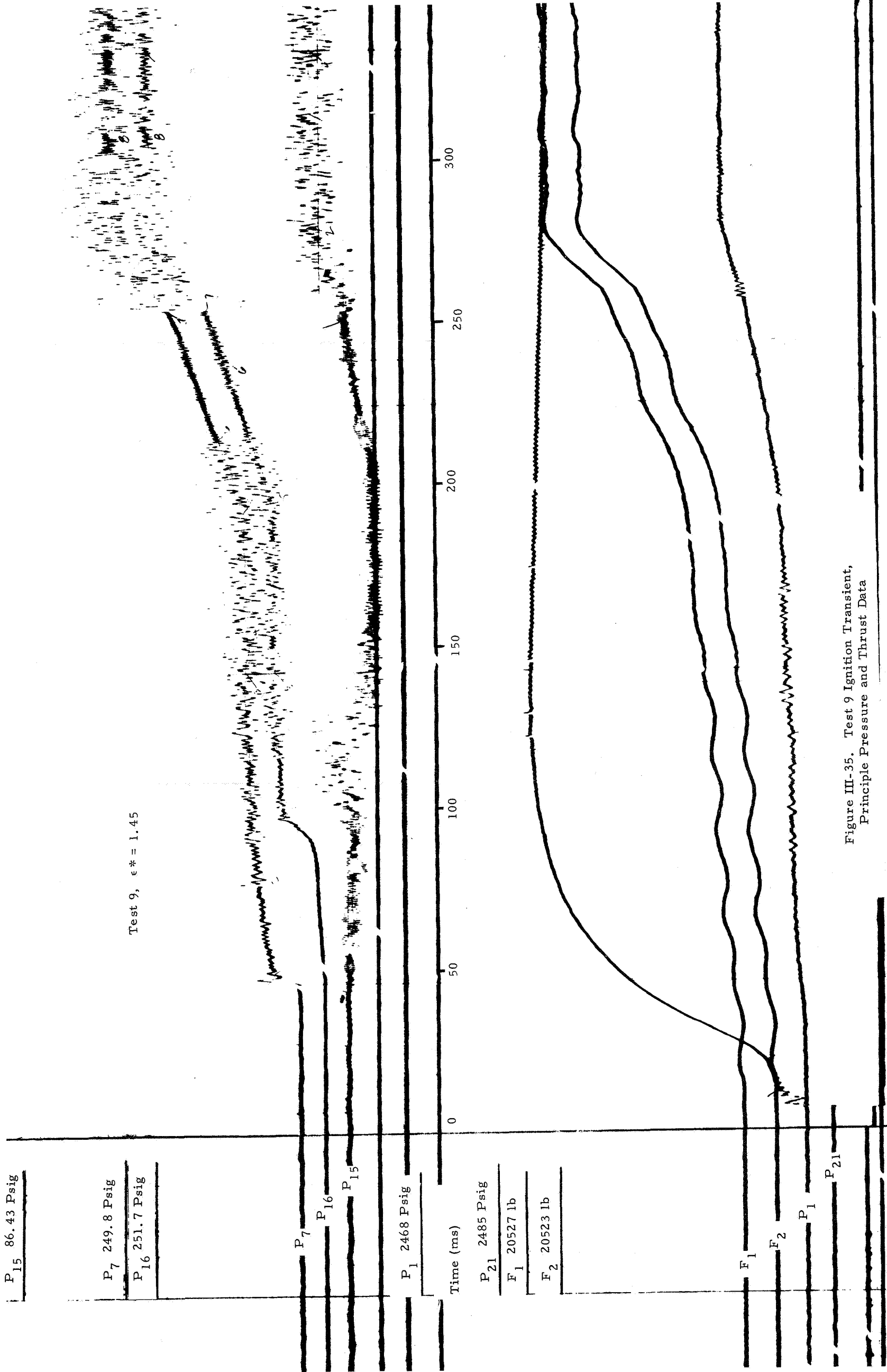


Figure III-34. Test 3 Ignition Transient,
Principle Pressure and Thrust Data

PRECEDING PAGE BLANK NOT FILMED.

NASA CR-72447



PRECEDING PAGE BLANK NOT FILMED.

NASA CR-72447

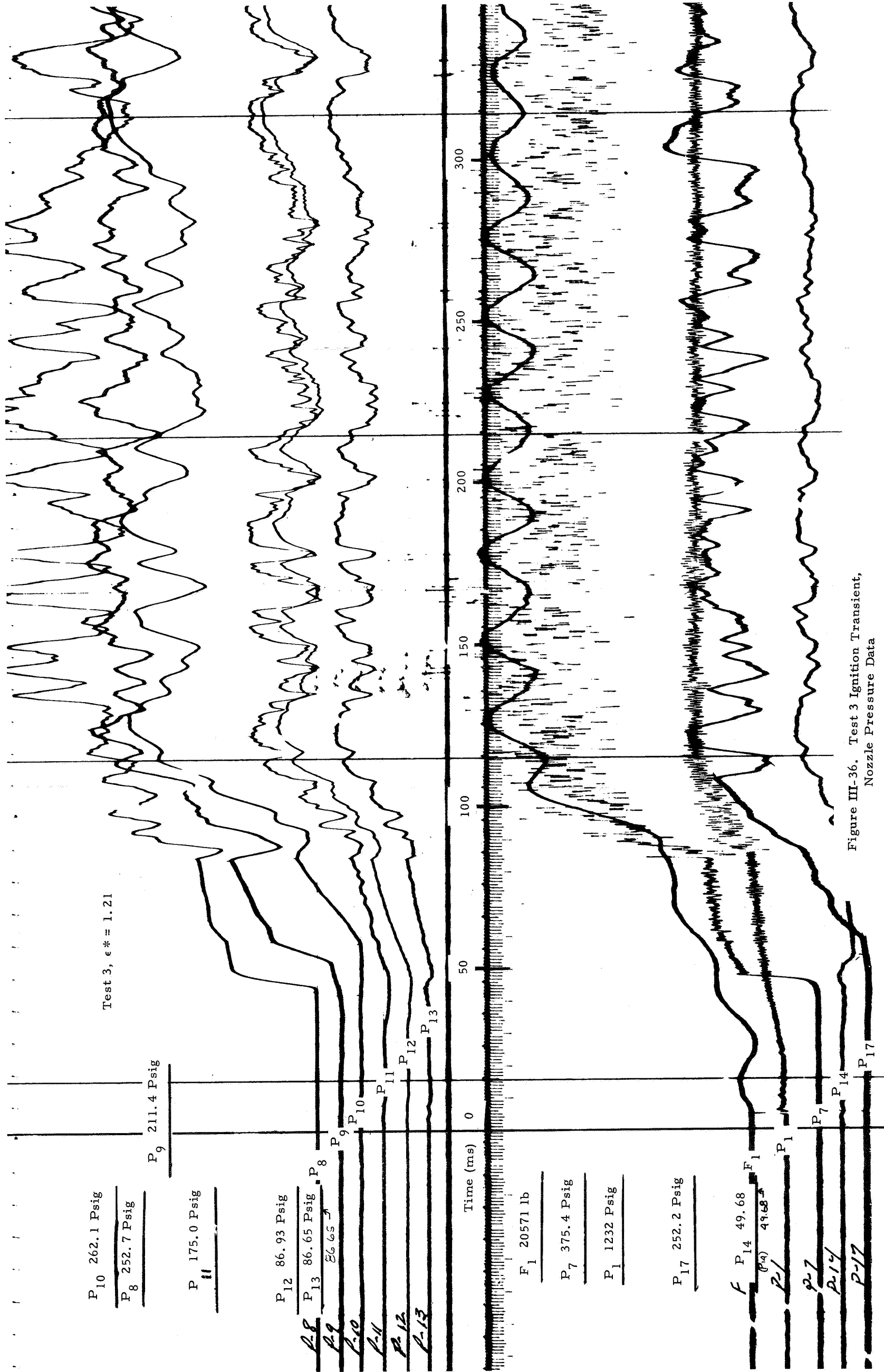


Figure III-36. Test 3 Ignition Transient, Nozzle Pressure Data

PRECEDING PAGE BLANK NOT FILMED.

NASA CR-72447

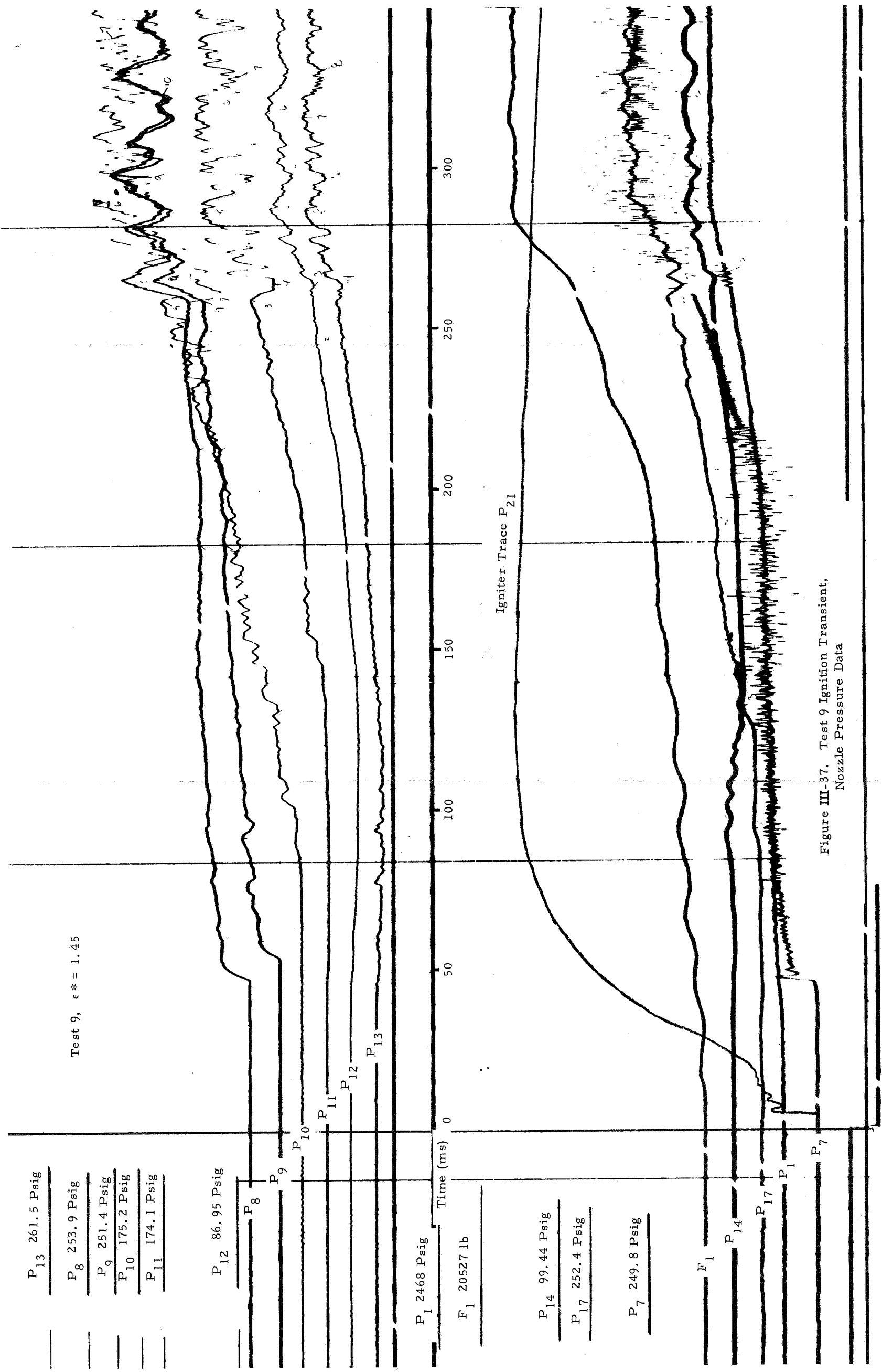


Figure III-37. Test 9 Ignition Transient, Nozzle Pressure Data

PRECEDING PAGE BLANK NOT FILMED.

NASA CR-72447

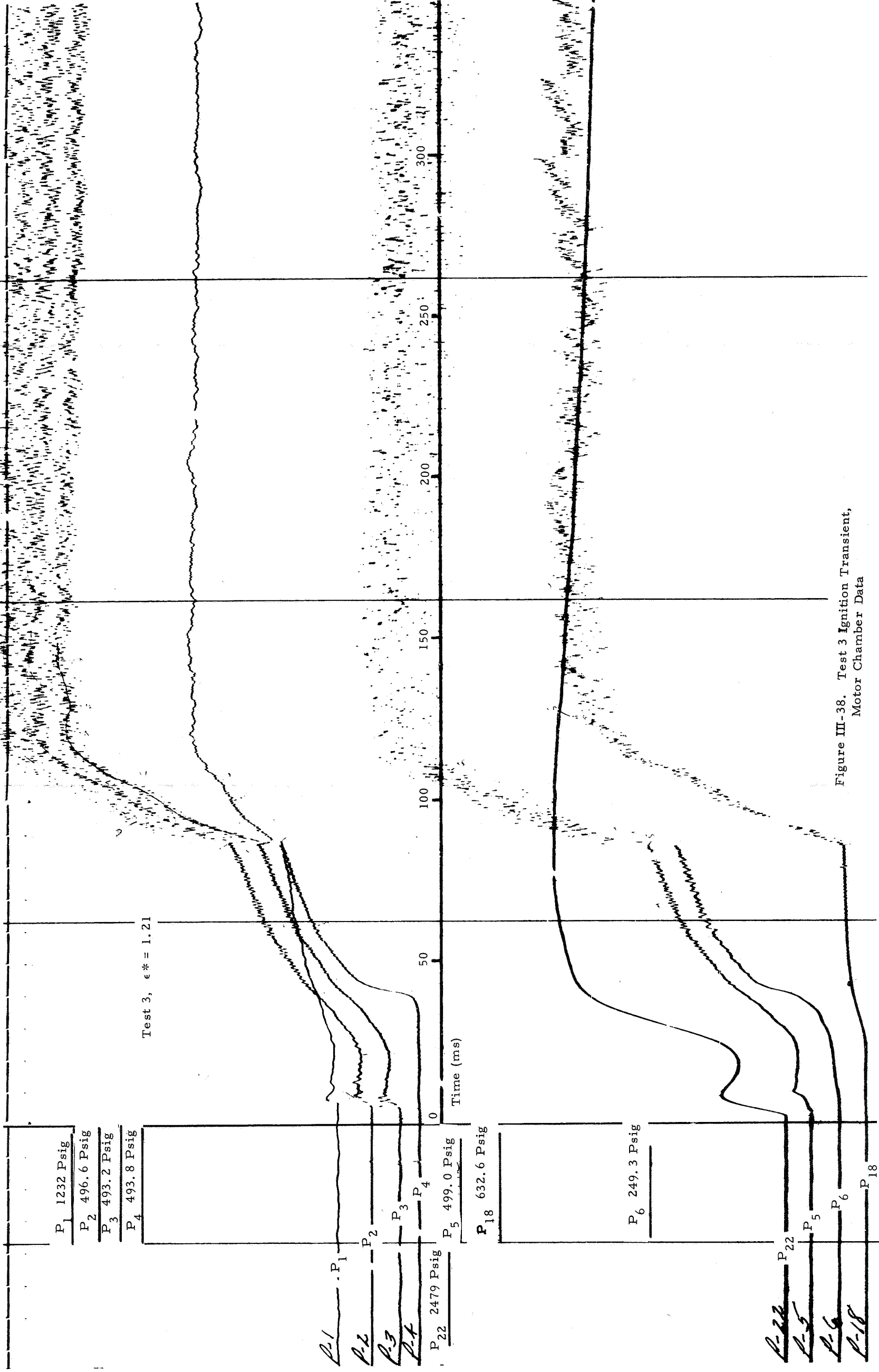


Figure III-38. Test 3 Ignition Transient, Motor Chamber Data

PRECEDING PAGE BLANK NOT FILMED.

NASA CR-72447

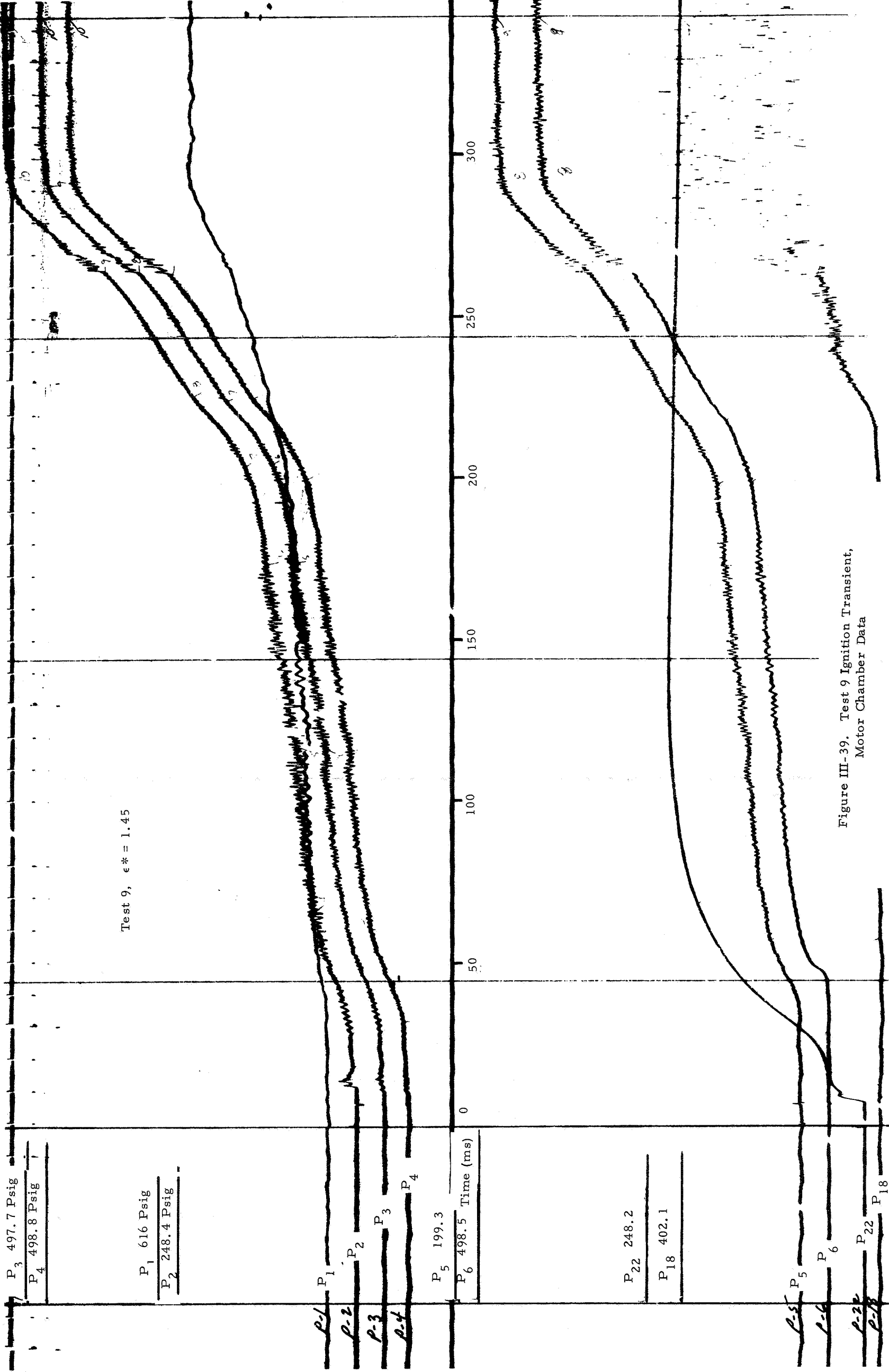


Figure III-39. Test 9 Ignition Transient, Motor Chamber Data

igniter operation, indicating coupling of the igniter and main motor flow interactions with the motor thrust. Corresponding thrust and pressure data are shown in figure III-35 for Test 9. Relative to Test 3, the amplitude of the thrust and pressure oscillation of Test 9 were considerably diminished.

The periods of relatively damped operation of the throat pressures in Test 9 correspond to periods of operation where there is no igniter jet blockage of the main motor throat. This indicates that the motor is operating in a marginally blocked mode and, in general, the percentage of time spent in the mode with the igniter jet interfering with the main motor throat flow decreased as the igniter pressure decayed and the main motor chamber increased, i. e., as the ratio of igniter to main motor total pressure decreased. In some cases, the throat pressure oscillations completely died out prior to the beginning of igniter tail-off. For the instances where the igniter jet interference with the main motor flow was intermittent as in Test 9, the degree of motor overpressure, if any, could not be distinguished from the normal variations in motor chamber pressure accruing from motor manufacturing and propellant processing tolerances. A primary use of the throat pressure measurements was to define the point of main motor throat unblocking.

The slow initial response of the throat pressure measurements as indicated in both Tests 3 and 9 were noted in varying degrees in the other tests. Several possible causes were postulated for these initial throat pressure measurement response failures. These causes included (1) slugging of the transducer pressure tap opening with condensed alumina (2) formation of an oxidized plug in the pressure tap from the silica grease used to provide thermal insulation for the transducer or (3) air bubbles in the viscous insulating grease. After the initial transducer hang-up, the response was apparently satisfactory in most instances until the time of igniter tail-off when the transducers begin to drift due either to the violent pressure oscillations or excessive heat input.

Also shown in figure III-35 is nozzle exit cone measurement P_{15} which is located near the nozzle exit plane. The initial drop below atmospheric pressure is attributed to overexpansion of the nozzle flow. The large oscillations which occur after steady state conditions are reached in the main chamber are due to upstream pressure disturbances and possible flow separation from the nozzle wall near the exit plane.

Measurements P_{19} and P_{20} shown in figure III-34 are measured at the igniter exit cone lip and on the igniter conical forebody, respectively (See figure III-24). Measurement P_{19} was relatively quiet on Test 3 indicating stable flow across the igniter lip. However, on other tests, especially Test 2, large saw-tooth oscillations were observed and were believed to be caused by transverse oscillations of the igniter jet. The igniter lip measurement was not recorded on all tests because of a tendency of alumina to plug the transducer pressure tap after igniter action, resulting in thermal damage to the transducers. The high frequency pressure disturbances recorded on the igniter forebody (P_{20}) are reflections of the pressure disturbances caused by interaction of the igniter and main motor flow field. These oscillations were considerably diminished after the igniter burn-out on Test 3, and in general, were far less severe during tests where the igniter was positioned at larger ϵ * locations.

Main motor nozzle wall pressure measurements for Tests 3 and 9 are shown in figures III-36 and III-37, respectively. These data graphically depict what is considered the most serious problem confronting aft-end ignition, e.g., the severe pressure disturbances induced by interaction of the igniter and main motor flow in motor nozzle and chamber. In Test 3, in which the worst conditions were recorded, nozzle throat pressure excursions of up to 250 psi were noted. Corresponding pressure oscillations at the motor head-end displayed a maximum peak-to-peak amplitude of approximately 150 psi as indicated by a high speed playback of semidigital data. The frequency of these oscillations was approximately one to two cycles per millisecond.

In addition to the induced pressure oscillations in the motor chamber, a significant increase in the instantaneous average head-end chamber pressure was noted. The maximum recorded head-end pressure at P_1 was approximately 707 psia. By comparison with the runs using the approximate grain burn area the corresponding chamber pressure without throat blockage should have been approximately 520 psia. This indicates an overpressure of about 35 percent.

Significant pressure oscillations were also noted in the nozzle wall pressure data. The first nozzle wall pressure tap downstream of the throat (P_9) displayed maximum pressure excursions in the order of 200 psi, at a frequency of approximately one cycle every ten milliseconds. At successive pressure taps at the higher expansion ratios along the exit cone, the maximum peak-to-peak pressure oscillation amplitudes decreased to a value of approximately 25 psi at pressure tap P_{13} . A comparison of P_{10} and P_{17} , located 90° from one another at the same axial station, shows that at times the pressure peaks appear

to be in phase and at other times out of phase. This indicates that the oscillation of the igniter and main motor flow interactions were lateral or rotational as well as axial.

Figure III-37 shows the nozzle pressure measurements for Test 9. As indicated, the pressure oscillations in the nozzle and main motor were considerably reduced in comparison with Test 3. The maximum peak-to-peak excursions for P_7 and P_8 were 90 and 80 psi respectively. Motor head-end pressure oscillations were only slightly greater than during unblocked operation and there was no discernable increase in average chamber pressure. The large excursions in throat pressure P_7 shown in this figure are believed to be due to an under-damped recorder galvanometer. A redundant measurement on recorder 2 (Figure III-35) and the measurement at throat pressure tap P_{16} show maximum peak-to-peak oscillations of approximately 90 psia, considerably less than those shown in figure III-37.

The nozzle pressure oscillations noted on most of the other tests were not as severe as those on Test 3, but were greater than Test 9. In general, the severity of the oscillations decreased with increasing ϵ^* and decreasing igniter mass flow parameter. Only in Test 1 did the nozzle exit cone pressure disturbances fail to be reflected in the throat and main motor pressure traces.

Motor chamber pressures measured at various locations from the nozzle entrance section to the motor head-end are shown in figures III-38 and III-39 for Tests 3 and 9 respectively. Nozzle pressure disturbances were seen to be fed back along the motor port to the head-end. The amplitudes of the oscillations were greatest at the nozzle end and appeared to be attenuated as the pressure waves traveled up the port. Maximum peak-to-peak oscillations at the nozzle inlet (P_6) were estimated from the data to be approximately 100 psia, while the pressure oscillation recorded at head-end (P_1) were in the order of 25 to 30 psia. However, a high speed play-back of data from the head-end chamber pressure (P_1) indicated pressure oscillations as high as 150 psi peak-to-peak. This fact and the general attenuation of the pressure oscillations as they approached the head-end indicate that these oscillations may be more severe than the oscillograph data show because of instrumentation system limitations.

Also shown in figure III-38 is the igniter chamber pressure (P_{22}), used for reference, and measurement P_{18} recorded at an area ratio of 5.30 in the igniter exit cone. At approximately 85 ms P_{18} was observed to show a sudden increase in pressure level. This was attributed to movement of a shock from downstream of the pressure tap to some

location upstream. The location of the shock was seen to stabilize when motor steady state operating conditions were reached. This sudden pressure increase noted at P_{18} was also indicated in the motor chamber pressure measurements and appeared to have originated at the main motor throat, propagating both upstream and downstream. The dramatic increase in motor pressure rise was believed caused by a coupling of the pressure disturbance with the pressure-dependent burn rate mechanism of the propellant and by a possible increase in throat blockage resulting from the induced shock in the igniter jet.

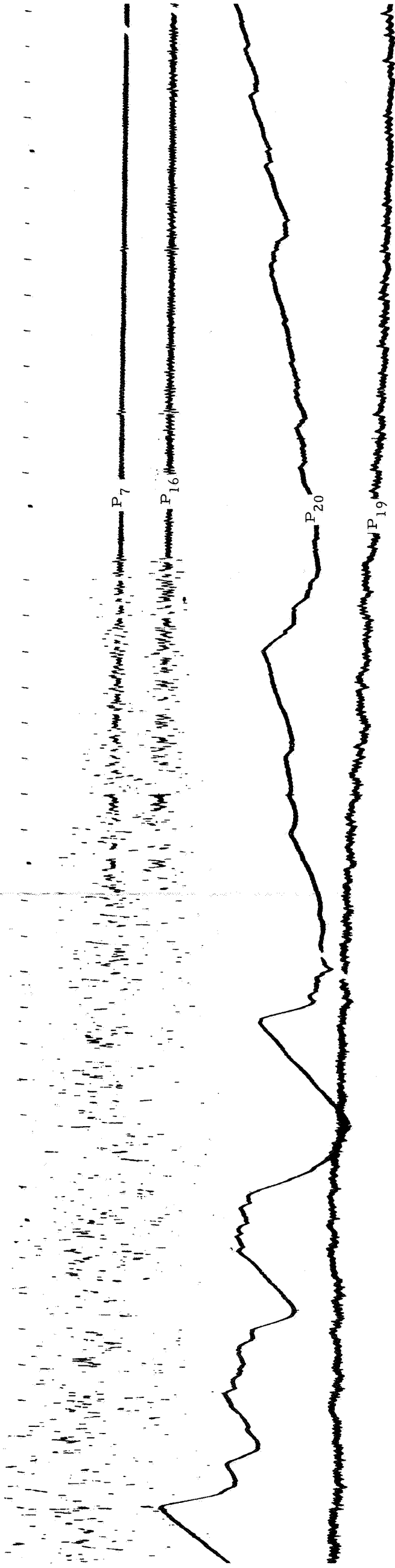
Figure III-39 shows the motor chamber pressure and igniter nozzle exit cone measurements for Test 9. For this test, the motor chamber pressure disturbances were considerably reduced. These data were more representative of the degree of pressure disturbances noted on the other tests than were the data from Test 3. The higher degree of instability of P_{18} as compared with Test 3 probably indicates that the igniter nozzle shock was at the approximate location of the pressure tap and was in a region of unstable igniter jet separation.

b. Late Steady State Operation and Igniter Tail-Off

Data which illustrate typical steady-state operating conditions observed during the nine test firings are presented in figure III-40 through III-43. These data from Tests 3 and 9 are shown during motor steady state operation prior to and during igniter tail-off. This time interval best illustrates igniter and main motor interactions during full igniter and main motor flow, and over the region where the final main motor unblocking was generally observed to occur.

Figure III-40 shows igniter chamber pressure, motor chamber pressure, motor throat pressure and motor thrust data for Test 3. Beginning with igniter tail-off, pressure oscillations in the motor head-end and throat decayed with decaying igniter chamber pressure, and died out completely just before igniter flow ceased. As indicated, the igniter chamber pressure did not return to zero, but to a value which was approximately the recovery stagnation pressure across the bow-shock in front of the igniter body. The thrust oscillations which also dampened out as igniter pressure decayed, continued to diminish until motor burn-out. The igniter lip and forebody measurements P_{19} and P_{20} , respectively, were also seen to stabilize as igniter flow ceased.

Similar motor throat, chamber pressure and thrust data for Test 9 are shown in figure III-41. In Test 9, throat and motor chamber oscillations appeared to cease at about 700 ms or were indistinguishable from normal



Test 3, $\epsilon^* = 1.21$

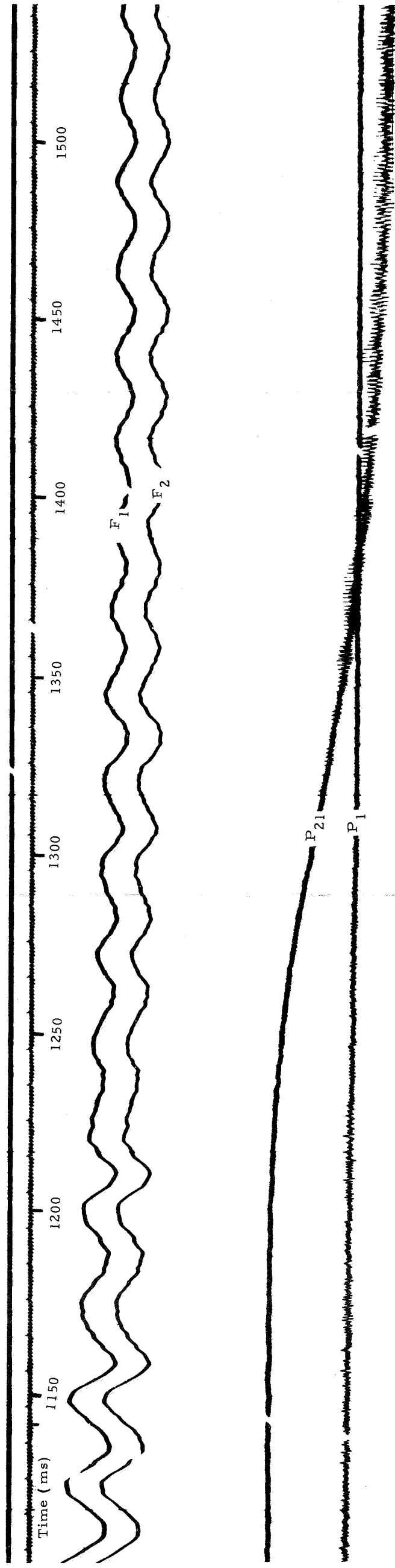


Figure III-40. Test 3 Igniter Tail-off,
Principle Pressure and Thrust Data

PRECEDING PAGE BLANK NOT FILMED.



Test 9, $\epsilon^* = 1.45$

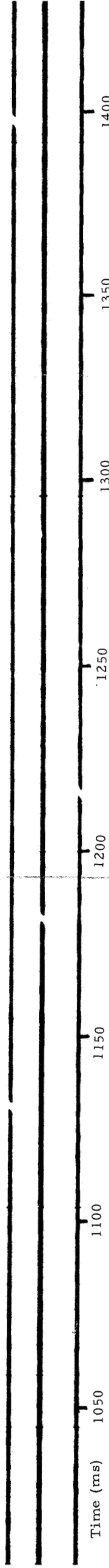


Figure III-41. Test 9 Igniter Tail-off, Principle Pressure and Thrust Data

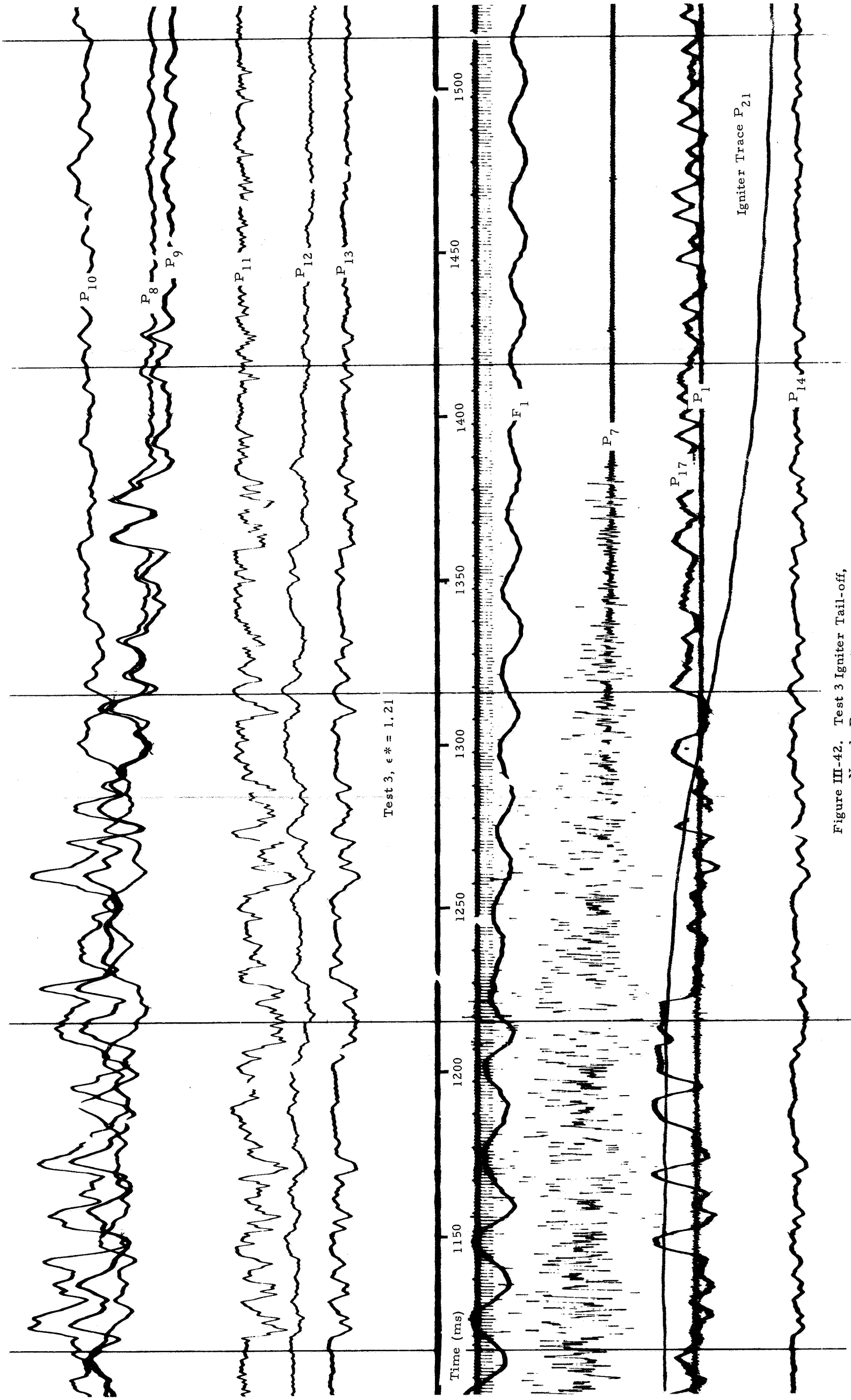


Figure III-42. Test 3 Igniter Tail-off,
Nozzle Pressure Data

PRECEDING PAGE BLANK NOT FILMED.

NASA CR-72447

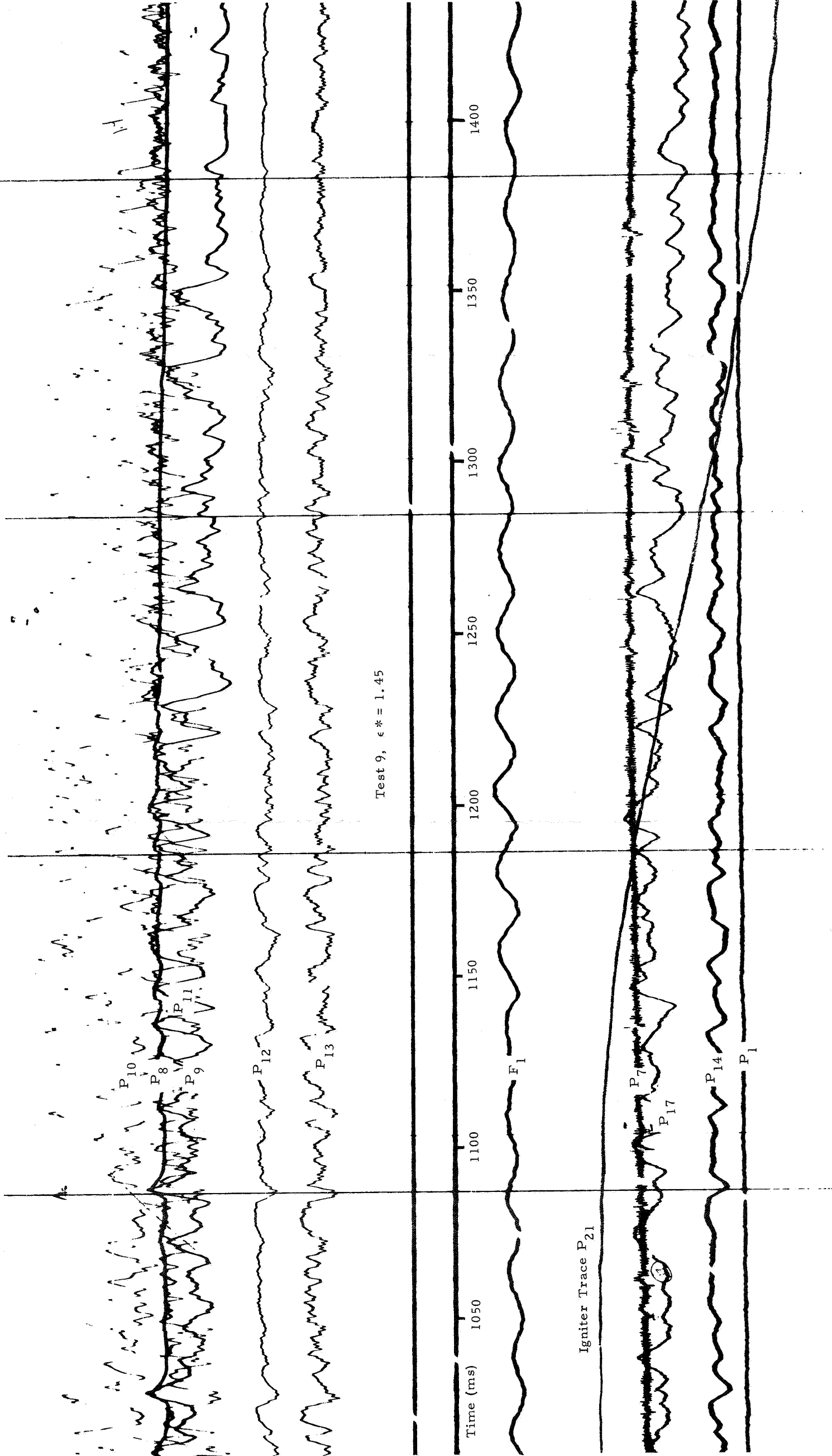


Figure III-43. Test 9 Igniter Tail-off,
Nozzle Pressure Data

PRECEDING PAGE BLANK NOT FILMED.

instrumentation noise. The thrust oscillations dampened out during igniter tail-off and retained about the same degree of oscillations noted in figure III-40. The oscillations on the motor nozzle exit cone measurement P_{15} are almost constant throughout the entire run until igniter tail-off when they were observed to dampen out considerably.

In other tests not shown, the characteristic motor throat, chamber and thrust measurement were observed to lie between the extremes of Tests 3 and 9. In general, the greatest degree of thrust and pressure disturbances were noted at low ϵ^* or high w/A .

The main motor nozzle exit cone pressure measurements for Tests 3 and 9 are shown in figures III-42 and III-43 respectively. The igniter chamber pressure has been added to these illustrations for comparison of igniter flow relative to the motor nozzle pressure data. Prior to igniter tail-off, the nozzle pressure excursions from Test 3 were considerably less severe than the corresponding data from the initial portion of the run (see figure III-36). For example, the maximum excursion on P_8 was approximately 110 psia as compared with 200 psi at the beginning of the test.

Chamber overpressurization was also considerably reduced over the run duration to igniter tail-off. A head-end chamber pressure of 644 psia was recorded at 1150 ms just before the igniter tail-off began. At that time the pressure should have been approximately 580 psia for the propellant burn area if no blockage was occurring. This corresponded to a 10 percent overpressure as compared to the 36 percent overpressure observed at the beginning of the test. This was consistent with the theoretical blockage model, which predicts that the degree of blockage at a given ϵ^* location will decrease with decreasing igniter to main motor total pressure ratio (P_i/P_m). In the tests where large initial blockage occurred, the pressure oscillations and motor overpressures tended to agree with the expected decaying trend with decaying P_i/P_m . However, exceptions were observed, as will be discussed in later sections.

Figure III-43 presents nozzle pressure data for Test 9. As in Test 3, large nozzle exit cone oscillations were observed during igniter steady state operation, dying out almost entirely with cessation of igniter action. However, a significant difference was that nozzle oscillations were not at that time propagated into the motor throat and chamber. Cessation of abnormal throat and chamber oscillation occurred at approximately 700 ms. This came after a gradual lessening of nozzle pressure oscillation intensities which corresponded to the decay in the igniter to main motor total chamber pressure ratio.

Motor chamber pressure data during the late steady state operation and igniter tail-off are not shown since no significant events were observed.

D. DATA EVALUATION AND CORRELATION

The data analysis and correlation activities were oriented toward the two fundamental areas of interest. The first was the initial penetration of the igniter jet into the motor chamber and the subsequent phenomena culminating in steady state burning of the grain. The second area was the motor nozzle interactions which take place between the igniter jet and main motor flow after the attainment of full-rated chamber pressure and thrust.

Quantitative analyses of tripwire data and a qualitative study of the thermocouple and motor pressure data provided significant information on the effects of igniter design and placement parameters. These analyses indicate the proper igniter design and placement parameters which are necessary to achieve satisfactory ignition. Because of the doubtful quality of the motor thermocouple data and the difficulty in obtaining meaningful motor port flow field data, the possible detailed correlation of the initial jet penetration, propellant grain heat-up, ignition and subsequent flame propagation was limited.

The major emphasis was placed on the nozzle flow interactions and associated phenomena. The nozzle flow interactions lead to unexpected blockage characteristics and more importantly, oscillatory and sometimes asymmetrical nozzle pressure forces which could produce serious consequences in an operating system. Particular attention has been given to developing an understanding of the transient behavior of the data and isolation of the flow field oscillation trigger mechanisms. Consequently, considerable effort was applied to interpretation of the similarities and differences between the tests with respect to the flow field interactions, and less in the development of engineering data correlations. Correlations were also limited by the relatively few tests conducted during the program, and by the fact that several motors exhibited nozzle flow field behavior which were uncharacteristic of the other motors, reducing the opportunity for correlating comparisons.

1. Penetration, Ignition and Flame Propagation

The most satisfactory ignition system is generally regarded as that which produces the most repeatable and reliable ignition without causing other serious consequences, such as overpressurization or

excessively long ignition intervals. Although the minimization of total time to development of rated chamber pressure is not usually a critical goal, short ignition times normally accompany the more essential requirements of repeatability and reliability. The evaluation of the events in the ignition process leading to steady state motor operation, i.e., igniter jet penetration, first ignition, and flame propagation, has therefore been approached with the total ignition interval established as a significant criterion in determining the quality of the ignition transient.

a. Jet Penetration

It was not possible to provide internal flow field instrumentation, such as pitot probes, in the motors for the direct measurement of the internal flow field. Consequently, the structure of the flow field and the extent to which the jet penetrated the closed end motor cavity was deduced by evaluation of the wall temperature measurements and the deactivation times of the pyrofuse breakwires. Although axial wall pressure data was recorded, examination of this data did not result in the establishment of quantitative flow processes relating to jet penetration. The observed pressures did reveal that the jet flow field was well established before first ignition, and in some cases where ignition was slow, e.g., Tests 9 and 6, an intermediate plateau pressure was reached during which the flow field was in a steady state condition (see figure III-44). At that time, the full jet exhaust flowed into the motor cavity at the elevated plateau pressure, turned and flowed out through the annulus formed by the throat and the incoming jet, as shown schematically in figure III-45. The pressure profile accompanying the sketch indicated that, at 60 ms, the flow outward was subsonic at the throat, was choked between the throat and the igniter exit plane, and was supersonic at the exit plane. The severe axial pressure gradient between the igniter exit plane and motor chamber probably affect the igniter jet, resulting in a ballooning, then contraction of the jet with accompanying shocks and total pressure losses. It was not possible to conclude, from analysis of the bore pressure data, that the jet stream passed through strong shocks after it entered the chamber. Thus, it appears reasonable to assume that the jet lost its forward momentum through a series of oblique shocks and viscous erosion and gradually dissipated its forward flow rate until, except for local turbulence, it could be said to have reached its maximum penetration.

The determination of the two zones of the grain surface which were or were not influenced by the jet prior to first ignition was made through evaluation of the thermocouple and breakwire data. Referring to figure III-45, it can be concluded that the surface of the grain in the vicinity

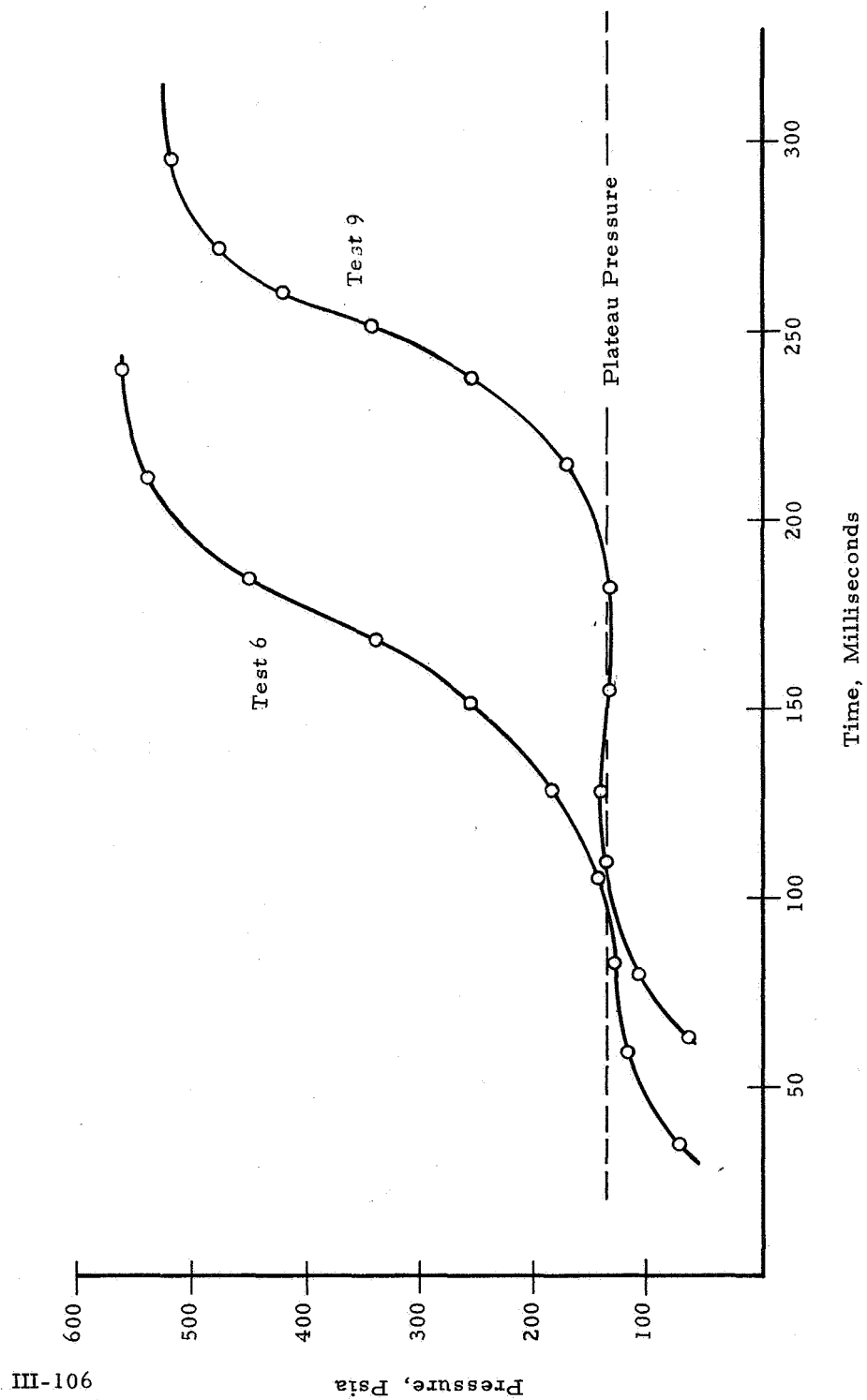


Figure III-44. Head-end Pressures During Ignition Transient

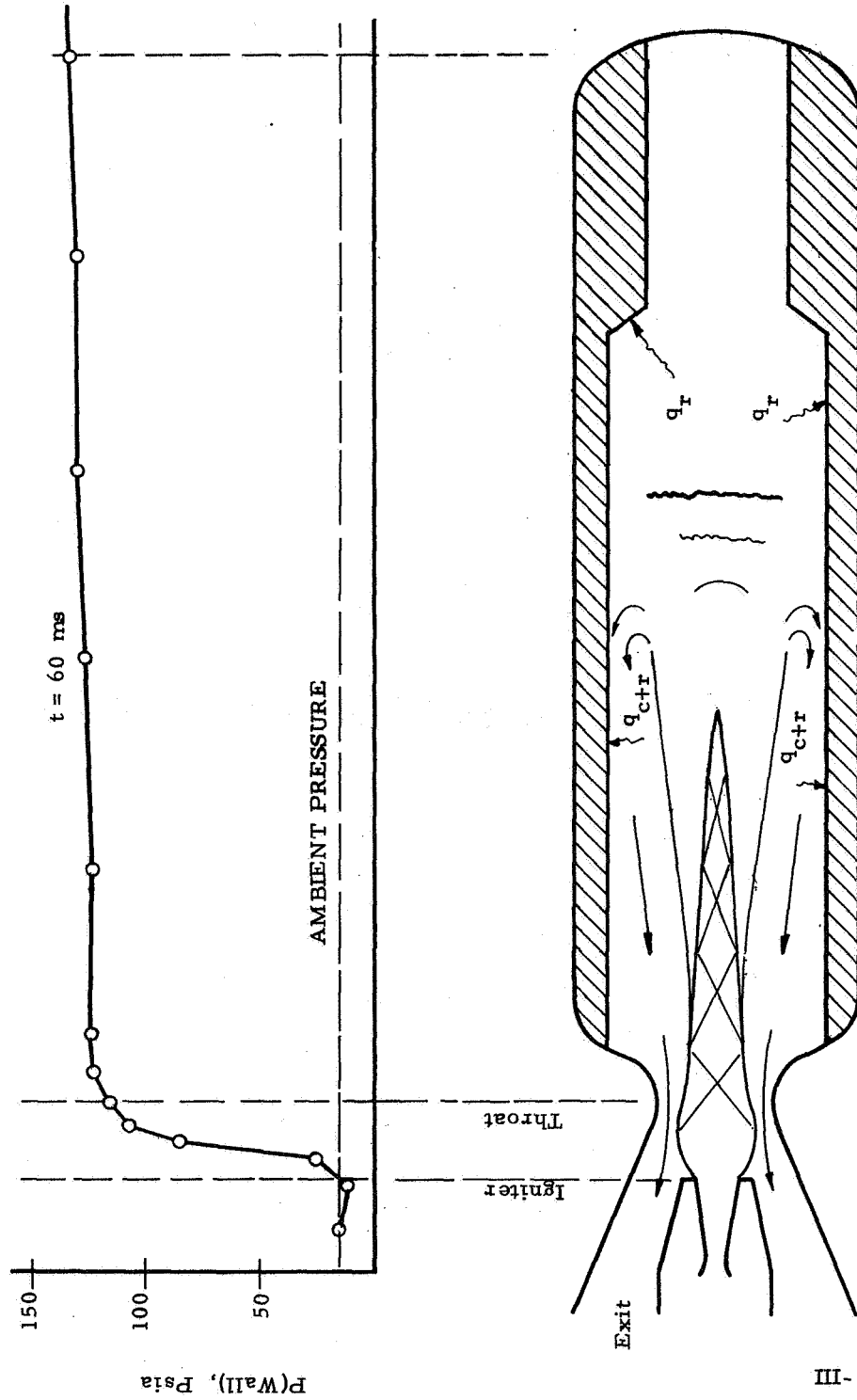


Figure III-45. Typical Penetration Flow Field and Pressure Distribution

of the jet was exposed to both convective and radiative heating, the greatest being at the aft-end and decreasing to the point of maximum penetration. In the forward end, the grain was exposed to minimal heating, consisting of radiation from the hot igniter gates in the aft-end jet and adiabatic compression of the atmospheric gases in the head-end. Assessment of the pre-ignition grain heating by the thermocouple response and by the surface temperature effects on flame surface propagation rates confirm these observations.

Figure III-46 shows the times for breakwire failure versus location for Test 4. The two lines represent somewhat arbitrarily established initial and final flame propagation rates which are taken to be characteristic of the two zones separated by the penetration stagnation plane. The intersection of the two is then assumed to identify the forwardmost point at which the jet had substantially influenced surface heating.

A second method of determining igniter jet penetration involved consideration of the pre-ignition axial temperature profiles. In the region of the jet, the surface was heated until first ignition occurred near the aft-end of the grain. In this region, the temperature gradient was greatest. As the flame progressed forward to the cooler surfaces, the temperature gradient in the area of the flame front steepened. This was most dramatically observed in Test 9, as shown in figure III-47. Accompanying this steepening was a change in the thermocouple-measured temperatures at which ignition occurred. This change in ignition temperature was believed due to response characteristics of the thermocouples which appeared to be a function of the thermocouple junction temperature and rate of heat input. The change of ignition temperature with time and position for Test 6 is shown in figure III-48. Here the maximum jet penetration point is taken as the location at which ignition occurs at the lowest temperature (T_{13}).

In spite of the crudity of these two methods, they are generally consistent and produce a semi-quantitative correlation between jet penetration and igniter mass flow parameter when applied to data from the nine ignition tests (see figure III-49). The trend is entirely reasonable and seems consistent with the hypotheses described previously. In the absence of jet underexpansion, attachment to the grain surface and formation of a stagnation region, the resistance to viscous erosion, characteristic of high total momentum jets, is the predominant factor in producing maximum jet penetration.

No appreciable effect of ϵ^* on jet penetration was found. The penetration data are presented in "broad band" form because of the semi-quantitative methods used. Additional study could be performed involving thermocouple

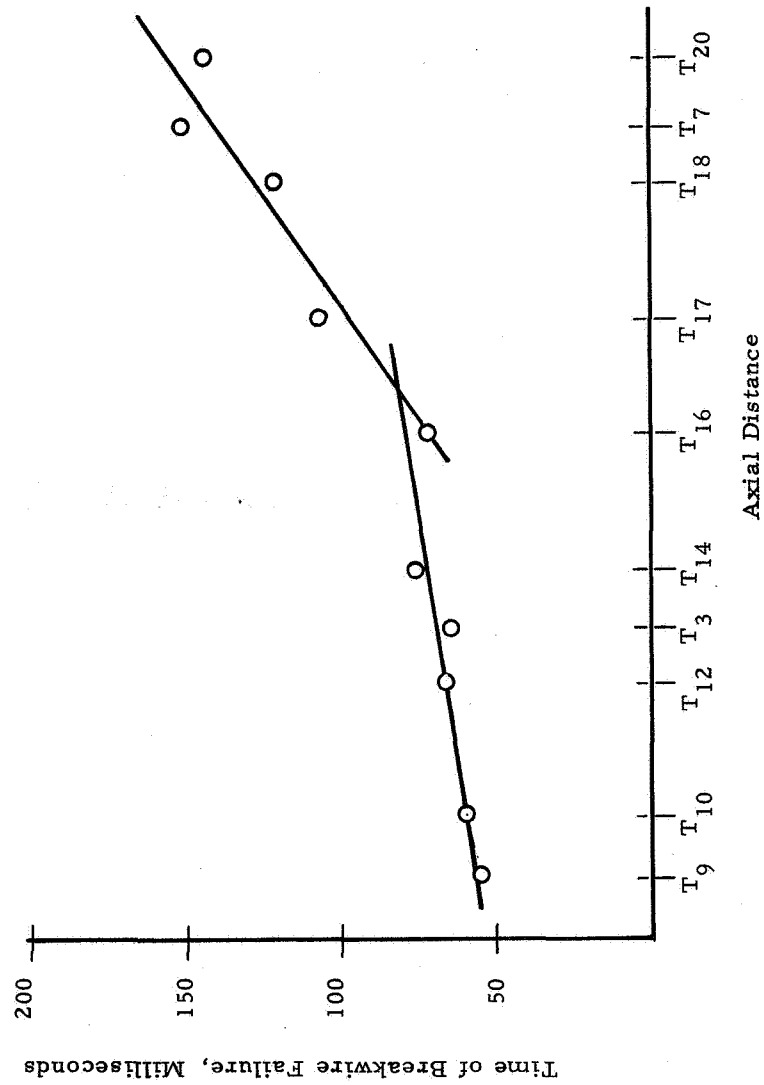
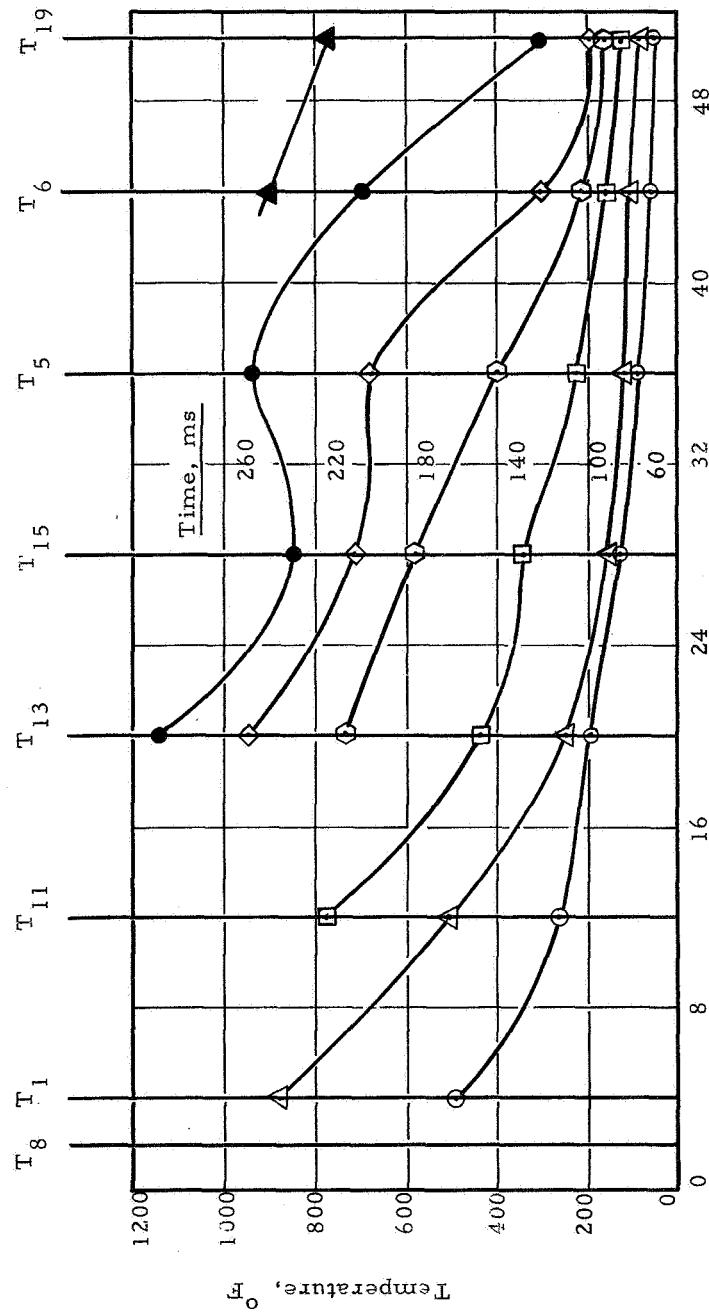


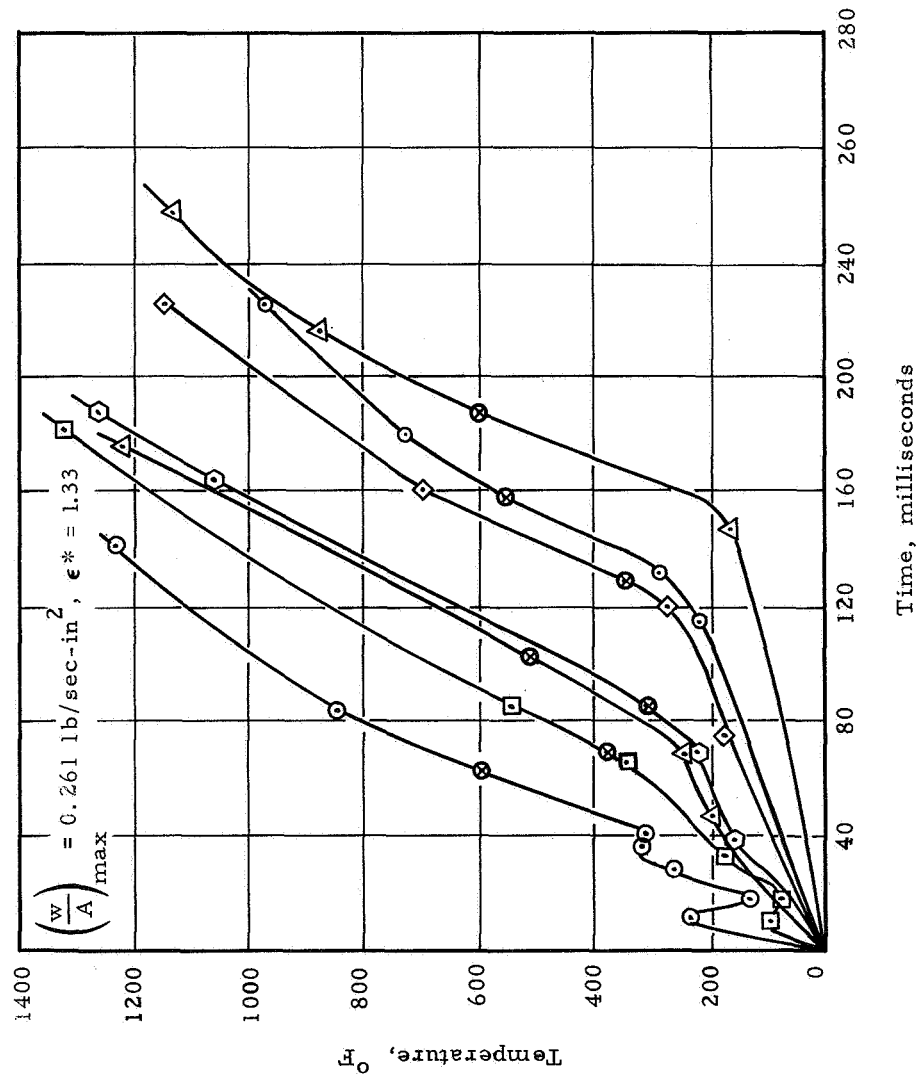
Figure III-46. Breakwire Response Times, Test 4

Test 9



Distance from grain aft-end, inches

Figure III-47. Motor Grain Thermocouple Temperatures, Test 9



Test 6

	Sensor	Ign. Temp.
○	T ₁	600
□	T ₁₁	380
△	T ₁₃	310
◇	T ₁₅	510
×	T ₅	345
○	T ₆	520
△	T ₁₉	600

⊗ Ignition from
Tripwire Data

Figure III-48. Comparison of Thermocouple Ignition Temperatures, Test 6

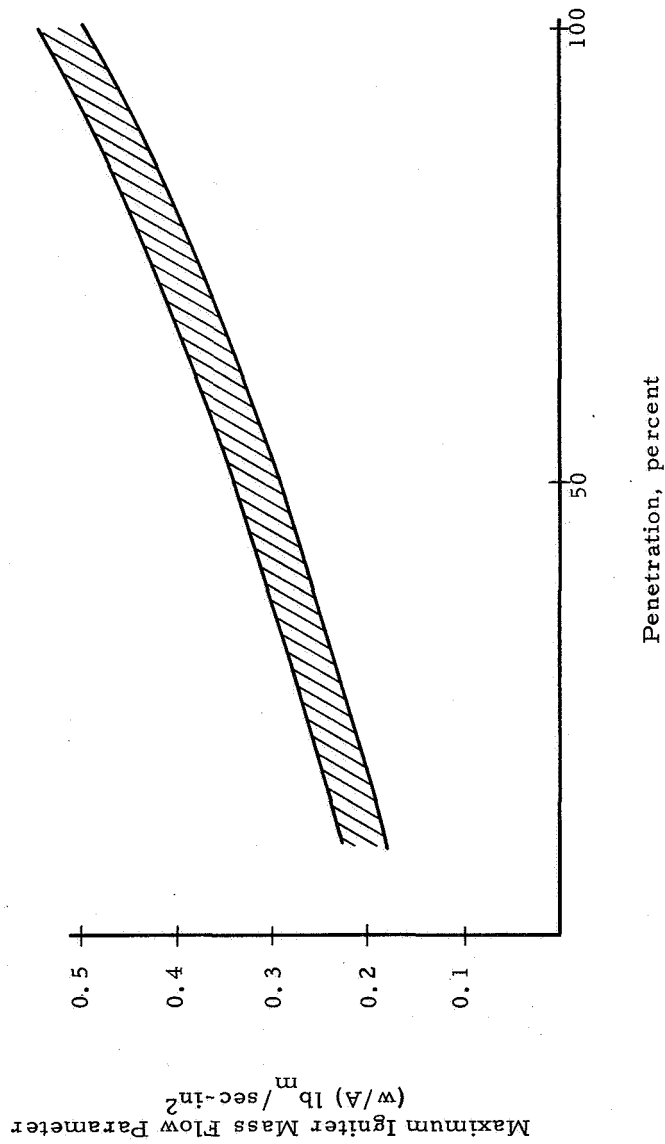


Figure III-49. Influence of $(w/A)_{\max}$ on Jet Penetration

and heat transfer calibration techniques which would result in much more precise correlations. These studies were not completed in this program, because the ignition characteristics were acceptable and because the nozzle flow oscillations discovered required intensive examination not originally anticipated.

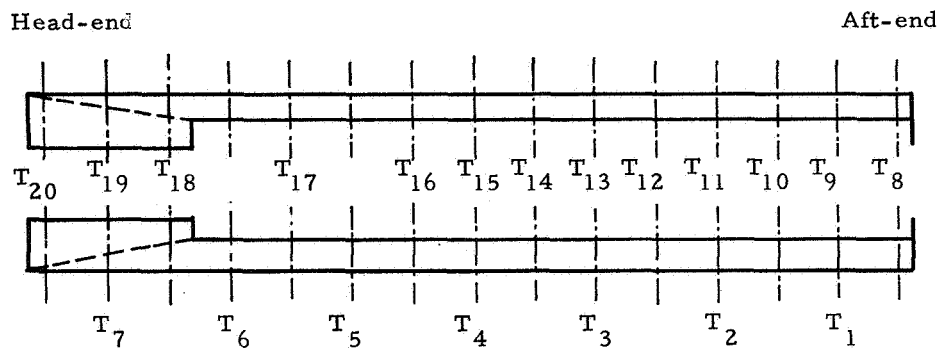
b. Ignition and Flame Propagation

Ignition and flame propagation are dependent upon the initial time history of heat input into the solid propellant grain. Ignition is achieved at a given location when sufficient heat has been transferred to the surface to raise it to the auto-ignition temperature. As discussed in the previous paragraphs, the length distribution of heating has been found to be dependent upon the degree of igniter jet penetration, which is a function of the igniter mass flux parameter and igniter to motor geometrical relationships.

An analysis of data from all tests indicated that the time to first ignition decreased and subsequent flame propagation increased with increasing igniter mass flux parameter and decreasing ϵ^* value. Contrary to previously reported behavior^(7, 9), no limitation on the jet penetration and apparent heat transfer rate was found for the range of maximum igniter mass flux parameters (w/A) below 0.561 lb/sec-in². Heat transfer data were not prepared because of extensive work which would have been required to calibrate thermocouple response.

Data on ignition and flame propagation was obtained by use of pyrofuse tripwires imbedded in solid propellant plugs, mounted with the face flush with propellant surface. This method of instrumentation was shown by Jensen⁽¹¹⁾ to produce satisfactory ignition and flame spread data. Reduced tripwire data from each of the nine tests are presented in Table III-6 along with the ϵ^* location and maximum igniter mass flow parameter recorded during the test. Deactivation times were referenced to the time of first observed pressure rise in the igniter. Tripwire deactivation times versus motor axial position for three different tests are presented in figure III-50. These data represent the fastest, the slowest, and an intermediate ignition and flame propagation sequence. Test 9, which was observed to have the longest ignition delay, was conducted at an $\epsilon^* = 1.45$ and a maximum igniter mass flux parameter $(w/A)_{\max}$ of 0.202 lb/sec-in². Test 7, which exhibited the shortest ignition delay, was run at an $\epsilon^* = 1.65$ and $(w/A) = 0.561$ lb/sec-in². In Test 4, intermediate ignition interval was noted for $\epsilon^* = 1.45$ and $(w/A)_{\max} = 0.356$ lb/sec-in². Test 3 conducted at the lowest ϵ^* (1.21) exhibited an ignition interval slightly greater than Test 7. Test 3 which

Motor Grain Instrumentation Probe Location Schematic



Tripwire Deactivation times - milliseconds

Test No.	ϵ^*	$\left(\frac{w}{A}\right)$	T ₉	T ₁₀	T ₁₂	T ₃	T ₁₄	T ₁₆	T ₁₇	T ₁₈	T ₇	T ₂₀
1	1.79	0.357	134	52	67	--	81	65	--	121	85	179
2	1.34	0.336	50	66	62	61	69	70	88	91	129	142
3	1.21	0.352	51	47	50	70	59	79	73	92	100	111
4	1.45	0.356	53	59	66	63	75	70	105	121	151	141
5	1.28	0.263	60	62	59	80	41	79	84	--	119	160
6	1.33	0.261	65	65	81	81	89	110	143	144	175	203
7	1.65	0.56	36	44	42	45	46	68	66	56	61	66
8	1.54	0.572	37	41	52	51	57	52	45	65	64	79
9	1.45	0.202	75	75	98	132	150	193	193	218	263	289

Table III-6. Reduced Tripwire Data

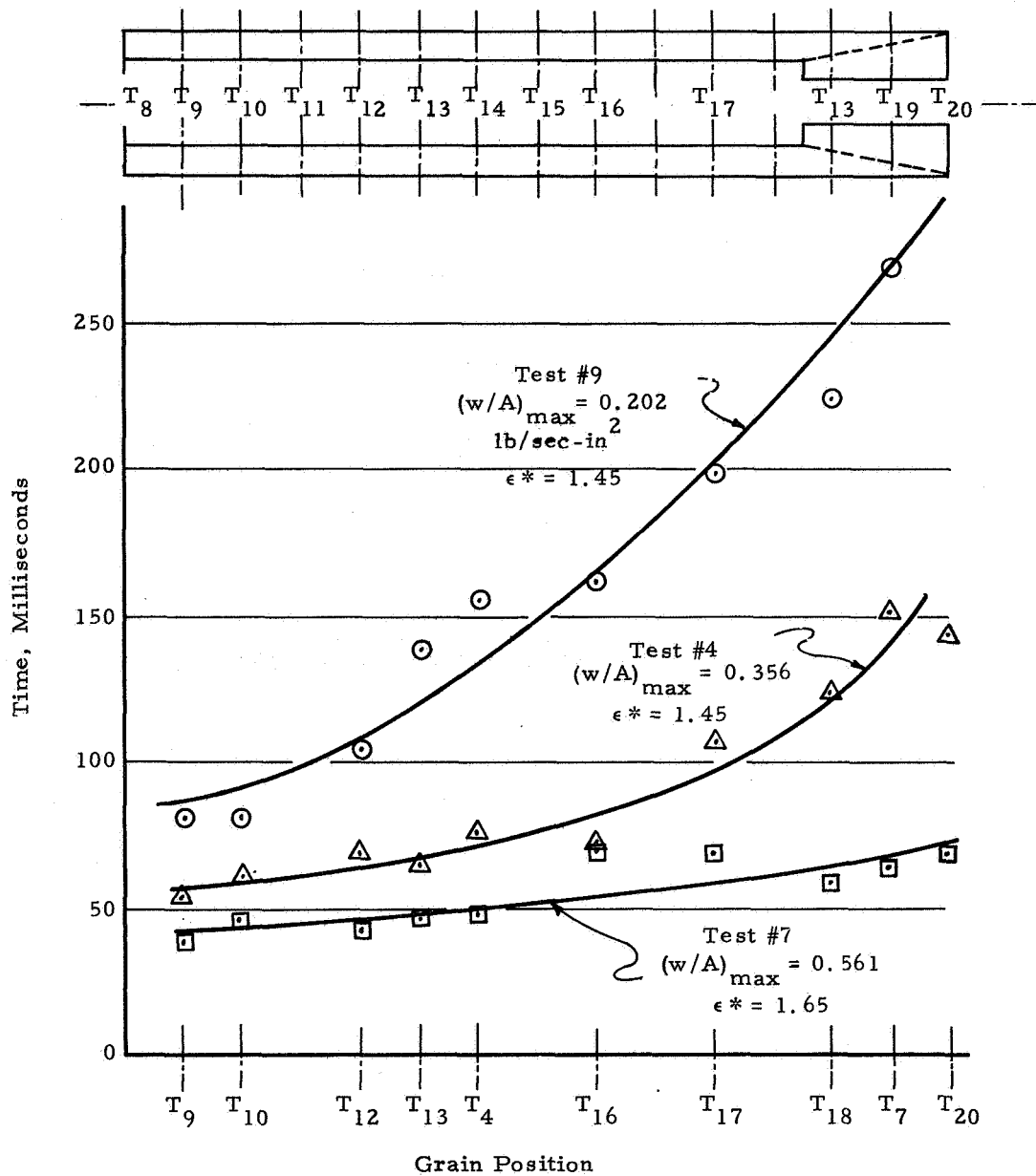


Figure III-50. Typical Plotted Tripwire Data

was run at the highest ϵ^* (1.79) had an ignition interval greater than Test 4, but less than Test 9.

In Tests 1 through 6 and Test 9, complete ignition of the surface was observed to occur as the motor chamber reached steady state operating conditions. This would indicate that for these tests that flame propagation was the rate controlling mechanism during ignition. In Tests 7 and 8, which were conducted at significantly higher igniter mass flow rates, complete surface ignition was observed to occur prior to attainment of steady state pressures. In these tests the chamber filling rate appeared to be limiting.

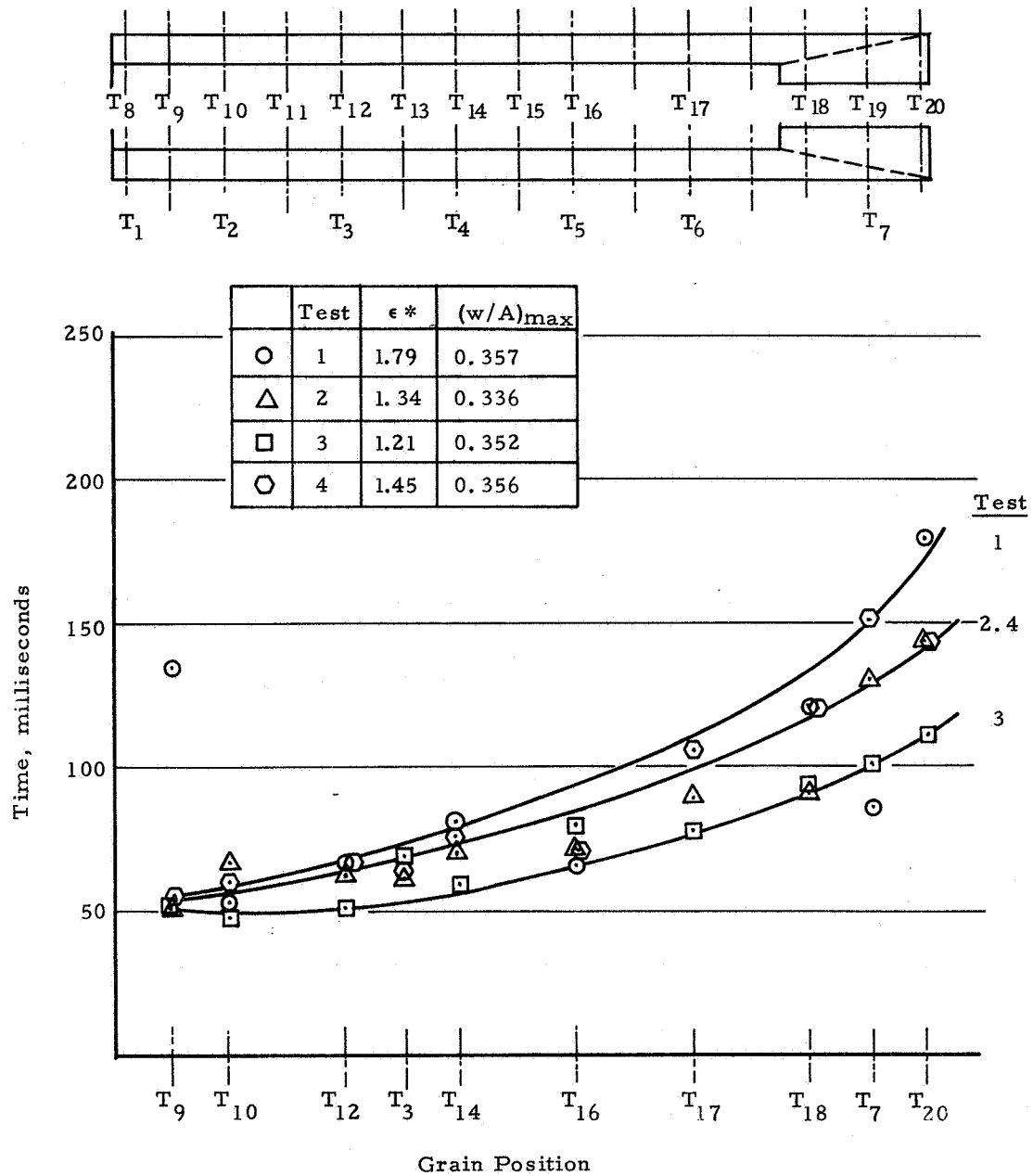
First ignition was observed to occur at essentially the same time for tests which were run with comparable maximum igniter mass flux parameters. However, the rate of flame propagation up the motor port increased with decreasing ϵ^* value. First ignition varied from 36 ms corresponding to a $(w/A)_{\max} = 0.56 \text{ lb/sec-in}^2$ to 75 ms at a $(w/A)_{\max} = 0.202 \text{ lb/sec-in}^2$. Times for completion of flame propagation ranged 68 ms to 289 ms.

Figure III-51 presents tripwire ignition data from Tests 1 through 4 which were conducted at maximum igniter flow parameters from 0.336 to 0.357 lb/sec-in^2 . The differences in flame propagation up the motor port was attributed to be primarily the result of higher instantaneous chamber pressurization rates caused by the effects of igniter ϵ^* location.

Several methods of correlating the tripwire data were investigated to determine the effects of ϵ^* and w/A upon an average rate of flame propagation rate (v_a). For this purpose v_a was defined by the formula:

$$v_a = \frac{V_T/A_p - V_t/A_p}{t_f - t_i}$$

Average flame propagation rates for the nine tests were plotted on log-log paper against several characteristic igniter mass flow parameters. These characteristic parameters included the maximum igniter mass flow parameter as well as the time average igniter mass flow parameter to (1) first ignition, (2) cessation of igniter jet penetration and (3) complete ignition. The maximum igniter mass flow parameter provided the least scatter for the correlation method used. The average motor flame propagation rate plotted in figure III-52 against the maximum igniter mass flow parameter indicates the relative dependency upon maximum

Figure III-51. Effect of ϵ^* on Flame Propagation

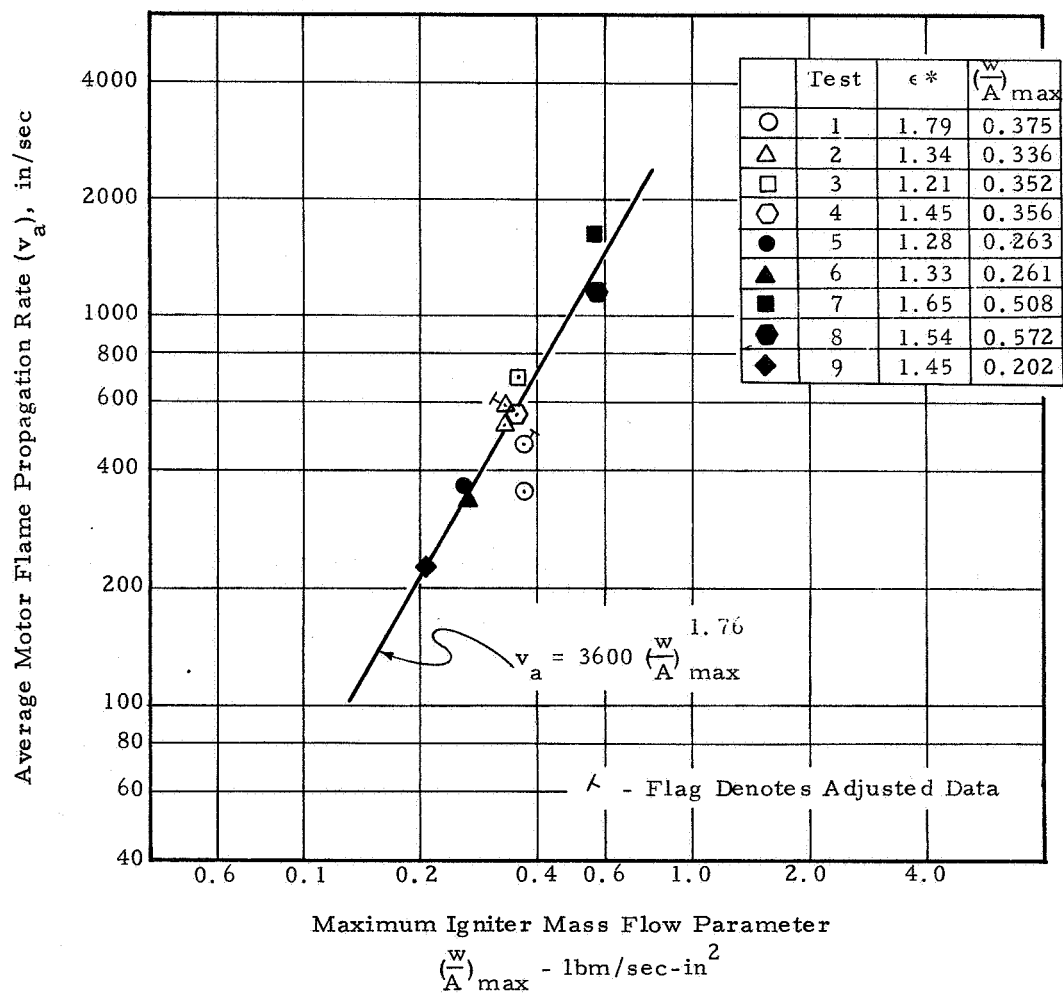


Figure III-52. Flame Propagation Dependency Upon Maximum Igniter Mass Flow Parameter

igniter mass flow. In figure III-53, the total correlational dependency upon ϵ^* and $(w/A)_{\max}$ was found to be:

$$v_a = 5570 \frac{(w/A)^{1.76}}{(\epsilon^*)^{1.35}}$$

It should be noted that this correlation can be applied only to aft-end igniters with the same relative igniter to motor design parameters used in this test series.

It has been reported^(7,9) that igniter jet penetration and subsequent heat transfer coefficient were substantially reduced at w/A values greater than 0.30 to 0.47 lbm/sec-in². No such limitation was noted in the current program even though maximum igniter mass flow parameters of 0.57 lbm/sec-in² were produced. This is believed due to use of igniter designs which provide greater jet penetrating potentials. The penetration-limited tests^(7,9) were conducted for lower igniter total pressures with the jet expanded to atmospheric conditions. In the current program much higher igniter chamber pressures were used and the nozzle was designed for optimum expansion from 1375 psia to 20 psia. Considering the much higher igniter chamber pressures and expansion ratios and large igniter nozzle half angle, it is probable that (1) the jet exhausts were characterized by higher velocity and mass flow rate per unit area, and (2) the jets retained their cohesive nature and reduced susceptibility to viscous erosion over a wide range of back pressure by virtue of clean flow separation in the igniter nozzle.

Another possibility may be due to the fact that in the current experiments a large percentage of the preignition heating of the grain surface occurred before the igniter mass flow reached the penetration limiting regime. The previously reported regimes of penetration limited flow^(7,9) were based upon essentially steady state igniter flow data. In the current experiments, the igniter pressures were observed to be in a transient state over the large percentage of the time during which initial penetration, motor grain heat-up and first ignition occurred. In Test 7, during which the shortest ignition interval was observed, the igniter had not reached its peak pressure of 2750 psia prior to the advent of first ignition (see figure III-54). At first ignition, 37 ms, the instantaneous igniter chamber pressure and mass flow parameter were 2640 psia and 0.540 lbm/sec-in² respectively. However, the time averaged chamber pressure over the interval to first ignition was only 1500 psia corresponding to an average igniter mass

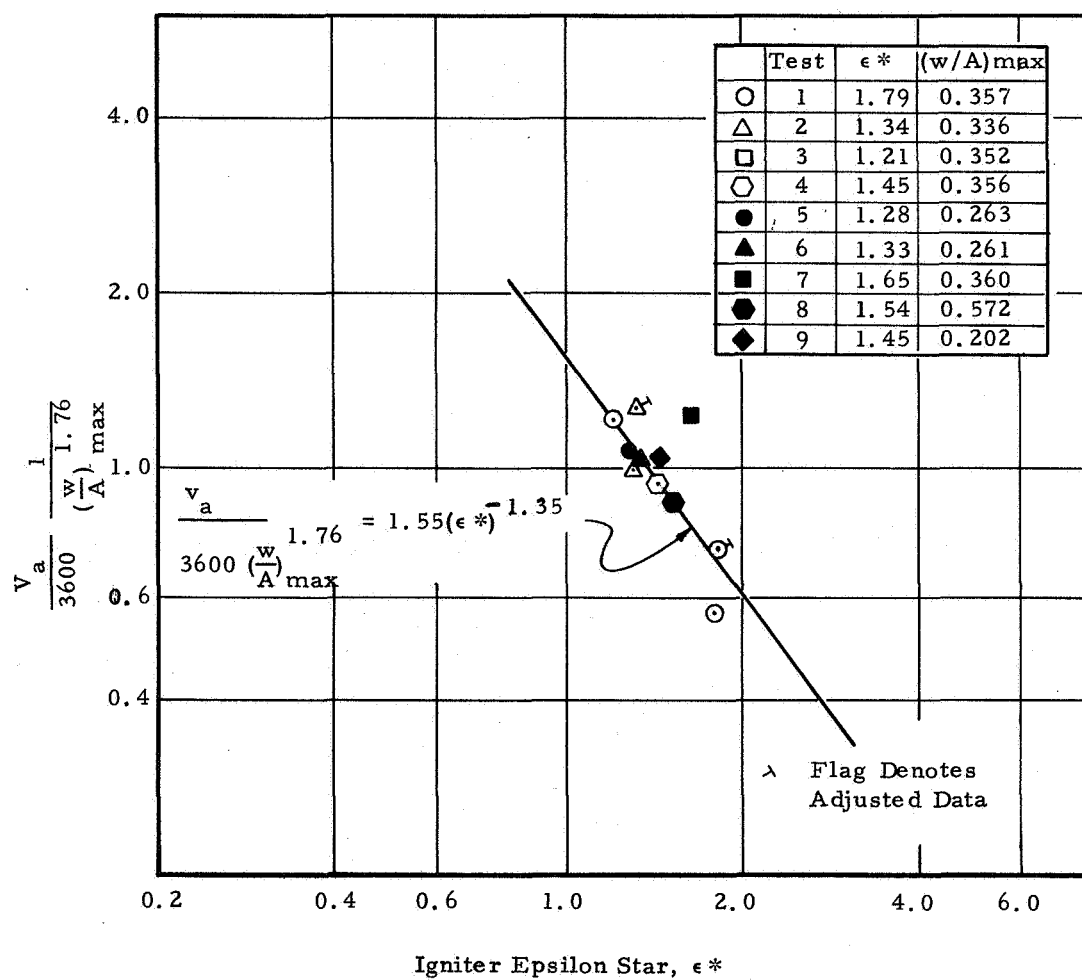
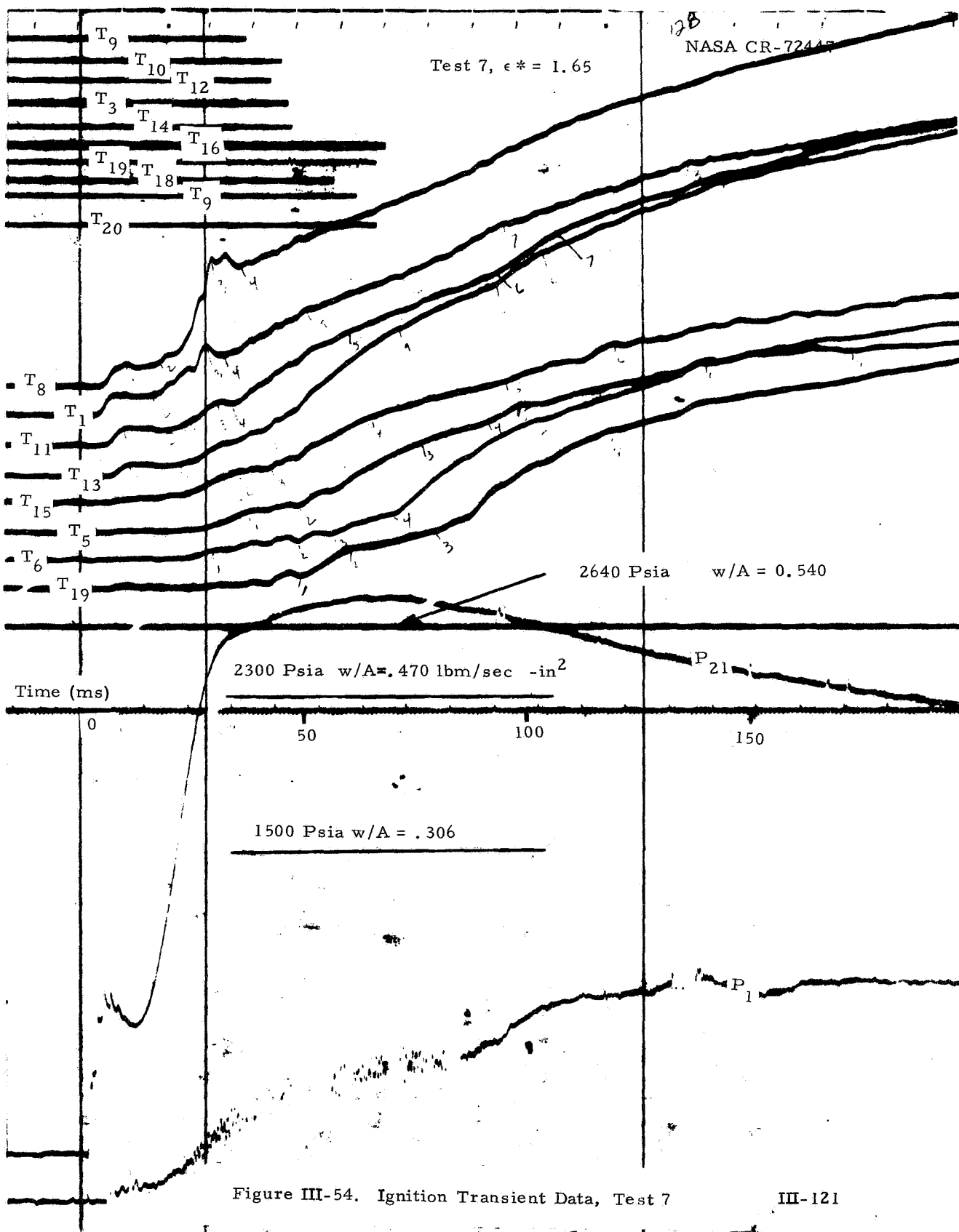


Figure III-53. Flame Propagation Rate Correlation



flow parameter of 0.306 lb/sec-in² (see figure III-55). Instantaneous igniter mass flow parameters of 0.306 and 0.470 lb/sec-in² were reached at approximately 19 and 24 ms respectively. Although igniter jet penetration to the forward most portions of the motor grain was probably greatly diminished by first ignition, a significant percentage of the effective pre-ignition heating occurred before the penetration limiting igniter mass flow regime was entered. Also, high igniter flows, which persisted after first ignition had stopped effective penetration, would enhance flame propagation because of higher chamber pressure induced by the large igniter mass flow.

Thermocouple instrumentation of the motor grain surface area was provided to obtain initial igniter heat transfer data and to augment ignition and flame propagation information recorded by the tripwire instrumentation.

The thermocouple data were observed to agree qualitatively with that anticipated until the time of surface ignition at which point the traces were expected to exhibit a sudden high rise rate. This did not occur, as shown in figures III-32, III-33 and III-54. Also, the measured temperatures at the time of ignition of the propellant do not correlate with expected theoretical propellant surface combustion temperatures for all locations on the grain surface. The expected surface ignition temperatures were recorded at the motor grain aft-end, but the ignition temperatures for grain locations toward the head-end were observed to be considerably less than the experimental values obtained from arc image furnace testing.⁽²⁰⁾ This is contrary to experimental results of Jensen⁽¹¹⁾, who reported that the ignition surface temperature was not dependent upon grain location and was in close agreement with propellant surface autoignition temperatures obtained from arc-image furnace data. Reduced thermocouple data for Tests 6 through 9 are presented in figure III-48 and figures III-56 through III-58, respectively. Also indicated are temperatures as determined from tripwire data at which ignition occurs. These data show that at axial locations upstream of the first several temperature sensors, the heat flux levels were initially relatively low as indicated by a gradual temperature rise rate. At some point in time, corresponding to a given axial location, the flux level rises considerably as the temperature curve slope increases. Ignition occurs shortly after this upward break. These upward breaks indicate a sudden increase in heat flux that travels forward along the grain just prior to first ignition.

The temperature at first ignition in all cases showed good correspondence with reported autoignition surface temperatures of from about 700 to 800°F.

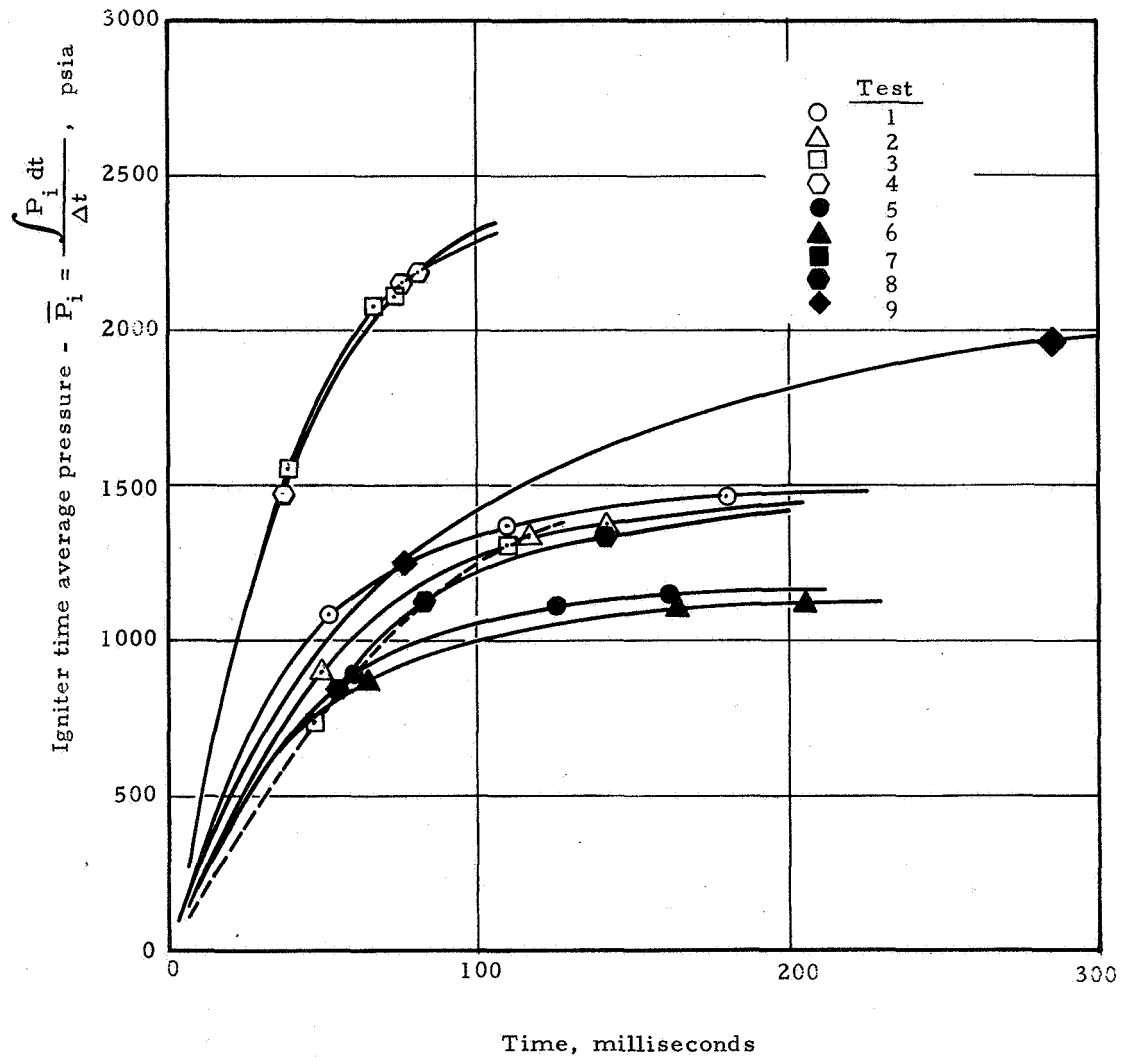


Figure III-55. Time Average Igniter Chamber Pressure

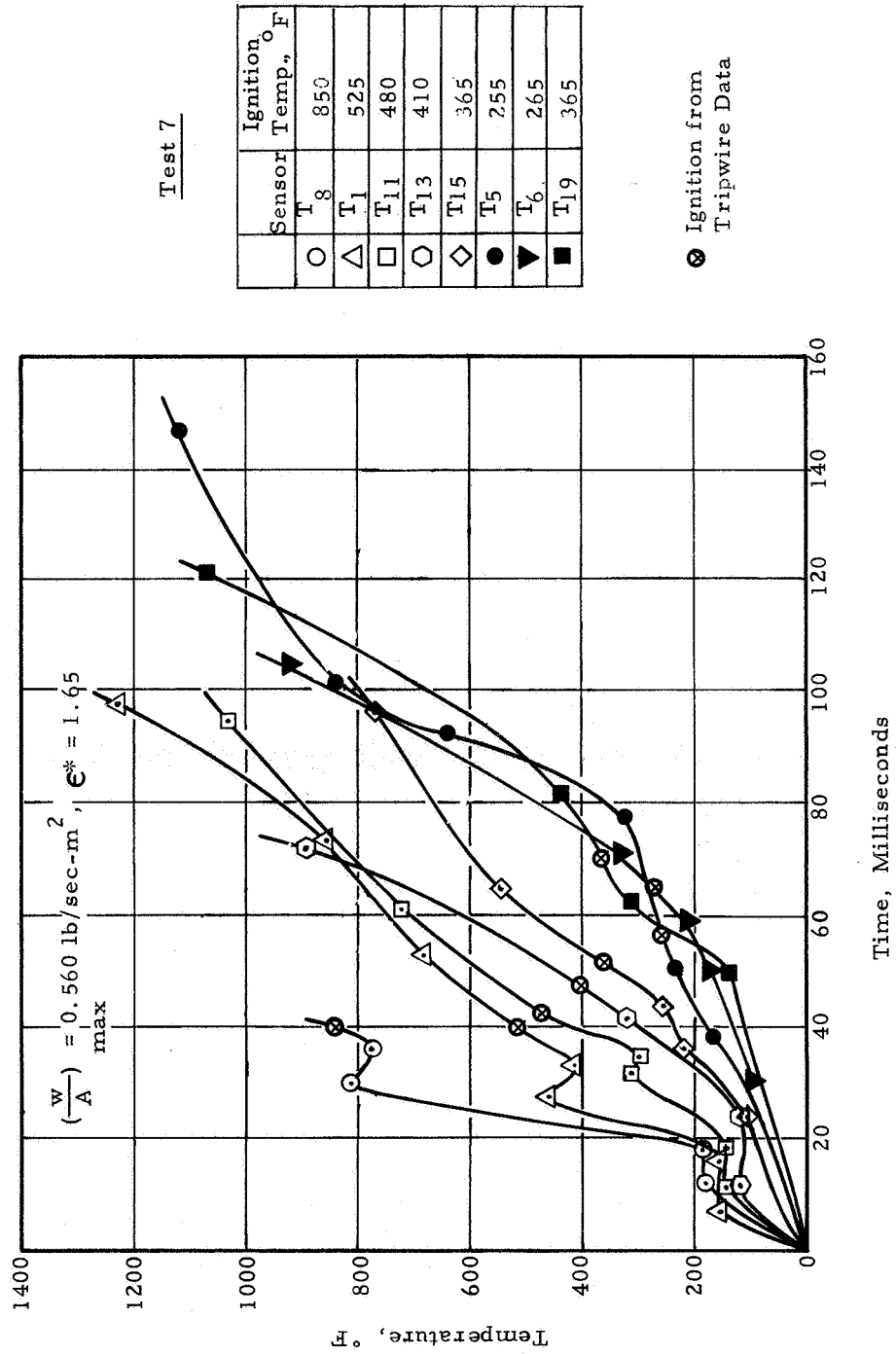
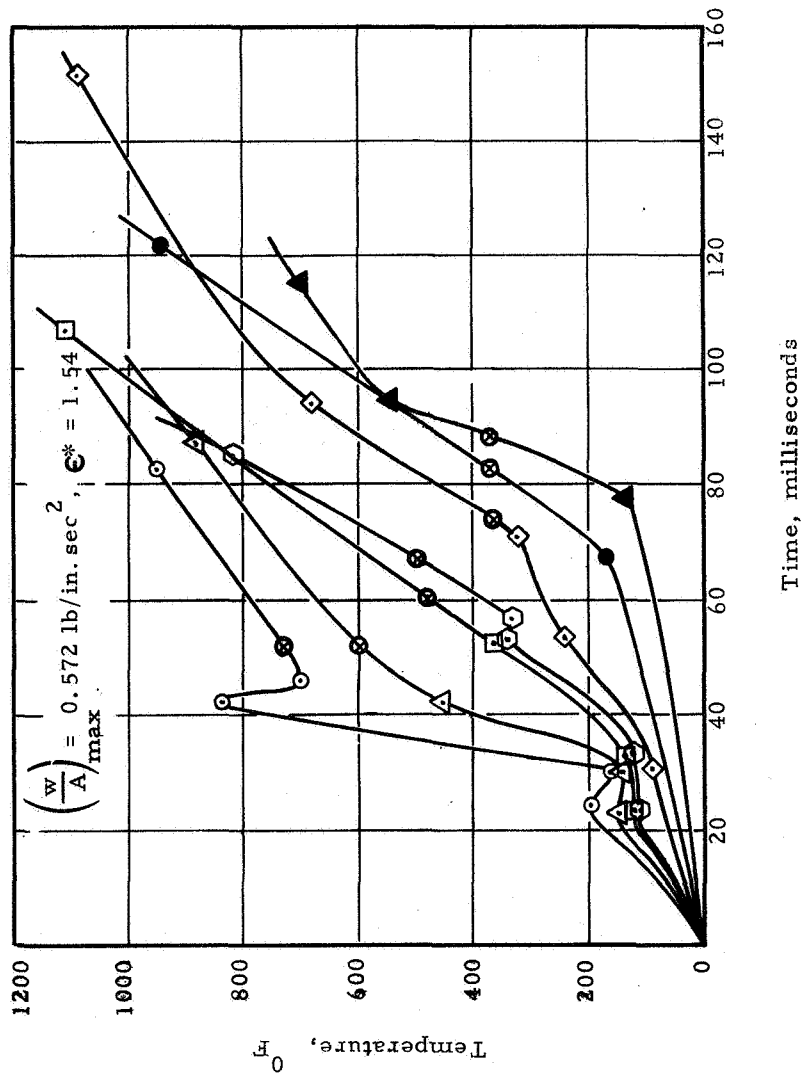


Figure III-56. Reduced Thermocouple Data, Test 7



Test 8

Sensor	Ign. Temp.
T ₈	735
T ₁	605
T ₁₃	470
T ₁₅	500
T ₅	365
T ₆	370
T ₁₉	370

Figure III-57. Reduced Thermocouple Data, Test 8

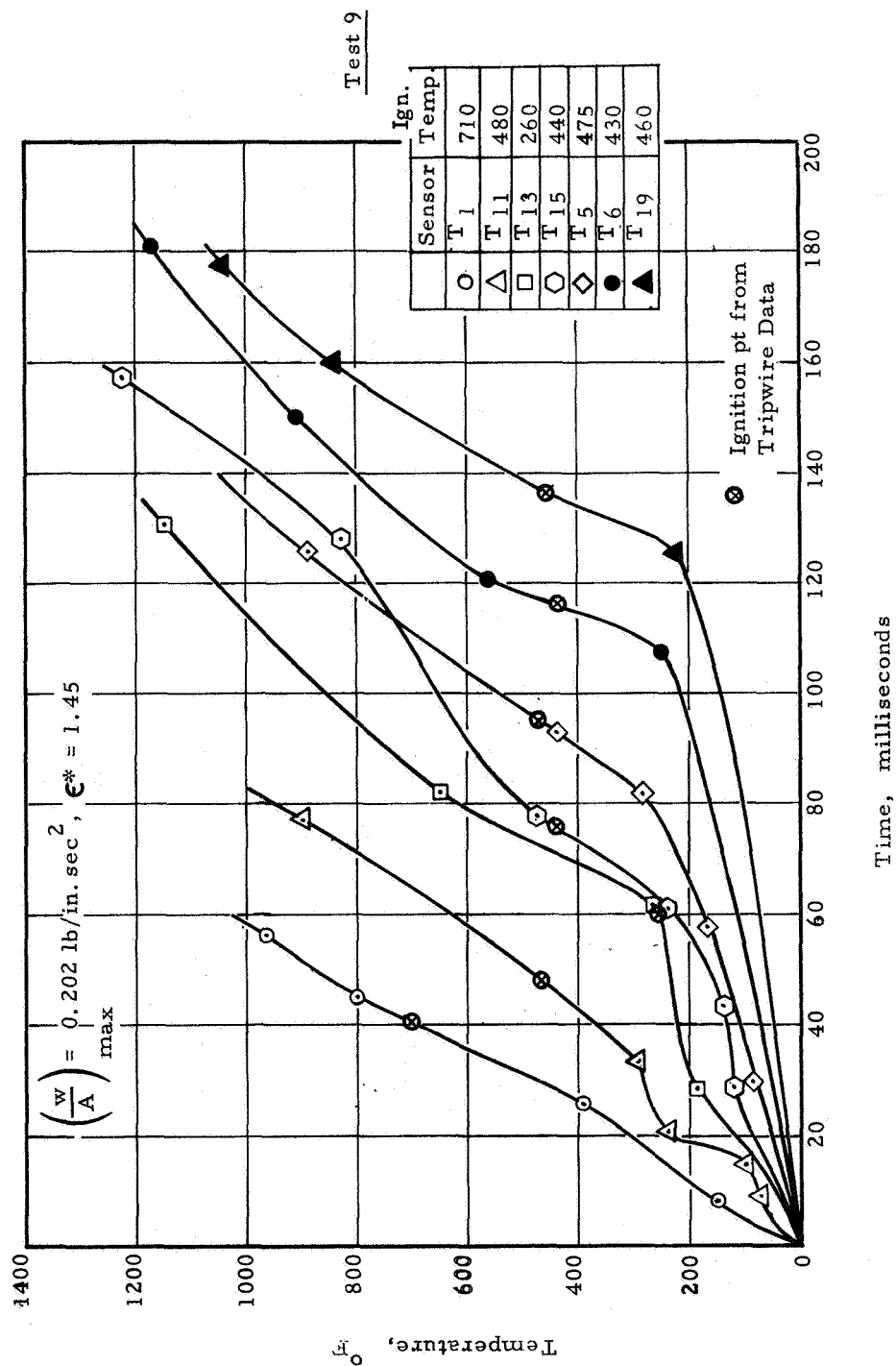


Figure III-58. Reduced Thermocouple Data, Test 9

In general, however, the temperature data taken at the time of ignition displayed a decrease in surface temperature at progressively larger distances from the grain aft-end.

The reason for low ignition temperature may have been caused by a limitation in the thermocouple response rates. Data from Test 9, figure III-58, show the usual trend in ignition temperature. For T_1 , the ignition temperature was around 710°F and limiting rise rate was on the order of 15° per millisecond. If the initial heat flux at the grain aft-end fell somewhat below the response limitation, then the ignition temperature indicated at T_1 should agree closely with the actual grain temperature. For sensors up the port different conditions hold. It is postulated that at locations up the port the grain was subjected to low rates of heating which the thermocouples could follow. As the ignition front approached the sensor location, the heat flux input probably exceeded the temperature rise-rate limitation of the thermocouple. Hence, the actual temperature was not followed by the sensor and its recording at the tripwire break time was low in comparison to actual grain temperature and the temperature recorded by other downstream sensors. The data from the other tests seem to confirm these general observations.

However, it should be noted that thermocouples similar to those used on the test program are reported to have shown temperature responses which are considerably higher than that recorded during the current program. (21) It may be that the test data are correct and some phenomenological ignition mechanism which is not clearly understood is causing the apparent discrepancy between the data and experimental observations reported by others. Further experimental work to investigate the response characteristics of the thermocouples under similar environmental condition is needed to resolve this problem.

Figures III-59 and III-47 show typical thermocouple temperature versus a motor grain axial location with time as parameter for Tests 8 and 9, respectively. The decreasing temperature gradient in the direction of the motor head-end is consistent with the lower heating rates at the head-end.

Test 8

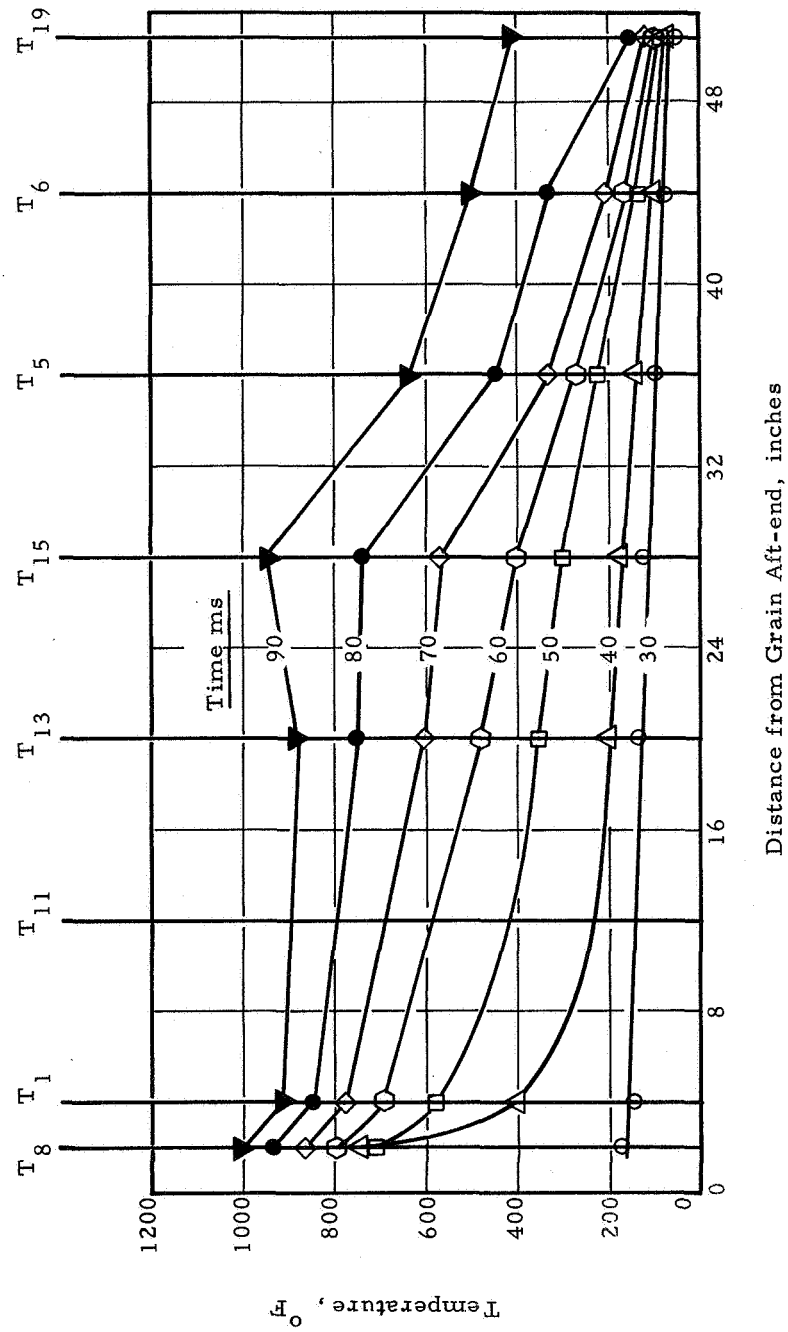


Figure III-59. Thermocouple Temperature Versus Axial Location, Test 8

2. Nozzle Flow Interactions

The major emphasis of the test data evaluation was placed on analysis of the nozzle flow interactions which resulted in severe main motor nozzle pressure oscillations or main motor flow blockage. A pattern of the interacting behavior emerged which best characterized the modes of interactions and the conditions under which they were most likely to occur. These flow interaction modes are described in terms of their observed nozzle pressure characteristics and the conditions for their existence. They encompass the entire range of phenomena from complete igniter jet penetration of the motor throat to momentary nozzle pressure disturbances, which were reflected as oscillations in the main motor chamber, but which did not result in sufficient motor flow blockage to cause average chamber pressure increases. While these modes correspond closely to the previously presented theoretical concepts, modifications and additions to account for the severe nozzle pressure disturbances observed in these experiments have been incorporated.

Evaluation of igniter and motor nozzle and motor chamber pressure distributions indicated that the igniter and motor flow interactions were directly related to several characteristic igniter nozzle flow separation patterns. The motor nozzle flow fields were observed to be either stable or unstable in character, for higher or lower ignition nozzle pressure ratios, (igniter chamber to effective back pressure), respectively.

Arens⁽²⁰⁾, Fraser⁽¹⁹⁾ and Summerfield⁽²¹⁾ report that overexpanded conical nozzle flows may be divided into distinct regimes which are, in order of decreasing igniter chamber to nozzle exit back pressure ratio:

- (1) Stable flow with oblique-shock-boundary layer interaction within the nozzle, but in the immediate proximity of the nozzle exit plane, or undisturbed flow in the nozzle with oblique shocks initiating in the nozzle exit plane.
- (2) Stable flow with symmetric oblique shock boundary layer separation forward of the exit plane.
- (3) Unstable oblique shock-boundary layer separation. The shock pattern is asymmetric and unsteady.
- (4) A normal shock at a low nozzle expansion ratio followed by subsonic flow. This condition occurs

for pressure ratios slightly above those required to choke the nozzle. It is postulated that the normal shock may be stable or unstable depending upon the stability of the back pressure.

Four modes of motor nozzle flow field interactions have been observed in this program and are believed to correspond to these four classical nozzle flow regimes. The interpretations are logically consistent with the limited experimental observations of the nozzle pressure distributions. However, confirmation of these observations and their interpretations require further experiments which will visually display the interacting motor and igniter flow fields.

The primary variables which establish the mode of flow interaction are igniter and motor chamber pressures and the igniter ϵ^* . For given igniter and motor chamber pressures, the ϵ^* location determines the effective igniter back pressure, the igniter nozzle pressure ratio and hence the igniter nozzle flow regime. The related main motor nozzle flow interactions are in turn determined by the igniter shock and/or separation patterns and the total pressure adjustment which must occur in the two mixing flows. The stable or unstable character of the nozzle flow interactions appear to reflect the stability or instability of the igniter nozzle. The ϵ^* location is also an important factor in determining whether main motor blockage will occur. Specifically, there is a minimum turn-around distance which is determined by the igniter jet penetration and dissipation length. Hence, main motor throat blockage may occur during any of the characteristic modes of nozzle flow interaction. However, it is noted that blockage at motor steady state operating conditions was not observed to occur in all modes in this test series.

The four modes of nozzle flow interaction are summarized in order of decreasing igniter nozzle pressure ratio in table III-7. The first mode was observed only during the initial portion of the motor pressure transient, and was characterized by penetration of the entire igniter jet through the main motor throat plane and into the port cavity. This mode corresponded to the greatest degree of throat blockage. It was noted only at high igniter to motor total pressure ratios prior to first ignition of the main motor propellant, after which, the motor chamber pressure and mass flow increased, preventing complete penetration of the igniter, and forcing operation of the igniter nozzle in the second nozzle flow regime. Main motor and igniter nozzle pressures in the first mode were stable.

Table III-7

Characteristic Nozzle Flow Operating Modes

<u>Operating Mode</u>	<u>Nozzle Flow Characteristics</u>	<u>Approx. Igniter Nozzle Pressure Ratio Range</u>	<u>Postulated Igniter Nozzle Flow Regime</u>
I	Stable	Near design pressure ratio	Full flow or oblique shock separation near exit
II	Stable	> 10	Stable oblique shock separation
III	Unstable-highly oscillatory	10-4	Unstable, asymmetric oblique shock separation
IV	From unstable-highly oscillatory to stable essentially one-dimensional flow	4-2	Unstable normal shock to stable normal shock

Unlike the first mode of operation, the second was observed to occur during motor steady state operation. Tests 1, 7, and 8, which were run at high ϵ^* values and high igniter to motor chamber pressures, were characterized by unblocked, stable main motor nozzle flow during a portion of steady state operation. During these three runs, as the igniter nozzle pressure ratio gradually decreased, the flow interactions began to transition into the third, unstable mode of operation. The transition period was characterized by short periods of stable flow interspaced with periodic nozzle pressure disturbances of considerable magnitude. As the igniter nozzle pressure ratio decreased the percentage of time in the unstable mode increased until the motor nozzle pressure disturbances were nearly continuous. During this period it appears that the igniter nozzle transitioned into an unstable oblique shock separation regime. Stable flow interactions in the second mode were observed only in an unblocked condition. However, it is postulated that second mode, stable blocked conditions could exist at lower ϵ^* values if the igniter design condition were such that the igniter nozzle could operate in a stable nozzle flow regime.

The third and fourth modes of operation, characterized by unstable main motor pressures, were observed to exist to some degree in all tests, the only distinction between the third and fourth modes was the apparent frequency of nozzle pressure disturbances and the postulated operation of the igniter in either the third or fourth igniter nozzle flow separation regimes. Nozzle flow characteristics in the third mode were as described in the previous paragraph for Tests 7 and 8. The fourth mode was observed, in Tests 2 through 6 and Test 9, which were conducted at relatively low ϵ^* values. In these tests the main motor nozzle pressure oscillations were recorded throughout motor steady state operation until igniter tail-off. The equilibrium condition in the fourth mode for these tests was one in which the igniter jet partially penetrated the motor throat plane or caused a minimum area for the main motor flow downstream of the actual motor throat, resulting in an increase in average motor operating pressure level. Although third mode operation was predominately characterized by blocked unstable nozzle flow conditions, it was also observed to occur without motor throat blockage in Test 1. To both the third and fourth mode, the extreme nozzle pressure oscillations which were propagated into the motor throat and chamber were unexpected. These oscillations resulted from the unstable character of the interacting igniter and motor flows and were apparently caused by pulsation of the igniter jet between two quasi-stable positions or between two igniter nozzle flow regimes.

In the following sections some of the effects of the flow interaction upon different motor operating characteristics will be discussed in a more detailed and specific manner. Subjects discussed will include:

- (1) flow field characteristics,
- (2) motor nozzle blockage prediction,
- (3) motor chamber overpressurization,
- (4) motor thrust modifications,
- (5) nozzle pressure oscillations and pressure distribution,
- (6) igniter flow shape and main stream bow shock, and
- (7) side forces due to asymmetric nozzle flow.

a. Flow Field Characteristics

The second, third and fourth modes of operation are of primary interest, since the first mode was observed to occur only during the early phases of the ignition transient before main motor operating conditions were achieved. The second mode occurred on all tests prior to the attainment of motor steady state operating conditions and during the early steady-state portions of Tests 1, 7 and 8 when stable, unblocked motor flow conditions were observed. Comparison of the tests which best illustrate the third and fourth modes of operation indicated that the modes were similar except for one significant difference. The difference was an apparent change in the operating regime of the over-expanded igniter nozzle, as determined by the igniter chamber pressure and ϵ^* location. In Tests 2 through 6, which typified the fourth blocked mode, igniter chamber to back pressures were in the neighborhood of 5:1 or 6:1 when operating conditions were reached in the main motor. In Tests 1, 7 and 8, which displayed intermittent nozzle pressure instabilities characteristic of operation in both the third and fourth modes, the igniter chamber to back pressure ratio was approximately 10:1 when igniter nozzle pressure oscillations first occurred. At higher igniter nozzle pressure ratios no severe main motor pressure disturbances were observed and it is believed that above this nozzle pressure ratio the igniter operated in the stable second nozzle flow regime without major flow disturbances.

In Test 9, the motor and igniter nozzle pressure exhibited oscillations similar to those observed in both the third and fourth mode. The igniter nozzle pressure ratio was in the range of 8 to 10 when full motor chamber pressure was reached. In Test 9, the igniter chamber pressure was more neutral than on the others and varied only from 2250 psia to 1900 psia just prior to igniter tail-off. At that time, the maximum back pressure, estimated from the motor nozzle pressures, was about 230 psia, giving a nozzle pressure ratio of approximately 8:1. These data

appear to indicate that nozzle flow in test 9 operated in the transition region between the third and fourth modes.

It was not clear from the data whether the operation of the igniter in an unstable nozzle flow regime, or the inherently unstable mixing processes of the igniter and main motor flows, triggered the disturbances noted in the igniter exit cone. However, it appeared that when the igniter was operating in an unstable nozzle flow regime, both the igniter nozzle flow and mixing processes were mutually exciting.

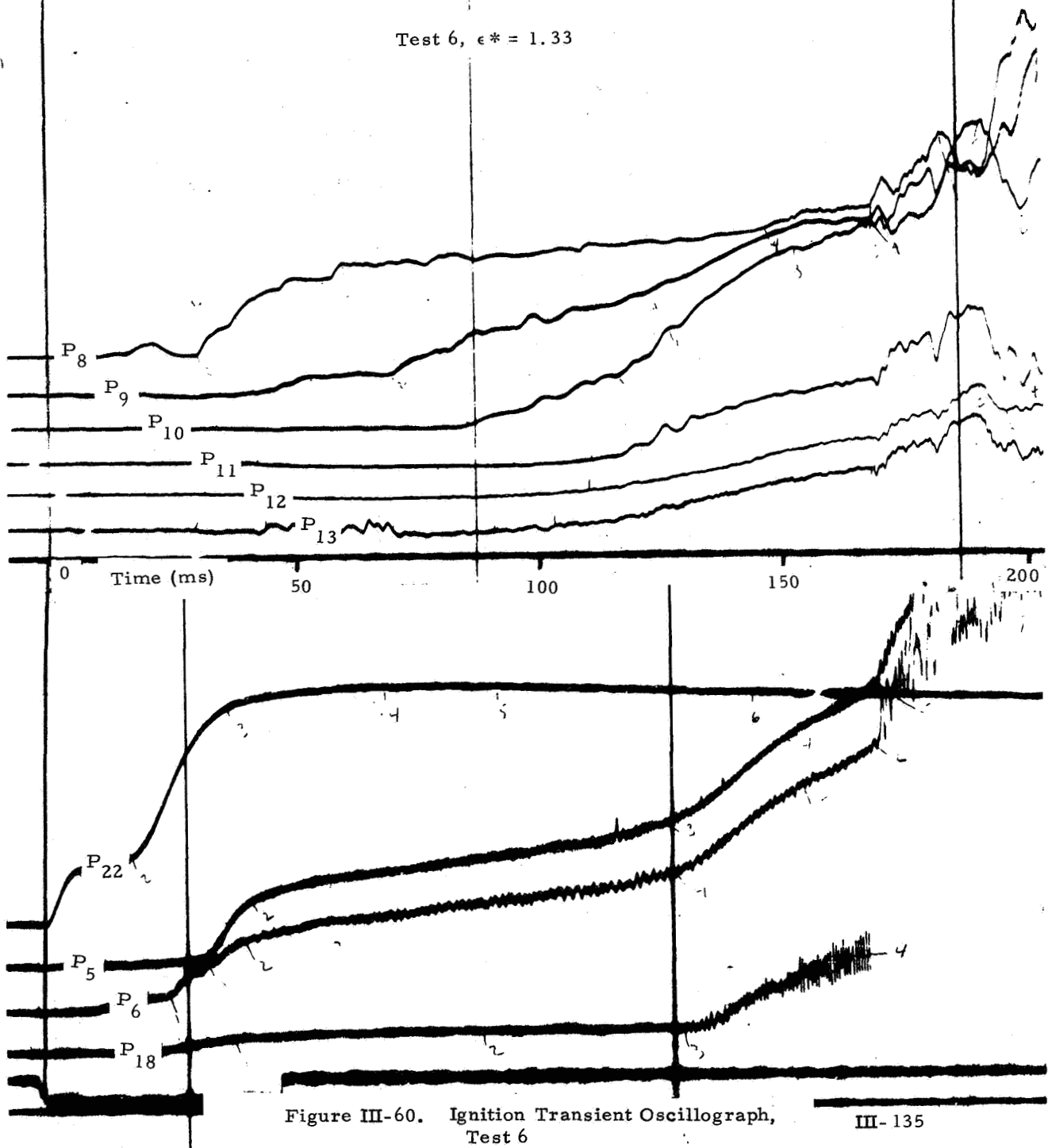
To maintain stable main motor flow without major nozzle pressure disturbance, the igniter should be designed to have a high chamber pressure and should be placed at an ϵ^* location which will assure that the effective back pressure will permit the igniter to operate in a stable nozzle flow regime. This requirement appears to be compatible with design criteria necessary to produce a satisfactory ignition.

In the following paragraphs, data are presented which illustrate the nozzle flow field interactions during the three characteristic modes of operation.

First Mode

Igniter and motor nozzle pressure data recorded during the ignition transient of Test 6 are presented in figure III-60. In figure III-61, these measured wall pressures were plotted vs the distance from the throat for selected times. Data for 6, 9, 10 and 30 ms indicate propagation and reflection of both compression and expansion waves which accompanied the starting process. At 30 ms, the motor appeared to be choked slightly downstream of the throat and slightly overexpanded in the nozzle. The low pressures at tap P5, 14 in. forward of the throat, are believed to be due to transducer or tap hangup and do not reflect actual conditions. At 100 ms the nozzle flow stabilized fairly well with the choked point still downstream from the throat. The nozzle was still overexpanded as indicated by the sub-atmospheric pressure. Between 130 and 170 ms, the igniter nozzle and motor nozzle pressures were observed to increase gradually, until at 170 ms the pressure data became characteristic of operation noted in the third or fourth unstable modes.

During the time interval between igniter ignition and 135 ms the effective igniter back pressure increased, as reflected by a gradual increase in igniter nozzle pressure measurement P_{18} (see figure III-60. During a major portion of that interval the operation was predominately the first or fully penetrating mode. At approximately 135 ms a sudden increase in P_{18} with associated pressure oscillations, was noted

Test 6, $\epsilon^* = 1.33$ Figure III-60. Ignition Transient Oscillograph,
Test 6

Test 6, $\epsilon^* = 1.33$

Wall Pressures

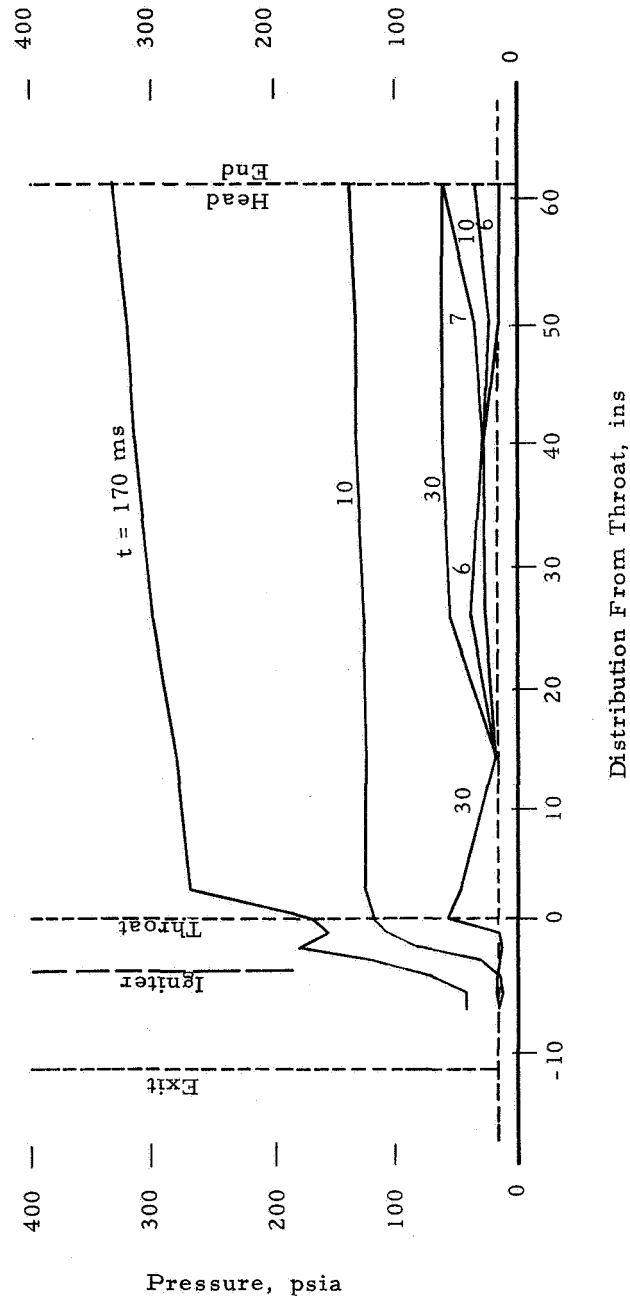


Figure III-61. Plotted Ignition Transient Pressure Data, Test 6

indicating nozzle flow separation at the pressure tap and operation in the second or stable oblique nozzle flow separation regime.

Second and Third Modes

In Tests 1, 7, and 8, the motor nozzle flow fell primarily into the second and third nozzle flow modes. After the motor initially unblocked the igniter nozzle operated in the second flow regime characterized by stable symmetric flow separation around the nozzle circumference as indicated by P_{18} . However, as the igniter chamber pressure decayed and motor chamber pressure increased, the igniter nozzle pressure ratio decreased and at some point entered the third nozzle flow regime in which the nozzle flow became unstable with asymmetric boundary-layer separation. The igniter jet appeared to pulsate periodically in a lateral or longitudinal manner, during which time the igniter nozzle pressure increased. These pulsating pressure increases were probably caused by (1) shifting of the igniter nozzle separation point to a lower expansion ratio or (2) oscillation of the igniter nozzle between the stable oblique shock separation regime and the unstable asymmetric oblique shock separation flow regime.

Test data from Test 7, showing typical igniter and motor nozzle pressure measurements, are shown in figures III-62 through III-64. Figure III-62 shows the ignition transient response of igniter nozzle pressure measurement P_{18} to igniter and motor pressure transients. For times prior to 100 ms, the igniter nozzle flow at P_{18} was probably unseparated since the recorded pressure agreed with one-dimensional isentropic flow relationships. At 63 ms, at an igniter chamber pressure of 2750 psia, a pressure of 86 psia was recorded at P_{18} compared to the theoretical value of 81 psia. Starting at 100 ms, separation began at the nozzle pressure tap location in response to the increased back pressure as illustrated by pressure rises at P_{10} and P_{11} . At approximately 128 ms, shortly before steady state motor chamber conditions were reached, a major pressure disturbance was noted on all the nozzle and chamber pressure measurements. This disturbance was caused by ejection of an object through the motor nozzle throat, as confirmed by test motion picture data. After the motor pressures stabilized, the motor operated in a stable unblocked mode without nozzle pressure disturbances until 530 ms. During that time interval the pressure at P_{18} gradually increased in response to increasing motor chamber pressure and decreasing igniter chamber pressure. At 530 ms a pressure pulse of less than 10 ms duration was observed in the igniter and motor nozzle pressures (see figure III-63). This pressure disturbance was not reflected in either the motor throat or chamber pressure measurements. At approximately 560 ms pressure disturbances were again noted in the

Test 7, $\epsilon^* = 1.65$

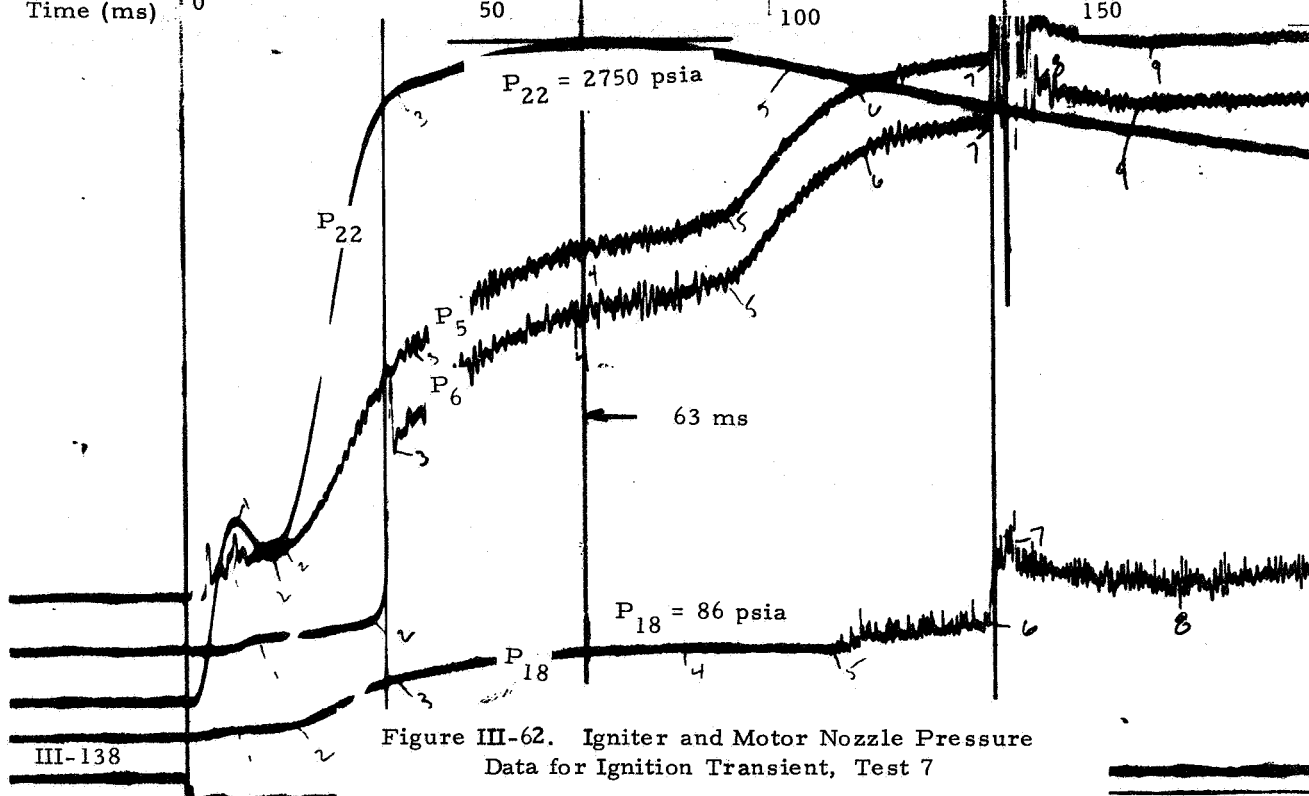
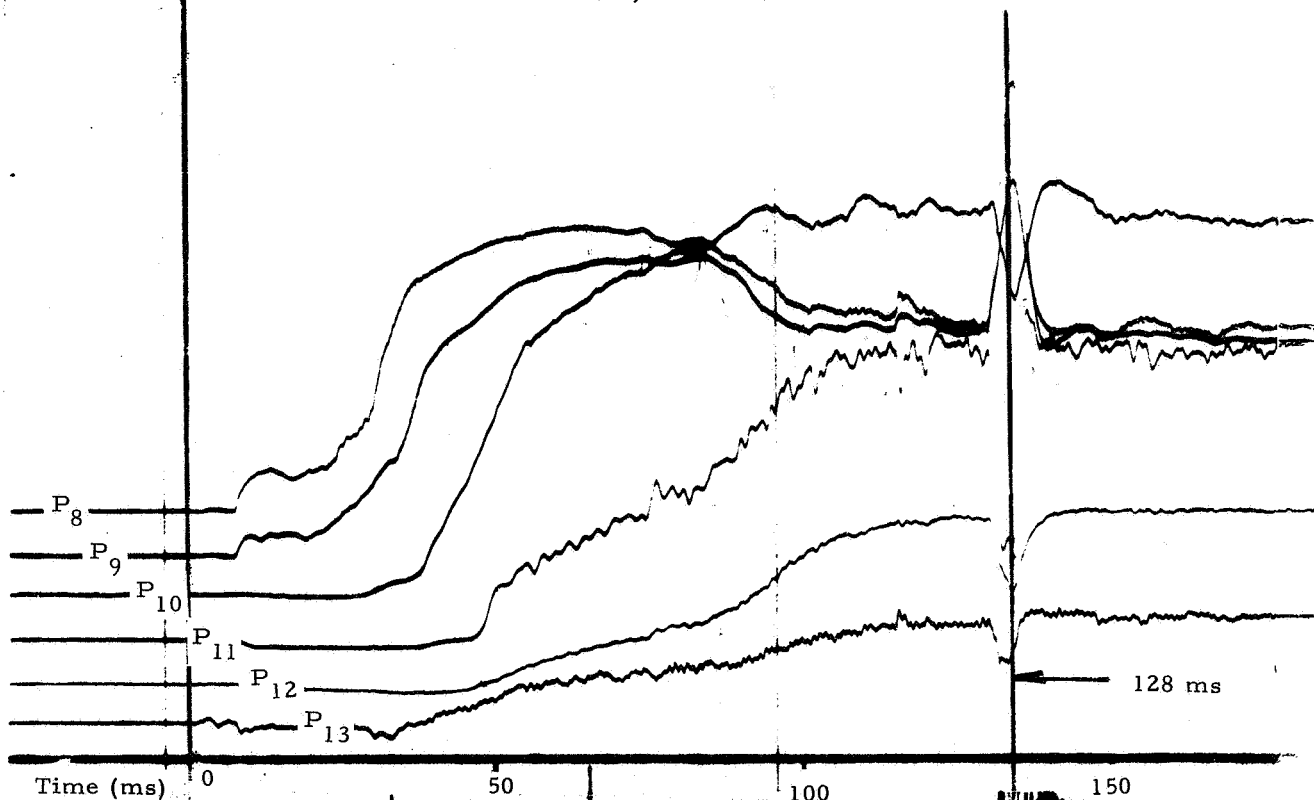


Figure III-62. Igniter and Motor Nozzle Pressure Data for Ignition Transient, Test 7

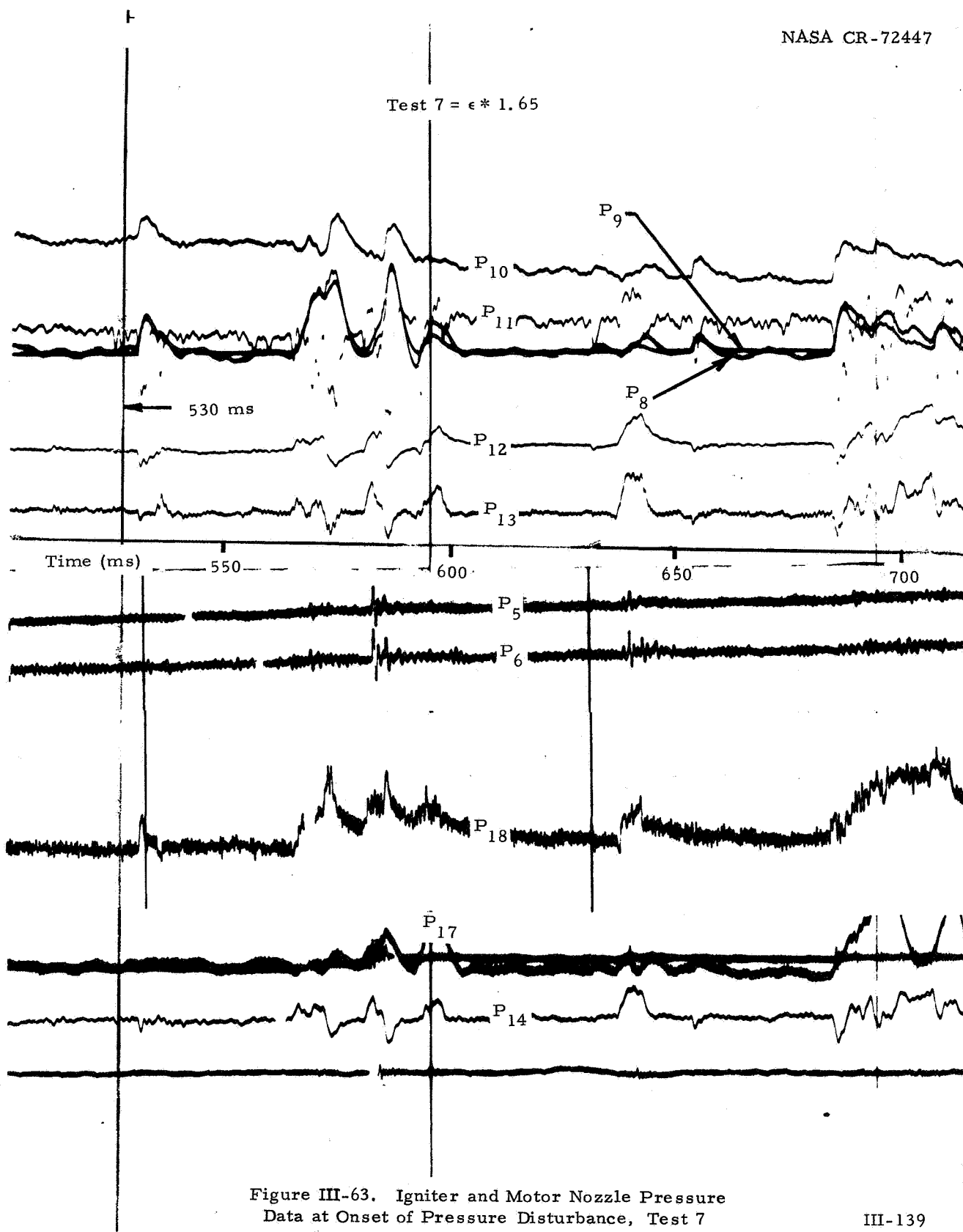


Figure III-63. Igniter and Motor Nozzle Pressure Data at Onset of Pressure Disturbance, Test 7

Test 7, $\epsilon^* = 1.65$

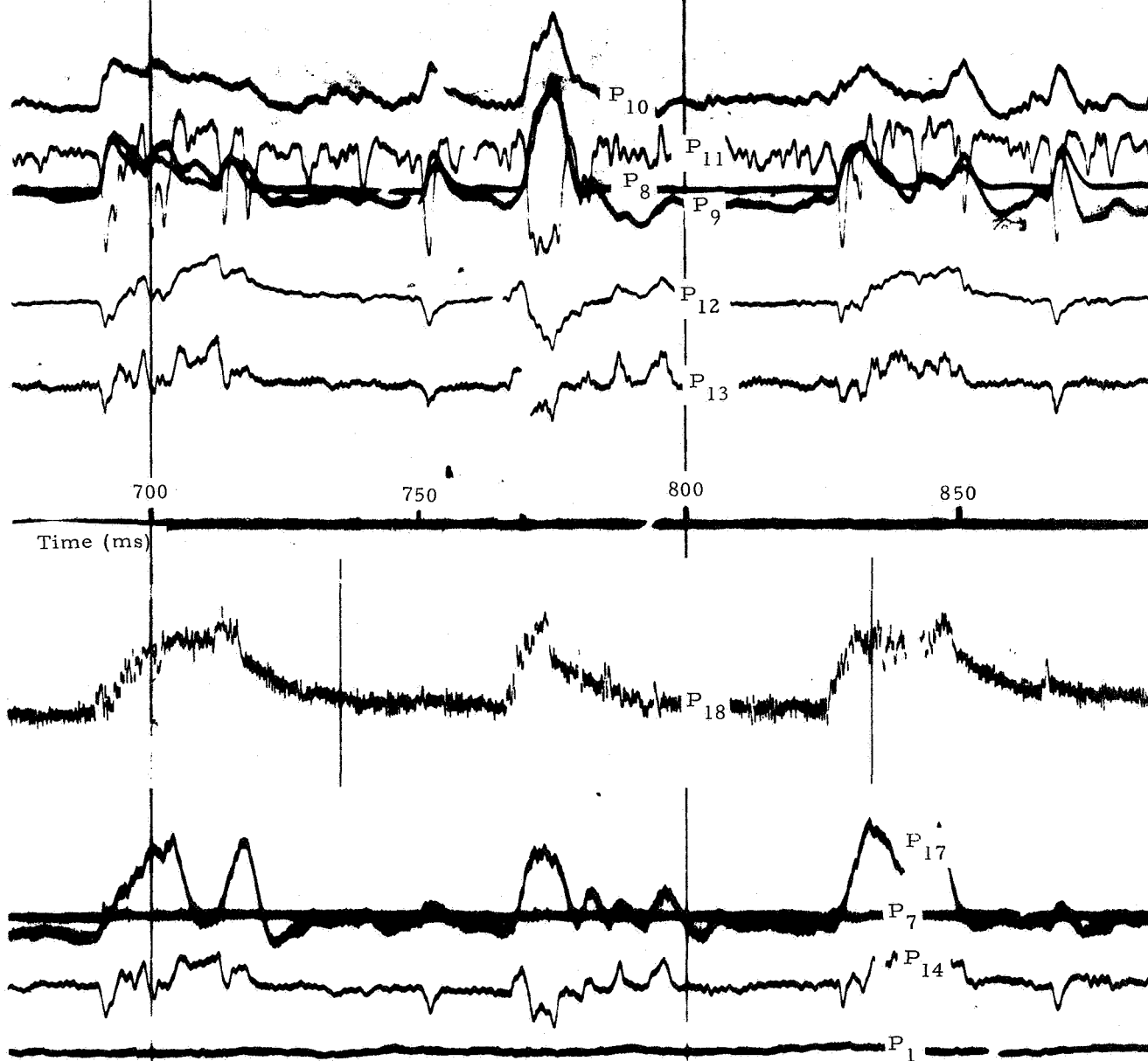


Figure III-64. Igniter and Motor Nozzle Pressure Data
During Maximum Disturbances, Test 7

igniter and nozzle pressure measurements. At that time they were also observed in the form of pressure oscillation in the chamber pressure measurements. The rate of occurrence of these nozzle pressure disturbances increased until igniter tail-off; however, the motor chamber pressure oscillations became increasingly less as the relative igniter to motor mass flows decreased.

Figure III-64 shows igniter and motor nozzle pressures during the period of the most severe pressure disturbances in Test 7. It is interesting to note the pressure similarities recorded at the igniter nozzle (P_{18}) and at motor nozzle pressure taps P_8 , P_9 , P_{10} and P_{11} . Unlike the fourth nozzle flow mode, the igniter nozzle pressure data recorded in the separated igniter nozzle flow region is of approximately the same magnitude as the igniter back pressure measured along the motor nozzle wall.⁺ Table III-8 presents pressure data recorded at 197 and 1000 ms. The first corresponded to a period of undisturbed steady state operation and the second to a period of quiescence between pressure disturbances. These data illustrate the fairly close agreement between the igniter nozzle pressure (P_{18}) and motor nozzle pressures.

Table III-8. Igniter and Motor Nozzle Pressure Data,
Test 7

<u>Test No. 7, $\epsilon^* = 1.65$</u>	<u>Pressures, psia</u>						
<u>Time ms</u>	<u>P_{18}</u>	<u>P_8</u>	<u>P_9</u>	<u>P_{10}</u>	<u>P_{11}</u>	<u>P_1</u>	<u>P_{21}</u>
197	157	158	184	216	176	510	2225
1000*	210	134	117	181	200	596	1717

In Test 8, similar coupling of the igniter and motor nozzle pressures were noted. Initial nozzle pressure disturbances produced some overpressurization in the chamber. However, these overpressurizations lasted only as long as the nozzle disturbances and by the time the igniter began to tail-off, effects on chamber pressure were noted as pressure oscillations only.

+ In Test 7, the igniter was positioned with its exit plane approximately 0.85 inches upstream of pressure tap P_{11} .

* quiescent period

Test 1 igniter and nozzle pressures reacted in a manner similar to Tests 7 and 8; however, motor throat flow blockage was not observed and the nozzle pressure oscillations were considerably less severe. Starting at approximately 200 ms, very small pressure disturbances were observed in the igniter and motor nozzle exit cone as shown in figure III-65. These disturbances continued at the rate of one or two every 100 ms until about 720 ms at which time they become more continuous, as shown in figure III-66. They continued at about this level until after the completion of igniter action.

Although the motor and igniter nozzle pressure disturbances indicated the typical coupling interactions noted in Tests 7 and 8, they were not nearly as severe and were not reflected in either the main motor throat or chamber pressure.

Fourth Mode

In Tests 2, 3, 4, 5 and 6, the fourth mode of operation was observed to occur. In these tests the motor operated in a mode which was both unstable and primarily blocked. The igniter nozzle pressure data (P_{18}) indicated that the igniter operated in the fourth nozzle flow regime characterized by a normal shock downstream of the throat followed by subsonic flow. Pressure tap P_{18} , which was located at an igniter exit cone area ratio of 5.28, should have indicated pressures in the range of 30 to 75 psia for unseparated supersonic nozzle flow. Pressures in the order of 300 to 500 psia were recorded indicating that a normal shock, followed by subsonic flow, was occurring at a lower expansion ratio upstream of the pressure tap. Figure III-67, which shows the ignition transient for Test 3, illustrates typical data for P_{18} observed during an unstable blocked mode of operation. Until approximately 85 ms, the recorded pressure corresponded reasonably well with that expected for one-dimensional isentropic unseparated nozzle flow. From 86 ms to 127 ms, a large pressure increase to approximately 503 psia was observed as the igniter nozzle flow reacted to the increased back pressure, resulting in establishment of a normal shock upstream of P_{18} .

During steady state operation the igniter and motor nozzle data indicated considerable interdependence. Figure III-68 presents a comparison of igniter and nozzle pressure data from Test 4, illustrating the igniter and motor nozzle flow pressure interactions. A definite correspondence was noted between the fluctuations in the igniter nozzle pressure (P_{18}) and motor nozzle pressures. For high pressures at P_{18} the main motor flow tended to be blocked, as indicated by the pressure oscillations at the motor throat (P_7). At 788 ms, which corresponds to a

Test 1, $\epsilon^* = 1.79$

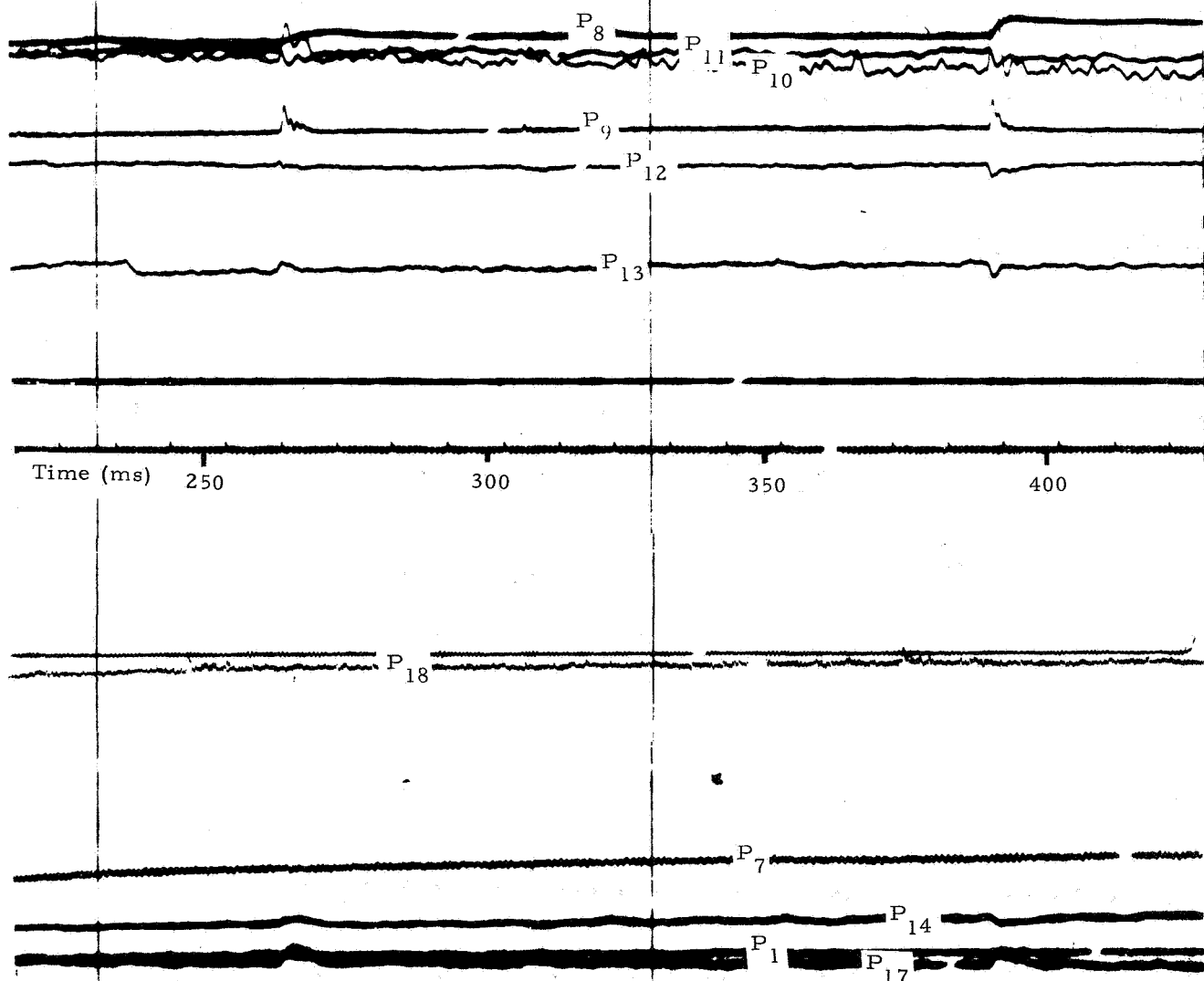


Figure III-65. Igniter and Motor Nozzle Pressure Data
at Onset of Pressure Disturbance, Test 1

Test 1, $\epsilon^* = 1.79$

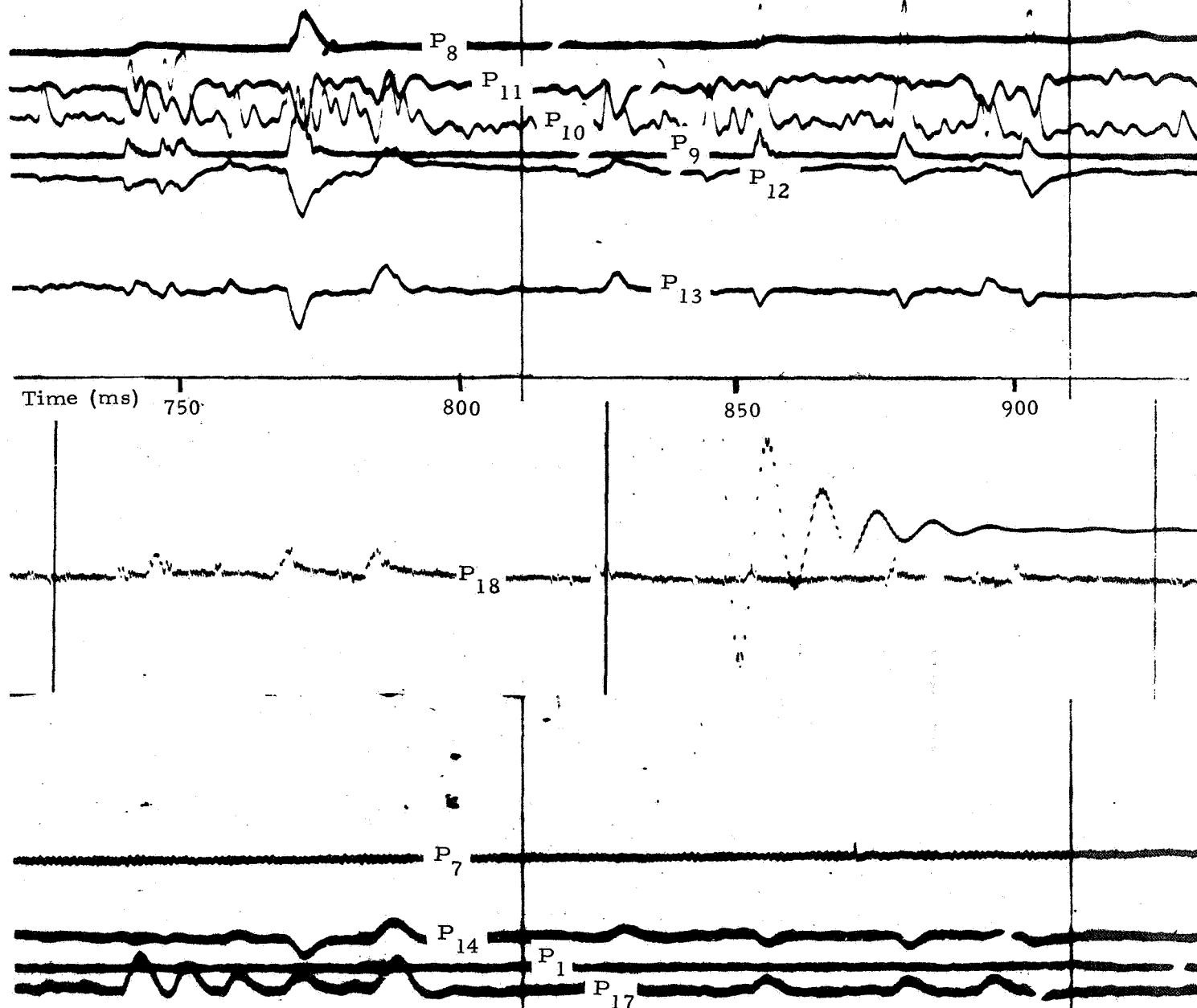


Figure III-66. Igniter and Motor Nozzle Pressure Data
During Maximum Pressure Disturbances, Test 1

Test 3, $\epsilon^* = 1.21$

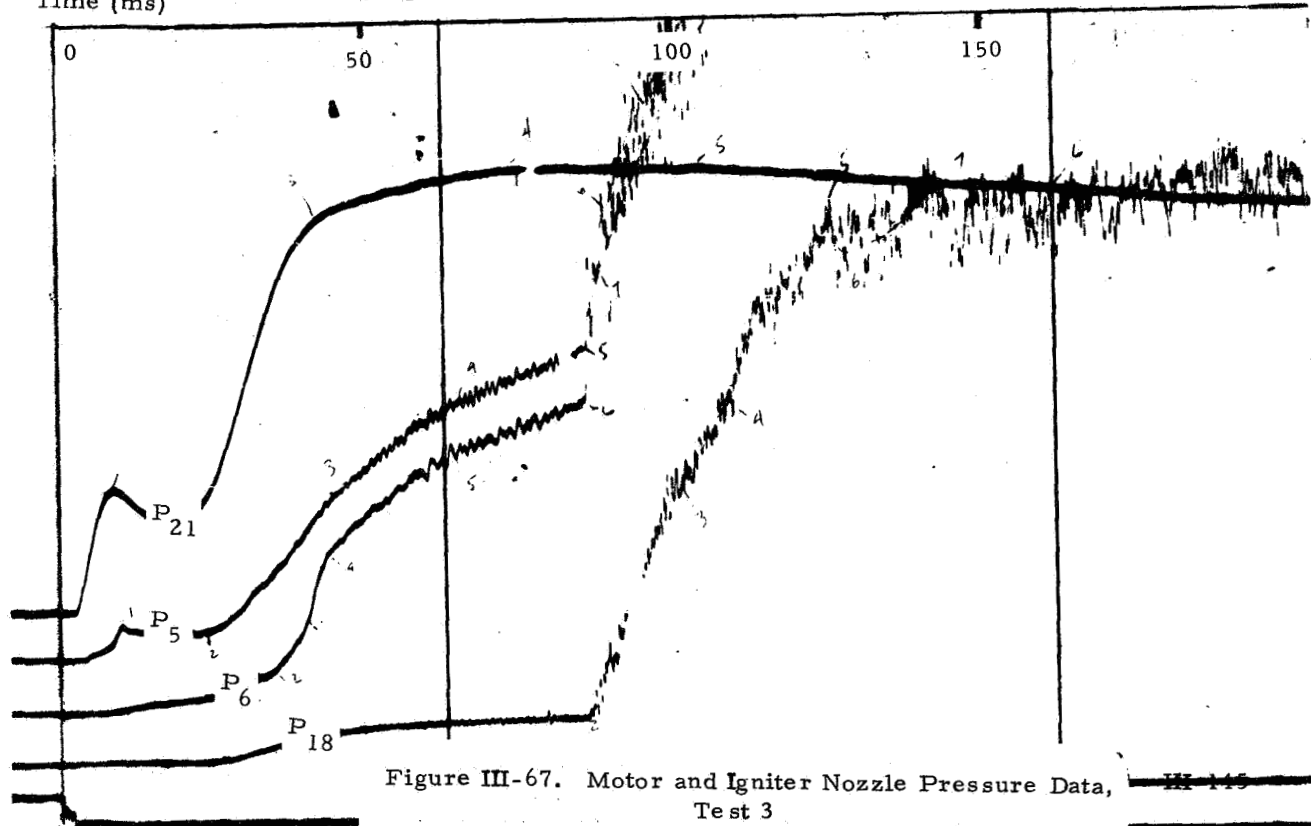
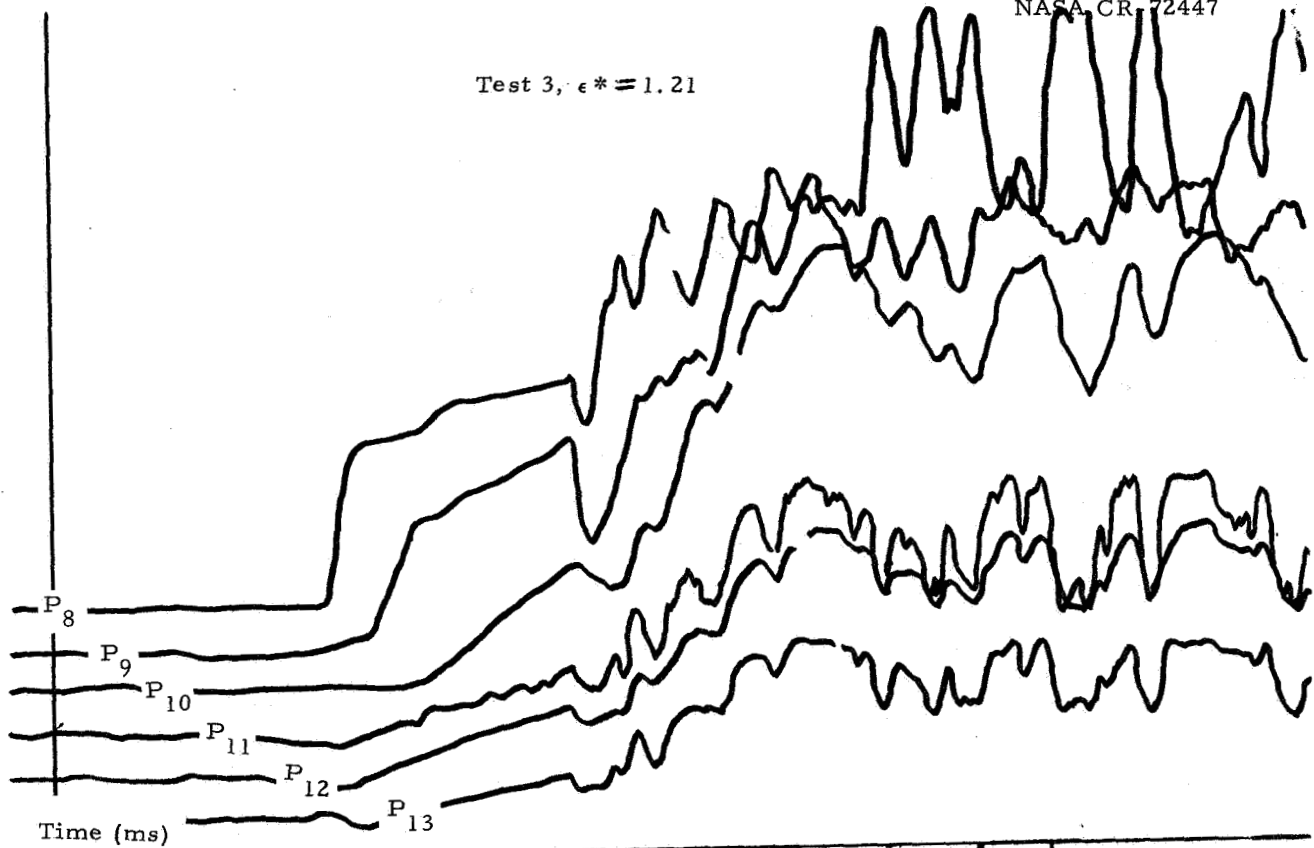


Figure III-67. Motor and Igniter Nozzle Pressure Data, Test 3

Test 4, $\epsilon^* = 1.45$

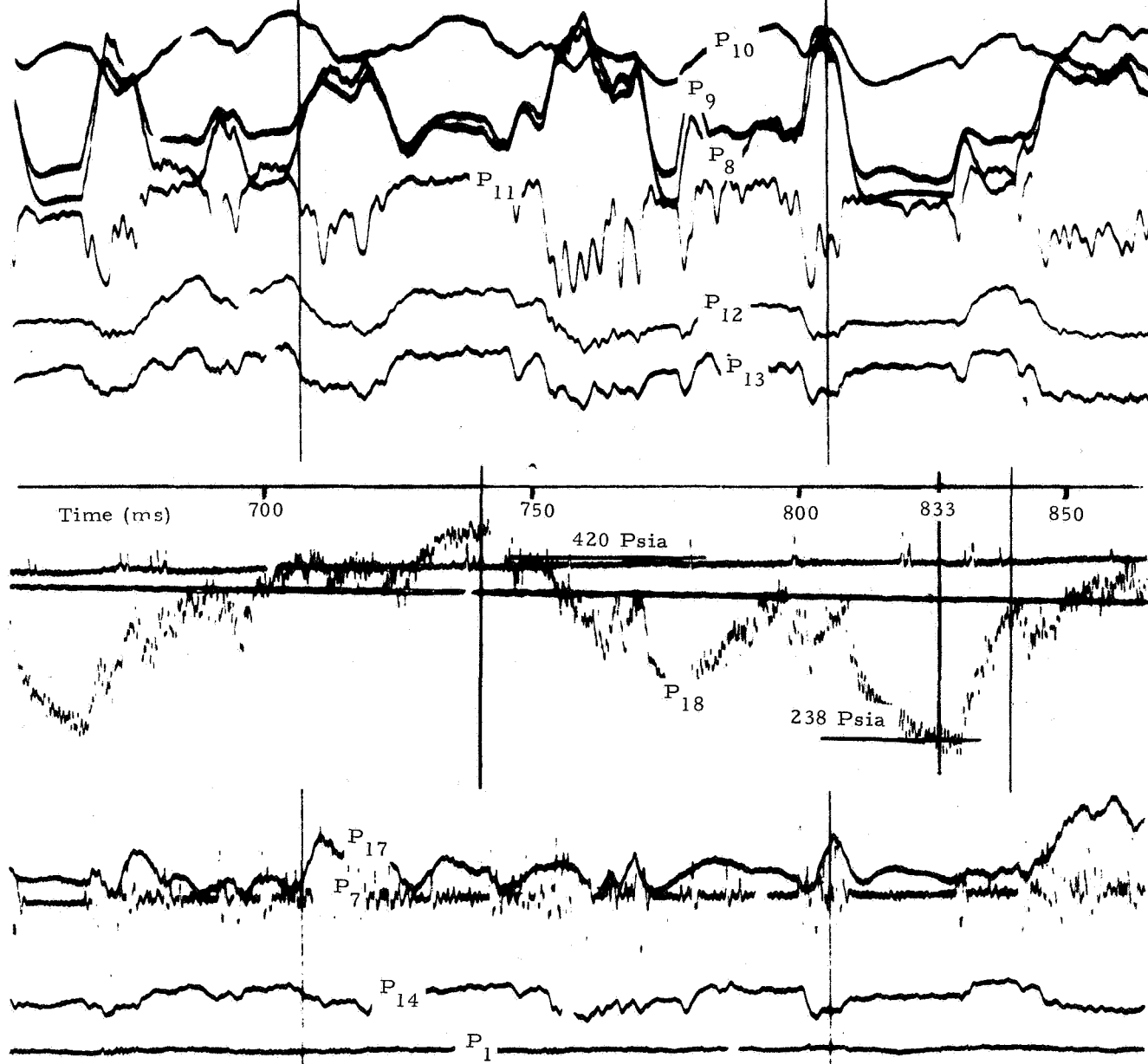


Figure III-68. Igniter and Motor Nozzle
Flow Interactions, Test 4

period of blocked operation, a pressure of 420 psia at P_{18} indicated a normal shock in the igniter nozzle upstream of P_{18} . At 833 ms the igniter nozzle pressure dropped to 238 psia and the normal shock either moved downstream to a relatively lower expansion ratio, or the nozzle flow separated and probably passed through a Mach reflection within or external to the igniter nozzle. In the latter cases at the lower igniter nozzle pressures, there were probably relatively higher total pressure losses and a decrease in igniter jet penetration.

The similarity in the general shape of igniter and motor nozzle pressure traces, specifically P_{18} , P_8 , P_9 , P_{10} and P_{11} , should also be noted. Periods of increased pressure at these motor nozzle locations correspond to periods where similar pressure rises were noted in the igniter nozzle. However, there was a significant difference in pressure levels as shown in Table III-9, which presents nozzle and chamber pressure data for Tests 2 through 5.

Table III-9. Nozzle and Chamber Pressure Data,
Tests 2 thru 5

Test No.	ϵ^*	time ms	P_{18}	P_{19}	P_8	P_9	P_{10}	P_{11}	P_1	P_{21}
2	1.31	1200	339	358	190	199	237	155	519	1267
3	1.21	1150	471	153	277	309	277	144	644	1586
4	1.45	1200	423	+	234	255	254	150	603	1223
5	1.28	1200	464	+	196	245	264	154	599	1100

Pressures in the igniter nozzle (P_{18}) are in the range between 339 and 471 psia. Corresponding maximum motor nozzle wall pressures were at least 100 psi lower in all cases and were as much as 200 psi lower in some. In all these tests the igniter was positioned with the nozzle exit plane in the neighborhood of nozzle wall tap P_{10} . For subsonic igniter nozzle flow downstream of P_{18} one would expect to have found an increase in pressure with the expanding subsonic igniter nozzle flow with the result that the pressures in the motor nozzle exit cone would be comparable to the igniter static pressure at the igniter exit plane. However, this was not the case, and the actual data indicated a significant pressure gradient from the igniter flow to the motor nozzle wall. This is indicative of a highly turbulent three-dimensional flow which cannot be described by normal one-dimensional flow theory.

b. Prediction of Motor Nozzle Blockage

It is desirable to predict igniter design and placement parameters so that motor nozzle throat blockage and subsequent overpressures are avoided. An analytical blockage model developed during the program for this purpose was presented in section IIIA. To establish the applicability and accuracy of this model, it is necessary to first compare the model with experimental data to ascertain the degree of agreement of the basic assumptions and finally to compare model predictions with experimental results.

Comparison of predicted model values with experimental results indicated good agreement for low ϵ^* values, with less accuracy at intermediate and high ϵ^* igniter locations as shown in figure III-69. Included in figure III-69 is a comparison of the experimentally determined igniter to motor total pressure ratio at unblocking for the igniter ϵ^* and the theoretical line which separates regions blocked and unblocked main motor operation. The initial theoretical blockage line is the one derived in section IIIA and the adjusted blockage line is the result of model modification by application of experimental data on the motor nozzle pressure distribution. A significant portion of the data scatter was due to the difficulty in establishing the total pressure at the motor throat and the exact time of unblocking.

A direct model comparison with experimental data was complicated by the fact that there were several criteria which can be applied to the test data to determine the exact unblocking point. These criteria include (1) establishment of a critical pressure ratio at the motor throat, (2) cessation of motor throat, and chamber pressure oscillations (3) verification of supersonic flow at all points downstream the motor throat as determined by motor nozzle pressure measurements and (4) calculation of effective throat area and relative overpressurization from the experimental data.

Since pressure measurements were taken at the motor throat and within the motor chamber unblocking should have corresponded to the ignition and motor conditions for which the theoretical critical pressure ratio was achieved. However, the time at which this critical pressure ratio was achieved was difficult to ascertain because of the uncertainty in determination of the total pressure at the motor throat plane. Motor chamber pressures were measured at the motor head-end and at 4 other locations along the motor length. The head-end pressure could not be used without a correction because of the total pressure drop down the port. Alternatively, the bore pressure data required both Mach number and total pressure loss corrections which were hard to

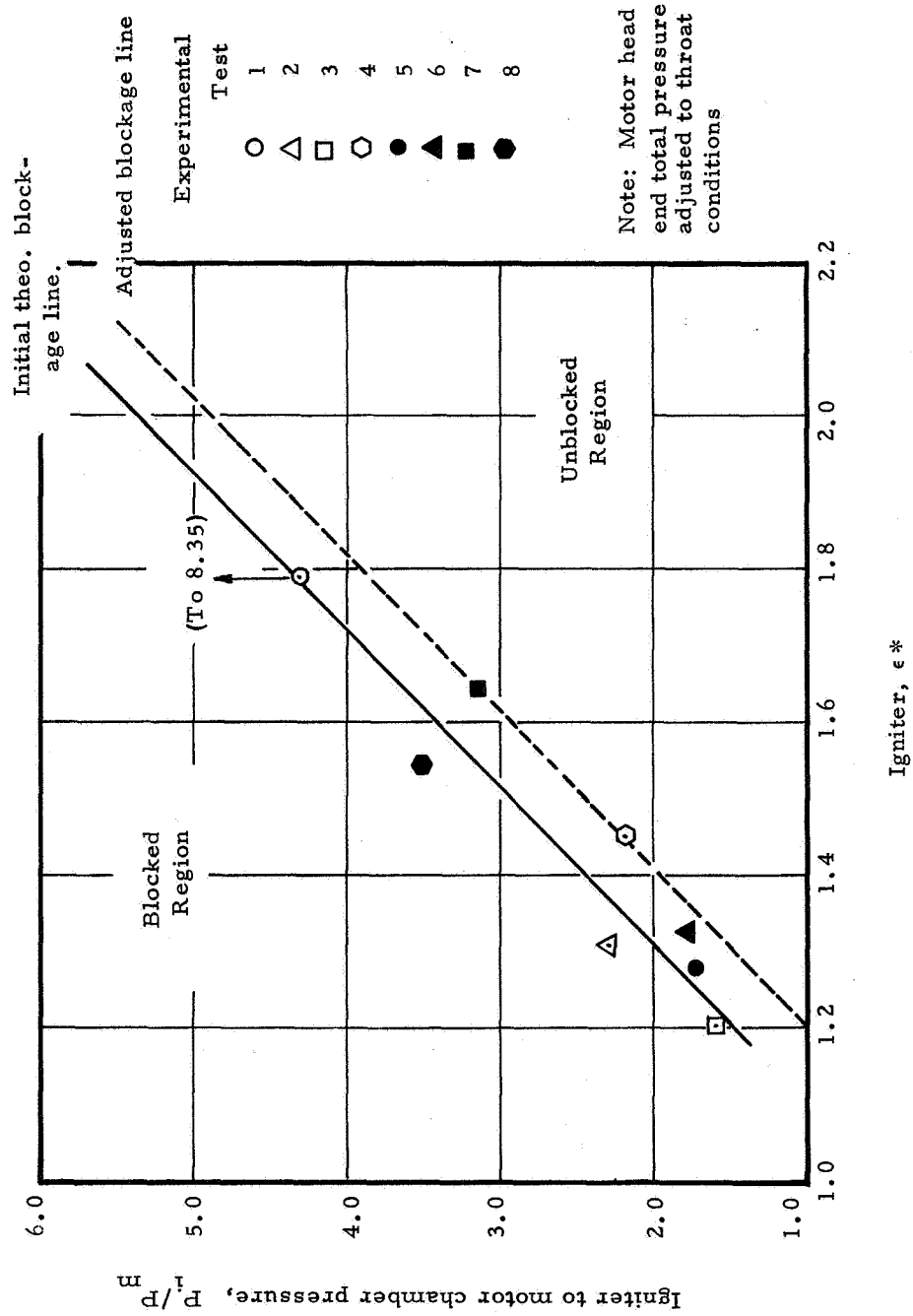


Figure III-69. Comparison of Analytical Blockage Model with Experimental Data

determine with any degree of accuracy. Consequently, the best method was not to use the exact quantitative value of the throat to motor chamber pressure, but was to use as criteria the establishment of a constant pressure ratio less than the theoretical critical pressure ratio as based upon the motor throat to head-end pressure ratio (P_7/P_1 or P_{16}/P_1). However, this criterion did not prove adequate for all tests. In tests where blocking was marginal; the time at which the ratio of the average throat to head-end pressure ratio became constant occurred prior to cessation of pressure oscillations in the motor nozzle and chamber pressures. These oscillations indicated a feed-back of nozzle pressure disturbances into the motor chamber which implied that true sonic conditions did not exist at the throat. Consequently, the added constraint that pressure disturbances in the nozzle should not be reflected in either the motor throat or chamber was needed.

Another criterion which seemed to show some correlation consistency was the condition at which the motor nozzle pressure data indicated supersonic flow at the pressure taps immediately downstream the motor throat. Pressure tap P_7 was located in the physical motor throat plane and P_8 was in the expansion cone downstream of P_7 at an area ratio of 1.1639. If the throat to motor pressure reached the neighborhood of critical pressure ratio and the pressure at P_8 was less than or equal to P_7 then it was postulated that the flow between P_7 and P_8 was supersonic. If P_7 was less than P_8 , then either the flow was subsonic and the throat had not unblocked or a shock existed between P_7 and P_8 raising the pressure at P_8 above P_7 . In general, cases in which a shock was observed to exist between P_7 and P_8 corresponded only to periods of longitudinal oscillation of the igniter bow shock resulting in intermittent blocking and unblocking. Complete unblockage was achieved only after the pressure at P_8 dropped below P_7 and remained there. This criterion for unblocking agreed closely with the criterion of cessation of pressure oscillations at the motor throat.

Another possible method which could be used to determine throat unblockage was to calculate the effective motor throat area and incremental motor overpressurization from test data by the method described in section III E2c. This method was not found to be as accurate as the preceding criteria, because of the uncertainty in determining the instantaneous propellant mass generation rate and the nozzle combustion product discharge rate.

Comparison of the predicted model values and the experimental results using these previously discussed criteria indicated good agreement for low ϵ^* values, with less accuracy at intermediate and high ϵ^* igniter

locations. Figure III-69 presents a comparison of the igniter to motor total pressure ratio (P_i/P_m) at unblocking. The criteria used for tests 2 through 8 were the final cessation of motor nozzle throat pressure oscillations. In Test 1, unblocking occurred prior to achievement of steady state operating pressure in main motor during a period of rapidly changing igniter to booster total pressure ratio. Depending on the criterion selected, unblocked flow could have been assumed to begin for igniter to motor ratios as high as 8.35 at 120 ms and as low as 4.26 at 190 ms. At 120 ms and a pressure ratio of 8.35, throat oscillations were observed to cease and P_8/P_7 becomes less than one. By 130 ms at a pressure ratio of 7.90, the throat to motor pressure ratio reached a semi-constant value. Between 150 and 160 ms, the ratio of pressure between P_8 and P_7 dropped to a value which indicated that the igniter slip surface had ceased to penetrate past the plane of P_8 . By 190 ms, at a pressure ratio of 4.26 relative changes between P_7 and P_8 ceased at values indicating stabilized supersonic flow in the motor throat region. Taken as a whole, these data indicated that initial unblocking occurred at the high pressure ratios which are furthest from the values predicted by the theoretical model. However, disagreement between model and experiment should be expected for this case since the experimental conditions deviated significantly from those assumed for the analytical model.

A basic assumption used in the model was that the igniter jet total pressure was reduced to the motor total pressure by a normal shock at the appropriate Mach number within the igniter nozzle exit cone. In Test 1, the igniter nozzle was observed to flow full until approximately 166 ms. at which time nozzle flow separation occurred indicating the nozzle was probably operating in the stable oblique shock nozzle flow separation regime.

As discussed in the previous section, the nozzle flow interactions in Tests 2 through 6 indicated general conformance with the flow mechanisms assumed for the analytical model. However, Tests 7 and 8 were observed to display a dual unblocking mode. As in Test 1, the initial unblocking occurred during the motor ignition transient while the motor was in the second mode of operation at igniter to motor pressure ratio considerably higher than that predicted by the analytical model. In Tests 7 and 8, as the effective igniter nozzle pressure ratio decreased, intermittent blockage was observed until the igniter to motor total pressure ratio dropped below a given value. During the short periods of blockage, the igniter nozzle pressure increased to a value somewhat lower than the main motor total recovery pressure measured after the cessation of igniter flow. As unblocked conditions were approached on run 7, the

igniter nozzle pressure during the periods of blocked operation were observed to approach the main motor total recovery pressure. It is postulated that the motor initially unblocked during the ignition transient while the igniter operated in the stable oblique shock nozzle flow regime. As the igniter nozzle pressure ratio dropped, intermittent blockage was again noted as the igniter nozzle flow entered and passed through the unstable oblique shock nozzle flow regime. It is hypothesized that final unblocking occurred as conditions of operation in igniter nozzle normal shock flow regime were approached.

A comparison of the basic assumptions of the analytical model with experimental data indicated some disagreement. The model assumptions which were most open to criticism were:

- (1) the pressure distribution on the motor nozzle walls, across the motor throat plane and across the annular area at the igniter, and
- (2) the total pressure adjustment through an igniter nozzle normal shock.

In order to determine the sensitivity of the model to some of these effects, parametric studies were made. However, because of time limitations, only the study of the effects of the motor nozzle wall pressure distribution or wall pressure integral upon the predicted unblocking conditions was completed. Figure III-70a presents the effect of pressure integral upon the predicted critical igniter to motor total pressure ratio for various igniter ϵ^* locations. Also shown is a line representing the values of pressure integral used in the analytical model. As indicated, there was a significant dependency of the predicted unblocking value of P_i/P_m upon the pressure integral value. Figure III-70b shows results of recomputing of the theoretical unblocking conditions using the pressure integrals derived from the experimental data. Although some data scatter is noted, an adjusted theoretical unblocking line may be constructed which agrees with the majority of points. This adjusted theoretical blockage line shown in figure III-70b indicates a conservative prediction of unblocking conditions.

The results of the study on nozzle wall pressure distribution effects indicated a considerable dependency of the predicted unblocking conditions on the pressure terms used in obtaining the momentum balance for the analytical model. Further studies should be made as to relative effects of the other pressure distribution terms and to possible model

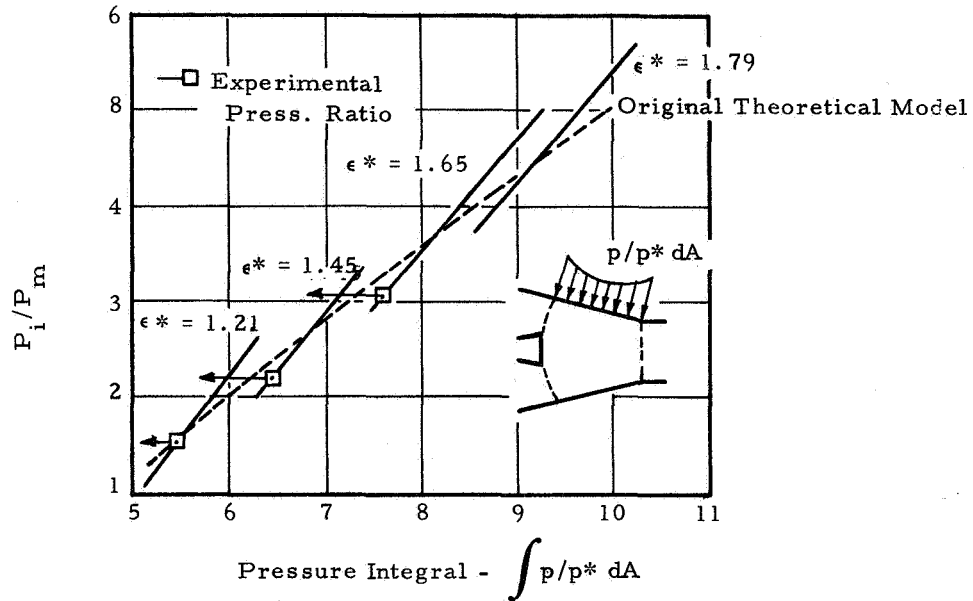


Figure III-70 a. Effect of Pressure Integral on Unblocking Pressure Ratio

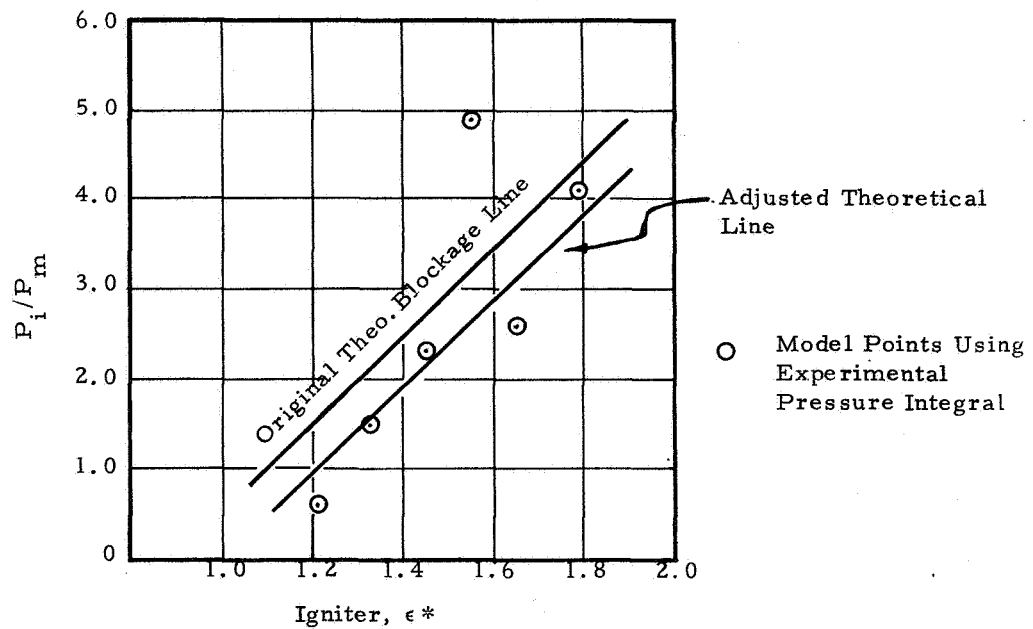


Figure III-70 b. Analytical Model Adjustment Using Experimental Pressure Integral

modifications which would result from this and more accurate estimation of igniter total pressure adjustment for shock structures other than the igniter normal shock postulated for the model.

c. Motor Overpressures

During the motor ignition phase prior to the attainment of steady state operating pressure, igniter jet interference with the motor flow may cause partial throat blockage and hence a reduction of the effective main motor throat flow area. This results in an increase in instantaneous pressurization rates and a corresponding shortening of the ignition time interval. If blockage persists after completion of the ignition phase, then motor overpressurization occurs, i.e., the motor is forced to operate at a chamber pressure which is in excess of design operating conditions.

Although motor overpressures are in general undesirable, they may, in some cases, be permissible if they are limited to a certain level. One possible case would be for a motor with a progressive pressure-time trace, in which the igniter induced overpressure did not exceed the maximum normal motor operating pressure.

Motor overpressures were observed to agree with overpressurization results of Salmi.⁽⁵⁾ In general, the degree of overpressurization increased with increasing igniter-to-motor total pressure ratio and decreasing igniter location. The highest overpressure of 36 percent of the normal chamber pressure was recorded on Test No. 3 ($\epsilon^* = 1.21$) immediately after the main motor reached steady state operating conditions at an igniter to main motor total pressure ratio of 2.28. The overpressures in tests run at lower ϵ^* values were in the range of 10 percent or less.

At low ϵ^* values and high igniter mass flow rates (Tests 2 and 3) maximum chamber pressures were observed early in the test just after the main motor reached steady state operating pressure. In the remaining tests maximum pressures were reached, at approximately 1.2 seconds at which time the main motor area relationship reached a maximum. For cases where blockage occurred, the peak was accented.

For Tests 2 through 6, the maximum percentage increase in chamber pressure above the theoretical unblocked pressure occurred at the beginning of the runs at high values of P_i/P_m . In Test 1, no overpressures were noted and Test 9 data indicated slight overpressures throughout the run with the maximum percentage recorded prior to

igniter tail-off. In Tests 7 and 8, no overpressures were recorded just prior to and after the achievement of steady state operation and only minimal overpressurizations were recorded thereafter. Maximum chamber pressures corresponding to the local maximum recorded at the beginning of motor steady state operation and at the approximate time of igniter tail-off are presented in table III-10. The variations in time at which the local maximums were recorded are primarily due to the variation in motor ignition interval resulting from the effects of igniter mass flow and ϵ * location. Also presented are reference pressures corresponding to no overpressure ($P_{m,0}$) the percentage overpressure ($P_1/P_{m,0}$) the igniter chamber pressure (P_{21}) and mass flow parameters (w/A), and the ratio of igniter to motor pressure (P_{21}/P_1). The approximate percentage of overpressure for each data point was found by dividing by a corresponding nominal motor chamber pressure without blockage. This nominal unblocked motor chamber pressure was derived from the tests where blockage did not occur or had ceased.

The maximum percentage overpressures from table III-10 are pre-plotted against igniter-to-motor total pressure ratio in figure III-71. Dotted parametric curves which depict the believed effect of ϵ * are also shown. In figure III-72 the incremental chamber pressure increases as referenced to unblocked chamber pressure were plotted versus igniter to unblocked motor chamber pressure. Also presented for comparison are Salmi's data⁽⁵⁾ for experimental model 4. These data show reasonable agreement, with only slightly higher incremental pressure increases noted for the solid propellant motor test data. This is consistent with the fact that actual motors should show higher increases in motor pressure (with the same throat blockage) because of the propellant burn rate pressure dependency.

To further investigate the effective throat area reduction and associated overpressurization, a computer program was developed to calculate instantaneous throat area and overpressure values from input experimental data. These calculations were made for the time interval between the completion of ignition and the beginning of igniter tail-off. The method of calculation and equations used in the computer code are presented in Appendix E. The basic equation used to calculate the instantaneous effective throat area was derived by equating formulas for the propellant mass generation rate in the motor chamber and the combustion product mass discharge rate from the motor. The chamber mass accumulation term was found to be important only during the initial pressure transient and was neglected. The equation used for determining the effective sonic throat area was:

Table III-10
Local Maximum Chamber Pressures

Test No.	ϵ *	time ms	P_1	$(P_{m,o})$	$\frac{P_1}{(P_{m,o})}$	P_{21}	P_{21}/P_1	$P_{21}/P_{m,o}$	w/A $lb_m/sec-in^2$
1	1.79	400	451	451	1.000	1540	2.95	2.95	0.314
			523*						
		1320	503	503	1.000	1200	2.04	2.04	0.254
			583*						
2	1.34	192	548	451	1.210	1555	2.45	2.96	0.316
			635*						
		1285	520	503	1.033	1225	2.03	2.10	0.250
			603*						
3	1.21	170	707	520	1.360	1615	2.28	3.10	0.330
		1020	670	600	1.115	1275	1.92	2.22	0.260
4	1.45	206	577	520	1.110	1504	2.61	2.89	0.307
		1250	609	600	1.015	1232	2.03	2.06	0.251
5	1.28	210	573	520	1.103	1205	2.10	2.32	0.246
		1115	608	600	1.015	1055	1.90	1.93	0.215
6	1.33	270	568	520	1.095	1185	2.09	2.29	0.242
		1250	620	600	1.035	1035	1.67	1.73	0.211
7	1.65	142	532	520	1.025	2400	4.50	4.61	0.490
		1200	632	600	1.040	1340	2.15	2.23	0.273
8	1.54	313	523	520	1.005	2000	3.82	3.84	0.408
		1100	615	600	1.025	1542	2.51	2.57	0.315
9	1.45	290	520	520	1.001	2125	1.80*	1.80*	0.189
		1200	607	600	1.012	1750	1.28*	1.295*	0.156*

* Adjusted value

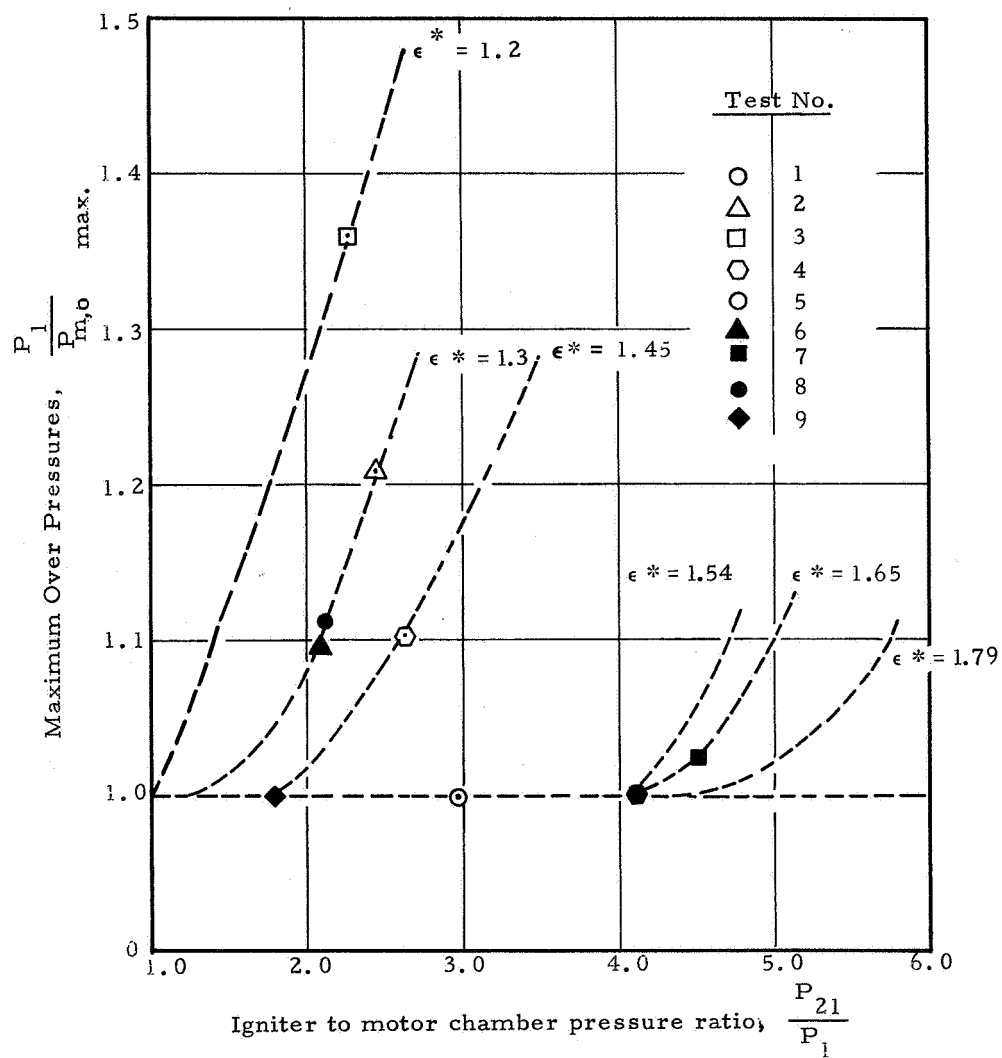


Figure III-71. Maximum Overpressurizations

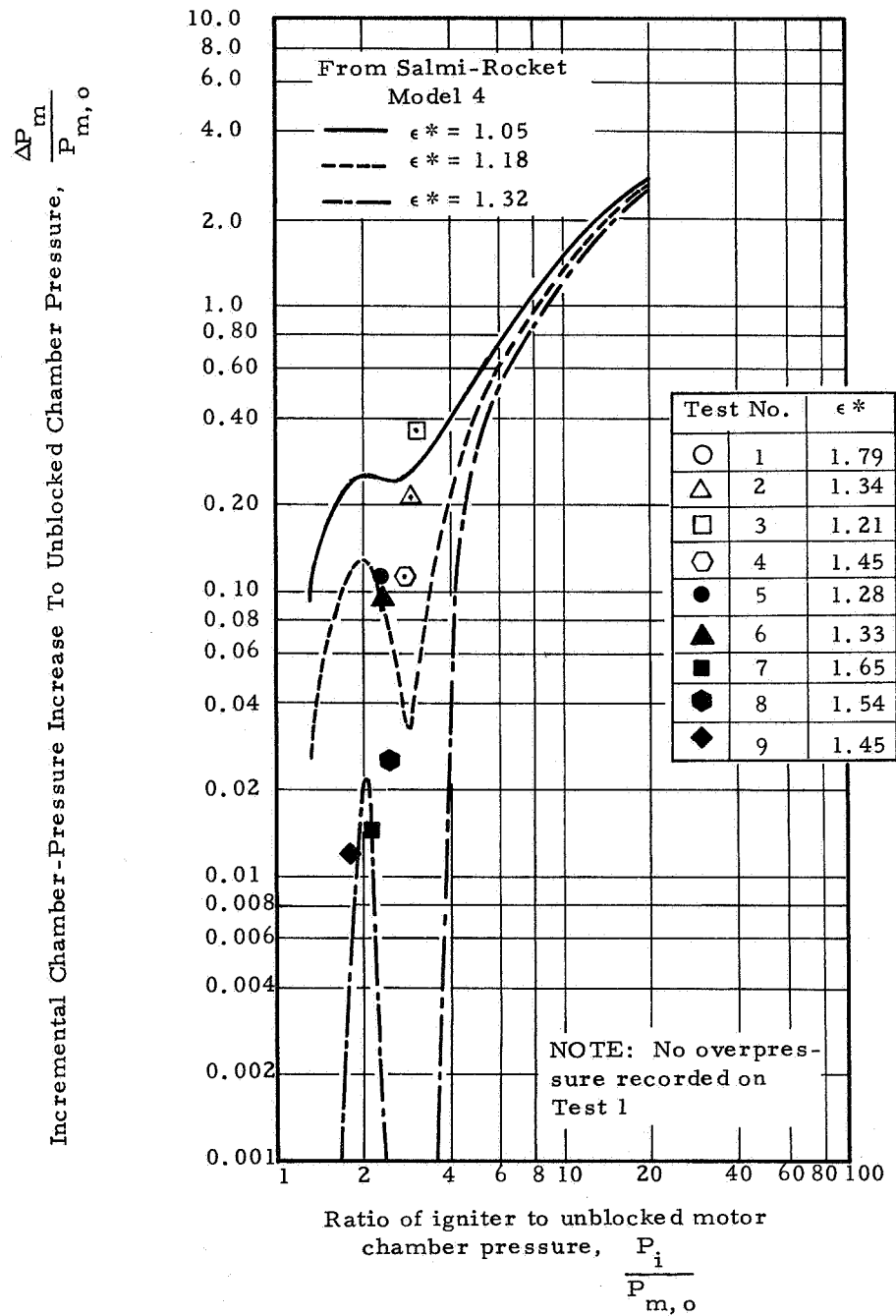


Figure III-72. Maximum Incremental Overpressures

$$A_m^* = \frac{c^* a \bar{P}^n A_b(r)}{P_{5,0} g_c}$$

In this equation the values of c^* , a and g_c are constants, and \bar{P} , P_5 and $A_b(r)$ are variables derived from the experimental data.

By assuming that overpressurizations were caused only by changes in the effective throat area the instantaneous incremental overpressure was calculated from the formula:

$$\frac{\Delta P_m}{P_{m,0}} = \left(\frac{A_{tm}}{A_m^*} \right)^{\frac{1}{1-n}} - 1$$

Using these equations the effective throat area and overpressurizations were calculated for each test except 1 and 7, for times between complete motor ignition and the beginning of motor tail-off. Tests 1 and 7 were used to obtain the relationship between surface burning area and web burn back distance since little if any overpressurization occurred during either of these two runs. The use of experimentally derived burn area relationships was necessary because the theoretical values did not reproduce the experimental pressure data during runs where blockage was not significant. This discrepancy was believed due to the modification of the burn area versus web burn back relationship by the finite rate of flame spread over the initial propellant surface area.

The computer calculations produced results which agreed closely with the data previously shown in table III-10. The computer results indicated that Tests 8 and 9 were essentially unblocked for the time duration from full ignition to tail-off. The results from Tests 2 through 6 indicated significant blockage. The maximum percentage overpressurization shown by the computer data for Test 3 was 30% as compared to 36% computed by the method discussed previously. Consistent with the other method, the computer calculations indicated that the blockage was greatest when the igniter pressure was at its highest with respect to the motor chamber pressure.

Typical data obtained with the data analysis computer program are shown in figures III-73 through III-75. The results from Test 3 shown in figure III-73 indicate that as igniter run time progressed the incremental overpressurization decreased and went through a local minimum and

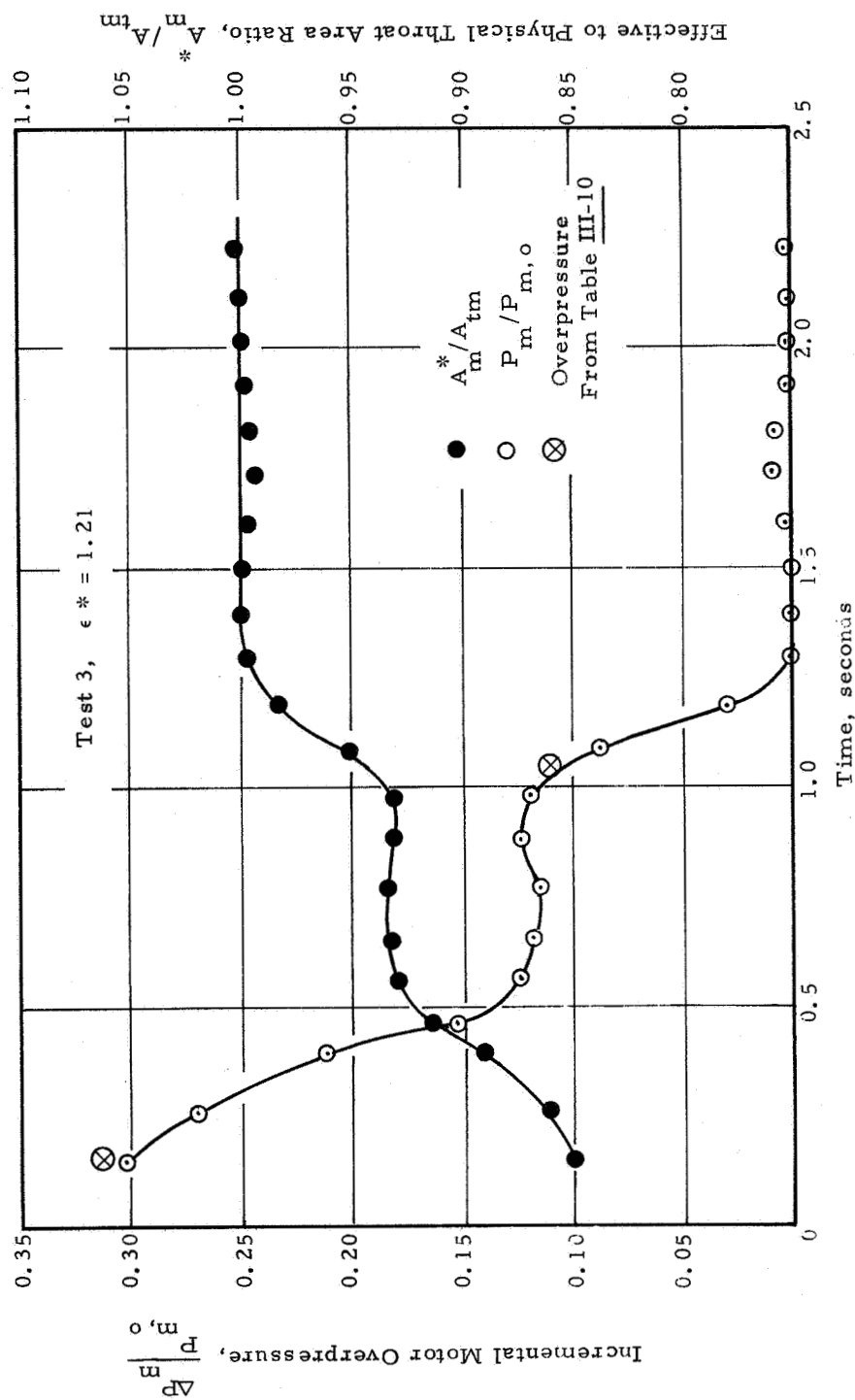


Figure III-73. Effective Throat Areas and Incremental Overpressures, Test 3

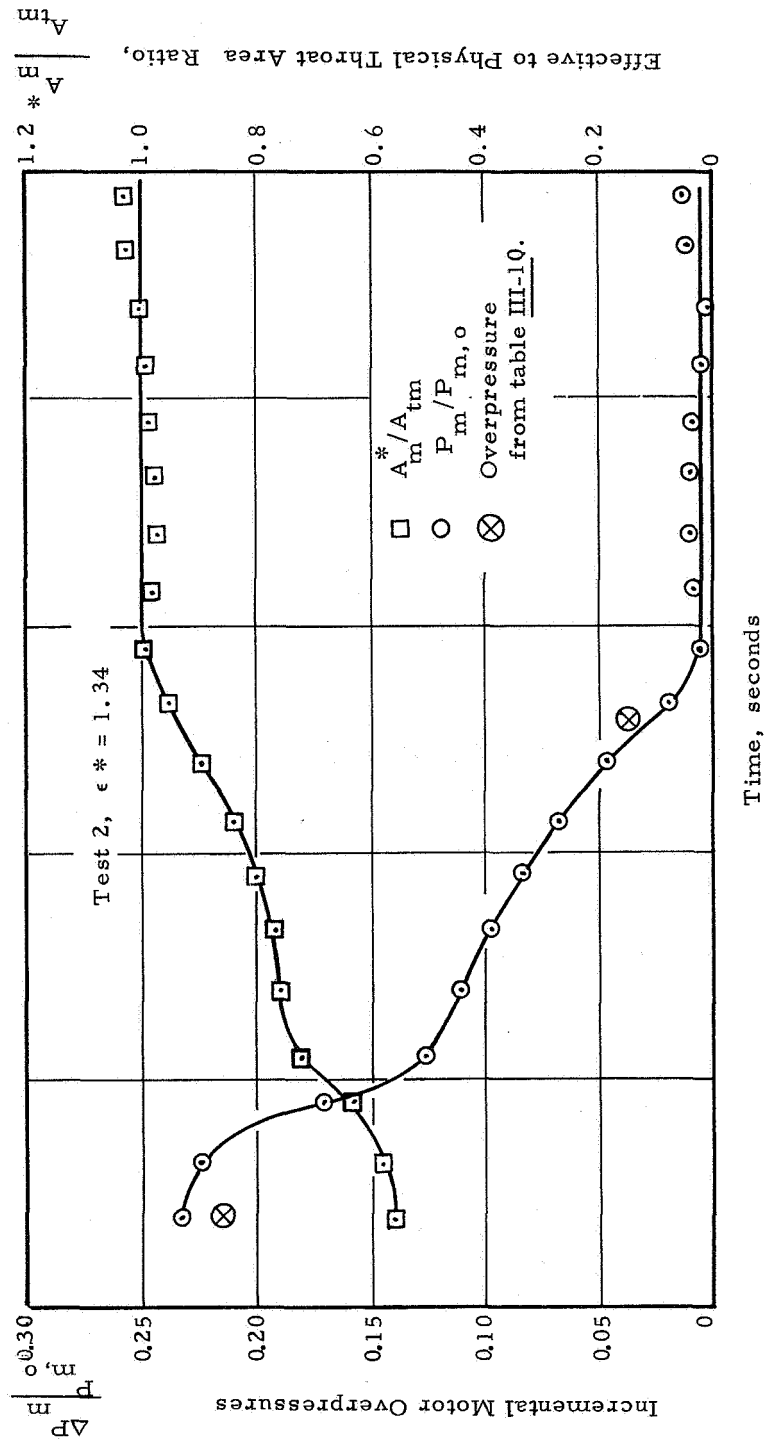


Figure III-74. Effective Throat Areas and Incremental Overpressures, Test 2

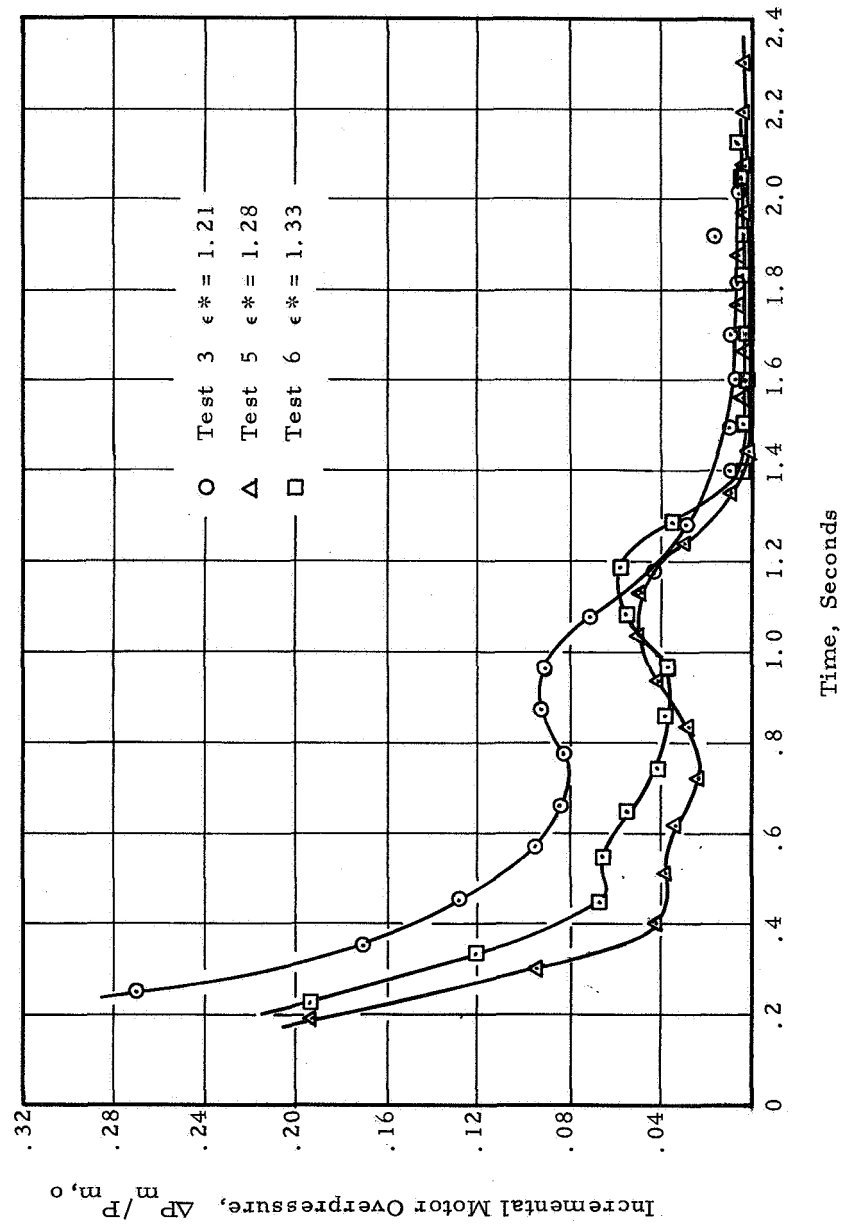


Figure III-75. Comparison of Typical Incremental Overpressures

maximum before reaching an unblocked condition at approximately 1.3 seconds. The effective throat area gradually increased and went through a plateau and a local minimum before reaching the unblocked area at 1.3 seconds. The local overpressure maximum shown at about 0.9 seconds was observed in all tests where computer data reduction was used except Test 2 (see figures III-74 and III-75). The local maximum in these data may probably be attributed to two sources. One possibility was the inability of the computer program to model the propellant mass generation and discharge rates. Specifically, the area of burn versus web burn back appeared to vary slightly in each run, probably due to differences in flame propagation during the ignition transient. Another possibility was that the data were reflecting the local reversal in overpressurization at igniter to motor pressure ratios between 2 and 3 noted by Salmi (see figure III-12). Results of the various computations made indicate that these local extremes in the computer reduced data may be attributed to both of these causes.

In figure III-76 the incremental overpressure computer data are plotted versus igniter to motor pressure ratio. Also shown are data from Salmi's experiments. As shown in figure III-76, there appears to be essential agreement between the shapes of the curves; however, the locations of the curves with respect to each other are not always consistent with the expected trend according to ϵ^* value. This is believed due to experimental differences in the individual tests which were not adequately modeled by the data reduction computer program.

d. Thrust Modifications

Main motor thrust modifications arise from several sources resulting from positioning the igniter in the main motor exit cone. These thrust modifications can, in general, be attributed to the following:

- (1) Thrust additions by the igniter jet flow
- (2) Increased nozzle pressure forces
- (3) Increased motor mass flow due to motor throat blockage and resultant motor overpressurizations
- (4) Separation and shock losses within the nozzle

Since a detailed study of the thrust resulting from each of these factors was beyond the scope of this study, the experimental test data is presented to show the effect of igniter ϵ^* location, igniter mass flow parameter, and at times, the igniter to motor chamber pressure ratios upon net motor thrust.

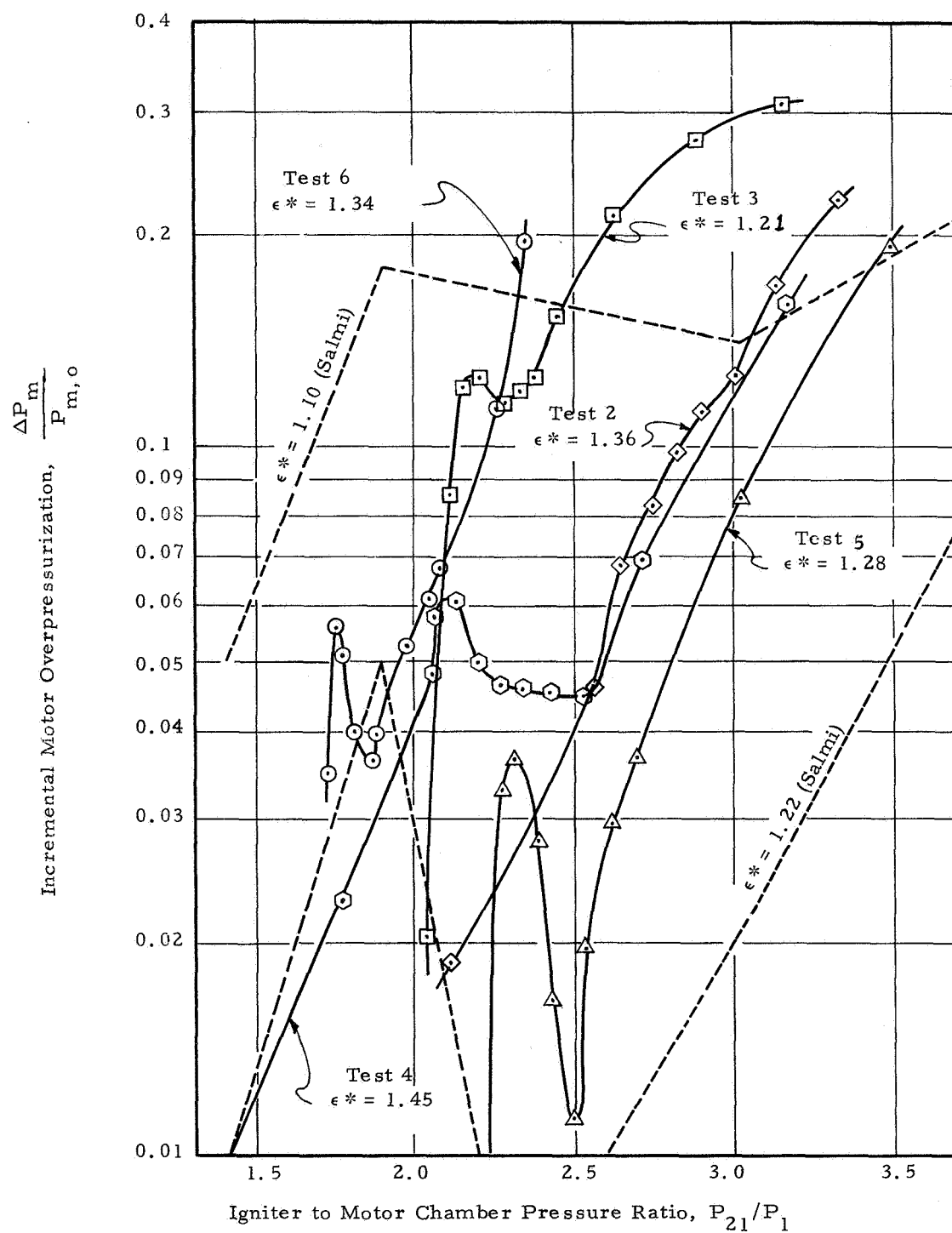


Figure III-76. Incremental Pressure versus Igniter to Motor Chamber Pressure Ratio

In all tests a net increase in thrust was noted from positioning of the igniter within the motor exit cone. Additionally level, thrust oscillations were also observed to occur during all tests. These oscillations were attributed to ringing of the thrust stand at a natural frequency. In some instances, coupling and excitation of these thrust oscillations with the motor nozzle pressure oscillations was observed. In fact, the nozzle pressure oscillations should show some perturbing effects upon instantaneous thrust level although perhaps not to the degree noted.

In general, the thrust level and amplitude of thrust oscillations were observed to increase with decreasing igniter ϵ^* and increasing igniter mass flow rate. The maximum percentage thrust increase was noted at the lowest ϵ^* value tested (1.21). The largest thrust oscillations were noted on the test with the highest igniter mass flow rate in which the igniter was positioned at an ϵ^* location of 1.54. In this latter case the extreme thrust oscillations occurred during a period of pulsating motor nozzle pressures. The pulsating motor nozzle pressures were observed to take place at a frequency in phase with the thrust oscillations.

The minimum relative net thrust increases and thrust oscillations were noted on Test 1 which was conducted with the igniter positioned at an $\epsilon^* = 1.79$. Figures III-77 through III-79 present thrust and motor nozzle pressure data recorded during Test 1. In figure III-77 the ignition transient is shown. Figure III-78 presents data recorded during a quiescent period with relative few nozzle oscillations. Figure III-79 shows data during the period of most active motor pressure disturbances recorded during Test 1. After the completion of igniter action, the thrust oscillations, almost completely dampened-out. Figure III-36 shows motor thrust and nozzle pressure data recorded during Test 3 at the time when the largest percentage thrust increase of any test was noted. Figure III-80 presents data from Test 8 showing the largest thrust oscillations noted. Tabular data on significant thrust parameters are presented in the Motor Ballistic Test summary, Table 1 of Appendix D.

Analysis of the test data indicated that for all cases the maximum thrust occurred at the pressure peak in the middle of the test; however, the maximum percentage thrust increase occurred at the beginning of the test at large values of the igniter to motor chamber pressure ratio (P_i/P_m). Maximum thrust increases of up to approximately 30% were noted for tests where significant overpressures did not occur. For the worst case a maximum thrust increase of approximately 70% was noted shortly after the main motor achieved steady state operating conditions.

Test 1, $\epsilon^* = 1.79$

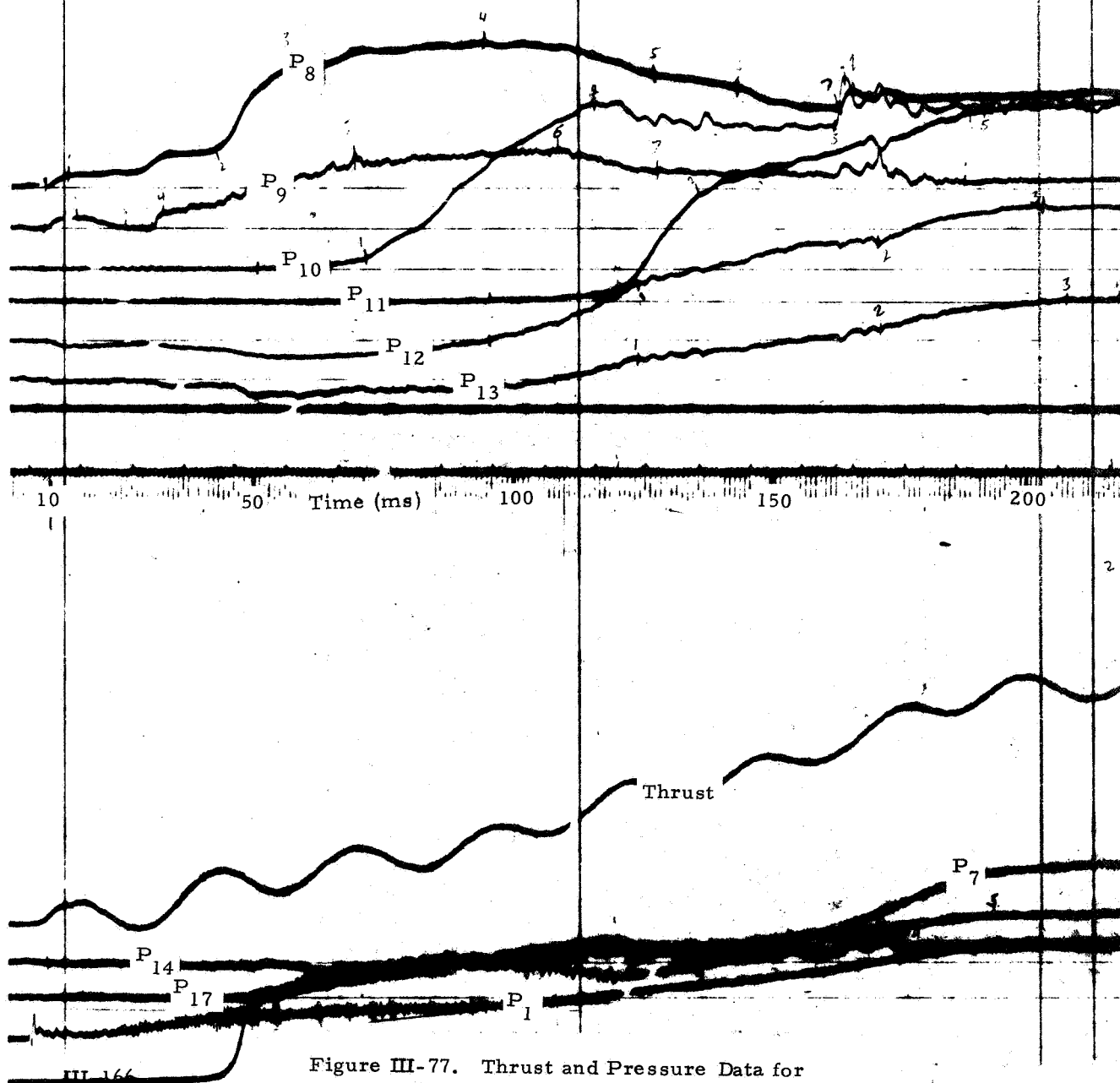


Figure III-77. Thrust and Pressure Data for Ignition Transient, Test 1

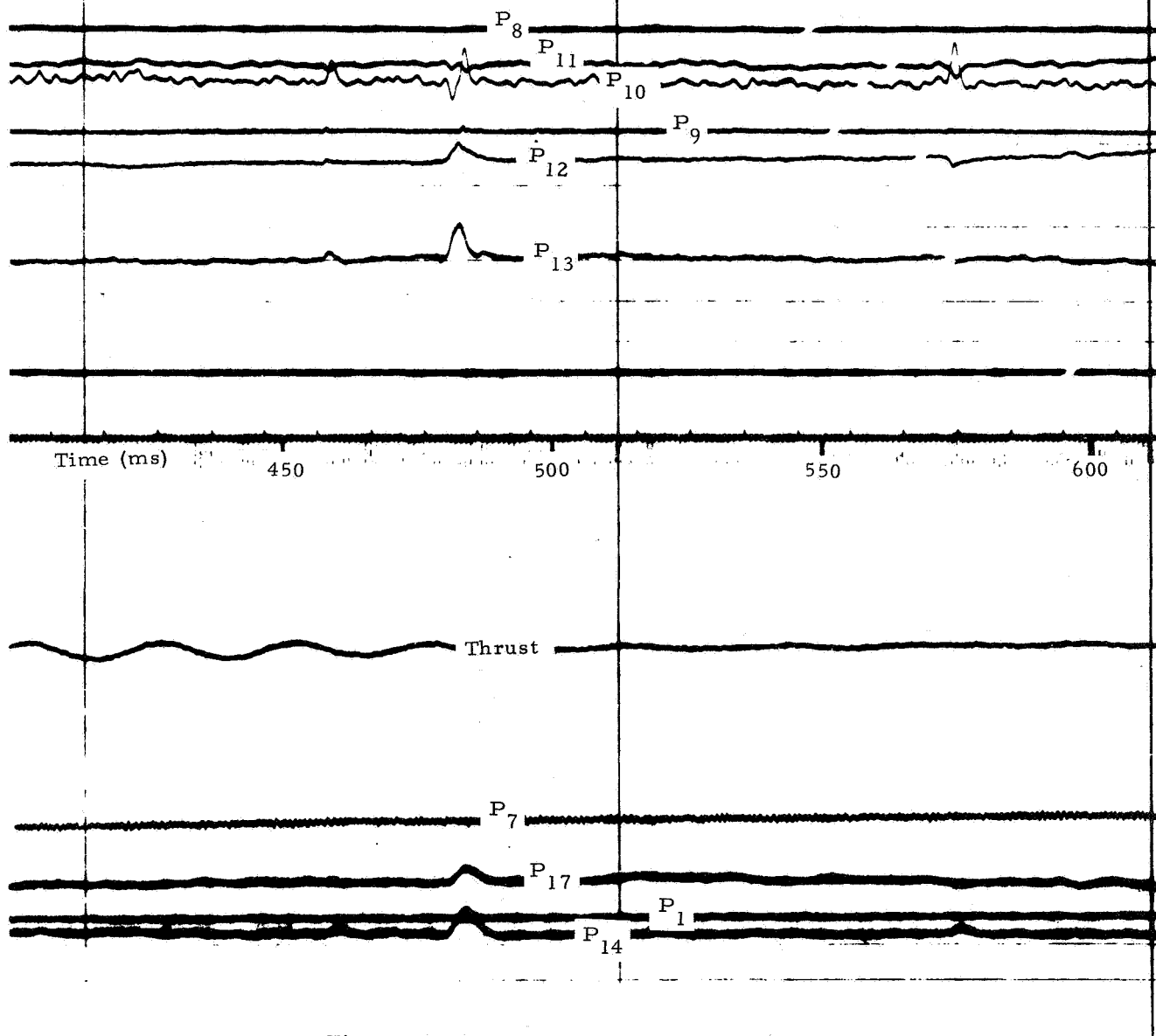
Test 1, $\epsilon^* = 1.79$ 

Figure III-78. Thrust and Pressure Data During Minimum Oscillations, Test 1

Test 1, $\epsilon^* = 1.79$

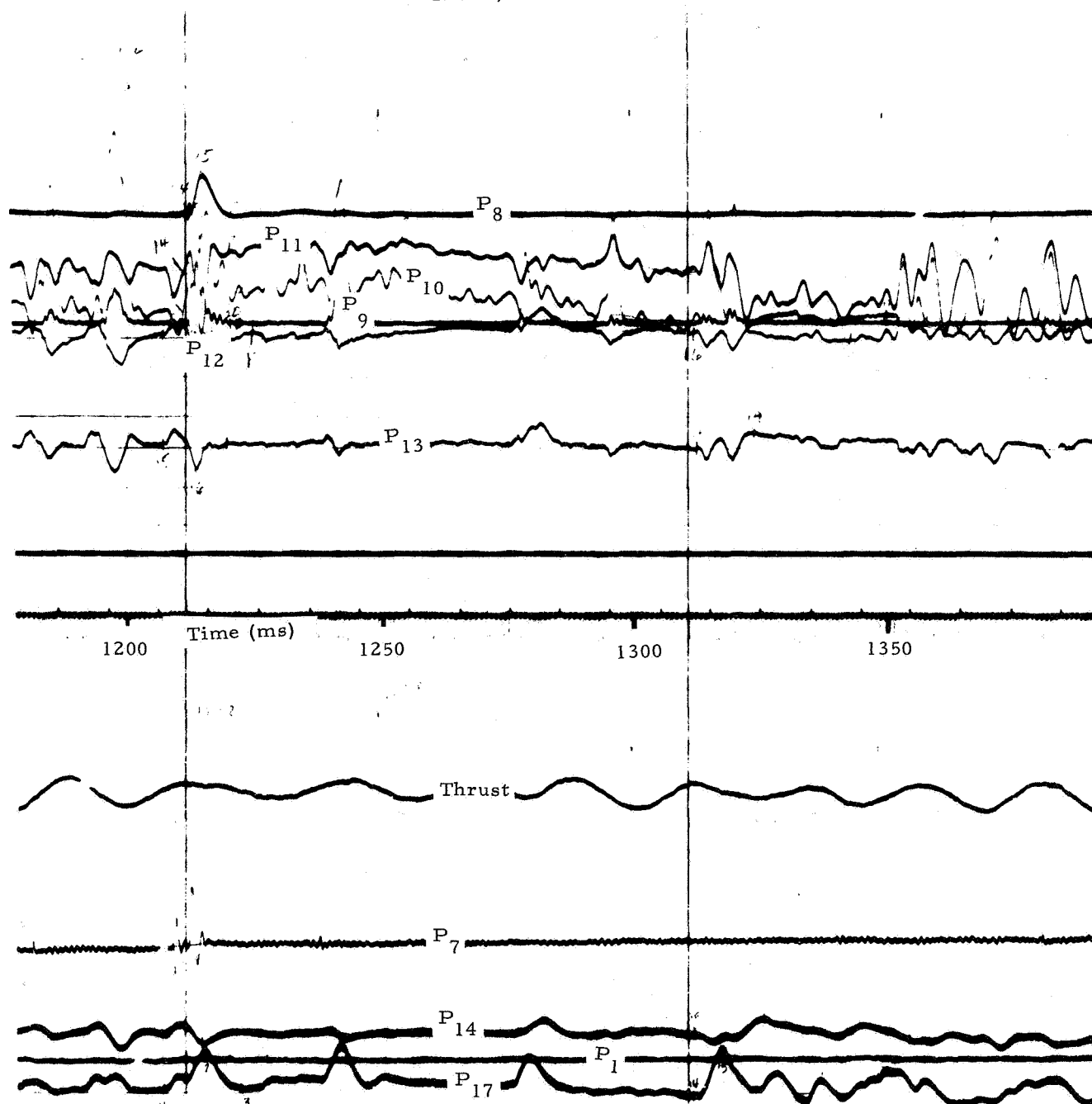


Figure III-79. Thrust and Pressure Data During Maximum Oscillations, Test 1

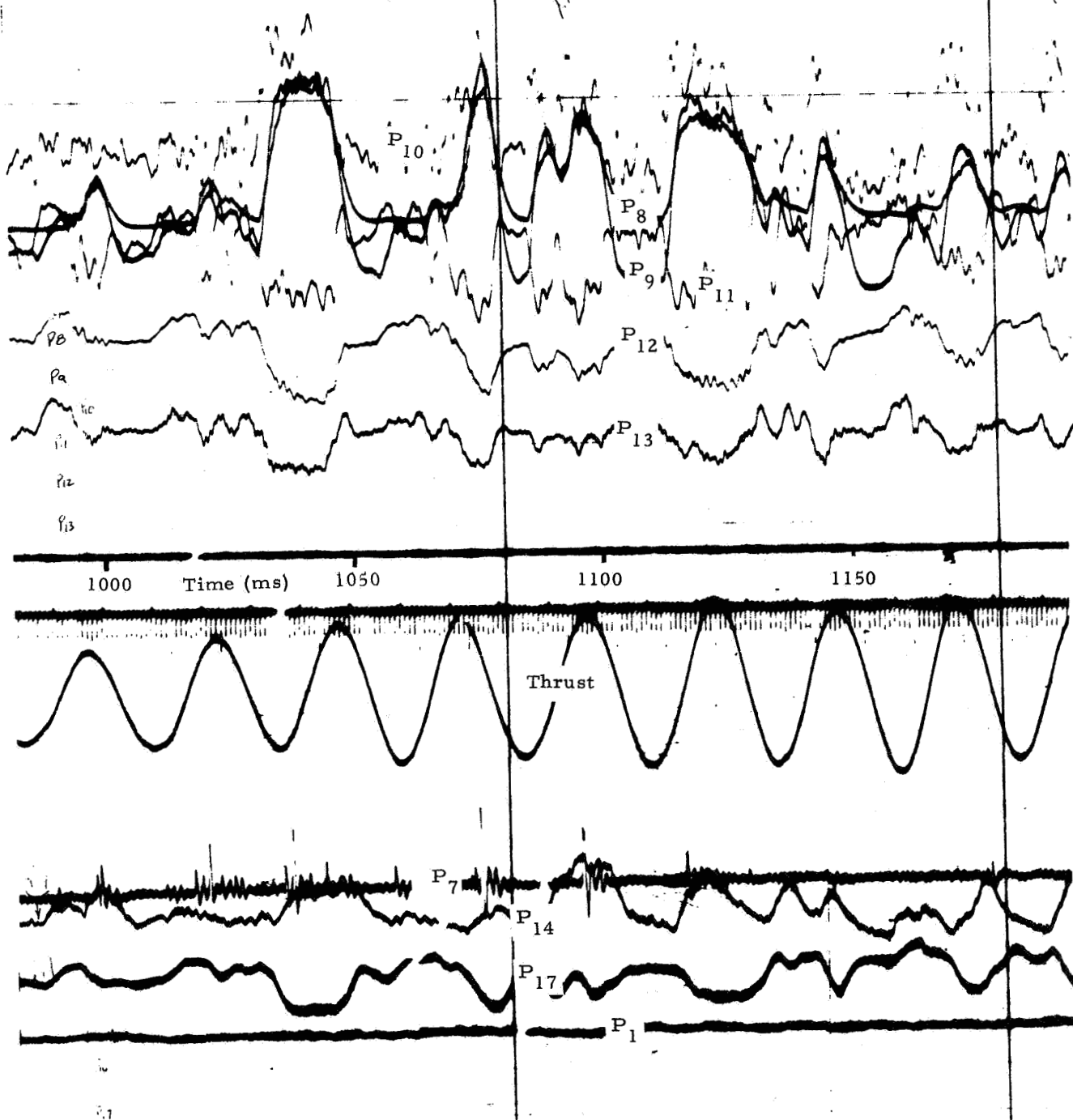
Test 8, $\epsilon^* = 1.54$ 

Figure III-80. Thrust and Pressure Data Showing
Maximum Thrust Oscillations, Test 8

Figure III-81 shows the main motor thrust without igniter flow (igniter off) and the maximum thrust recorded during each test. The scatter in "igniter-on" conditions resulted from thrust differences for each of the data points corresponding to various igniter and motor mass flow rates. Thrusts for Tests 1 and 2 which had lower motor chamber pressures, due to low propellant burn rates, were adjusted by multiplying the recorded thrusts by the ratio of corrected to actual chamber pressures.

A normalized thrust or thrust amplification coefficient was found to be convenient in analysis of the thrust data. It is given by the formula:

$$F_{act}/F_{theo} = \frac{F_{act}}{(C_{F'} P_{m,o} A_{tm})_{theo}}$$

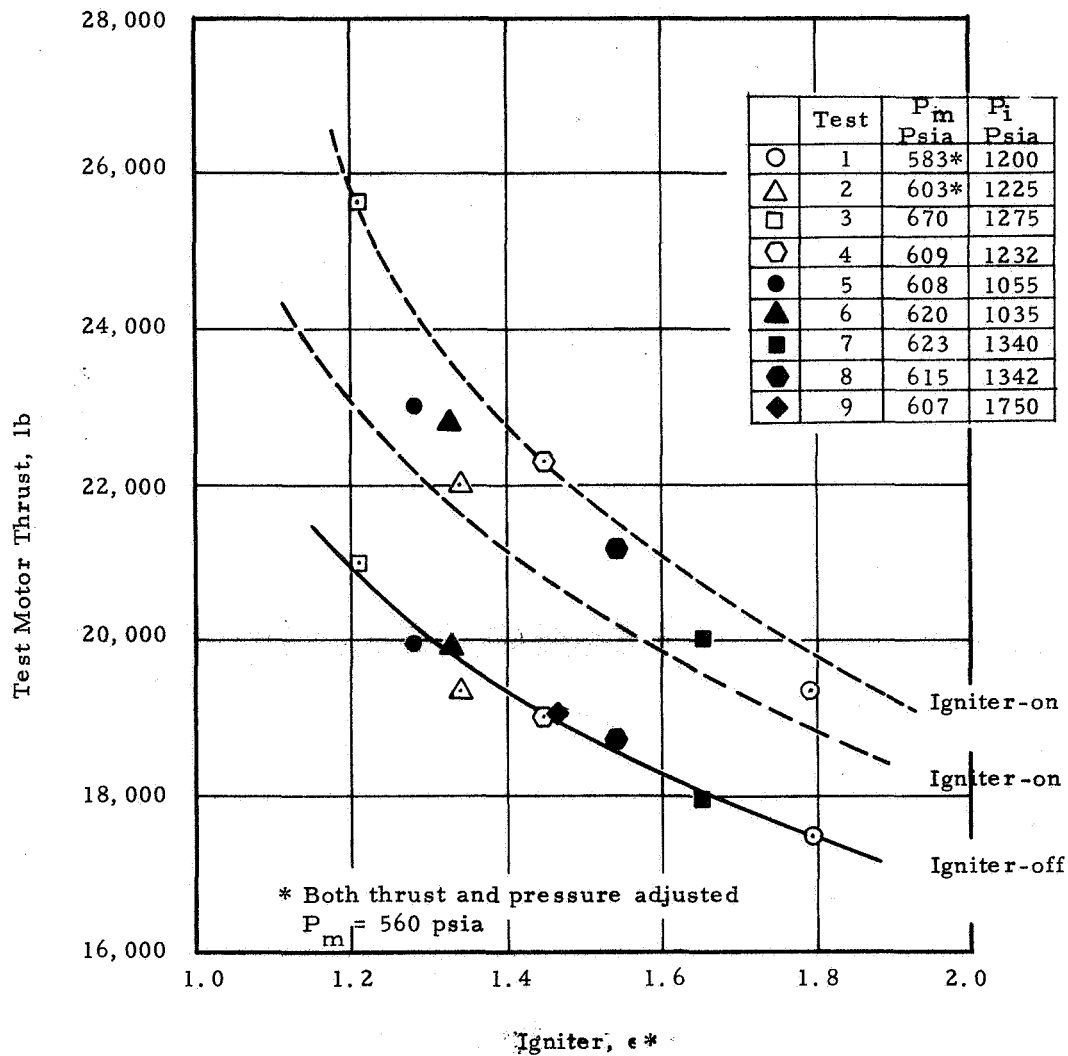
Normalized igniter-off thrusts, motor burn average thrusts and maximum thrusts are shown in figure III-82 as a function of ϵ^* . Data scatter along the average and maximum lines are mainly due to difference in igniter mass flow.

Figure III-83 shows the effect of igniter mass flux parameter on the thrust amplification factor for constant ϵ^* locations. The thrust amplification factor was increased as the ϵ^* location was decreased and as w/A increased.

In general, the thrust data show the qualitative trends of relative thrust change which were expected from theoretical considerations. While the experimental data provided a good estimate of the thrust modifications relative to igniter design and position location parameters, further analytical studies should be made to more accurately define the effects of the various parameters involved.

e. Nozzle Pressure Oscillations and Pressure Distribution

Motor nozzle pressure distributions and pressure oscillations associated with aft-end ignition are of vital interest to propellant motor and launch vehicle designers. The current study revealed motor significant nozzle pressure levels and oscillations for certain igniter operating conditions. Although the results of this study do not provide a demonstrated method of avoiding these oscillations it is believed that the areas in which further studies should be made to solve this problem have been indicated.

Figure III-81. Effect of ϵ^* on Test Motor Thrust

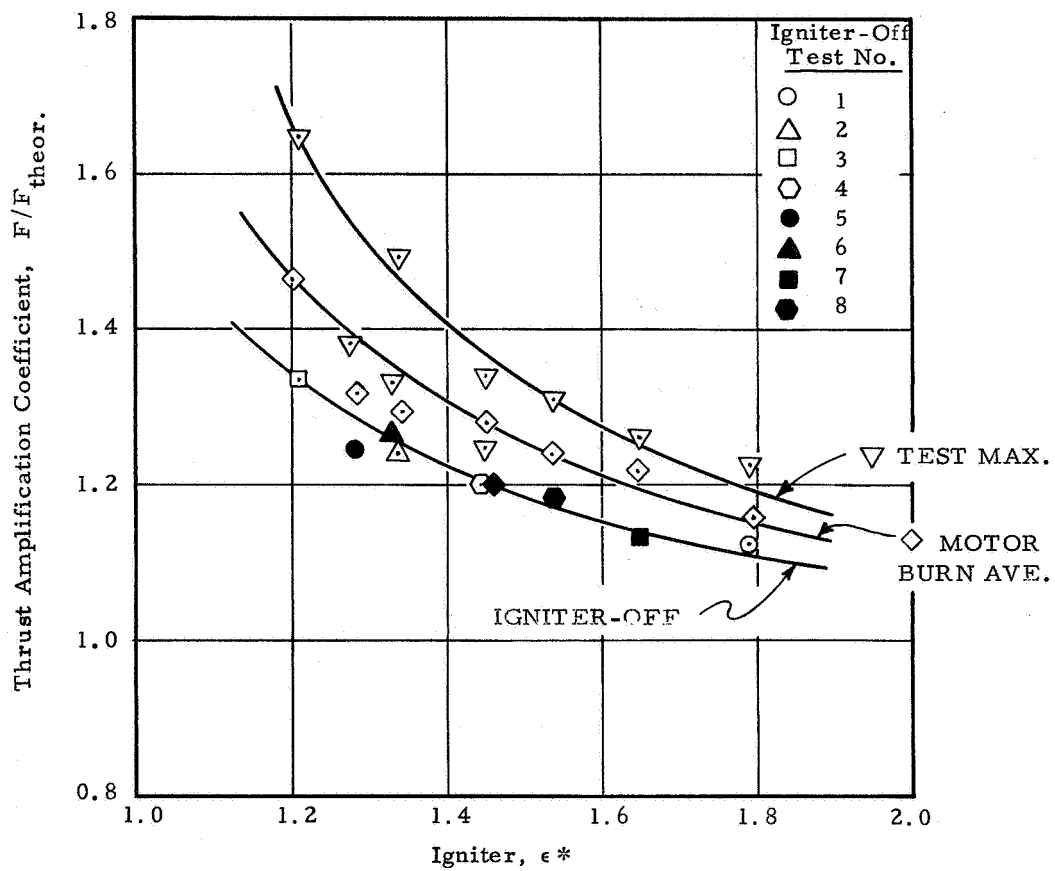


Figure III-82. Effect of ϵ^* on Thrust Amplification Coefficient

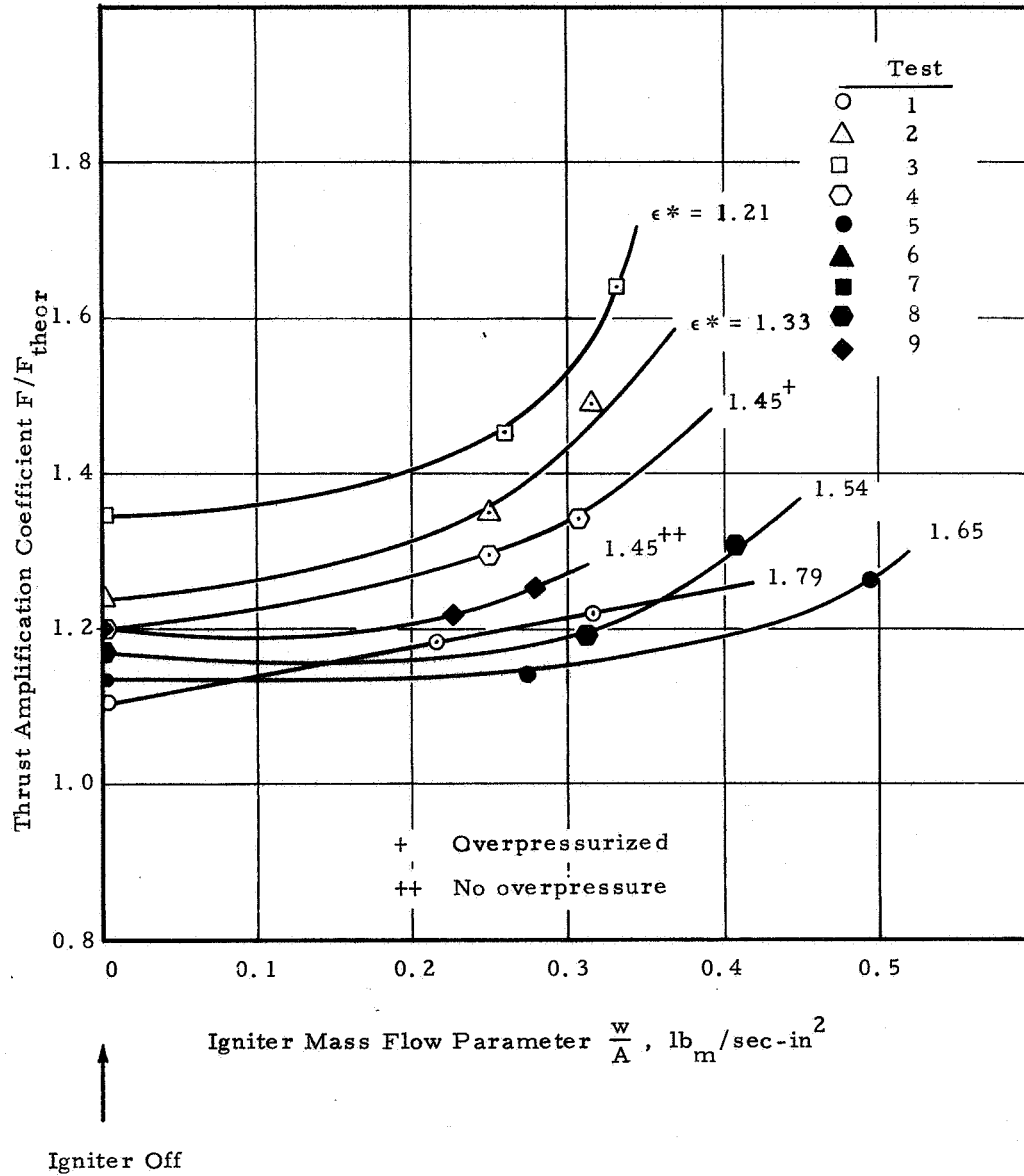


Figure III-83. Effect of Igniter Mass Flow Parameter and ϵ^* on Thrust Amplification

In section IIIC4 data was presented showing the pressure oscillations which occur in the motor nozzle exit cone. In section IID2a, the mechanisms which characterize the igniter and motor flow interactions and which result in the observed pressure disturbances were discussed. The following paragraphs will be devoted to a more detailed study of the motor nozzle pressure oscillations and pressure distribution.

Motor nozzle pressure disturbance can best be characterized by a study of several pressure cycles observed to occur during a typical test. Test 6 was selected because it exhibited intermittent periods of blocked and unblocked operation with characteristically different nozzle pressure distributions. These nozzle pressure differences appeared to exhibit a bi-modal character. The preferred mode which did not result in throat penetration or flow blockage was characteristic of the phenomena observed with low or zero igniter flow or high ϵ^* values. The other, undesirable mode, was generally unstable and produced severe oscillations in the throat and substantially different nozzle pressure distributions from the preferred mode. Figure III-84 presents a reproduction of the pressure traces for nozzle throat taps 7 and 16, and nozzle exit cone taps 8, 9, 11, 12 and 13. The exit cone taps were in the same axial plane as tap 7 at successive distances down the nozzle (see figure III-23). As shown, data cuts were made starting at 750, 1140 and 1340 ms into the run. At 753 ms, the interactions were in the stable mode, with P_8 indicating a pressure of 199 psi, P_{11} a pressure of 156 psi, and minimal oscillations at P_7 . After transition to the unstable mode P_8 rose to 280 psi, P_{11} dropped to 101 psi, and P_7 began to oscillate violently. It is interesting to note that P_8 and P_9 were in phase with one another, whereas, P_{10} , P_{11} , P_{12} and P_{13} were in phase in the opposite direction. After the pressure distribution returned to the unblocked mode, the oscillations of P_7 died out. The next transition began after 1140 ms. Although the shifts in pressure at P_8 and P_9 were severe, the nozzle throat oscillations at P_7 were diminished from the previous pressure cycle at 750 ms. Also, it is interesting to note that P_{10} was in phase with P_8 and P_9 out of phase with P_{11} , P_{12} and P_{13} . This indicates that the shock impingement point had moved from upstream P_{10} to a location downstream. The transition to the undesirable mode shown at 1340 ms although similar in most respects to the other two did not result in severe throat oscillations, indicating that the disturbance was considerably attenuated before reaching the throat. These characteristically bi-modal pressure disturbances persisted until the igniter tailed off completely. However, nozzle throat oscillations due to these perturbations ceased just after the beginning of igniter tail-off.

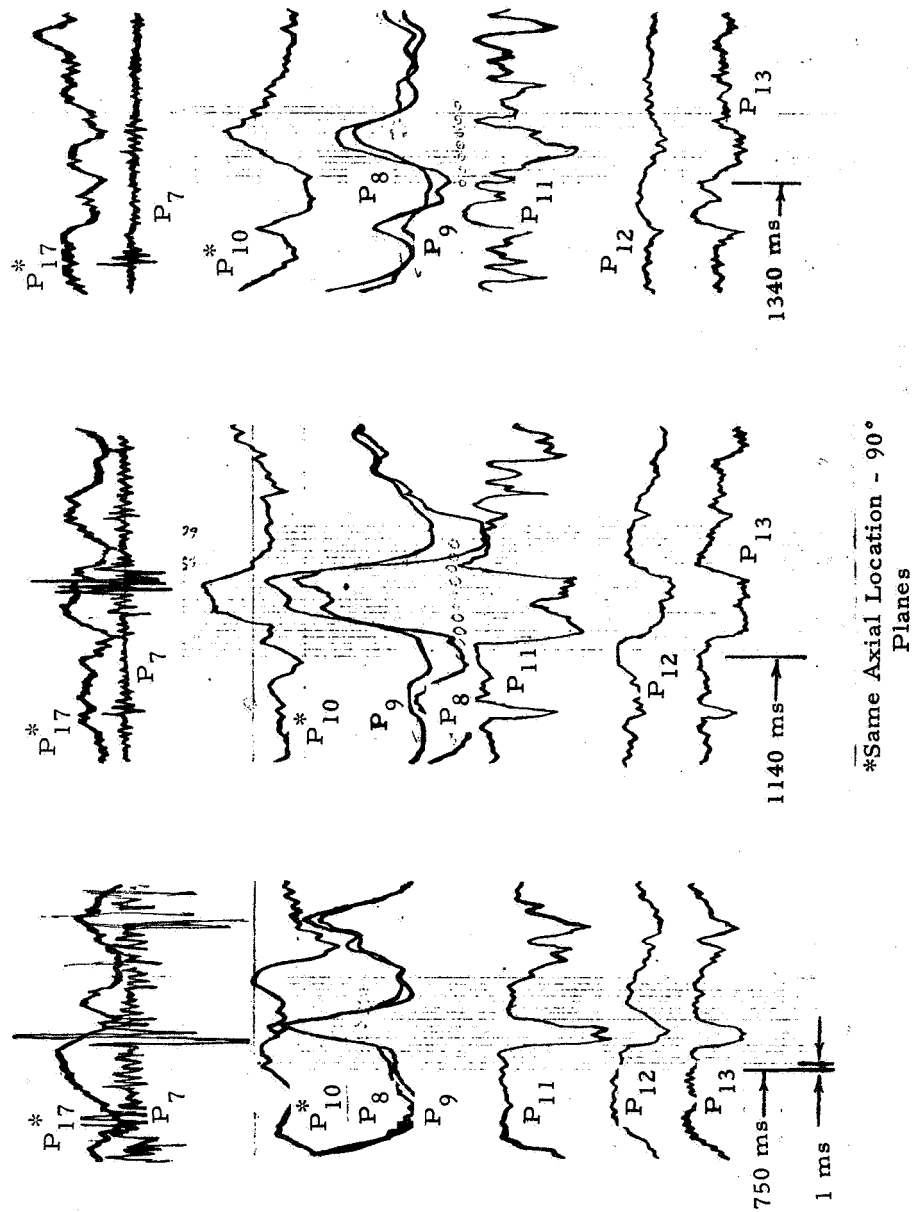


Figure III-84. Typical Nozzle Pressure Oscillation, Test 6

In an effort to establish the origin of these excursions from the unblocked mode of operation, the wall pressures were normalized with respect to throat pressure. These normalized wall pressure distributions are shown for selected times before, during and after the perturbations in figure III-85. To avoid confusion, the zero point for each time period was shifted one tick mark from the one preceding, resulting in a relative displacement of the curves. At 750 ms, the throat pressure was quiescent with a substantial pressure gradient downstream to P_8 . The igniter bow shock-boundary layer interactions appeared to occur predominantly between taps P_8 and P_{10} . At 753 ms, the situation was similar. Between 753 and 755, the transition began. The shock impingement location began to move upstream, and the pressure at the throat started to oscillate as indicated by the black dot. The pressure peak continued to move forward until it appeared to be at its forward-most point at 757 ms. Subsequently, the pressure peak fell back and moved away from the motor throat until at 761 and 763 ms the pressure distribution had returned to the original shape. A similar situation occurred beginning at 1,140 ms except that the shock appeared to be located further downstream than in the previous case. Here it is noted that a greater shock travel over a longer duration was required to induce oscillations at the throat. However, the same progression of shock from its aft-most position forward and then back again was observed. The same shock repositioning was produced at 1340 ms except that the pressure excursions were much less severe and were not accompanied by oscillations at P_7 . These data seem to indicate that the unstable nozzle pressures originated in the flow interaction between the steady main motor flow and the igniter flow. The quiescent behavior of the motor pressures, especially at P_7 , which persisted until after the shock had begun to move forward, indicated that this transitory behavior was probably not triggered by oscillations in the main motor flow. Instead there were data, as discussed in section IIIE2a, which indicate that the igniter flow was unstable and may oscillate longitudinally or laterally as the igniter flow separated or detached from the igniter nozzle.

The hypothesis of nozzle flow field asymmetry is substantiated by the results shown in figure III-86. Pressure taps 17 and 10, which were positioned 90° apart at the same axial station, clearly demonstrated this nonsymmetric behavior. In the first region, shown in figure III-86, the two were approximately opposite in phase. In the second region, they appeared to be almost exactly in phase, whereas in the third region, they were out of phase by approximately 90° . The exact nature of these transverse fluctuations is unclear because of the limited peripheral distribution of pressure taps.

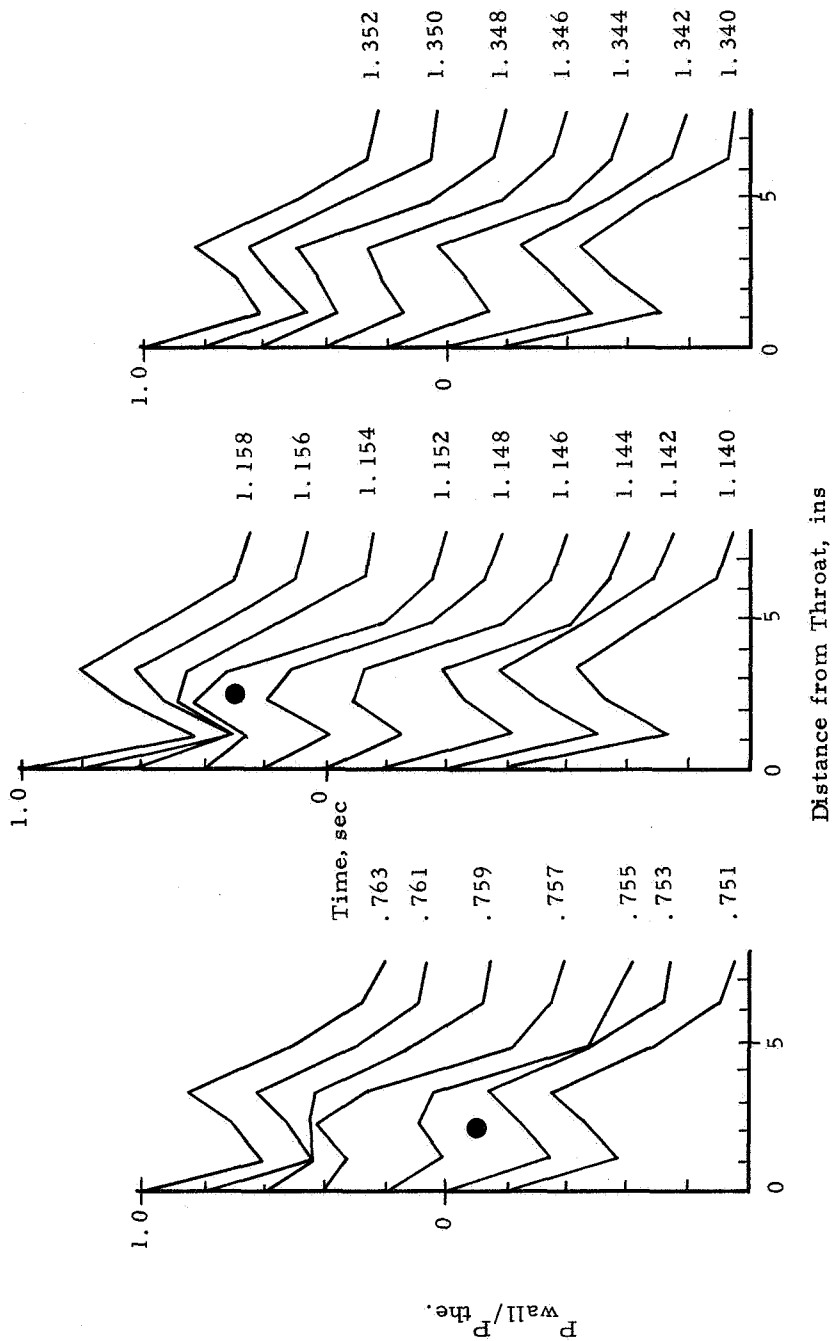


Figure III-85. Nozzle Pressure Distribution During Typical Pressure Oscillation Cycles, Test 6

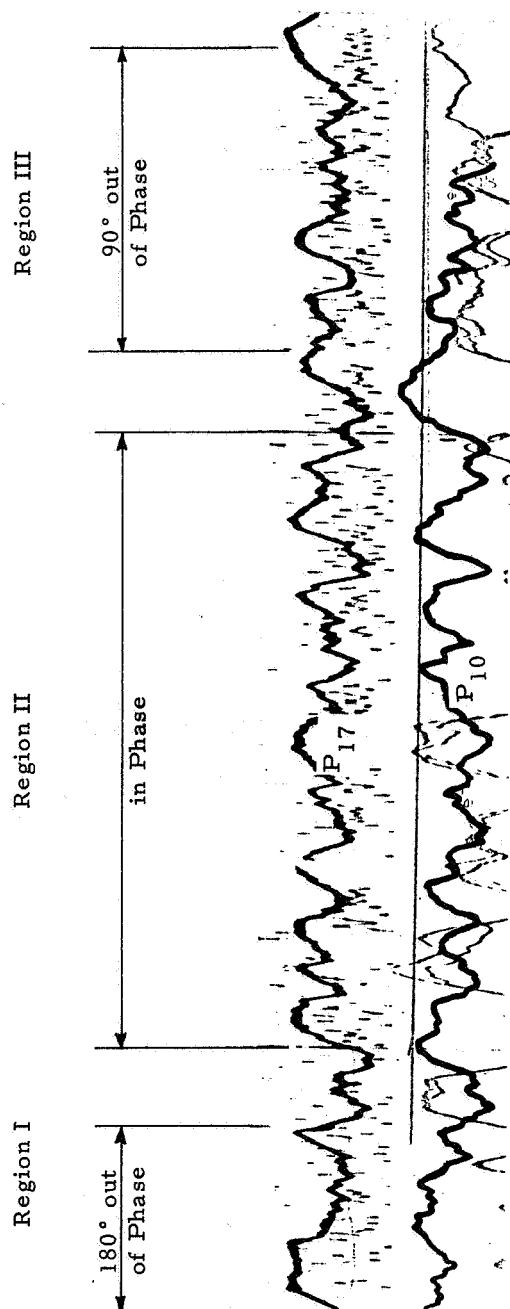


Figure III-36. Asymmetric Nozzle Pressures, Test 6

In similar data from the other tests, the motor nozzle pressure distribution was observed to change radically during each motor nozzle pressure disturbance cycle. The average nozzle pressure levels were observed to increase with decreasing ϵ^* location and increasing igniter mass flow. Figures III-87 through III-89 show the relative effects of igniter ϵ^* location upon motor nozzle pressure distribution. It is noted by comparison of these figures that as the igniter ϵ^* values became decreasingly small, the motor nozzle pressures became correspondingly larger, especially in the region upstream of the igniter exit plane. Data from each illustration show the effects of igniter mass flow. In figure III-87, which illustrates data from test 1 ($\epsilon^* = 1.79$), the nozzle pressure distribution is given for three different times. The first pressure curve at 140 ms was prior to motor steady state operating conditions, but after throat unblocking. At 1200 ms, the igniter was about to begin tailing-off and at 1500 ms effective igniter action has ceased. All these data correspond to unblocked nozzle flow with little if any pressure disturbances. It is noted that as relative igniter to main motor flow decreased, the pressure level at any given wall location also decreased. Included for comparison in these figures is the theoretical nozzle pressure distribution for one dimensional isentropic flow as determined by the available area ratio. Figure III-88 presents data for Test 6 with the igniter at an $\epsilon^* = 1.33$. The pressures at 200 ms corresponded to a period of relative blockage, i. e., during the peak period when the nozzle pressures move furthest upstream from the igniter exit plane. The pressures at 1030 ms were taken for the relatively unblocked condition noted when the nozzle pressures were lowest. This pressure distribution was nearly the same as that observed with the igniter-off shown at 1480 ms.

Figure III-89 presents data from Test 3 conducted at an $\epsilon^* = 1.21$. The pressure data at 1200 and 1300 ms were taken for a lower level of throat blockage; the latter being during igniter tail-off. At 1280 ms, the pressure corresponded to relatively blocked conditions and at 1420 ms igniter action is virtually complete.

The increase in relative pressure levels in Tests 3 and 6 to levels higher than those observed in Test 1 were due to the ϵ^* effect. The lower absolute nozzle throat pressure in Test 1 resulted primarily from a low motor operating pressure caused by a low propellant burn rate.

Ignition transient nozzle pressure distribution data recorded during test 8 are shown in figures III-90 and III-91. Figure III-90 shows the oscillograph data during the ignition phase and figure III-91 presents plotted nozzle pressure distributions for selected times. Motor throat unblocking was observed between 108 and 118 ms as indicated by the relative pressures at pressure taps P_7 and P_8 .

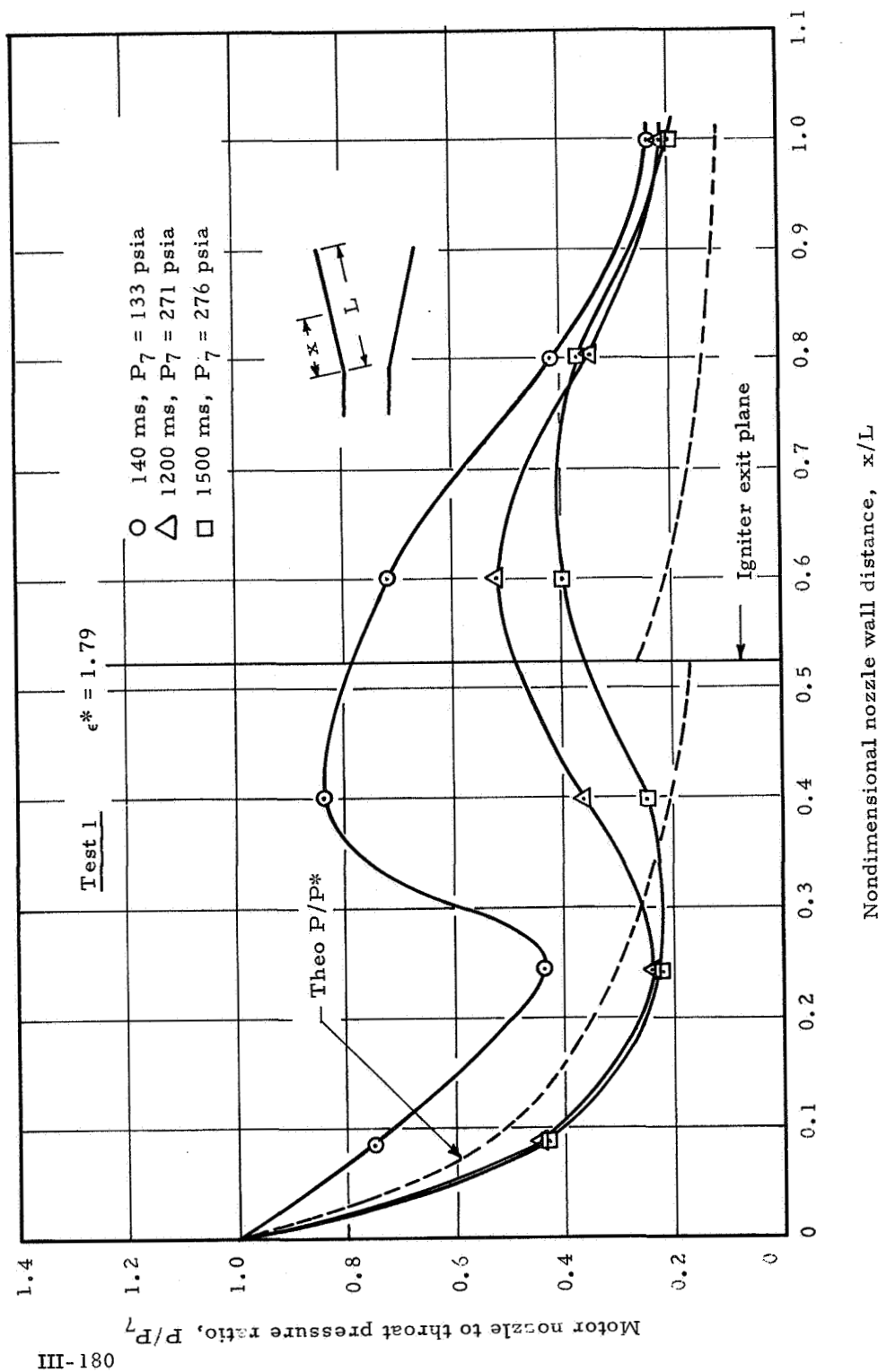


Figure III-87. Nozzle Wall Pressure Distribution, Test 1

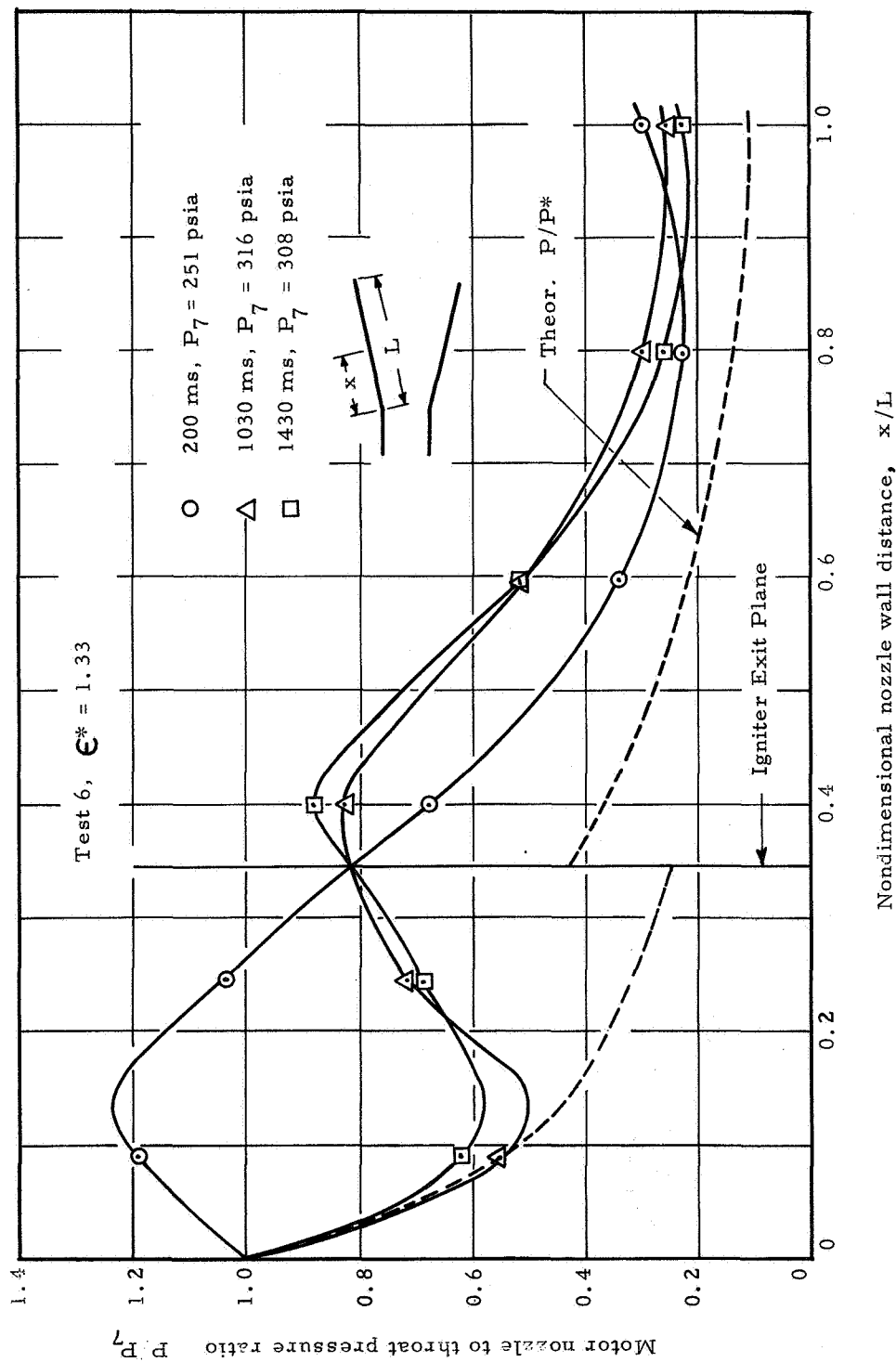
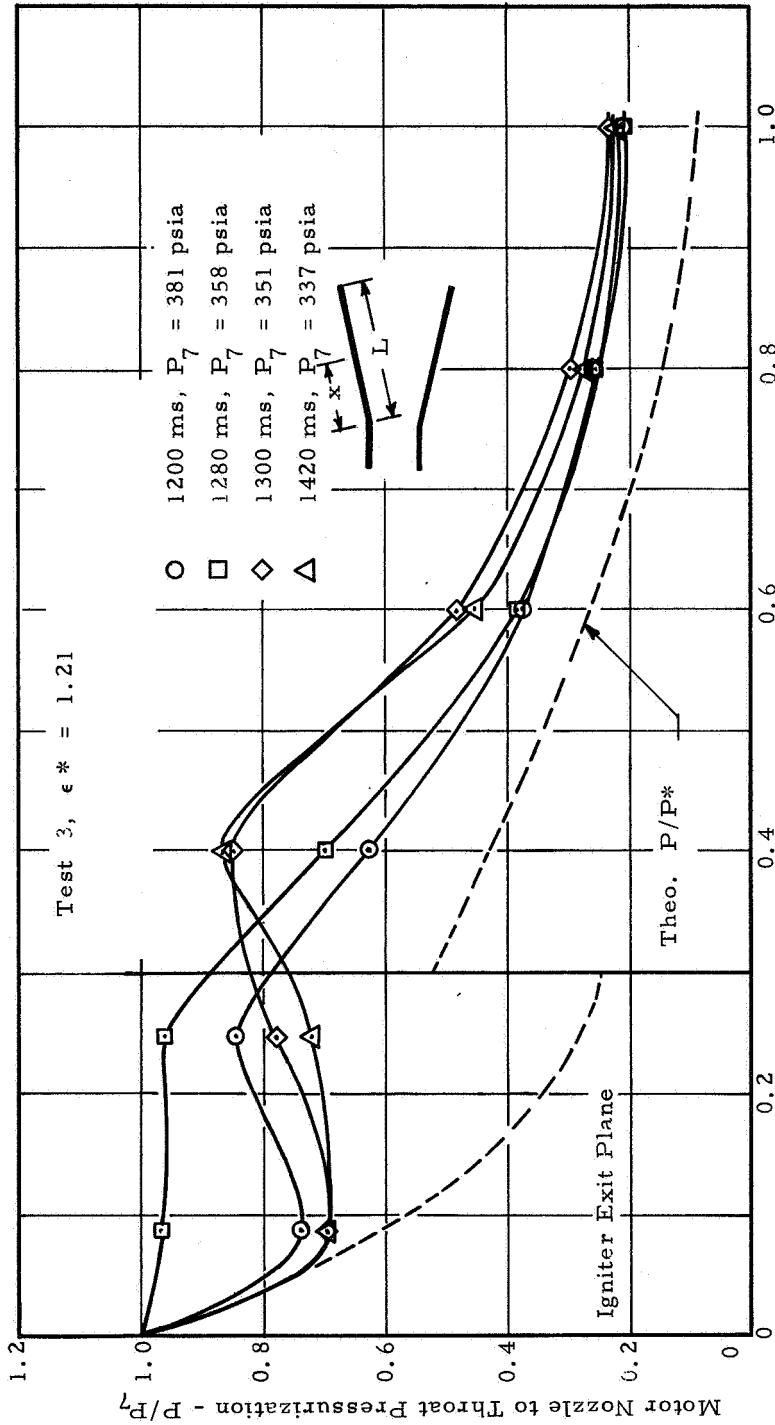


Figure III-88. Nozzle Wall Pressure Distribution, Test 6



Nondimensional nozzle wall distance, x/L .

Figure III-89. Nozzle Wall Pressure Distribution, Test 3

Test 8, $\epsilon^* = 1.54$

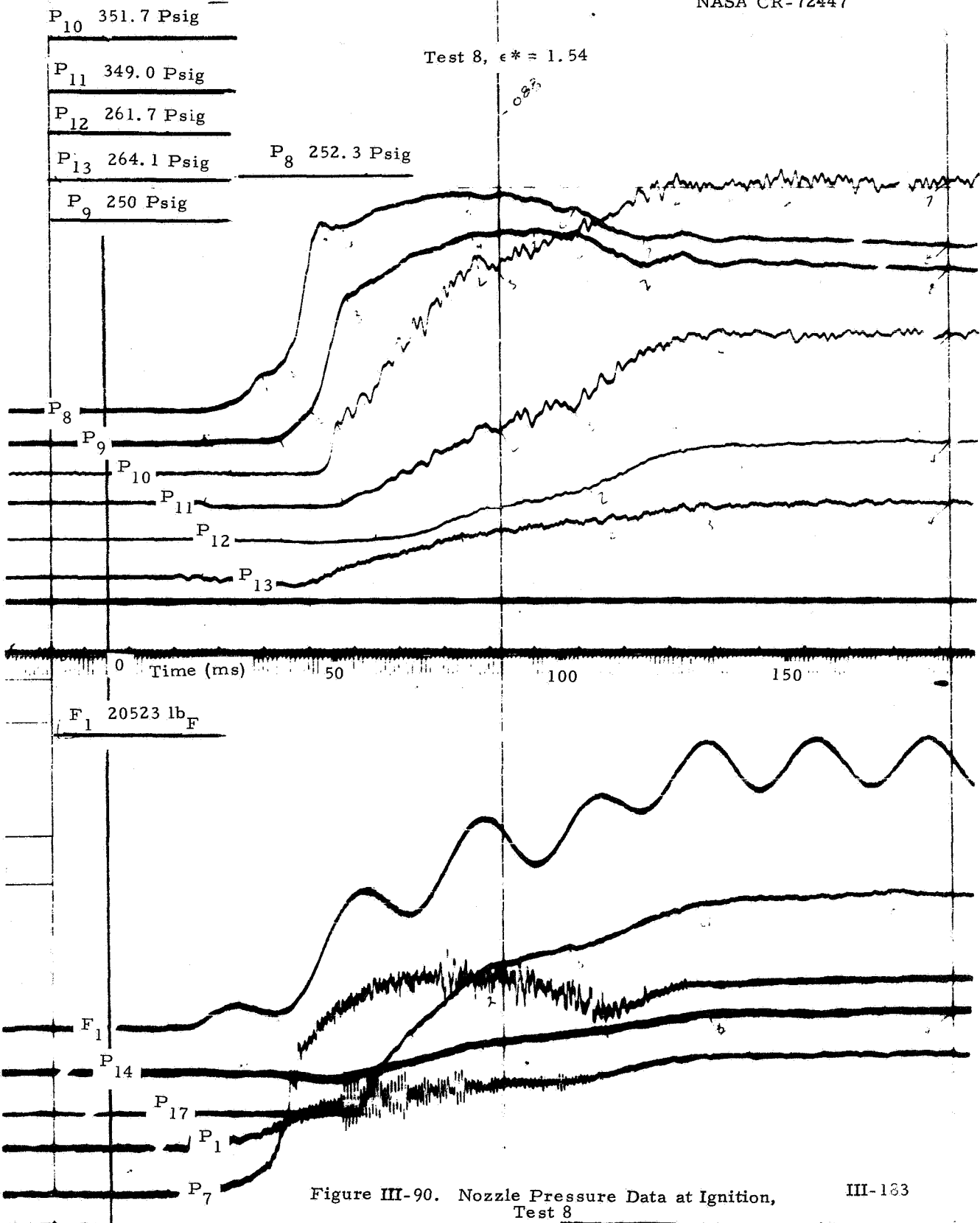


Figure III-90. Nozzle Pressure Data at Ignition, Test 8

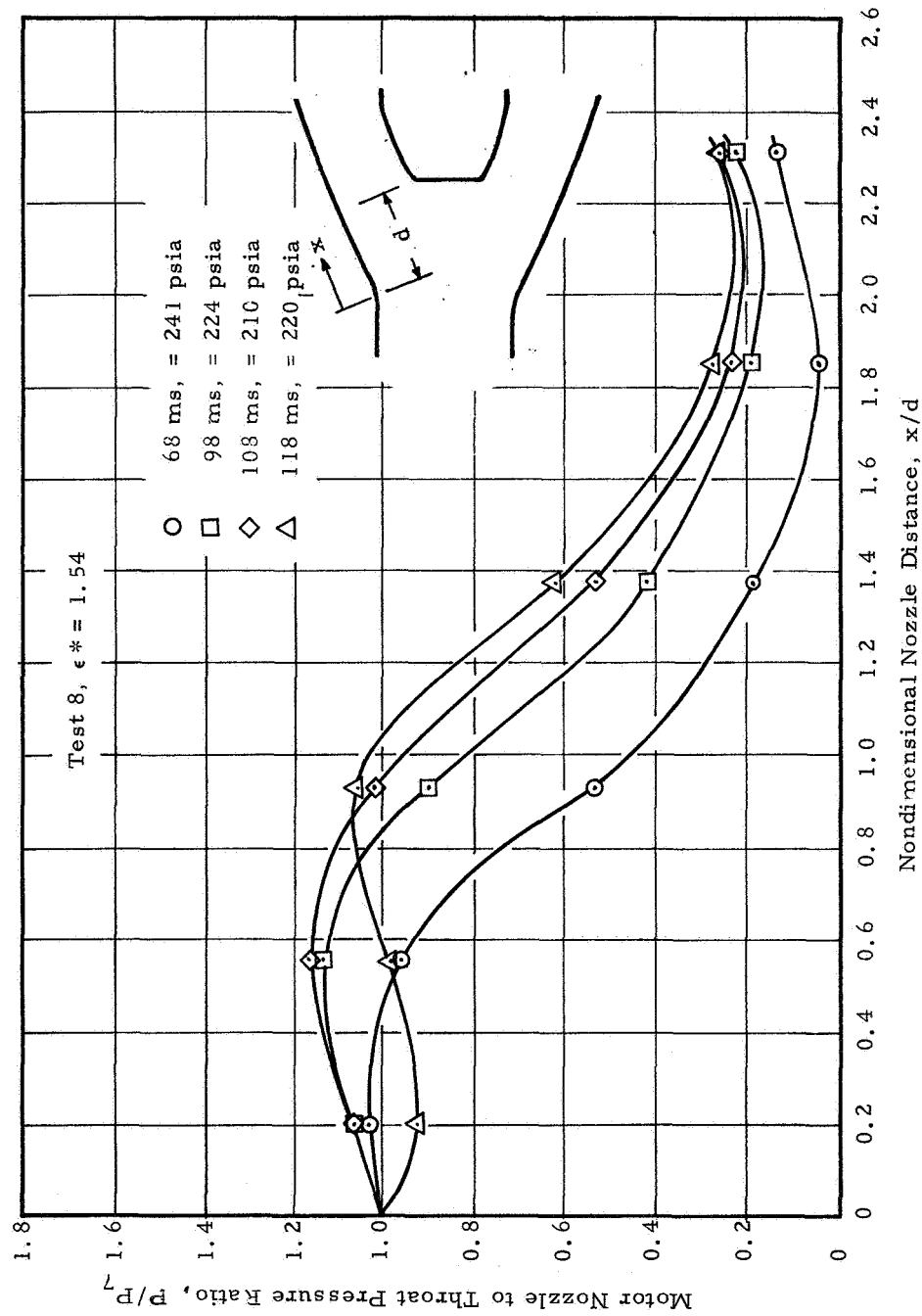


Figure III-91. Nozzle Wall Pressure Distribution, Test 8

The pressure distribution during typical pressure disturbance cycles in Test 8 are shown in figures III-92 through III-94. Figure III-92 presents the recorded nozzle pressure data and figures III-93 and III-94 show the plotted pressure distribution for selected times.

These previous data indicated that pressure disturbances with maximum pressures in excess of one and a half times the throat pressure were not unusual for some test conditions. Alternatively pressures only slightly higher than those which would be seen without igniter interference were noted for Test 1. Obviously high nozzle pressure levels and large pressure oscillations cannot be tolerated in weight limited systems. The igniter must be designed and placed to eliminate these nozzle pressure problems if aft-end ignition is to be feasible.

f. Slip Surface, Bow-Shock Location and Sonic Surface

Determination of the slip surfaces, bow-shock and sonic surface locations is helpful in visualizing the nozzle flow phenomena. Analysis of nozzle data indicated that the complex nozzle flow field was in most cases non-isentropic and featured mixed subsonic and supersonic flows. Because of these facts and limited nozzle instrumentation simplifying assumptions were required in order to approximate the slip surface, bow-shock and shifted sonic surface locations.

Two methods were used to obtain the location of the slip surface and bow-shock. The first which neglected shock effects, made use of isentropic flow relationships and the experimental nozzle pressure distribution to compute the slip surface and then the bow shock location. The second used the experimental pressure distribution to locate the vertex of the bow shock.

For cases of blocked flow, the location of both the new sonic surface and slip surface were computed. The slip surface as determined by method I was used to find the minimum flow area downstream of the motor throat and hence establish the approximate location of the new sonic surface.

Method I. In determining the slip surface a set of locations along the main motor nozzle were selected and the nozzle areas were completed at these locations as if the igniter was not present. From the graph of pressure vs. nozzle location, the pressure ratios (p/p_{tm}) were read and used to compute the (A/A_{tm}) values. The areas of flow were then calculated and the difference between the nozzle area and area of flow was used to obtain the radius of the slip surface.

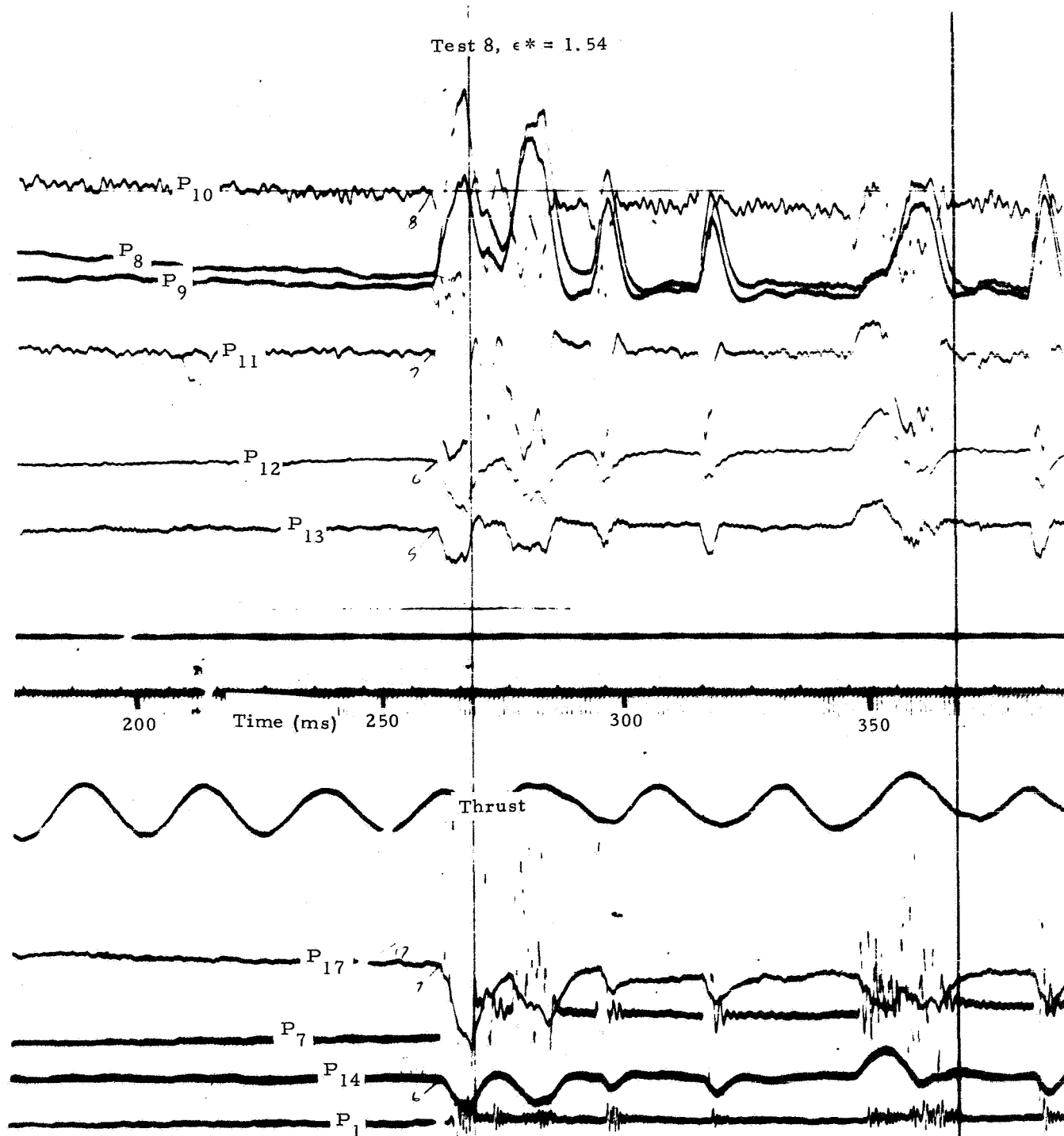


Figure III-92. Nozzle Pressure Data at Onset of Pressure Disturbances, Test 8

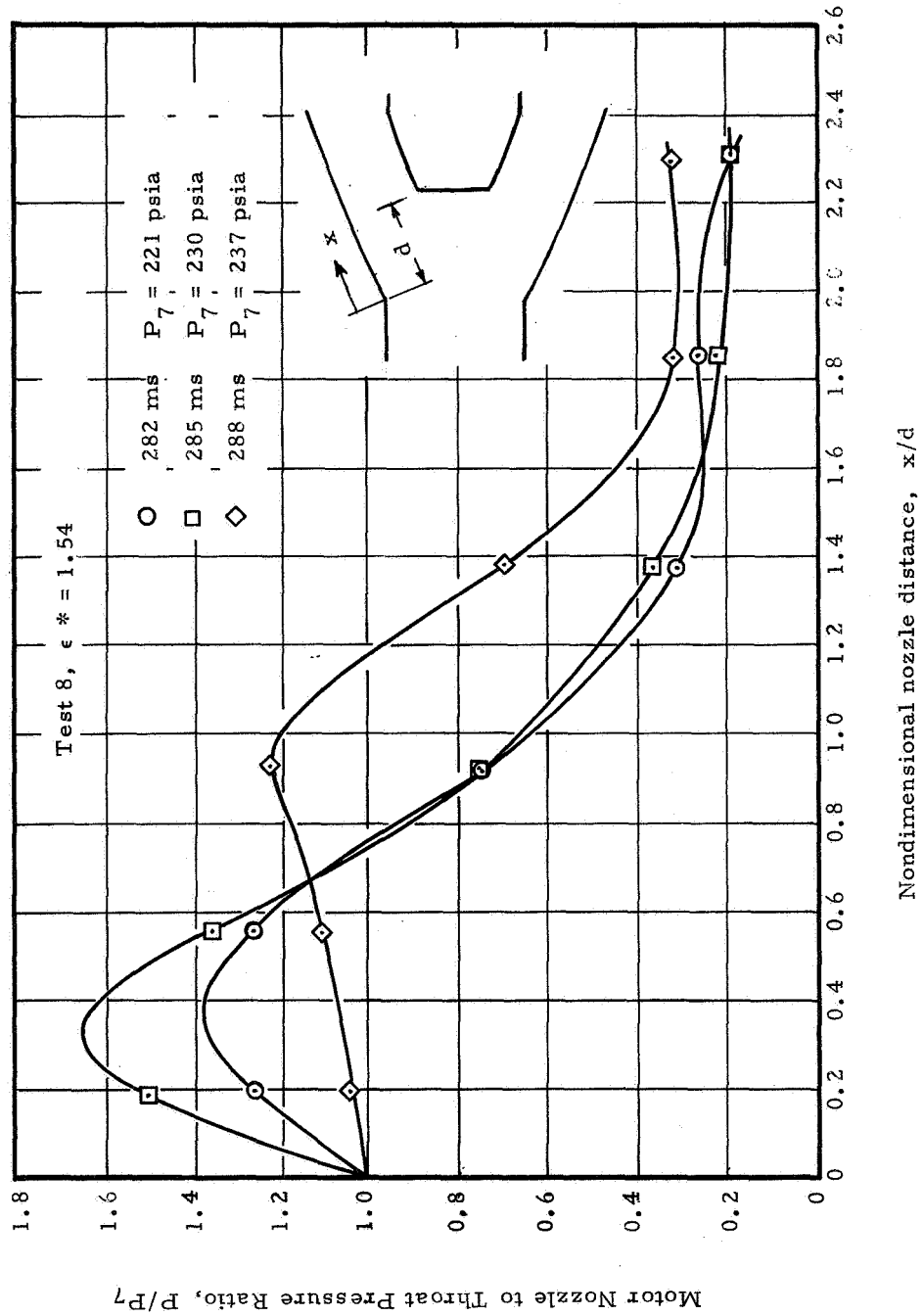


Figure III-93. Nozzle Pressure Distribution During Pressure Cycle, Test 8

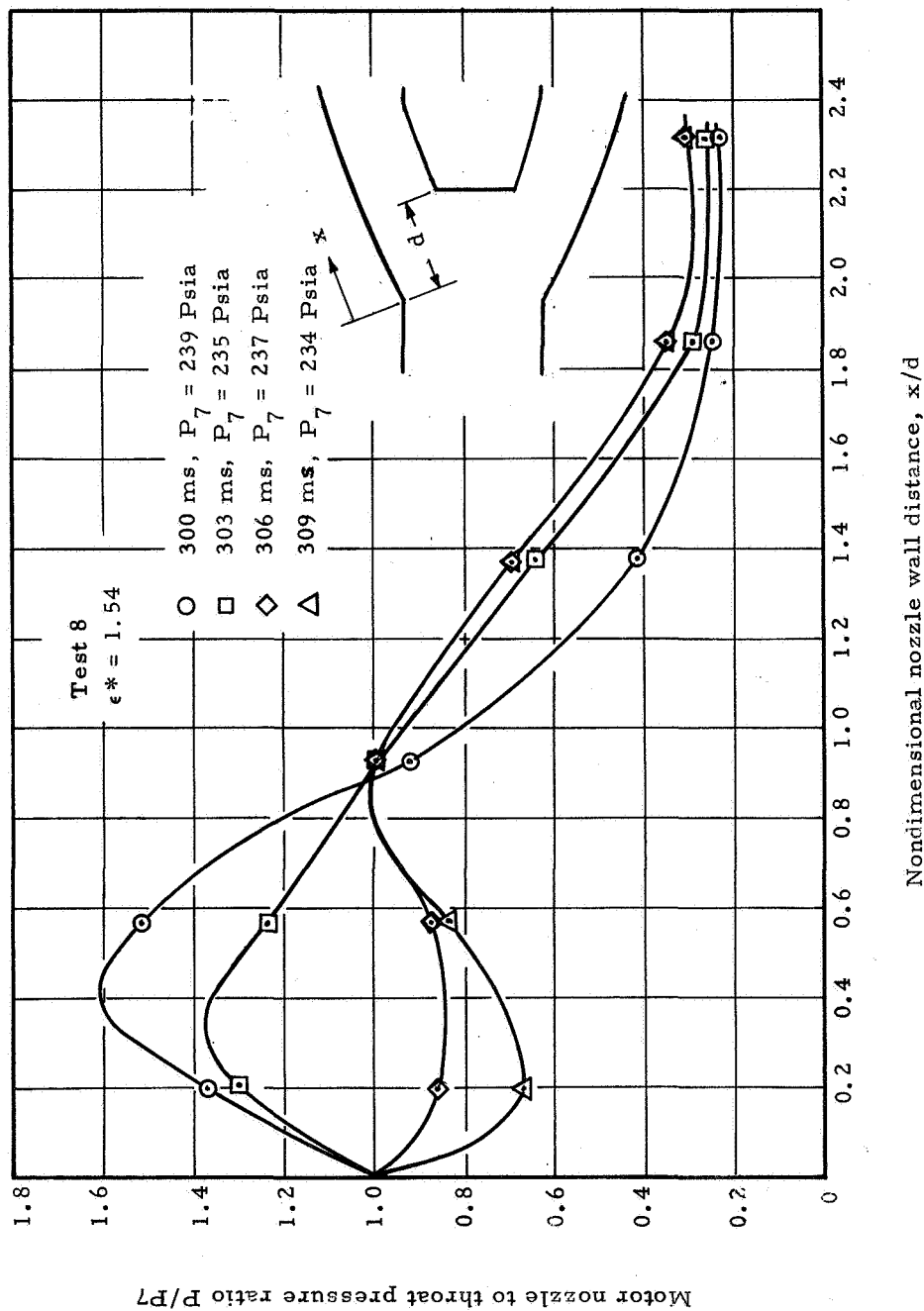


Figure III-94. Nozzle Pressure Distribution During Pressure Cycle (Cont'd), Test 8

To obtain the bow shock location, the main motor nozzle flow was considered to be at some free stream Mach number M_∞ which impinged upon the igniter jet body contained within the slip surface. A value for M_∞ was obtained by computing nozzle flow Mach numbers up to the slip surface by use of the nozzle pressure ratios, and by selecting the free stream Mach number value which presented the most reasonable bow shock wall intersection point. The bow-shock was approximated using the approximate method of locating detached shock waves given in reference 22.

Figure III-95 gives slip surfaces, at different times, as determined by this method, during Test No. 8. The upper half of the figure contains slip surfaces for unblocked conditions at three different P_i/P_m values. Notice that as P_i/P_m decreases the slip surface moves downstream towards the igniter, as expected. The slip surface for $P_i/P_m = 3.7$ is probably more accurate than the other slip surfaces since shock effects will be less for the surface which extends furthest into the motor nozzle.

The slip surface drawn in the lower half of figure III-95 is for blocking conditions and is shown in more detail in figure III-96. At the time for which this slip surface was determined oscillations were observed in the nozzle throat pressure indicating feed-back of the igniter induced pressure disturbances. This indicates that the effective throat or sonic surface area had moved downstream of the physical throat and that the motor was operating in a blocked mode.

Figure III-97 shows the bow-shock obtained for the case of $P_i/P_m = 3.02$ along with the associated nozzle pressure distribution. In this case, M_∞ was taken to be 1.61. Although shock locations and shapes were also computed for $M_\infty = 1.7$ and $M_\infty = 1.5$, the value of $M_\infty = 1.61$ was most reasonable since the location of the shock impingement on the wall was nearest the observed nozzle pressure peak.

Method II. The pressure trace along the nozzle wall defines the quantities needed to determine the shock location. Figure III-97 shows pressure versus nozzle sensor location in which the pressure goes through a minimum around sensor P_8 , passes through a maximum near P_{10} and then decreases. The dotted line was drawn to show the probable behavior of the actual pressure. The minimum in the dotted line was taken as the minimum pressure before the bow shock and the maximum was taken to be the maximum pressure after the shock. The total pressure of the motor, P_m , was computed from the pressure at taps P_1 and P_5 from the formula:

$$P_m = (P_1 + P_5)/2$$

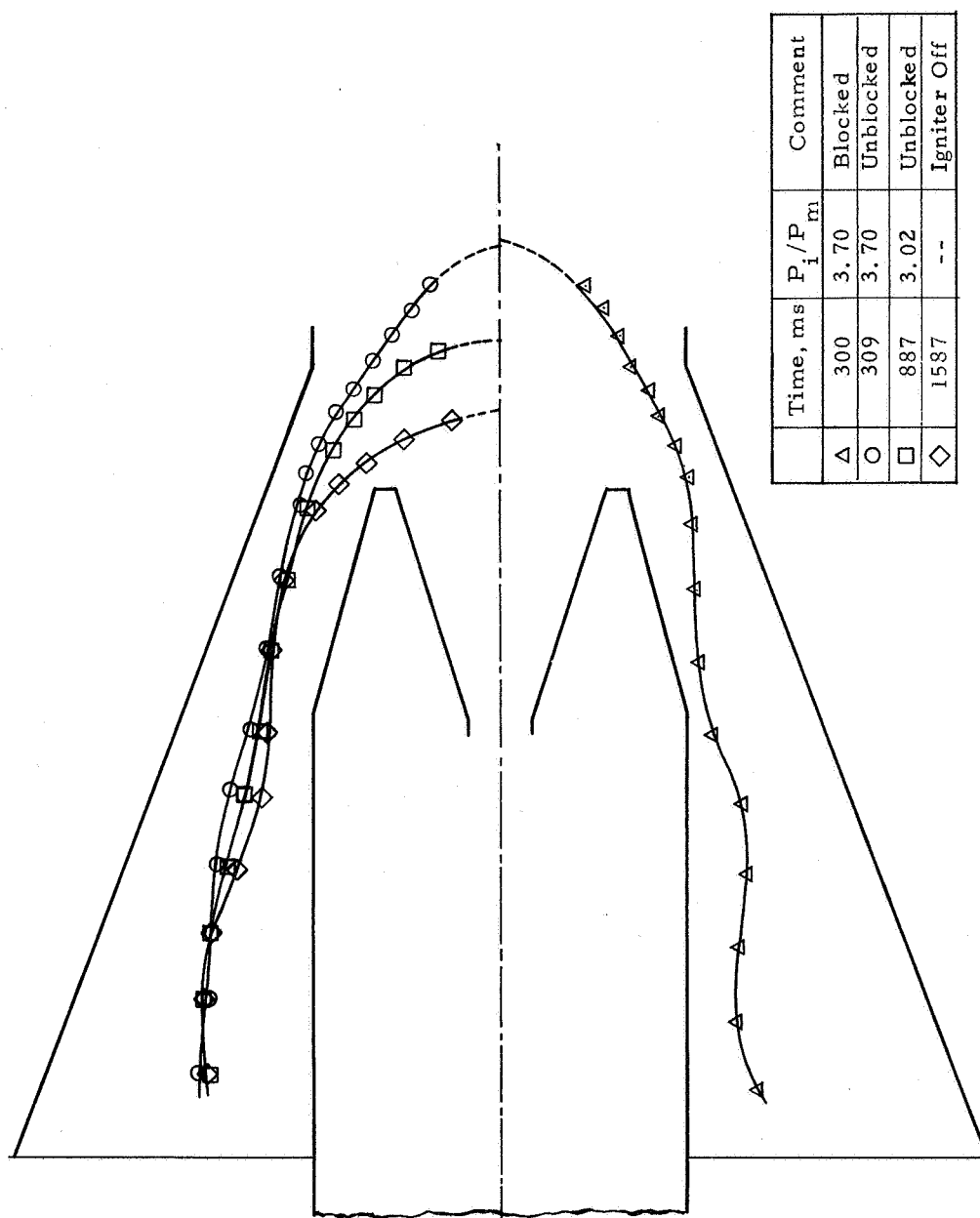


Figure III-95. Typical Slip Surfaces, Test 6

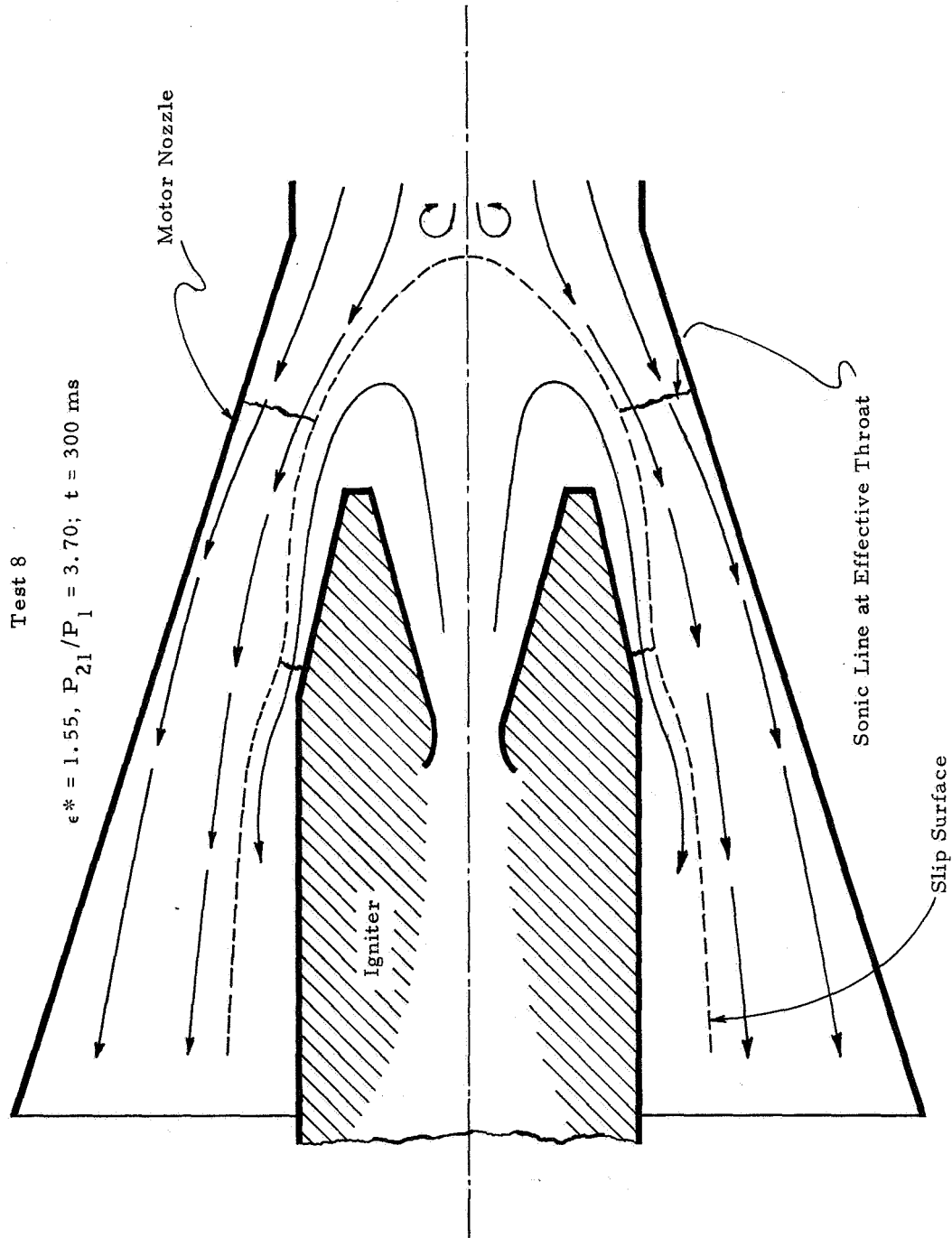


Figure III-96. Igniter and Motor Nozzle Streamlines, Slip Surface and Sonic Surfaces, Test 8

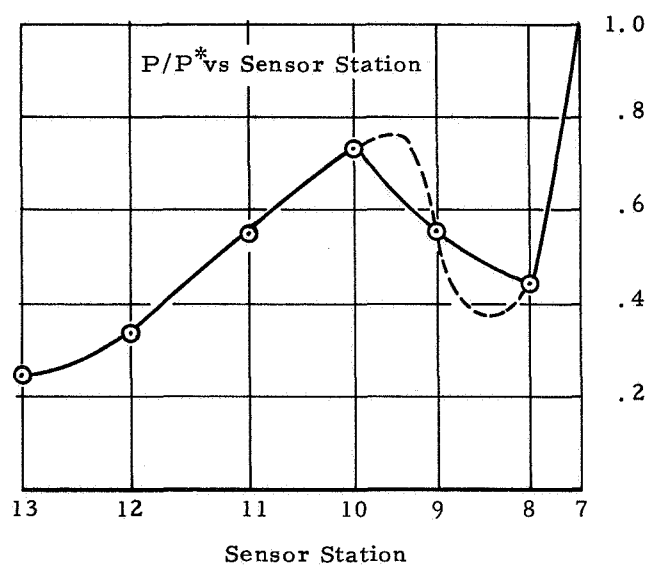
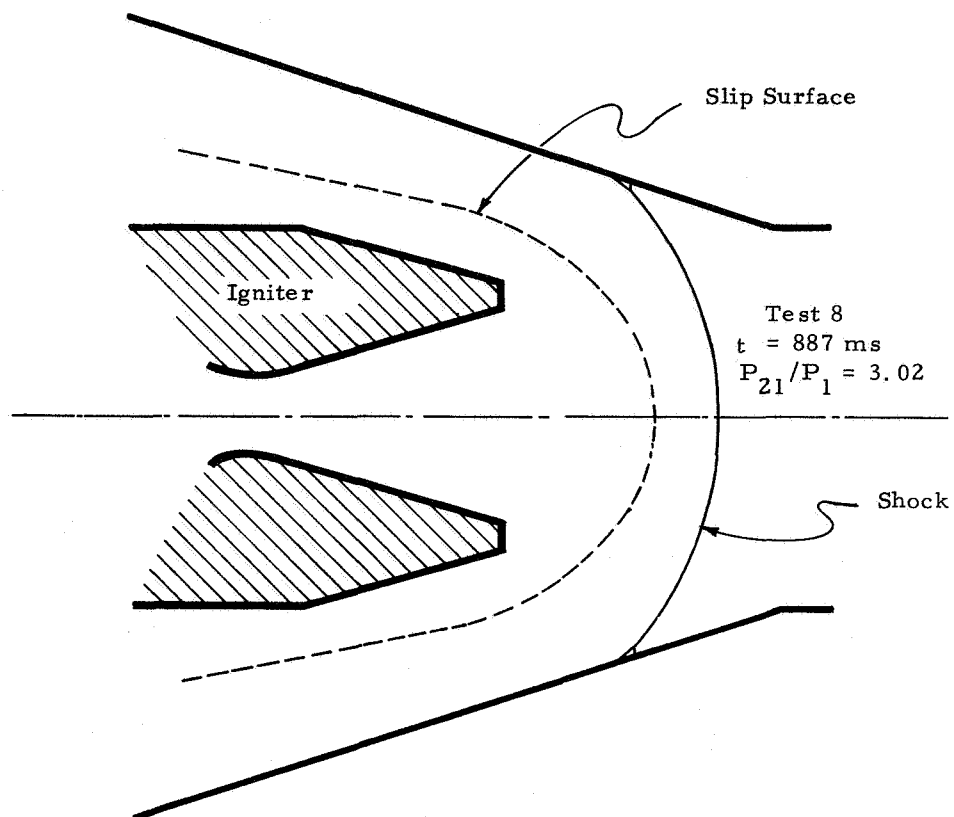


Figure III-97. Bow Shock, Slip Surface and Nozzle Pressure Distribution, Test 8

The pressure ratio p_{\min}/P_m was then used to determine M_{∞} , the free stream Mach number of the flow at the shock. The ratio P_{\max}/P_{\min} was related to M_{∞} through the formula:

$$P_{\min}/P_{\max} = M_{\infty} \sin \sigma$$

where σ is the shock angle at the wall. In terms of the notation in reference 22, y was used for the radius from the axis of the flow to the point on the wall where the shock impinges. Assuming the shock to be a hyperbola, the quantities y , σ and

$$\beta = \sqrt{M_{\infty}^2 - 1}$$

were used to compute the shock vertex location using the equations on page 884 of Reference 22.

Having located the shock vertex, the sonic points on the shock were computed, and the sonic points on the slip surface were computed with the other relations as given on pp. 884-885 of Reference 22.

The second method gives only two points on the slip surface, and, for that reason, is less desirable than the first. It has the advantage, however, of not assuming the shock to be insignificant in determining the slip surface.

There is one difficulty in the application of this method in that the pressure trace was not known well enough to locate the pressure shock peak impingement position. In order to find the peak, an interpretation of the pressure data was drawn in as shown by the dotted line on the pressure trace in figure III-97. It is considered that this interpretation of the data was more correct than the solid line for purposes of locating the shock.

Figures III-98 and III-99 show the bow shocks found by Method II. The slip surface points were determined for only one case and for that case the results were not realistic. Figure III-98 shows that the ϵ^* value has a large effect upon the bow shock for the same igniter flow. Movement of the igniter from $\epsilon^* = 1.55$ to $\epsilon^* = 1.79$ moves the bow shock downstream about as far as the igniter is moved. The effect of igniter flow, upon bow shock location is shown in figure III-99. As expected, the bow shock for the igniter-off condition moved downstream from the shock location for $P_i/P_m = 6.22$.

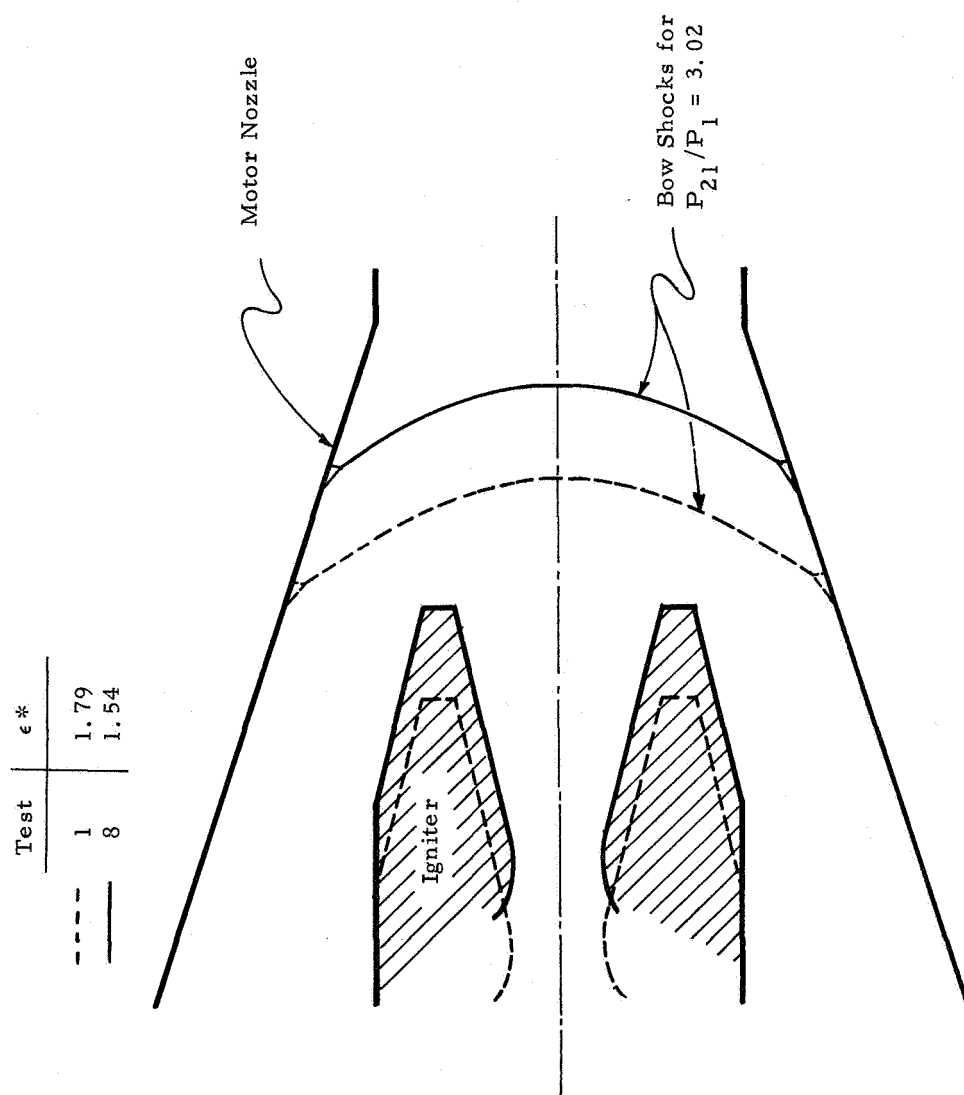


Figure III-98. Effect of ϵ^* on Bow Shock Location, Test 8

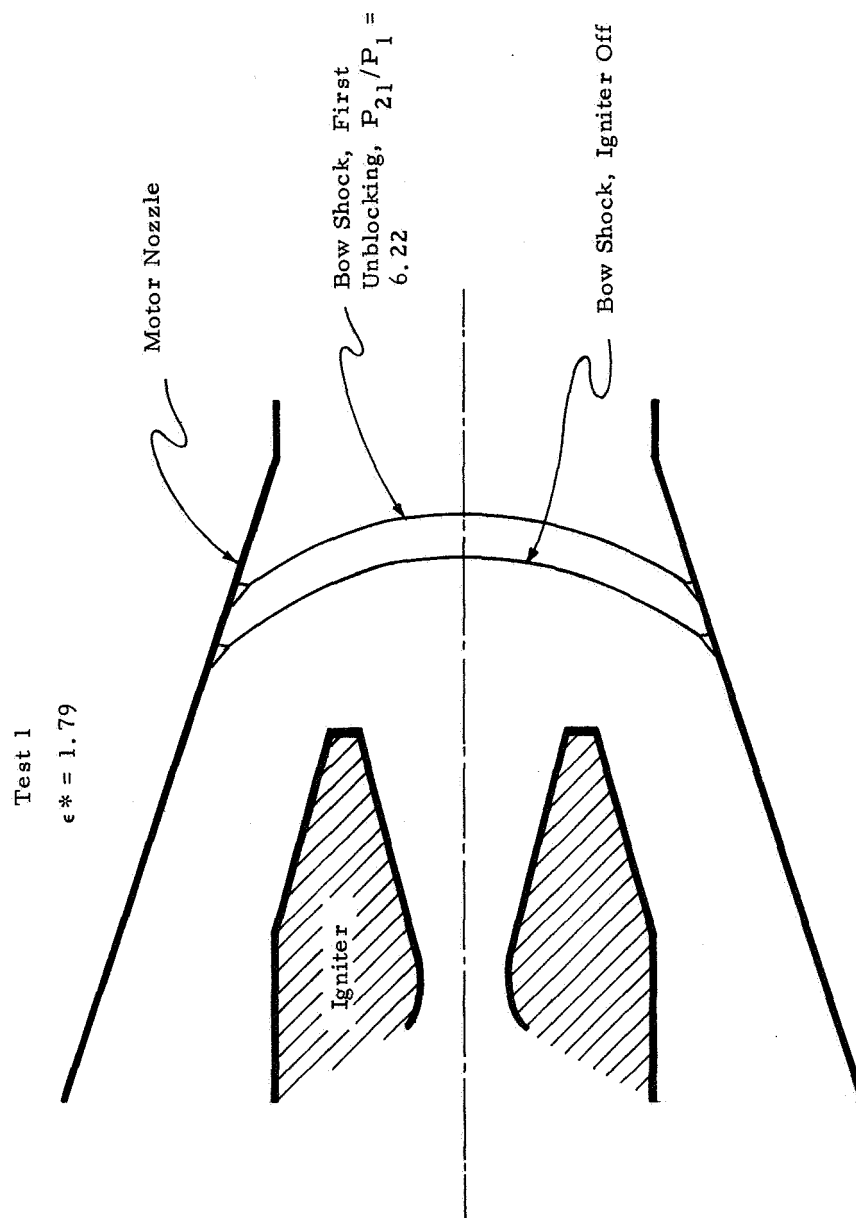


Figure III-99. Effect of Igniter Flow on Bow Shock Location, Test 8

The two methods give comparable results for the bow-shock determined for Test 8 with $P_i/P_m = 3.02$, as shown in figures III-97 and III-98, although the values for M_∞ differed. For Method I, it was determined to be 1.61; and for Method II, it was 1.77.

Pressure traces were also investigated to determine if there were any significant effects downstream of the bow-shock, on the nozzle pressures due to bow-shock reflections. Typical nozzle pressure behavior at three different times during Test 8 is shown in figure III-100 for three different igniter flows. The peak in the pressure ratio, which locates the bow-shock impingement point, is followed by a pressure ratio dropoff at increasing distances down the nozzle. After the peak, the P/P_7 curves converge together and are very nearly the same at taps P_{14} and P_{15} . At tap P_{13} or $x/L = 2.3$, there was a point where the curves diverged somewhat and this may be due to the changing bow shock reflections because of the changing igniter flows. Below this point, the pressure differences were small (on the order of 10 psi). Overall, these curves seem to suggest that pressures downstream of the bow-shock were not significantly affected by bow-shock reflections.

g. Nozzle Side Forces

Axial flow field oscillations occurring during the blocking modes may be accompanied by lateral or peripheral nozzle pressure gradients which can produce nozzle side forces. With one exception, the pressure taps were all on one side of the nozzle, hence detailed knowledge of the asymmetrical distribution was not possible. However, the one exception, pressure tap P_{10} at 90° to the others, clearly indicated that a degree of asymmetry existed. Further, the pressure distribution asymmetry was consistent with the previously discussed postulation of lateral movement of the igniter jet during igniter flow nozzle separation. Such lateral movement would affect the flow and render the pressure distribution on the nozzle wall asymmetrical.

To approximate the degree of side forces which were experienced, the side force due to a worst case asymmetrical distribution was calculated by comparison of the axial pressure distributions at the peak of an oscillation and at its ebb. These pressure forces were assumed to be acting at opposite sides of the nozzle at the same time. Further the pressure was assumed to vary linearly from one side of the nozzle to the other.

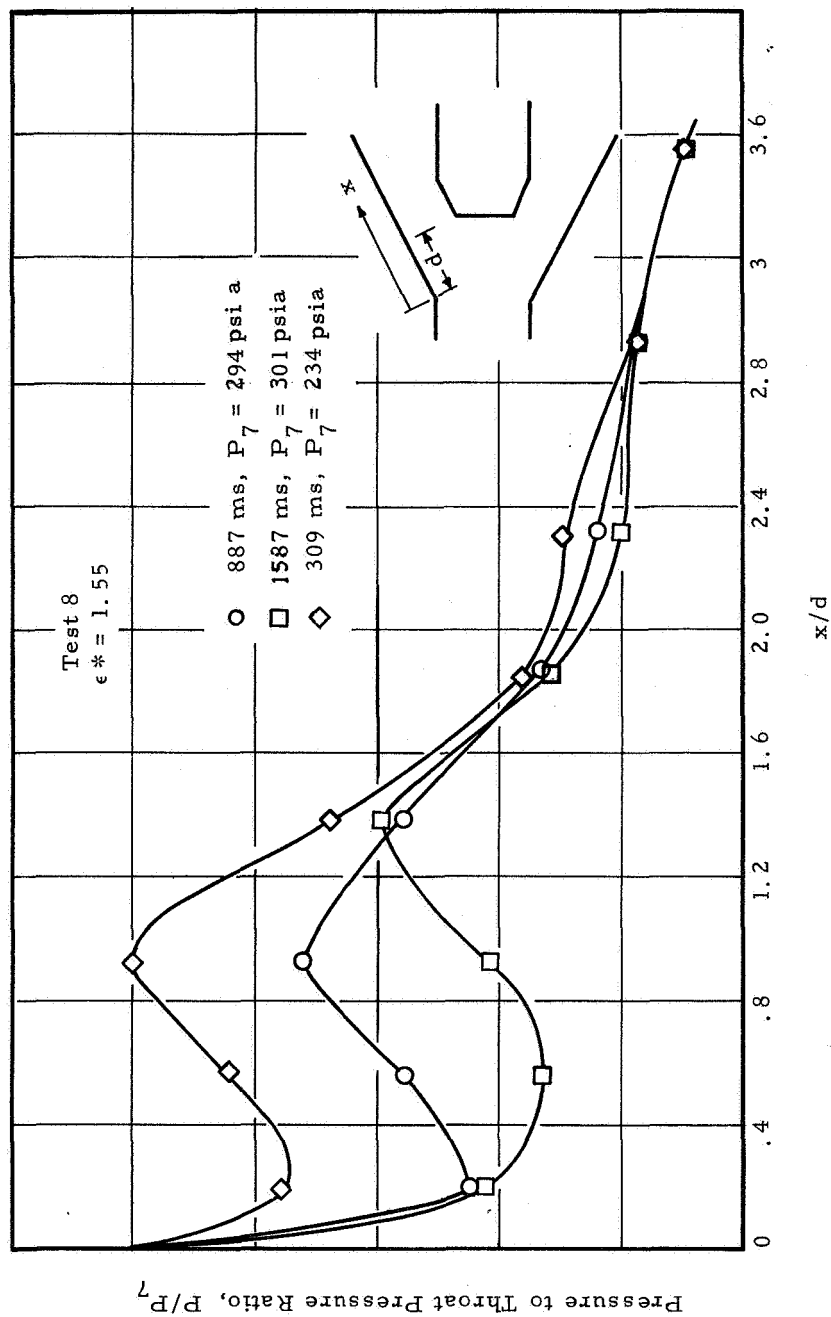


Figure III-100. Nozzle Pressure Distributions at Selected Times, Test 8

The net lateral side forces calculated by this method were not severe but the assymmetrical side forces probably produce bending moments in the nozzle which may require special design considerations. The method of analysis used for approximating the nozzle side forces are presented in the following paragraphs.

Method of Analysis

If ϕ is the angular coordinate varying from 0 to π around the nozzle and p_{\max} is the pressure at the peak, and p_{\min} the pressure at the ebb, then the pressure at any ϕ is:

$$p = p_{\max} + (p_{\min} - p_{\max}) \phi / \pi \quad (1)$$

Letting x be the coordinate varying along the length of the nozzle, the force per unit length acting laterally at x would be:

$$\frac{dF}{dx} = 2 \int_0^{\pi} p(x) \mu(x) \cos \phi d\phi \quad (2)$$

where:

- F = force per unit length at x ,
- p = pressure at x and ϕ ,
- μ = radius of nozzle at x ,
- $\cos \phi$ = factor to obtain the component of force acting in $\phi = 0$ direction.

Replacing $p(x)$ by (1) and integrating with respect to ϕ one obtains:

$$\frac{dF}{dx} = \frac{4}{\pi} (p_{\max} - p_{\min}) \mu(x) \quad (3)$$

One can obtain the total lateral force by integrating with respect to x :

$$F = 4/\pi \int_0^L (p_{\max} - p_{\min}) \mu(x) dx \quad (4)$$

where:

- L = length of nozzle

Formulas (3) and (4) were evaluated for an oscillation occurring during Test 8 when blocking was of the third mode. The pressure distribution was found at 300 ms, the peak of the oscillation, and also at the ebb,

9 ms later. The pressure traces are shown in Figure III-94. Note that the curve at 300 ms has a higher peak than the curve at 309 ms, but crosses over and falls below after x/L reaches 0.9.

The loading function, dF/dx , was calculated and shown in figure III-101. The loading becomes rather high, 218 lb/in near the throat at the nozzle and then changes sign and decreases as one moves along the nozzle. The net lateral force on the nozzle is 97.8 lb which by itself does not appear to be excessive. However, the local asymmetric loading may produce severe bending moments in the nozzle case, requiring special design consideration. It is emphasized that the "worst case" selected for this evaluation on the basis of these tests may not in fact, be the most severe distribution. Any future work should provide extensive peripherally located instrumentation in order to accurately measure the rotational and axial pressure distribution.

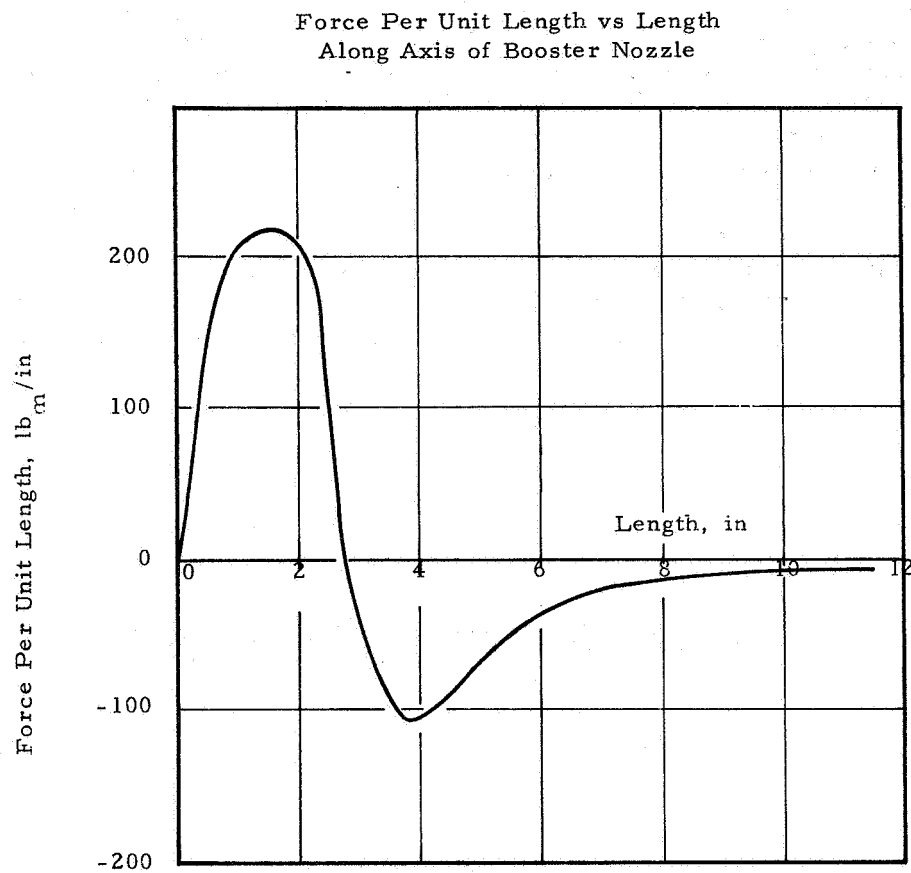


Figure III-101. Nozzle Wall Force Distribution

IV. CONCLUSIONS AND RECOMMENDATIONS

The aft-end ignition program was satisfactorily completed without major technical difficulties. Primary accomplishments of the program were:

- (1) Development of a successful analytical model for predicting nozzle blockage and overpressurization.
- (2) Development of an analytical model predicting the jet penetration phenomena and a computer program framework for solution of the model.
- (3) Development of igniter design parameters which provide full jet penetration in high L/D motors and which result in ignition intervals equal to or better than comparable head-end igniters.
- (4) Satisfactory aft-end ignition of nine (9) solid propellant rocket motors and determination of their blockage and overpressurization characteristics.
- (5) Discovery and evaluation of previously unreported oscillations of significant magnitude in the motor nozzle pressure, caused by interaction between the fully developed igniter and main motor flows.

The general conclusions and recommendations from this program should be considered quantitatively valid, except in those circumstances where analysis has clearly indicated that the flow field phenomena cannot be scaled to the dimensions applicable to 260" solid motors.

A. CONCLUSIONS

1. Jet Penetration, Ignition and Flame Propagation

The successful ignition of all 9 tests and the consistency of the ignition sequences over a wide variation of igniter location and mass flux clearly demonstrated that satisfactory, repeatable ignition by a fixed position aft-end igniter can be accomplished without overpressurization.

Furthermore, the following conclusions have been drawn concerning the ignition effects of the igniter parameters:

a. No jet penetration limitations were found to occur for the values of igniter mass flow parameters tested, contrary to previously reported programs. Penetrations ranged from 30% at a w/A of $0.2 \text{ lb}_m/\text{sec-in}^2$ to 100% at a w/A of $0.5 \text{ lb}_m/\text{sec-in}^2$. The high penetrations achieved resulted from the high momentum characteristics of the igniter jets which were produced by careful igniter design, i. e., high igniter total pressure and expansion to near ambient conditions.

b. The ignition interval was strongly influenced by the igniter mass flux level. The rate of chamber pressure rise, the time to first ignition and the rate of flame propagation were all favorably effected by increasing w/A . Measured ignition intervals varied from 70 ms to 200 ms.

c. The igniter ϵ^* effects were not as significant as those of w/A , and were limited to the rate of chamber pressure increase and flame propagation. No effects on first ignition time were noted.

2. Nozzle Flow Field Interactions

The nozzle flow field interactions were found to be greatly dependent upon igniter placement and mass flow. In addition, previously unreported and unexpectedly severe oscillations which pose potentially serious problems for flight systems were encountered in these interactions. Because the instrumentation provided for these tests was not adequate to positively determine the structure, origin and effects of the oscillations, the following conclusions must be regarded as somewhat conditional pending further testing.

a. Several nozzle flow interaction modes exist. They are characterized by different igniter and motor nozzle pressure distributions which may be either steady or highly oscillatory in nature. It is postulated that four nozzle flow interaction modes exist and that they correspond to operation of the igniter nozzle in four overexpanded nozzle flow regimes. The origin of the nozzle pressure oscillations which characterize two of the nozzle flow modes have not been positively identified; however, it is believed that the oscillations originate in the nozzle flow operating regimes.

b. Motor overpressures occur at high igniter mass flows and low ϵ^* values. Peak average overpressures of 36% were observed. Certain runs exhibited no discernible average chamber overpressures.

c. The analytical model for blockage correlates well with the data in predicting qualitative trends in blockage. More importantly, it provides threshold values at a given ϵ^* , of igniter to motor flow rates (or chamber pressure ratios) below which overpressure will not occur.

d. The measured wall pressure distribution, which has been incorporated into this model, may be subject to Reynolds number effects in the shock-boundary layer interactions. Therefore, the results of this model should be applied to the 260" motor with conservatism.

B. RECOMMENDATIONS

The following recommendations pertain specifically to the aft-end ignition of the 260" motor but they also apply to the technology in general:

1. Ignition

a. Analytical

The formulation and checkout of the ignition computer program should be continued to completion. This program has the prospect of becoming a valuable tool for the qualitative and quantitative investigation of aft-end ignition events under different conditions of size, configuration, and igniter flow parameters. It will have special importance in quantitatively defining 260" ignition characteristics.

b. Experimental

No further axially aligned subscale testing for the 260" motor, oriented toward ignition, is necessary. Sufficient data exists from the current program to provide for analytical model correlation. Additional evaluation of these data is necessary, however, particularly with respect to the correlation and refinement of the heat transfer data.

Additional testing of the ignition events using a misaligned igniter is recommended.

2. Nozzle Interactions

a. Experimental

It is recommended that additional extensively instrumented experiments be conducted to further characterize the multiple mode

nozzle flow interactions and isolate the trigger mechanisms which produce the nozzle pressure oscillations. These studies should be performed first with axially aligned igniters, and then with misaligned igniters. The apparatus should be instrumented to measure both axial and transverse or peripheral pressure distributions along the main nozzle, within the igniter nozzle, and along the igniter after-body within the main motor nozzle exit cone. The effects of igniter location and resulting back pressure, nozzle expansion ratio and contour, and igniter total pressure and flow rate on the interactions should be evaluated. In addition, elimination of the igniter jet instability by use of artificial means to induce clean igniter nozzle flow separation should be explored.

b. Analytical

Studies to develop analytical models of the nozzle flow interactions should be coupled with experimental work to characterize the fundamental mechanisms and flow phenomena involved.

In the event that additional experimental studies are not undertaken in the near future, more rigorous and detailed analysis of the existing data from this program and other sources should be pursued. It is believed that additional insight into the problems can be gained through the application of sophisticated analyses which were beyond the scope of this program.

REFERENCES

1. Fullman, C. H. and F. B. Nielsen, "(U) Theoretical and Experimental Investigations of Ignition Systems for Very Large Solid Propellant Motors," United Technology Center UTC 2012-FR2, Contract AF04(611)-7559, 8 May 1963, (CONFIDENTIAL)
2. Aerojet General Corporation "Final Report Aft-End Ignition-Large Solid Rocket Program - Phase II", Contract No. AF04(611)-8012, Program No. 623A (Report No. SSD-TDR-62-103).
3. Aerojet General Corporation, "Final Phase Report 260-In. -Dia. Motor Feasibility Demonstration Program, Vol. I, 260-SL Motor Aft-End Ignition System Development", Contract No. NAS3-6284.
4. Bretting, Maj. M. and Lt. W. Niessen, "The Study of an Ignition Technique for Large Solid Rocket Motors," 11th Annual AFSC Science and Engineering Symposium, Brooks, A.F.B., 20-22 October 1964.
5. Salmi, R. J., "Compressed Air-Model Investigation of Solid Rocket Overpressures Due to Interference from Aft-End Ignition Rocket," NASA TND-3537, August 1966.
6. Plumley, A. G., "Development of an Analytical Model to Determine Aft-End Igniter Design Parameters," Aerojet-General Corporation Technical Paper 136 SRP, Contract AF04(695)-350, March 1964.
7. Carlson, L. W., and J. D. Seader, "A Study of the Heat Transfer Characteristics of Hot Gas Ignition", Final Report, June 1965, Air Force Rocket Propulsion Laboratory, Edwards, California.
8. Mullis, B. G., "Heat Transfer Studies of Solid Rocket Igniters", United Technology Center UTC 2096 FR, Contract NAS 7-302, September 1963.
9. Wrubel, J. A. and L. W. Carlson, "Study of Heat Transfer Characteristic of Hot-Gas Igniters", Technical Report AFRPL-TR-67, Rocketdyne, July 1967.
10. Kilgroe, J. D., "Studies on Ignition and Flame Propagation of Solid Propellants", United Technology Center, Final Report, Project 2229, August 1967.

11. Jensen, G. E. and D. A. Cose, "Studies in Ignition and Flame Propagation of Solid Propellants", United Technology Center Final Report, Contract NAS 7-329, October 1965.
12. Cose, D. A., "Aft End Ignition of Solid Propellant Motors", Technical Memo TM-11-66-U1, August 1966.
13. Abramovich, G. N., The Theory of Turbulent Jets, M. I. T. Press, Massachusetts, Cambridge Mass., 1963, pp. 444-452,
14. Ibid., pp. 452-459.
15. Howarth, L., "Concerning the Effect of Compressibility on Laminar Boundary Layers and Their Separation," Proceedings of Royal Society (London) Vol. 194, p. 16 (1948)
16. Schlichting, H., "Boundary Layer Theory," McGraw Hill, 4th Edition, 1960.
17. Channapragada, R. S., and J. P. Woolley, "Turbulent Mixing of Parallel Compressible Free Jets," AIAA Paper No. 65-606, AIAA Propulsion Joint Specialist Conference, Colorado Springs, June 1965.
18. Tollmein, W., "Berechnung der turbulenten Ausbreitungsvorgaenge," Zamm, 6, pp. 460-479, 1926 (also NACA TM 1085, 1945).
19. Romeo, D. J. and J. R. Sterrett, "Exploratory Investigation of the Effect of a Forward Facing Jet on the Bow Shock of a Blunt Body in a Mach 6 Free Stream" (NASA TN D-1605), Langley Research Center, February 1963.
20. Beyer, R. B., "Ignition of Solid Propellant Motors Under Vacuum", Final Report, Contract No. AF 04(611)-9701, United Technology Center, April 1965.
21. Nanigian, J., "Rocket Igniter Characteristics," Instrumentation and Control Systems, May 1967.
22. Fraser, R. P., Eisenklam, P., and Wilkie, D., "Investigation of Supersonic Flow Separation in Nozzles," J. Mech. Eng. Sci. 1, 267-279 (1959).

23. Arens, M. and E. Spiegler, "Shock Induced Boundary Layer Separation in Overexpanded Conical Exhaust Nozzles", AIAA Journal, Vol. 1, No. 3, March 1963.
24. Summerfield, M., C. R. Foster, and W. C. Swan, "Flow Separation in Overexpanded Supersonic Exhaust Nozzles", Jet Propulsion 24, 319-321 (1954).
25. Shapiro, A. F., The Dynamics and Thermodynamics of Compressible Fluid Flow (Ronald Press, New York, 1953), Vol. II, Pp. 140-141.

NASA CR-72447

APPENDICES

APPENDIX A

BLOCKAGE MODEL

A. SUMMARY

This appendix presents the analytical development of the blockage model in more detail than discussed in the body of the report. The control volume is described, the basic assumptions of the model are reiterated and the method of calculation of variables used in the momentum balance equation is shown. The assumptions regarding the pressure distributions are discussed, as well as modification of the model by the use of the empirically derived distribution along the main booster nozzle. The input and output of the program is described and the nondimensionalization of the calculations in the program are discussed.

The basic program calculates the pressure ratio P_i/P_m below which unblockage occurs, for a given ϵ^* and booster-igniter configuration. Here P_i = stagnation pressure of igniter and P_m = stagnation pressure of main motor. The program, however, can be modified to calculate the Mach no. at the throat M_t for given P_i/P_m and ϵ^* . In this method P_i/P_m and ϵ^* are selected and M_t is iterated upon until the mass and momentum equations are satisfied.

B. ANALYTICAL DEVELOPMENT

A control volume is set up as shown in figure A-1. The inlet and outlet boundaries of the volume are shown by dotted lines. The one dotted line "t" is across the booster throat. The dotted line "s"

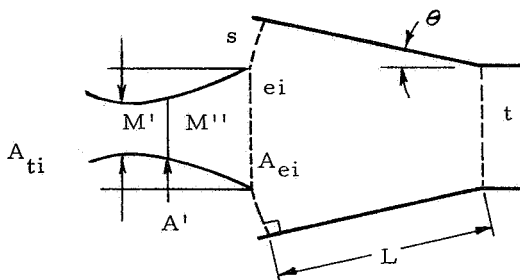


Figure A-1

extends from the normal booster wall to the exit plane of the igniter. The line "ei" is at the exit plane of the igniter.

The following assumptions are made about the flow into and out of the control volume:

- (1) To all gas flow one may apply one-dimensional isentropic perfect gas relations.
- (2) Flow at "t" is choked.
- (3) The stagnation pressure of the gas in the control volume is P_m . There exists, in the igniter nozzle, a normal shock which reduces igniter total pressure from P_i to P_m .
- (4) The flow into the volume, from the igniter at "ei" and from the motor at "t", passes out through the annular surface "s" with a supersonic Mach no. and in such a way that conditions (pressure and velocity) are uniform across "s".
- (5) Along the nozzle surface from "t" to "s" the pressure varies from the pressure at "t" to that at "s" according to:

$$(a) \quad p^2 = p_t^2 + x/L (p_s^2 - p_t^2)$$

where L = distance from "t" to "s" along the nozzle, and x is the coordinate from "t" to the point at which the pressure is evaluated. This is an analytical fit of Salmi's⁽⁵⁾ empirical pressure distribution data.

- (6) Along the plane "ei", it is assumed that the pressure varies from that at the axis of symmetry, p_i , to that at inner edge of the exit cone p_s , in the fashion,⁺

$$(b) \quad p = p_i (1 - 3\eta^2) + p_s (3\eta^2 - 2\eta^3)$$

+ While the pressure is assumed to vary over the igniter exit plane the velocity and Mach number at "ei" are assumed constant at average values V_{ei} and M_{ei} .

where $\eta = r/r_a$, and
 $r =$ coordinate radius,
 $r_a =$ inner radius of igniter nozzle exit plane .

The polynomial has the property that its maximum, p_i occurs at the axis of symmetry and its minimum, p_s , occurs at $\eta = 1$ with zero slope. Such a distribution seems reasonable because the pressure is expected to drop off from p_i , decaying continuously into p_s . The actual pressure distribution was not predicted or measured experimentally.

Using these assumptions, one calculates the momentum balance for the control volume at a given pressure ratio P_i/P_m . If this balance is satisfied, it is said that the booster is not blocked below this pressure ratio. For practical calculations the momentum balance is computed as a function of P_i/P_m and at the point where the momentum balance passes through zero, a linear interpolation is made to obtain the value of P_i/P_m at which unblockage occurs.

The steps of a calculation of the momentum balance is started by setting the values of $M_t=1$ and ϵ^* at a designated value and by selecting an initial value of P_i/P_m for iteration. Then p_{ei} , V_{ei} , M_{ei} , w_{ei} , or pressure, velocity, Mach no. and mass flow at "ei" are obtained. To calculate the Mach no. M' at which the igniter shock occurs, the formula used is:

$$\frac{P_m}{P_i} = \left[\frac{(\gamma+1)M'^2}{(\gamma-1)M'^2 + 2} \right]^{\frac{\gamma}{\gamma-1}} \left[\frac{\gamma+1}{2\gamma M'^2 - (\gamma-1)} \right]^{\frac{1}{\gamma-1}} \quad (1)$$

M' is obtained by inversion of (1). Next the Mach no. after the shock is calculated by the formula:

$$M''^2 = \frac{(\gamma-1)M'^2 + 2}{2\gamma M'^2 - (\gamma-1)} \quad (2)$$

The area at the shock is given by:

$$A' = A_i^* \left[\left(\frac{\gamma+1}{2} \right)^{\frac{\gamma+1}{2(\gamma-1)}} M \left(1 + \frac{\gamma-1}{2} M^2 \right)^{-\frac{(\gamma+1)}{2(\gamma-1)}} \right]^{-1} \quad (3)$$

where A_i^* is area of igniter throat.

The area of the effective throat (A_{eff}^*) for which the flow at A' is M'' is given by:

$$A_{eff}^* = A' \left[\left(\frac{\gamma+1}{2} \right)^{\frac{\gamma+1}{2(\gamma-1)}} M'' \left(1 + \frac{\gamma-1}{2} M''^2 \right)^{-\frac{(\gamma+1)}{2(\gamma-1)}} \right] \quad (4)$$

Now, since the igniter exit area (A_{ei}) is known, the effective Mach number, M_{ei} , at the exit plane is obtained by inverting the formula:

$$\frac{A_{eff}^*}{A_{ei}} = \left(\frac{\gamma+1}{2} \right)^{\frac{\gamma+1}{2(\gamma-1)}} M_{ei} \left(1 + \frac{\gamma-1}{2} M_{ei}^2 \right)^{-\frac{(\gamma+1)}{2(\gamma-1)}} \quad (5)$$

With the Mach no., M_{ei} , one may calculate p_{ei}/P_m , V_{ei} , and the flow through the igniter, w_{ei}

$$p_{ei}/P_m = \left(1 + \frac{\gamma-1}{2} M_{ei}^2 \right)^{-\frac{\gamma}{\gamma-1}} \quad (6)$$

$$(V_{ei}/a_{io})^2 = M_{ei}^2 \left(1 + \frac{\gamma-1}{2} M_{ei}^2 \right)^{-1} \quad (7)$$

$$W_{ei} = A_{ei} \sqrt{\frac{\gamma}{R T_o}} P_{ei} M_{ei} \left(1 + \frac{\gamma-1}{2} M_{ei}^2 \right)^{1/2} \quad (8)$$

where a_{io} is the velocity of sound at the igniter and motor stagnation temperature T_o . These calculations give all the desired quantities across section "ei".

Calculation of the main motor flow properties across "t" can be made using the fact that the sonic condition is assumed to exist at the motor throat. Hence $M_t = 1$ and p_t , $V_t = V_m^*$ and w_m are computed as below:

$$\frac{p^*}{p_m} = p_t/p_m = ((\gamma + 1)/2)^{\frac{-\gamma}{\gamma - 1}} \quad (9)$$

$$\left(\frac{a_m^*}{a_{m_0}} \right)^2 = (V_m^*/a_{m_0})^2 = ((\gamma + 1)/2)^{-1} \quad (10)$$

$$w_m = A_{m_t} \sqrt{\frac{\gamma}{R T_0}} p_m^* ((\gamma + 1)/2)^{1/2} \quad (11)$$

where A_{m_t} is the throat area of the main motor and a_{m_0} is the sonic velocity corresponding to the motor total temperature.

Finally, the conditions across "s" are computed. From assumption (3), one has a flow of w_s given by

$$w_s = w_i + w_m \quad (12)$$

This flow is related to the Mach no. at "s", M_s , and the resulting formula is inverted to get M_s .

$$w_s = A_s \cdot \sqrt{\frac{\gamma}{R T_0}} p_m M_s \left(1 + \left(\frac{\gamma - 1}{2} \right) M_s^2 \right)^{\frac{-(\gamma + 1)}{2(\gamma - 1)}} \quad (13)$$

Here A_s is the slant area represented in figure 1, by dotted line "s". Computation of p_s/p_m and the velocity of the flow V_s at "s" are made using the Mach no., M_s :

$$\frac{p_s}{p_m} = \left(1 + \frac{\gamma - 1}{2} M_s^2 \right)^{\frac{-\gamma}{\gamma - 1}} \quad (14)$$

$$\left(\frac{V_s}{a_m^*} \right)^2 = M_s^2 \left(1 + \frac{\gamma - 1}{2} M_s^2 \right)^{-1} \quad (15)$$

Now that conditions have been calculated at the different surface areas one may compute the momentum balance:

$$p_{tm} A_{tm} + F_{st} - p_s A_s - F_{is} = w_i V_i + w_s V_s \cos \theta - w_m V_t \quad (16)$$

where A_s is the projected area of surface "s" perpendicular to the axis of symmetry. The $\cos \theta$ term multiplies the flow at "s" because the flow of interest here is the component along the axis. The force terms F_{st} and F_{is} are computed in accordance with assumptions (5) and (6) by noting that

$$x/L = \frac{r - r_t}{r_s - r_t}.$$

They are:

$$F_{st} = 2 \pi \int_{r_t}^{r_s} \left[\left(\frac{r_s - r}{r_s - r_t} \right)^2 p_t + \left(\frac{r - r_t}{r_s - r_t} \right)^2 p_s \right]^{1/2} r \, dr \quad (17)$$

$$F_{is} = r^2 \left(0.3 p_i + 0.7 p_s \right) + (r_b^2 - r_a^2) p_s \quad (18)$$

where r is the radius to the intersection of "s" with the main nozzle wall, r_a is the inner radius of the igniter exit cone, r_b is the outside radius of the igniter exit cone, and r_t is the throat radius. The indicated mathematical operations have been carried to completion in equation (18) while equation (17) has been left in a less cumbersome integral form.

C. AGREEMENT WITH EXPERIMENTAL DATA

From the experimental measurements, a numerical result was obtained for the pressure distribution term along the motor exit cone (F_{st}). However, in general, this makes the model inconsistent at the intersection of the exit cone and the surface "s" since the measured pressure at the tap near "s" is not in conformity with the p_s value as predicted by the model. This indicates that a modification is needed to the pressure distribution across the igniter exit cone or across the annular area. The adjustment to the model made by incorporating experimental pressure distributions, discussed in the main body of the report, was made without modifying the model to account for this discontinuity at "s". This resulted in adjustment of the analytical model line providing a more conservative prediction of unblocking conditions. It should be noted, however, that to obtain a more accurate prediction of unblocking over a wide range, added improvements should be made to make the model assumptions conform more closely with experimental data. Modifications which should be looked into are pressure matching at section "s" and the igniter jet shock location and structure.

D. PROGRAM INPUT AND OUTPUT

The input quantities needed to run the program are:

- (1) D_a = inner diameter of igniter exit cone
- (2) D_b = outer diameter of igniter exit cone
- (3) θ = one half angle of booster nozzle
- (4) D_{tm} = throat diameter of booster nozzle
- (5) γ = specific heat ratio of gas
- (6) ϵ^* = ratio of area at surface "s" to the motor throat area.
- (7) D_{ti} = igniter throat diameter

As the program is set up, variables (1) thru (5) may be given once, while variables ϵ^* , and D_{ti} may be given successively in pairs. (The fact that the total quantities T_o and P_m need not be established results from the fact that the momentum balance quantities were computed as non-dimensional ratios; see the next section.)

The primary output for one set of data is the pressure ratio at which unblocking occurs. However, the input data for each case is printed out along with the areas and diameters calculated in the course of calculation of P_i/P_m .

E. NON-DIMENSIONAL QUANTITIES

In the program it was assumed that all the gases in the control volume were of the same stagnation pressure and temperature. The programmed variables with subscripts 'p' are related to the variables in the cgs system of units as follows:

$$p_p = p/P_m \quad (19)$$

$$A_p = A \quad (20)$$

$$v_p = v/a_m^* \quad (21)$$

$$w_p = \sqrt{\frac{R T_o}{P_m}} w \quad (22)$$

The programmed variables can then be related in the momentum balance equation by the equation

$$p_p A_p = \sqrt{\gamma} v_p w_p \quad (23)$$

The proof of (23) is obtained by replacing the programmed variables with their equivalents as determined by (19) thru (22).

Since $a_m^* = \sqrt{R T_o}$, equation (23) reduces to:

$$pA = \gamma wv \quad (24)$$

APPENDIX B

PENETRATION MODEL

A. INTRODUCTION

The following sections present the analytical development of the jet penetration model and some comments on the limitations of the analysis. Symbols are as defined in the text or in the symbol section in the main body of the report.

B. INITIAL PRESSURE BUILDUP AND PENETRATION IN THE BOOSTER CHAMBER

It is assumed that the gases initially within the motor port are trapped and that their mass and the volume of the chamber remains constant. The temperature of the trapped gases is assumed to increase due to isentropic compression. One-dimensional energy balance relationships are assumed to be adequate for purposes of analysis.

Total energy in the chamber is

$$E = m_{t_r} c_{v_{t_r}} T_{t_r} + m_c c_{v_c} T_c + KE \quad (1)$$

The contribution from the kinetic energy is assumed to be negligible. A noticeable point here is that the amount of heat lost to the surroundings is neglected. At the very initial stages, heat is lost in heating the grain surface, however, because of the low conductivity of the propellant surface and the relatively high gas flow rate, it is assumed that energy heat transfer losses in the gases may be neglected. Also, T_c refers to some average temperature of the gas jet in the chamber. Subscript t_r refers to the trapped gas and c to the gas in the chamber. m is the mass of the individual gases.

Also

$$\frac{\partial E}{\partial t} \cong \int (h + \frac{u^2}{2})_i dw_i - \int (h + \frac{u^2}{2})_c dw_c \quad (2)$$

$$= h_{i0} w_i - h_{c0} w_c \quad (3)$$

At $t = 0$, mass of the gas in the chamber, $m = 0$. At any given later time mass is accumulated instantaneously in the chamber as give by:

$$\dot{m}_c = \frac{dm}{dt} = \dot{w}_i - \dot{w}_c \quad (4)$$

where \dot{w}_i = mass rate of flow of the igniter gas
and \dot{w}_c = mass rate of flow out of the chamber passing through the annular area (A_{an}).

For the case where the gas is completely trapped,

$$\frac{dE}{dt} = m_{tr} C_{v_{tr}} \frac{dT_{tr}}{dt} + C_{v_i} \frac{d}{dt} (m_c T_c) \quad (5)$$

Due to the assumption of isentropic compression of the trapped gas,

$$\frac{P_{amb}}{P_c} = \left[\frac{T_{amb}}{T_{tr}} \right]^{\frac{\gamma}{\gamma-1}} \quad (6)$$

Hence

$$T_{tr} = T_{amb} \left[\frac{P_c}{P_{amb}} \right]^{\frac{\gamma-1}{\gamma}} \quad (7)$$

Therefore

$$\frac{dT_{tr}}{dt} = \left(\frac{T_{amb}}{P_{amb}^{\frac{\gamma-1}{\gamma}}} \right) \left(\frac{\gamma-1}{\gamma} \right) \left(P_c^{-\frac{1}{\gamma}} \right) \frac{dP_c}{dt} \quad (8)$$

If V_o = total volume in the booster chamber, the equation of state is written as

$$P_c V_o = m_{tr} R_{tr} T_{tr} + m_c R_c T_c \quad (9)$$

Hence

$$V_o \frac{dP_c}{dt} = m_{tr} R_{tr} \frac{dT_{tr}}{dt} + R_c \frac{d}{dt} (m_c T_c) \quad (10)$$

Therefore

$$\frac{d}{dt} (m_c T_c) = \frac{V_o}{R_c} \frac{dP_c}{dt} \left[1 - \left(\frac{\gamma-1}{\gamma} \right) \left(\frac{P_{amb}}{P_c} \right)^{\frac{1}{\gamma}} \right] \quad (11)$$

From Equations (5) and (11) one obtains

$$\frac{dE}{dt} = V_o \frac{dP_c}{dt} \frac{C_{Vi}}{R_c} \left[1 + \frac{\gamma-1}{\gamma} \left(\frac{P_{amb}}{P_c} \right)^{\frac{1}{\gamma}} \left(\frac{R_c}{R_{tr}} \frac{C_{Vtr}}{C_{Vi}} - 1 \right) \right] \quad (12)$$

From Equations (3) and (12), it finally yields,

$$(h_{ic} w_c - h_{cc} w_c) = V_o \frac{dP_c}{dt} \frac{C_{Vi}}{R_c} \left[1 + \frac{\gamma-1}{\gamma} \left(\frac{P_{amb}}{P_c} \right)^{\frac{1}{\gamma}} \left(\frac{R_c}{R_{tr}} \frac{C_{Vtr}}{C_{Vi}} - 1 \right) \right] \quad (13)$$

Also

$$w_c = f(P_c, M_t, A_{tm}, T_c) \quad (14)$$

where M_t = Mach number at the throat in the annular area defined by A_{tm} . As both these quantities are unknown, they can be obtained by considering the mixing characteristics of the igniter jet and its development in the booster chamber.

C. AXISYMMETRIC JET FLOW DISCHARGING INTO A DEAD-END CHANNEL

A simplified diagram of the propagation of a turbulent jet in a dead-end channel similar to that described by Abramovich⁽¹⁾ is shown in Figure B-1. This figure describes the longitudinal section of a channel with a height or diameter $2H$. A jet of initial diameter $2b$ is discharged into the channel at the open end with a constant velocity U_o in the initial section. ⁽¹⁻²⁾ As one moves downstream from the jet section (1), the thickness "b" of the zone in which the jet mixes with the surrounding fluid is enlarged and the constant velocity core in the jet is narrowed and ultimately becomes zero. The region beyond this point is called the "principal area of the jet," where the axial velocity " U_m " drops as the distance from the initial section increases. At a certain section 3, the jet begins to turn and as a result the direction of the flow is reversed. Between the lateral boundary of the jet and the channel wall there is a region of back fluid flow and between the sections

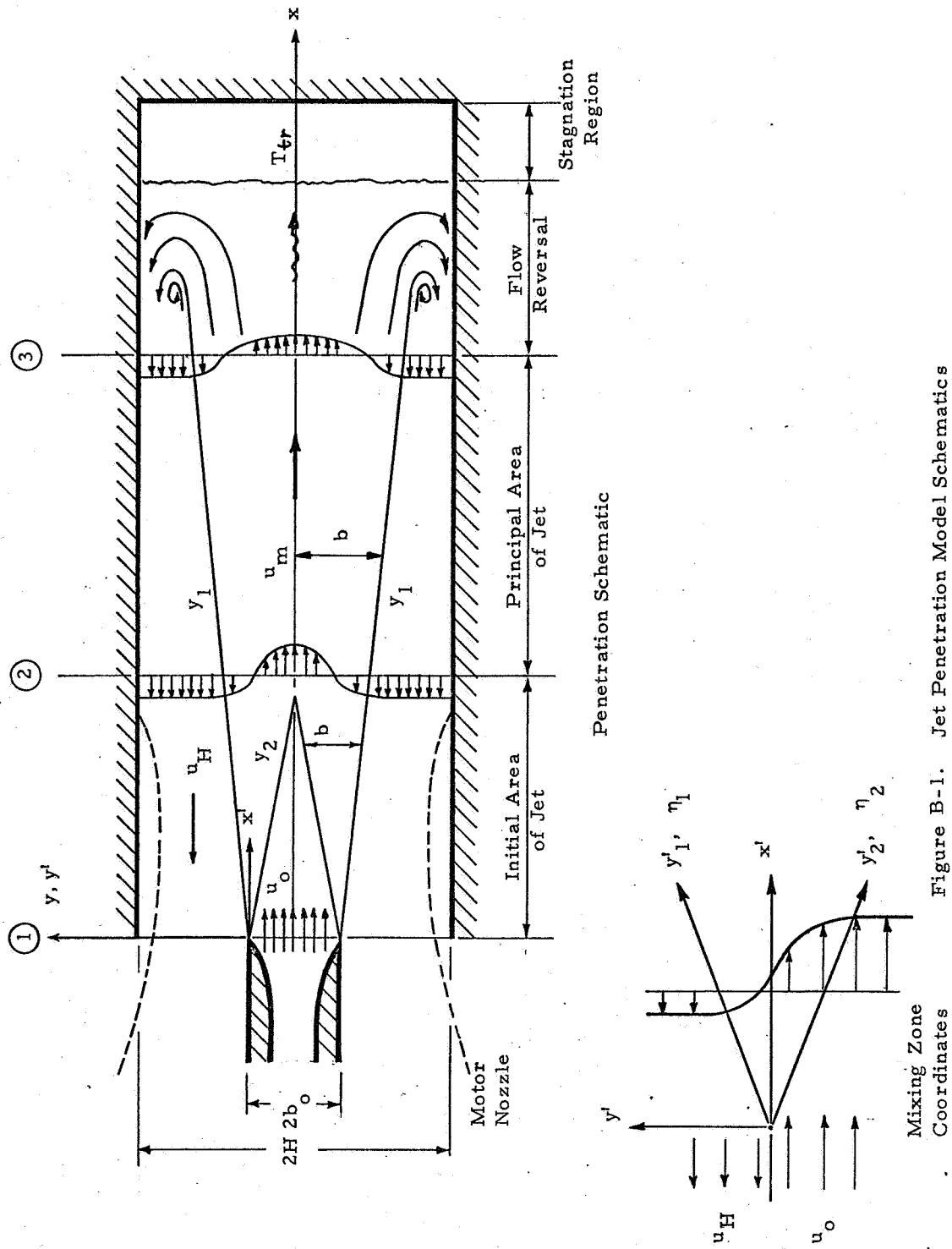


Figure B-1. Jet Penetration Model Schematics

(3) and (1). In the mixing zone, which in effect is a boundary layer which forms during counterflow of the fluid jets, the flow velocity varies in magnitude and direction between U_o (in the initial area of the jet) or U_m (in the principal region) and U_H^o .

The problem on hand is to provide analytical means to construct the velocity field induced by the jet in the dead-end channel and to determine the coordinates of the characteristic sections like the end of the initial area of the jet, beginning of the reverse flow of the jet, and boundaries of the mixing zone. Hence, the complete flow region is divided into two separate regions; (i) the initial area of the jet in which the turbulent jet spreads through a counter flowing stream of fluid and (ii) the principle area of the jet where the turbulent jet continues to spread and the center line velocity decays in response to viscous interaction of the jet mixing zones. Note, also, that the initial area of the jet is assumed to be under a region of constant pressure.

Referring to Figure 3, one can write that at any section mass flow can be written as

$$\pi \rho_H U_H (H^2 - b_o^2) + \pi \rho_o U_o b_o^2 = \dot{m}_c \quad (15)$$

where
$$m_c = \int_0^t (\dot{w}_{io} - \dot{w}_c) dt$$

is the mass accumulated in the booster chamber during time t

Hence, Equation (14) can be written as

$$1 + \lambda_1 \alpha \left[\frac{1 - b_o^{*2}}{b_o^{*2}} \right] = \frac{\dot{m}_c}{\pi \rho_o U_o b_o^2} \quad (16)$$

where
$$b_o^* = b_o / H \quad ; \quad \alpha = U_H / U_o \quad (16a)$$

and
$$\lambda_1 = \rho_H / \rho_o = T_o / T_H = h_o / h_H$$

Momentum at Section (1) is given by

$$I_1 = \pi \rho_o U_o^2 b_o^2 + \pi \rho_H U_H^2 (H^2 - b_o^2) \quad (17)$$

From Equation (16a), Equation (17) can be written as

$$I_1 = \pi \rho_0 u_0^2 b_0^2 \left[1 + \lambda_1 \alpha^2 \left(\frac{1 - b_0^{*2}}{b_0^{*2}} \right) \right] \quad (18)$$

Between Sections (1) and (2), conservation of mass yields

$$\dot{m}_c = \pi \rho_0 u_0 y_2^2 + \lambda \pi \int_{y_2}^{y_1} \rho u y dy + \pi \rho_H u_H (H^2 - y_1^2) \quad (19)$$

where y_1 and y_2 are the respectively the upper and lower edges of the mixing zone.

The conservation of momentum gives:

$$I_1 = \pi \rho_0 u_0^2 y_2^2 + 2\pi \int_{y_2}^{y_1} \rho u^2 y dy + \pi \rho_H u_H^2 (H^2 - y_1^2) \quad (20)$$

Equations (19) and (20) can be written as

$$\frac{\dot{m}_c}{\pi \rho_0 u_0 H^2} = y_2^{*2} + 2 \int_{y_2^*}^{y_1^*} \frac{\rho u}{\rho_0 u_0} y^* dy^* + \alpha \lambda_1 (1 - y_1^{*2}) \quad (21)$$

and

$$y_2^{*2} + 2 \int_{y_2^*}^{y_1^*} \frac{\rho u^2}{\rho_0 u_0^2} y^* dy^* + \alpha^2 \lambda_1 (1 - y_1^{*2}) = b_0^{*2} \left[1 + \alpha^2 \lambda_1 \left(\frac{1 - b_0^{*2}}{b_0^{*2}} \right) \right] \quad (22)$$

where

$$b_0^* = \frac{b_0}{H}; \quad \alpha = \frac{u_H}{u_0}$$

$$y^* = y/H \text{ and } \lambda_1 = \rho_H / \rho_0$$

Between regions (2) and (3), that is, in the principal area of the jet, conservation of mass yields

$$\dot{m}_c = 2\pi \int_0^b \rho u y dy + \rho_H u_H \pi (H^2 - b^2) \quad (23)$$

and conservation of momentum gives,

$$2\pi \int_0^b \rho u^2 y dy + \pi \rho_H u_H (H^2 - b^2) = \pi \rho_c u_o^2 b_o^2 \left[1 + \alpha^2 \lambda_1 \left(\frac{1 - b_o^{*2}}{b_o^{*2}} \right) \right] \quad (24)$$

Rewriting Equations (23) and (24), with $\xi = y/b$, and normalizing with respect to the centerline values ρ_m , U_m , one obtains:

$$\frac{\dot{m}_c}{\pi \rho_m U_m b^2} = 2 \int_0^1 \frac{\rho u}{\rho_m U_m} \xi d\xi + \frac{\rho_H u_H}{\rho_m U_m} \left(\frac{H^2}{b^2} - 1 \right) \quad (25)$$

and

$$2 \int_0^1 \frac{\rho u^2}{\rho_m U_m^2} \xi d\xi + \frac{\rho_H u_H^2}{\rho_m U_m^2} \left(\frac{H^2}{b^2} - 1 \right) = \left(\frac{b_o^{*2}}{b^{*2}} \right) \left(\frac{U_o}{U_m} \right)^2 \left[1 - \frac{\gamma-1}{2} M_o^2 \left(\frac{U_m^2}{U_o^2} - 1 \right) \right] \left[1 + \alpha^2 \lambda_1 \left(\frac{1 - b_o^{*2}}{b_o^{*2}} \right) \right] \quad (26)$$

Notice that in Equations (21), (22), (25) and (26), the velocity profiles U/U_o and U/U_m are not known. Also, the density profiles are not known. Assuming the flow to be entirely inviscid, the density ratio can be related to the velocity ratio by using the Crocco integral relation and the equation of state. But still the velocity profiles have to be determined. The velocity profile U/U_o in the mixing zone of the initial area of jet is determined as follows.

It is assumed, at the outset, that the laws governing the plane-parallel jets are also valid for axisymmetric flow as far as velocity profile is concerned. In an actual motor the average wall flow velocity will be modified by the area ratio effect of the motor throat between sections (2) and (1). In the test motor design, the actual port-to-throat area ratio was in the neighborhood of 1.8. Also during the early portion of the ignition transient before first ignition the pressure gradient down the port is not large. It is therefore assumed for the current model that the increased wall velocity and the small port pressure gradient will have negligible effect upon the mixing zone profile, such that it may be assumed that $dp/dx = 0$. Hence, referring to Figure 3(b), the compressible

equations of motion (for zero pressure gradient flow) are:

$$\text{Cont: } \frac{\partial}{\partial x'} (\rho u) + \frac{\partial}{\partial y'} (\rho v) = 0 \quad (27)$$

$$\text{Mom: } \rho u \frac{\partial u}{\partial x'} + \rho v \frac{\partial u}{\partial y'} = \frac{\partial \tau}{\partial y'}$$

where τ is the shear stress.

Coordinate transformation to incompressible plane is achieved by employing the Howarth's ⁽²⁾ transformation. It is

$$x'' = x' \\ y'' = \int_0^{y'} \rho / \rho_r dy' \quad \text{where } \rho_r = \text{Ref. Density} \quad (28)$$

Hence, Equation (27) (with the application of Mager's ⁽³⁾ shear stress invariancy under the transformation) transforms to,

$$\frac{\partial u'}{\partial x''} + \frac{\partial v'}{\partial y''} = 0 \\ u' \frac{\partial u'}{\partial x''} + v' \frac{\partial u'}{\partial y''} = \frac{1}{\rho_r} \frac{\partial \tau'}{\partial y''} \quad (29)$$

According to Prandtl's mixing length theory (Ref. Schlichting) ⁽⁴⁾

$$\tau' = \rho_r \ell^2 \left(\frac{\partial u'}{\partial y'} \right)^2 \quad (30)$$

where $\ell = \beta C x'$, β and C are constants.

Defining a similarity parameter, $\eta_i = \sigma_i y' / x'$ and
the incompressible jet spread parameter ⁽⁵⁾ $\sigma_i = (2\beta^2 C^2)^{-\frac{1}{3}}$
and the incompressible stream function $\psi_i = U_0 \frac{x'}{\sigma_i} F(\eta_i)$ ⁽³¹⁾

equation (29) can be combined into one total differential equation given by

$$F'''(\eta_i) + F(\eta_i) = 0 \quad (32)$$

Solution to Equation (32) is given by Tollmein⁽⁶⁾ as

$$F(\eta_i) = C_1 e^{-\eta_i} + C_2 e^{\eta_{i/2}} \cos \frac{\sqrt{3}}{2} \eta_i + C_3 e^{\eta_{i/2}} \sin \frac{\sqrt{3}}{2} \eta_i \quad (33)$$

Boundary Conditions

- (i) At $\eta_i = \eta_2$, $u' = U_0$ Hence $F'(\eta_2) = 1$
(ii) At $\eta_i = \eta_2$, $\frac{\partial u'}{\partial y'} = 0$ Hence $F''(\eta_2) = 0$
(ii) At $\eta_i = \eta_2$, $v' = 0$ Hence $F(\eta_2) = \eta_2$ (34)
(iv) At $\eta_i = \eta_1$, $u' = -U_H$ Hence $F'(\eta_1) = -\alpha$
(v) At $\eta_i = \eta_1$, $\partial u' / \partial y' = 0$ Hence $F''(\eta_1) = 0$

Using Equation (33), Equation (34) can be written as follows:

$$\begin{aligned} -C_1 e^{-\eta_2} + \left(\frac{C_2}{2} + \frac{\sqrt{3}}{2} C_3\right) e^{\eta_{2/2}} \cos \frac{\sqrt{3}}{2} \eta_2 + \left(\frac{C_3}{2} - \frac{\sqrt{3}}{2} C_2\right) e^{\eta_{2/2}} \sin \frac{\sqrt{3}}{2} \eta_2 &= 1 \\ C_1 e^{-\eta_2} + \left(\frac{\sqrt{3}}{2} C_3 - \frac{C_2}{2}\right) e^{\eta_{2/2}} \cos \frac{\sqrt{3}}{2} \eta_2 - \left(\frac{\sqrt{3}}{2} C_2 + \frac{C_3}{2}\right) e^{\eta_{2/2}} \sin \frac{\sqrt{3}}{2} \eta_2 &= 0 \\ C_1 e^{-\eta_2} + C_2 e^{\eta_{2/2}} \cos \frac{\sqrt{3}}{2} \eta_2 + C_3 e^{\eta_{2/2}} \sin \frac{\sqrt{3}}{2} \eta_2 &= \eta_2 \quad (35) \\ -C_1 e^{-\eta_1} + \left(\frac{C_2}{2} + \frac{\sqrt{3}}{2} C_3\right) e^{\eta_{1/2}} \cos \frac{\sqrt{3}}{2} \eta_1 + \left(\frac{C_3}{2} - \frac{\sqrt{3}}{2} C_2\right) e^{\eta_{1/2}} \sin \frac{\sqrt{3}}{2} \eta_1 &= -\alpha \\ C_1 e^{-\eta_1} + \left(\frac{\sqrt{3}}{2} C_3 - \frac{C_2}{2}\right) e^{\eta_{1/2}} \cos \frac{\sqrt{3}}{2} \eta_1 - \left(\frac{\sqrt{3}}{2} C_2 + \frac{C_3}{2}\right) e^{\eta_{1/2}} \sin \frac{\sqrt{3}}{2} \eta_1 &= 0 \end{aligned}$$

The five unknowns C_1 , C_2 , C_3 , η_1 and η_2 in the above equations can be solved for any given value of α . The velocity profile u/u_0 is then given by $F'(\eta_i)$.

From the assumption of perfect gas relation, one can write, for a constant pressure region,

$$P_o/\rho = h/h_o = T/T_o \quad (36)$$

From the Crocco integral relation, the enthalpy profile h/h_o can be related to the velocity profile by

$$h/h_o = A_1 + A_2 F'(\eta) + A_3 [F'(\eta)]^2 \quad (37)$$

where

$$A_1 = \left(\frac{\alpha - \lambda_2}{\alpha - 1} \right) \left(1 + \frac{\gamma - 1}{2} M_o^2 \right)$$

$$A_2 = \left(\frac{\lambda_2 - 1}{\alpha - 1} \right) \left(1 + \frac{\gamma - 1}{2} M_o^2 \right)$$

$$A_3 = - \left(\frac{\gamma - 1}{2} \right) M_o^2$$

$$\alpha = U_H/U_o = \text{velocity ratio of the two streams}$$

$$\lambda_2 = h_{tH}/h_{to} = \text{stagnation enthalpy ratio of the two streams}$$

and M_o = Mach number of the main stream or jet.

Also, the reference enthalpy ratio, $\frac{h_r}{h_o}$ is given by (Ref. 5)

$$\frac{h_r}{h_o} = \frac{T_r}{T_o} = 1 + \frac{1 - \lambda_1}{2\lambda_1} + 0.7(\gamma - 1)M_o^2(1 - \alpha)^2 \quad (39)$$

where

$$\lambda_1 = P_u/\rho_o = h_o/h_u \quad (40)$$

is the static enthalpy ratio (or the density ratio) of the two streams.

Using the above relations for the velocity profile u/u_o , the enthalpy ratio h/h_o and the other pertinent relationships, Equations (21) and (22) take the following final form

$$\frac{y_2^{*2} + \frac{\chi^*}{\pi \sigma_i H}}{\left[1 + \frac{1 - \lambda_1}{2\lambda_1} + 0.7(\gamma - 1)M_o^2(1 - \alpha)^2 \right]} + \frac{(F_1 - F_2)}{\dot{m}_o / \pi \rho_o u_o H^2} + \alpha \lambda_1 (1 - y_1^{*2}) = \quad (41)$$

$$y_2^{*2} - \frac{x^*}{\pi \sigma_i H} \frac{(\alpha F_1 + \eta_2)}{\left[1 + \frac{1-\lambda_1}{2\lambda_1} + 0.7(\gamma-1)M_o^2(1-\alpha)^2\right]} + \alpha^2 \lambda_1 (1-y_1^{*2}) = b_o^{*2} \left[1 + \alpha^2 \lambda_1 \left(\frac{1-b_o^{*2}}{b_o^{*2}}\right)\right] \quad (42)$$

where F_1 and F_2 refer to the value of the function F (given by Equation 33) at $\eta = \eta_1$ and η_2 respectively.

The velocity profile u/u_m in the principal area of the jet between sections (2) and (3) is assumed to be given by

$$\frac{u-u_m}{u_m-u_o} = \left[1 - \left(\frac{y}{b}\right)^{1.5}\right]^2 = \left[1 - \left(\frac{r}{r_o}\right)^{1.5}\right]^2$$

Hence

$$\frac{u}{u_m} = \frac{\alpha + (1 - \left(\frac{r}{r_o}\right)^{1.5})^2 \left(\frac{u_m}{u_o} - \alpha\right)}{u_m/u_o}$$

Assuming that the stagnation enthalpy remains constant along the center line in the booster chamber and further employing the Crocco integral relation, the enthalpy ratio in the principal area of the jet is given by

$$\frac{h}{h_m} = \frac{\left[\frac{\alpha - \lambda_2 \frac{u_m}{u_o}}{\alpha - u_m/u_o} + \frac{(\lambda_2 - 1) \frac{u_m}{u_o}}{\alpha - u_m/u_o} \left(\frac{u}{u_m}\right) - \left(\frac{u}{u_m}\right)^2\right]}{\left[1 + \frac{\gamma-1}{2} M_o^2\right]^{-1} \left[1 - \frac{\gamma-1}{2} M_o^2 \left(\frac{u_m^2}{u_o^2} - 1\right)\right]} + \left(\frac{u}{u_m}\right)^2 \quad (43)$$

Substituting from Equation (43) into Equations (25) and (26), they yield

$$2\left(\frac{u_m}{u_o}\right) \int_0^1 \left(\frac{u}{u_m}\right) \left\{ \frac{\left[\frac{\alpha - \lambda_2 \frac{u_m}{u_o}}{\alpha - u_m/u_o} + \frac{(\lambda_2 - 1) \frac{u_m}{u_o}}{\alpha - u_m/u_o} \left(\frac{u}{u_m}\right) - \left(\frac{u}{u_m}\right)^2\right]}{\left[1 + \frac{\gamma-1}{2} M_o^2\right]^{-1} \left[1 - \frac{\gamma-1}{2} M_o^2 \left(\frac{u_m^2}{u_o^2} - 1\right)\right]} + \left(\frac{u}{u_m}\right)^2 \right\} \frac{u}{u_m} d\left(\frac{u}{u_m}\right) \quad (44)$$

$$= \alpha \lambda_1 \left[1 - \frac{\gamma-1}{2} M_o^2 \left(\frac{u_m^2}{u_o^2} - 1\right)\right] \left[\frac{1-b^{*2}}{b^{*2}}\right]$$

$$= \frac{\dot{m}_o}{\pi \rho_o u_o H^2} \cdot \frac{1}{b^{*2}} \left[1 - \frac{\gamma-1}{2} M_o^2 \left(\frac{u_m^2}{u_o^2} - 1\right)\right]$$

and

$$2 \left(\frac{u_m}{u_o} \right)^2 \int_0^1 \left(\frac{u}{u_m} \right)^2 \left\{ \frac{\left[\frac{\alpha - \lambda_2 \frac{u_m}{u_o}}{\alpha - u_m/u_o} + \frac{(\lambda_2 - 1) u_m/u_o}{\alpha - u_m/u_o} \left(\frac{u}{u_m} - \frac{u}{u_m} \right)^2 \right]}{\left(1 + \frac{\gamma-1}{2} M_o^2 \right)^{-1} \left[1 - \frac{\gamma-1}{2} M_o^2 \left(\frac{u_m^2}{u_o^2} - 1 \right) \right]} + \left(\frac{u}{u_m} \right)^2 \right\}^{-1} d \xi$$

$$+ \alpha^2 \lambda_1 \left[1 - \frac{\gamma-1}{2} M_o^2 \left(\frac{u_m^2}{u_o^2} - 1 \right) \right] \left[\frac{1 - b^{*2}}{b^{*2}} \right] \quad (45)$$

$$= \left[1 - \frac{\gamma-1}{2} M_o^2 \left(\frac{u_m^2}{u_o^2} - 1 \right) \right] \left(\frac{b_o^{*2}}{b^{*2}} \right) \left[1 + \alpha^2 \lambda_1 \left(\frac{1 - b_o^{*2}}{b_o^{*2}} \right) \right]$$

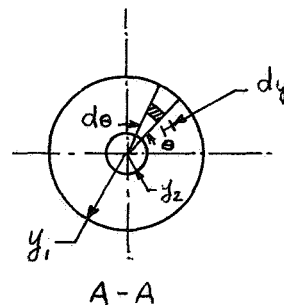
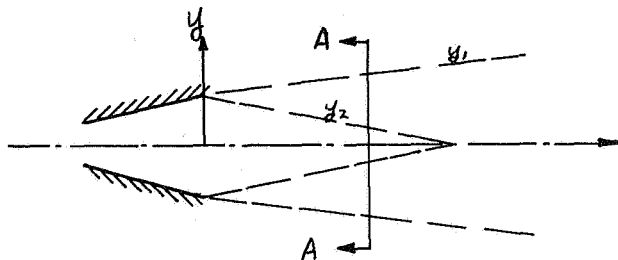
where $b^* = cx^*$ (46)

The constant c in the above equation is determined from the condition $x^* = x_2^*$ and $y_1^* = b^*$ at Section (2), (Figure B-1).

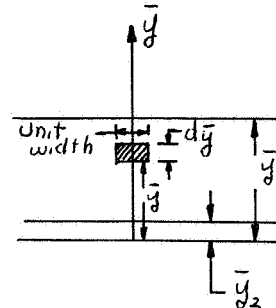
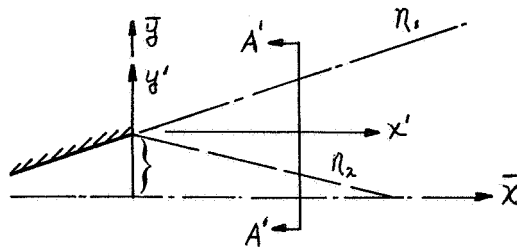
D. SUPPORTING DERIVATIONS

In Equation (21) to evaluate the integral $2 \int_{y_1^*}^{y_2^*} \frac{\rho u}{\rho_o u_o} y^* dy^*$ it is enough if the velocity profile (U/U_o) is specified because the density distribution (ρ/ρ_o) can be related to the velocity profile by means of the Crocco Integral due to the assumption of perfect gas relation. But the difficulty arises due to the fact that the velocity profile (U/U_o) determined, is for a two-dimensional mixing of two counterflowing parallel jets. Hence the integral has to be transformed from the axisymmetric coordinates to the two-dimensional incompressible plane before the velocity profile U/U_o can be utilized. This is done as follows.

(a) Axisymmetric Plane



(b) Two dimensional plane



Consider an elemental mass $\rho u dy d\theta$ in the axisymmetric plane at a distance y from the origin. Then the total mass at section AA within the radii y_2 and y_1 is given by

$$m_{axisym} = \int_0^{2\pi} d\theta \int_{y_2}^{y_1} \rho u y dy = 2\pi \int_{y_2}^{y_1} \rho u y dy \quad A(1)$$

Similarly by the total mass at section A'A' within the mixing zone \bar{y}_2 and \bar{y}_1 , in the two dimensional plane is

$$m_{two-dim} = \int_{\bar{y}_2}^{\bar{y}_1} \bar{\rho} \bar{u} d\bar{y} \quad A(2)$$

If the mass flow in both the coordinate planes have to be the same, then it is necessary that

$$2\pi \int_{y_2}^{y_1} \rho u y dy = \int_{\bar{y}_2}^{\bar{y}_1} \bar{\rho} \bar{u} d\bar{y} \quad A(3)$$

By a translation of the coordinates defined by

$$x' = \bar{x} \quad \text{and} \quad \bar{y} = b_0 + y' \quad A(4)$$

the right hand integral in Eqn A(3) becomes

$$\int_{\bar{y}_2}^{\bar{y}_1} \bar{\rho} \bar{u} d\bar{y} = \int_{y_2'}^{y_1'} \bar{\rho} \bar{u} dy' \quad A(5)$$

With the application of Howarth's compressible transformation given by

$$x_i = x' ; \quad y_i = \int_0^{y'} \rho/\rho_n dy' \quad A(6)$$

Eqn. A(5) can be written as,

$$\int_{y_2'}^{y_1'} \bar{\rho} \bar{u} dy' = \int_{y_{2i}}^{y_{1i}} \rho_n \bar{u} dy_i \quad A(7)$$

Finally employing the similarity coordinate defined by

$$\eta = \sigma_i y_i / x_i \quad A(8)$$

Eqn. A(7) yields

$$\int_{y_{2i}}^{y_{1i}} \rho_n \bar{u} dy_i = \frac{x_i}{\sigma_i} \int_{\eta_2}^{\eta_1} \rho_n \bar{u} d\eta \quad A(9)$$

Writing Eqn. A(9) in the non-dimensional form, it yields

$$\begin{aligned} \frac{x_i}{\sigma_i} \int_{\eta_2}^{\eta_1} \rho_n \bar{u} d\eta &= \frac{x_i^* H}{\sigma_i} (\rho_o u_o) \left(\frac{\rho_n}{\rho_o} \right) \int_{\eta_2}^{\eta_1} \frac{\bar{u}}{u_o} d\eta \quad A(10) \\ &= \frac{x_i^* H}{\sigma_i} (\rho_o u_o) \left(\frac{\rho_r}{\rho_o} \right) (F_1 - F_2) \end{aligned}$$

where

$$\bar{u}/u_o = F'(\eta). \quad \text{It is also noted that}$$

$$2\pi \int_{y_2}^{y_1} \rho u y dy = 2\pi \rho_0 u_0 H^2 \int_{y_2^*}^{y_1^*} \frac{\rho}{\rho_0} \frac{u}{u_0} y^* dy^* \quad A(11)$$

Therefore finally, by using equation A(3)

$$2 \int_{y_2^*}^{y_1^*} \frac{\rho u}{\rho_0 u_0} y^* dy^* = \frac{\chi_i^*}{\pi \sigma_i H} \left(\frac{\rho_2}{\rho_0} \right) (F_1 - F_2) \quad A(12)$$

(B) As before, the integral $2 \int_{y_2^*}^{y_1^*} \frac{\rho u^2}{\rho_0 u_0^2} y^* dy^*$ in Eqn. (22) can be written as

$$2 \int_{y_2^*}^{y_1^*} \frac{\rho u^2}{\rho_0 u_0^2} y^* dy^* = \frac{\chi_i^*}{\pi \sigma_i H} \left(\frac{\rho_2}{\rho_0} \right) \int_{\eta_2}^{\eta_1} [F'(\eta)]^2 d\eta \quad B(1)$$

Now

$$\int_{\eta_2}^{\eta_1} [F'(\eta)]^2 d\eta = [FF']_{\eta_2}^{\eta_1} - \int_{\eta_2}^{\eta_1} FF'' d\eta \quad B(2)$$

But from Eqn. (33)

$$F(\eta) = -F'''(\eta) \quad B(3)$$

Hence

$$\int_{\eta_2}^{\eta_1} [F'(\eta)]^2 d\eta = [FF']_{\eta_2}^{\eta_1} + \left[\frac{F''^2}{2} \right]_{\eta_2}^{\eta_1} \quad B(4)$$

From the boundary conditions given by Eq. (34)

$$\int_{\eta_2}^{\eta_1} [F'(\eta)]^2 d\eta = -(\alpha F_1 + \eta_2)$$

Therefore

$$2 \int_{y_2^*}^{y_1^*} \frac{\rho u^2}{\rho_0 u_0^2} y^* dy^* = - \frac{\chi_i^*}{\pi \sigma_i H} \left(\frac{P_2}{P_0} \right) (\alpha F_1 + \eta_2) \quad B(5)$$

(C) The enthalpy profile in the principal area of the jet between Sections (2) and (3) (Figure B-1) can be written down, after applying the boundary conditions given by

$$\begin{aligned} \text{(i)} \quad & \text{at } y = 0; U = U_m; h_{\text{stag}} = h_{\text{tm}} = h_{\text{to}} \\ \text{(ii)} \quad & \text{at } y = b; U = U_H; h_{\text{stag}} = h_{\text{tH}} \end{aligned} \quad C(1)$$

$$\text{as } \frac{h}{h_m} = \left[\frac{\alpha - \lambda_2 U_m / U_0}{\alpha - U_m / U_0} \right] \left[\frac{h_{\text{to}}}{h_m} \right] + \left[\frac{(\lambda_2 - 1) \frac{U_m}{U_0}}{\alpha - U_m / U_0} \right] \left(\frac{h_{\text{to}}}{h_m} \right) \left(\frac{U}{U_m} \right) - \frac{U_m^2}{2 h_m} \quad C(2)$$

Assumption of constant stagnation enthalpy along the centerline (axis) of the jet, that is,

$$h_0 + \frac{U_0^2}{2} = h_m + \frac{U_m^2}{2} \quad \text{along } y=0, \quad C(3)$$

yields,

$$\frac{U_m^2}{2 h_m} = \left(\frac{h_0}{h_m} \right) \left(1 + \frac{\gamma-1}{2} M_0^2 \right) - 1 \quad C(4)$$

where

$$\frac{h_m}{h_0} = 1 - \frac{\gamma-1}{2} M_0^2 \left\{ \frac{U_m^2}{U_0^2} - 1 \right\} \quad C(5)$$

Using the above relations and employing the perfect gas relation, one can write

$$\frac{P_m}{\rho} = \frac{h}{h_m} = B_1 + B_2 \left(\frac{U}{U_m} \right) + B_3 \left(\frac{U}{U_m} \right)^2 \quad C(6)$$

where

$$B_1 = \left[\frac{1 + \frac{\gamma-1}{2} M_0^2}{1 - \frac{\gamma-1}{2} M_0^2 \left(\frac{u_m^2}{u_0^2} - 1 \right)} \right] \left[\frac{\alpha - \lambda_2 \frac{u_m}{u_0}}{\alpha - u_m/u_0} \right]$$

$$B_2 = \left[\frac{1 + \frac{\gamma-1}{2} M_0^2}{1 - \frac{\gamma-1}{2} M_0^2 \left(\frac{u_m^2}{u_0^2} - 1 \right)} \right] \left[\frac{(\lambda_2 - 1) \frac{u_m}{u_0}}{\alpha - \frac{u_m}{u_0}} \right] \quad C(7)$$

and

$$B_3 = - \left[\frac{\left(\frac{\gamma-1}{2} M_0^2 \right) \frac{u_m^2}{u_0^2}}{1 - \frac{\gamma-1}{2} M_0^2 \left(\frac{u_m^2}{u_0^2} - 1 \right)} \right]$$

E. LIMITATIONS OF THE ANALYSIS

In the transient pressure buildup analysis, it is assumed that no heat is lost to the surroundings. This is a severe restriction, which was used to simplify an otherwise very complex problem. A solution accounting for both convective and radiative heat transfer may be made at a later date.

Even though there is a pressure gradient inside the booster chamber, it is assumed that an average constant booster chamber pressure p_c prevails in the chamber. Consistent with the assumption, the velocity profile in the "mixing" zone is analyzed only for a constant pressure situation. In the principal area of the jet, inside the chamber, the most important mechanism that would decelerate the jet and allow the flow to reverse its direction is the strong pressure gradient that is present inside the chamber. The present analysis does not account for a pressure gradient. Hence, the solution obtained will not indicate the centerline velocity of the jet decaying. One way of correcting this is to formulate a pressure gradient function from the experimental results, account for them in the equations and solve for the velocity profile a second time. This is only a postulation and the merit of this suggestion can only be established after the experimental results are available.

REFERENCES

1. Abramovich, G. N., "The Theory of Turbulent Jets," MIT Press, 1963.
2. Howarth, L., "Concerning the Effect of Compressibility on Laminar Boundary Layers and Their Separation," Proceedings of Royal Society (London) Vol. 194, p. 16, (1948).
3. Mager, A., "Transformation of Compressible Turbulent Boundary Layer," Journal of Aerospace Sciences, Vol. 27, p. 297, (1960).
4. Schlichting, H., "Boundary Layer Theory," McGraw Hill, 4th Edition, 1960.
5. Channapragada, R. S. and Woolley, J. P., "Turbulent Mixing of Parallel Compressible Non-Isoenergetic Streams", CETEC Corporation, Mountain View, California, preprint of paper presented in Astronautica Acta, 1968.
6. Tollmein, W., "Berechnung der turbulenten Ausbreitungsvorgaenge", Zamm, 6, pp. 460-479, 1926 (Also NACA TM 1085, 1945).

APPENDIX C MOTOR BALLISTIC COMPUTER DATA

DISK OPERATING SYSTEM/360 FORTRAN 360N-FQ-451 21

C PRESSURE AND THRUST TIME ANALYSIS PROGRAM FOR SINGLE PROPELLANT,
C BUT WITH CHANGING PROPELLANT PROPERTIES AND THROAT AREA.

FIRST CARD

C XAT THE INDICATOR FOR THROAT DIAMETER VERSUS TIME. IF XAT=1 A SERIES
C OF POINTS ON A CURVE ARE REQUIRED. IF XAT=0 DT IS CONSTANT.
C XVOL THE INDICATOR FOR SELECTING BURNING SURFACE OR VOID VOLUME.
C XVOL=1 IS FOR VOLUMES. XVOL=0 IS FOR BURNING SURFACES.
C XNU THE DESIRED NUMBER OF PRESSURE, THRUST, AND TIME OUTPUT POINTS.
C TEMP (1),(2),(3) ARE THE TEMPERATURES AT WHICH PARAMETERS ARE DESIRED.
C TEM(L) MUST BE NON-ZERO FOR CALCULATION. ZERO INDICATES NONE REP.

SECOND CARD

C TR REFERENCE TEMPERATURE.
C PA AMBIENT PRESSURE AT ALTITUDE.
C CFR REFERENCE THRUST COEFFICIENT.
C ETA NOZZLE EFFICIENCY FACTOR.
C PCR REFERENCE CHAMBER PRESSURE.
C ER EXPANSION RATIO OF THE NOZZLE.

THIRD CARD

C DT INITIAL NOZZLE THROAT DIAMETER.
C CAF NOZZLE CONE HALF-ANGLE.

FOURTH CARD THRU THE NUMBER REQUIRED FOR SURFACE WEB TRACE

C AP (1) BURNING SURFACE OR VOID VOLUME. NO BLANK CARDS ACCEPTABLE.
C WB (1) WEB POSITION (VARIES FROM 0 ON THE INSIDE TO MAXIMUM WEB).
C XN (1) PRESSURE EXPONENT.
C RD (1) PROPELLANT DENSITY.
C R (1) REFERENCE BURNING RATE.
C XISP (1) STD. DEL. PROP. SPECIFIC IMPULSE.
C PIP (1) TEMPERATURE SENSITIVITY FACTOR AT CONSTANT PRESSURE.
C GAM (1) RATIO OF SPECIFIC HEATS.

C THROAT DIAMETER DECK FOLLOWS IF XAT=1.0.

C DIMENSION AP(30),WB(30),TEMP(3),XN(30),RD(30),R(30),XISP(30),XDT(6
1),XTT(6),VOL(30),PIP(30),GAM(30)

500 FORMAT (6F10.5)

510 FORMAT (8F10.4)

600 FORMAT (1H1,57HINPUT DATA FOR PRESSURE AND THRUST TIME ANALYSIS PR
10GRAM.)

601 FORMAT (1H1,30X,48HPRESSURE AND THRUST TIME ANALYSIS PROGRAM OUTPU
1T,7/35X,23HPROPELLANT TEMPERATURE=,FR.2//)

603 FORMAT (3X,14HPRESSURE = ,F14.5,3X,14HTIME = ,F14.5,3X,1
14HPRESS. INTEG.=,F14.5)

604 FORMAT (3X,14HFLOW RATE = ,F14.5,3X,14HTHRUST = ,F14.5,3X,1

```

02/15/68      FORTMAIN
14HAVE. PRESSURE=,F14.5)
605  FORMAT (3X,14HWGHT. PROP. = ,F14.5,3X,14HDELTA W PRO = ,F14.5,3X,1
14HAVE. THRUST =,F14.5)
606  FORMAT (3X,14HDLIVRD ISP = ,F14.5,3X,14HTOTAL IMPLS = ,F14.5,3X,1
14HEXP. RATIO =,F14.5)
607  FORMAT (3X,14HTHROAT AREA = ,F14.5,3X,14HWEB = ,F14.5,3X,1
14HBURN SURFACE =,F14.5,/)
C
1  READ (1,500) XAT,XVOL,XNW,TEMP(1),TEMP(2),TEMP(3),TR,PA,CFR,ETA,PC
1R,ER,DT,CAF
WRITE (3,600)
WRITE (3,500) XAT,XVOL,XNW,TEMP(1),TEMP(2),TEMP(3),TR,PA,CFR,ETA,P
1CR,ER,DT,CAF
ED=DT*ER**0.5
AE=3.14159*ED**2/4.0
AT=3.14159*DT**2/4.0
IF(XVOL)611,611,615
611  DO 4 I=1,30
M1=I
READ (1,510) AP(I),WB(I),XN(I),RO(I),R(I),XISP(I),PIP(I),GAM(I)
WRITE (3,510) AP(I),WB(I),XN(I),RO(I),R(I),XISP(I),PIP(I),GAM(I)
IF(AP(I))619,619,4
4  CONTINUE
GO TO 619
615  DO 616 I=1,30
M1=I
READ (1,510) VOL(I),WB(I),XN(I),RO(I),R(I),XISP(I),PIP(I),GAM(I)
WRITE (3,510) VOL(I),WB(I),XN(I),RO(I),R(I),XISP(I),PIP(I),GAM(I)
IF(VOL(I))700,700,616
616  CONTINUE
700  L=M1-1
DO 617 I=1,L
AP(I)=(VOL(I+1)-VOL(I))/(WB(I+1)-WB(I))
WB(I)=(WB(I+1)+WB(I))/2.0
XN(I)=(XN(I+1)+XN(I))/2.0
RO(I)=(RO(I+1)+RO(I))/2.0
R(I)=(R(I+1)+R(I))/2.0
617  GAM(I)=(GAM(I+1)+GAM(I))/2.0
XISP(M1)=XISP(L)
AP(M1)=AP(L)
XN(M1)=XN(L)
RO(M1)=RO(L)
R(M1)=R(L)
GAM(M1)=GAM(L)
619  IF(XAT)631,631,620
620  DO 630 I=1,10
READ (1,500) XDT(I),XTT(I)
WRITE (3,500) XDT(I),XTT(I)
AMX=3.14159*XDT(I-1)**2/4.0
IF(900.0-XTT(I))631,631,630
630  CONTINUE
631  ZZ=DT
Dw=WB(M1-1)/XNW
ZV=AT
DO 900 L=1,3

```

02/15/68 FORTMAIN

```

      IP=0
      IF(TEMP(L))632,900,632
632  DT=ZZ
      AT=ZV
      ER=AE/AT
      DTR=DT
      DTC=DT
      TS=TEMP(L)
      VVV=0.0
      WDOT=0.0
      WPU=0.0
      APC=0.0
      TPC=0.0
      FA=0.0
      DWPU=0.0
      XITOT=0.0
      ROSL=0.0
      ASL=0.0
      TDEL=0.0
      CNT1=0.0
      PA12=0.0
      PASS=0.0
      W=0.0
      PPASS=0.0
      TIME=0.0
      WDOTL=0.0
      WRITE (3,601) TEMP(L)
800  IF(W-WB(M1))12,11,11
11   AS=AP(M1)
      GO TO 16
12   I=1
13   IF(WB(I+1)-W)14,14,15
14   I=I+1
      GO TO 13
15   AS=((AP(I+1)-AP(I))/(WB(I+1)-WB(I)))*(W-WB(I))+AP(I)
      XS=((XN(I+1)-XN(I))/(WB(I+1)-WB(I)))*(W-WB(I))+XN(I)
      RX=((RO(I+1)-RO(I))/(WB(I+1)-WB(I)))*(W-WB(I))+RO(I)
      Q=((P(I+1)-P(I))/(WB(I+1)-WB(I)))*(W-WB(I))+P(I)
      XISS=((XISP(I+1)-XISP(I))/(WB(I+1)-WB(I)))*(W-WB(I))+XISP(I)
      PIK=((PIP(I+1)-PIP(I))/(WB(I+1)-WB(I)))*(W-WB(I))+PIP(I)
      GAS=((GAM(I+1)-GAM(I))/(WB(I+1)-WB(I)))*(W-WB(I))+GAM(I)
      CSTS=32.2*XISS/(CFR*ETA)
16   CSTRS=CSTS
      XNS=XS
      ROS=RX
      RS=Q
      XISPR=XISS
      CNST=(ROS*CSTRS/32.2)**(1.0/(1.0-XNS))
      RR=RS*(2.7183**((TS-TR)*PIK))/(PCR**XNS)
20   PC=CNST*((AS*RR/AT)**(1.0/(1.0-XNS)))+0.00001
      PCL = PC
      WDOT=PC*32.2*AT/CSTRS
      IF(PA12)31,31,699
699  CONTINUE
      DWPU=(ASL*ROSL+AS*ROS)*0.5*DW

```

```

02/15/68          FORTMAIN
      TDEL=2.0*DWP/((WDOT+WDTL)
      IF(PASS)21,21,27
21      IF(CNT1)24,24,27
24      PC=(PC+PCL)*0.5
      CNT1=1.0
      IF(XAT)650,650,635
635     DO 640 I=1,10
      IF (TIME-XTT(I+1))636,640,640
636     DTC=((XDT(I+1)-XDT(I))/(XTT(I+1)-XTT(I)))*(TIME-XTT(I))+XDT(I)
      GO TO 650
640     CONTINUE
650     AT=3.1416*DTC*DTC*0.25
      IF(AT-AMX)20,26,26
26      AT=AMX
      PPASS=1.0
      GO TO 20
27      CNT1=0.0
      DT=DTC
      IF(PASS)31,31,30
30      WPU=WPU+DWP
31      WDOT=PC*32.2*AT/CSTRS
      ER=AE/AT
      CAF1=3.14159*CAF/180.0
C      IPSCAL
      GP=GAS+1.0
      GM1=GAS-1.0
      A=2.0/GP
      B=GM1/GP
      C=GP/(2.0*GM1)
      GM = 1.1
101     GMS=GM*GM
      ZETA=A+B*GMS
      ZETAX=ZETA**C
      F=ZETAX/GM-ER
      FPRIME=ZETAX*(1.0/ZETA-1.0/GMS)
      FRATIO=F/FPRIME
      GM=GM-FRATIO
      IF(ABS(FRATIO)-0.005)200,200,101
200     AM=GM
      ALM=0.5+0.5*COS(CAF1)
      PR=(1.0+AM*AM*GM1/2.0)**(-GAS/GM1)
      CF=(PR*ER*(1.0+ALM*GAS*AM*AM)-ER*PA/PC)
      TIME=TIME+TDEL
      IF(CF-1.0)40,43,43
40      CF=1.0
43      XISPD=XISPR*CF/CFR
      IF(PASS)39,39,38
38      XITOT=XITOT+0.5*(XISPD+VVV)*DWP
      TPC=TPC+(PC+PCL)*TDEL*0.5
      APC=TPC/TIME
      FA=XITOT/TIME
39      T=XISPD*WDOT
      PASS=1.0
      IF(PA12)45,45,42
45      PA12=1.0

```

```

02/15/68          FORTMAIN
      TDEL=2.0*DWPW/(WDOT+WDOTL)
      IF(PPASS)21,21,27
21     IF(CNT1)24,24,27
24     PC=(PC+PCL)*0.5
      CNT1=1.0
      IF(XAT)650,650,635
635    DO 640 I=1,10
      IF (TIME-XTT(I+1))636,640,640
636    DTC=((XDT(I+1)-XDT(I))/(XTT(I+1)-XTT(I)))*(TIME-XTT(I))+XDT(I)
      GO TO 650
640    CONTINUE
650    AT=3.1416*DTC*DTC*0.25
      IF(AT-AMX)20,26,26
26     AT=AMX
      PPASS=1.0
      GO TO 20
27     CNT1=0.0
      DT=DTC
      IF(PASS)31,31,30
30     WPU=WPU+DWPW
31     WDOT=PC*32.2*AT/CSTRS
      ER=AE/AT
      CAF1=3.14159*CAF/180.0
C      IPSCAL
      GP=GAS+1.0
      GM1=GAS-1.0
      A=2.0/GP
      B=GM1/GP
      C=GP/((2.0*GM1))
      GM = 1.1
101    GMS=GM*GM
      ZETA=A+B*GMS
      ZETAX=ZETA**C
      F=ZETAX/GM-ER
      FPRIME=ZETAX*(1.0/ZETA-1.0/GMS)
      FRATIO=F/FPRIME
      GM=GM-FRATIO
      IF(ABS(FRATIO)-0.005)200,200,101
200    AM=GM
      ALM=0.5+0.5*COS(CAF1)
      PR=(1.0+AM*AM*GM1/2.0)**(-GAS/GM1)
      CF=(PR*ER*(1.0+ALM*GAS*AM*AM)-ER*PA/PC)
      TIME=TIME+TDEL
      IF(CF-1.0)40,43,43
40     CF=1.0
43     XISPD=XISPR*CF/CFR
      IF(PASS)39,39,38
38     XITOT=XITOT+0.5*(XISPD+VVV)*DWPW
      TPC=TPC+(PC+PCL)*TDEL*0.5
      APC=TPC/TIME
      FA=XITOT/TIME
39     T=XISPD*WDOT
      PASS=1.0
      IF(PA12)45,45,42
45     PA12=1.0

```



```

02/15/68          FORTMAIN
DWPU=0.0
42  WRITE (3,603) PC,TIME,TPC
    WRITE (3,604) WDOT,T,APC
    WRITE (3,605) WPU,DWPU,FA
    WRITE (3,606) XISPD,XITOT,ER
    WRITE (3,607) AT,W,AS
    IP=IP+1
    IF(IP-6)670,660,660
660  WRITE (3,601) TEMP(L)
    IP=0
670  CONTINUE
    WDOTL=WDOT
    W=W+DW
    PCI=PC
    VVV=XISPD
    ASL=AS
    ROSL=ROS
    IF(W-WB(M1))800,800,900
900  CONTINUE
    GO TO 1
    END

```

INPUT DATA FOR PRESSURE AND THRUST TIME ANALYSIS PROGRAM.

1.00000	0.0	20.00000	70.00000	0.0	0.0
70.00000	14.70000	1.63300	0.960001	000.00000	7.07520
5.00000	17.50000				
1503.0000	0.0	0.3800	0.0640	0.9200	243.0000
1535.0000	0.3600	0.3800	0.0640	0.9200	243.0000
1539.0000	0.7200	0.3800	0.0640	0.9200	243.0000
1530.0000	1.0800	0.3800	0.0640	0.9200	243.0000
1511.0000	1.4400	0.3800	0.0640	0.9200	243.0000
1490.0000	1.6500	0.3800	0.0640	0.9200	243.0000
0.0	1.6600	0.3800	0.0640	0.9200	243.0000
5.00000	0.0				
5.000001	000.00000				

PRESSURE AND THRUST TIME ANALYSIS PROGRAM OUTPUT

PROPELLANT TEMPERATURE= 70.00

PRESSURE = 560.76538 TIME = 0.0 PRESS. INTEG. = 0.0
 FLOW RATE = 71.03320 THRUST = 15912.42969 AVE. PRESSURE = 0.0
 WGT. PROP. = 0.0 DELTA W PRO = 0.0 AVE. THRUST = 0.0
 DLVRD ISP = 224.01398 TOTAL IMPLS = 0.0 EXP. RATIO = 7.07520
 THROAT AREA = 19.63492 WEB = 0.0 BURN SURFACE = 1503.00000

PRESSURE = 565.18506 TIME = 0.11155 PRESS. INTEG. = 63.04802
 FLOW RATE = 71.59306 THRUST = 16053.28906 AVE. PRESSURE = 565.18481
 WGT. PROP. = 7.95519 DELTA W PRO = 7.95519 AVE. THRUST = 15982.83594
 DLVRD ISP = 224.22971 TOTAL IMPLS = 1782.93164 EXP. RATIO = 7.07520
 THROAT AREA = 19.63492 WEB = 0.08250 BURN SURFACE = 1510.33325

PRESSURE = 569.61792 TIME = 0.22277 PRESS. INTEG. = 126.40173
 FLOW RATE = 72.15457 THRUST = 16194.57812 AVE. PRESSURE = 567.39705
 WGT. PROP. = 15.94910 DELTA W PRO = 7.99391 AVE. THRUST = 16053.26562
 DLVRD ISP = 224.44290 TOTAL IMPLS = 3576.25562 EXP. RATIO = 7.07520
 THROAT AREA = 19.63492 WEB = 0.16500 BURN SURFACE = 1517.66650

PRESSURE = 574.06299 TIME = 0.33367 PRESS. INTEG. = 190.06102
 FLOW RATE = 72.71764 THRUST = 16336.26172 AVE. PRESSURE = 569.61304
 WGT. PROP. = 23.98172 DELTA W PRO = 8.03263 AVE. THRUST = 16123.75781
 DLVRD ISP = 224.65340 TOTAL IMPLS = 5379.96484 EXP. RATIO = 7.07520
 THROAT AREA = 19.63492 WEB = 0.24750 BURN SURFACE = 1524.99976

PRESSURE = 578.52295 TIME = 0.44423 PRESS. INTEG. = 254.02606
 FLOW RATE = 73.28259 THRUST = 16478.39844 AVE. PRESSURE = 571.83057
 WGT. PROP. = 32.05305 DELTA W PRO = 8.07135 AVE. THRUST = 16194.33594
 DLVRD ISP = 224.86107 TOTAL IMPLS = 7194.05859 EXP. RATIO = 7.07520
 THROAT AREA = 19.63492 WEB = 0.33000 BURN SURFACE = 1532.33325

PRESSURE = 580.50244 TIME = 0.55457 PRESS. INTEG. = 318.07422
 FLOW RATE = 73.53334 THRUST = 16541.50000 AVE. PRESSURE = 573.55566
 WGT. PROP. = 40.15234 DELTA W PRO = 8.09929 AVE. THRUST = 16257.12109
 DLVRD ISP = 224.95241 TOTAL IMPLS = 9015.64063 EXP. RATIO = 7.07520
 THROAT AREA = 19.63492 WEB = 0.41250 BURN SURFACE = 1535.58325

PRESSURE AND THRUST TIME ANALYSIS PROGRAM OUTPUT

PROPELLANT TEMPERATURE= 70.00

PRESSURE	=	581.06201	TIME	=	0.66481	PRESS. INTEG.=	382.13084
FLOW RATE	=	73.60422	THRUST	=	16559.32812	AVE. PRESSURE=	574.80005
WGHT. PROP.	=	48.26263	DELTA W PRO	=	8.11029	AVE. THRUST =	16305.75391
DLIVRD ISP	=	224.97798	TOTAL IMPLS	=	10840.17187	EXP. RATIO =	7.07520
THROAT AREA	=	19.63492	WEB	=	0.49500	BURN SURFACE =	1536.49976

PRESSURE	=	581.62085	TIME	=	0.77501	PRESS. INTEG.=	446.22559
FLOW RATE	=	73.67500	THRUST	=	16577.13281	AVE. PRESSURE=	575.76978
WGHT. PROP.	=	56.37776	DELTA W PRO	=	8.11513	AVE. THRUST =	16343.07812
DLIVRD ISP	=	225.00354	TOTAL IMPLS	=	12666.00000	EXP. RATIO =	7.07520
THROAT AREA	=	19.63492	WEB	=	0.57750	BURN SURFACE =	1537.41650

PRESSURE	=	582.18140	TIME	=	0.88517	PRESS. INTEG.=	510.35864
FLOW RATE	=	73.74602	THRUST	=	16595.00781	AVE. PRESSURE=	576.56738
WGHT. PROP.	=	64.49773	DELTA W PRO	=	8.11997	AVE. THRUST =	16373.32031
DLIVRD ISP	=	225.02925	TOTAL IMPLS	=	14493.12500	EXP. RATIO =	7.07520
THROAT AREA	=	19.63492	WEB	=	0.66000	BURN SURFACE =	1538.33325

PRESSURE	=	582.24463	TIME	=	0.99530	PRESS. INTEG.=	574.48560
FLOW RATE	=	73.75403	THRUST	=	16597.01953	AVE. PRESSURE=	577.19556
WGHT. PROP.	=	72.62039	DELTA W PRO	=	8.12267	AVE. THRUST =	16397.96094
DLIVRD ISP	=	225.03209	TOTAL IMPLS	=	16320.97266	EXP. RATIO =	7.07520
THROAT AREA	=	19.63492	WEB	=	0.74250	BURN SURFACE =	1538.43750

PRESSURE	=	580.98608	TIME	=	1.10548	PRESS. INTEG.=	638.49902
FLOW RATE	=	73.59462	THRUST	=	16556.91406	AVE. PRESSURE=	577.57349
WGHT. PROP.	=	80.73798	DELTA W PRO	=	8.11749	AVE. THRUST =	16415.80859
DLIVRD ISP	=	224.97453	TOTAL IMPLS	=	18147.43359	EXP. RATIO =	7.07520
THROAT AREA	=	19.63492	WEB	=	0.82500	BURN SURFACE =	1536.37500

PRESSURE	=	579.72803	TIME	=	1.21576	PRESS. INTEG.=	702.42627
FLOW RATE	=	73.43524	THRUST	=	16516.80859	AVE. PRESSURE=	577.76880
WGHT. PROP.	=	88.84448	DELTA W PRO	=	8.10661	AVE. THRUST =	16426.78906
DLIVRD ISP	=	224.91667	TOTAL IMPLS	=	19970.97656	EXP. RATIO =	7.07520
THROAT AREA	=	19.63492	WEB	=	0.90750	BURN SURFACE =	1534.31250

PRESSURE AND THRUST TIME ANALYSIS PROGRAM OUTPUT

PROPELLANT TEMPERATURE= 70.00

PRESSURE	=	578.47217	TIME	=	1.32612	PRESS. INTEG.=	766.26758
FLOW RATE	=	73.27617	THRUST	=	16476.79297	AVE. PRESSURE=	577.82739
WGHT. PROP.	=	96.94019	DELTA W PRO	=	8.09572	AVE. THRUST =	16432.61719
DLIVRD ISP	=	224.85883	TOTAL IMPLS	=	21791.60156	EXP. RATIO =	7.07520
THROAT AREA	=	19.63492	WEB	=	0.99000	BURN SURFACE =	1532.25000
PRESSURE	=	577.21631	TIME	=	1.43657	PRESS. INTEG.=	830.02295
FLOW RATE	=	73.11708	THRUST	=	16436.75391	AVE. PRESSURE=	577.78052
WGHT. PROP.	=	105.02501	DELTA W PRO	=	8.08483	AVE. THRUST =	16434.48437
DLIVRD ISP	=	224.80051	TOTAL IMPLS	=	23609.30859	EXP. RATIO =	7.07520
THROAT AREA	=	19.63492	WEB	=	1.07250	BURN SURFACE =	1530.18750
PRESSURE	=	574.69556	TIME	=	1.54716	PRESS. INTEG.=	893.57886
FLOW RATE	=	72.79776	THRUST	=	16356.41797	AVE. PRESSURE=	577.56030
WGHT. PROP.	=	113.09343	DELTA W PRO	=	8.06843	AVE. THRUST =	16431.78516
DLIVRD ISP	=	224.68300	TOTAL IMPLS	=	25422.62109	EXP. RATIO =	7.07520
THROAT AREA	=	19.63492	WEB	=	1.15500	BURN SURFACE =	1526.04150
PRESSURE	=	572.05444	TIME	=	1.65794	PRESS. INTEG.=	956.95068
FLOW RATE	=	72.46321	THRUST	=	16272.23437	AVE. PRESSURE=	577.19214
WGHT. PROP.	=	121.13942	DELTA W PRO	=	8.04600	AVE. THRUST =	16423.93750
DLIVRD ISP	=	224.55861	TOTAL IMPLS	=	27229.91797	EXP. RATIO =	7.07520
THROAT AREA	=	19.63492	WEB	=	1.23750	BURN SURFACE =	1521.68750
PRESSURE	=	569.41626	TIME	=	1.76891	PRESS. INTEG.=	1020.14111
FLOW RATE	=	72.12903	THRUST	=	16188.14453	AVE. PRESSURE=	576.70459
WGHT. PROP.	=	129.16241	DELTA W PRO	=	8.02301	AVE. THRUST =	16411.78516
DLIVRD ISP	=	224.43318	TOTAL IMPLS	=	29031.04687	EXP. RATIO =	7.07520
THROAT AREA	=	19.63492	WEB	=	1.32000	BURN SURFACE =	1517.33325
PRESSURE	=	566.78320	TIME	=	1.88008	PRESS. INTEG.=	1083.15015
FLOW RATE	=	71.79550	THRUST	=	16104.23047	AVE. PRESSURE=	576.11816
WGHT. PROP.	=	137.16243	DELTA W PRO	=	8.00002	AVE. THRUST =	16396.08594
DLIVRD ISP	=	224.30701	TOTAL IMPLS	=	30826.00781	EXP. RATIO =	7.07520
THROAT AREA	=	19.63492	WEB	=	1.40250	BURN SURFACE =	1512.97925

PRESSURE AND THRUST TIME ANALYSIS PROGRAM OUTPUT

PROPELLANT TEMPERATURE= 70.00

PRESSURE	=	562.87256	TIME	=	1.99150	PRESS. INTEG.=	1145.86182
FLOW RATE	=	71.30013	THRUST	=	15979.58984	AVE. PRESSURE=	575.37720
WGHT. PROP.	=	145.13383	DELTA W PRO	=	7.97142	AVE. THRUST =	16376.27734
DLVRD ISP	=	224.11728	TOTAL IMPLS	=	32613.29297	EXP. RATIO =	7.07520
THROAT AREA	=	19.63492	WEB	=	1.48500	BURN SURFACE =	1506.50024

PRESSURE	=	557.90942	TIME	=	2.10324	PRESS. INTEG.=	1208.20703
FLOW RATE	=	70.67145	THRUST	=	15821.40625	AVE. PRESSURE=	574.44922
WGHT. PROP.	=	153.06636	DELTA W PRO	=	7.93253	AVE. THRUST =	16350.09609
DLVRD ISP	=	223.87270	TOTAL IMPLS	=	34390.13672	EXP. RATIO =	7.07520
THROAT AREA	=	19.63492	WEB	=	1.56750	BURN SURFACE =	1498.25024

PRESSURE	=	552.96313	TIME	=	2.21537	PRESS. INTEG.=	1270.20850
FLOW RATE	=	70.04489	THRUST	=	15663.76172	AVE. PRESSURE=	573.36182
WGHT. PROP.	=	160.95532	DELTA W PRO	=	7.88897	AVE. THRUST =	16320.20312
DLVRD ISP	=	223.62466	TOTAL IMPLS	=	36155.28125	EXP. RATIO =	7.07520
THROAT AREA	=	19.63492	WEB	=	1.65000	BURN SURFACE =	1490.00024

IJT2191

APPENDIX D

SUPPLEMENTAL TEST DATA

Detailed tabular test data from the two igniter open air firings and the nine aft-end ignition tests are presented in tables D-1 and D-2. The following sections present a short narrative of the pertinent information for each test.

Test 1

Test 1 was conducted with the igniter placed at an ϵ^* of 1.79 and with a maximum igniter mass flow parameter of 0.358, $\text{lb}_m/\text{sec-in.}^2$. A peak igniter pressure of 1750 psia was recorded at approximately 85 ms. This pressure decayed to 1320 psia at 1.06 seconds at which time igniter instrumentation was lost because of burn-through of the instrumentation cable.

Time to achieve full chamber pressure was approximately 190 ms. The first tripwire broke at 55 ms and the last in the head-end at 182 ms. A review of thermocouple indicated possible limited response rates.

The ratios P_8/P_7^+ and P_7/P_1^{++} indicated that the motor unblocked around 140 ms at an igniter to main motor chamber pressure ratio (P_{21}/P_1) of 6.22. All nozzle instrumentation indicated smooth operation until approximately 730 ms at which time intermittent oscillations of low amplitude were evident until about time of the end of igniter action.

These pressure oscillations were not reflected in either the throat or chamber pressure data indicating sonic throat conditions which would prevent any feedback of the igniter and main motor flow interactions into the main motor chamber.

+ For subsonic flow between P_7 and P_8 the ratios of $P_8/P_7 > 1.0$ and for supersonic flow $P_8/P_7 < 1.0$.

++ The stabilization of P_7/P_1 to a constant value which, in general, is less than the theoretical critical pressure ratio is taken as an indication of sonic conditions at the throat. The stabilized value of the pressure ratio corresponds to supersonic flow because of the total pressure loss in P_1 , the exact total pressure at the throat being hard to determine.

	Test No.								
Main Motor	1	2	3	4	5	6	7	8	9
Specified Epsilon Star (ϵ^*) Test Value	2.00	1.36	1.21	1.45	1.28	1.33	1.65	1.55	1.45
Pre-Test Average ϵ^* Value (A_{an}/A_{tm})	1.79	1.34	1.21	1.45	1.28	1.33	1.65	1.54	1.45
Post-Test Average ϵ^* Value (A_{an}/A_{tm})	1.92	1.42	1.28	1.52	1.38	1.91	1.72	1.60	1.53
(w/A) _{ave} - lbm/sec-in ²	--	0.2740	0.2755	0.2618	0.2225	0.2208	0.384	0.383	0.2015
(w/A) _{max} - lbm/sec-in ²	0.3572	0.3362	0.3522	0.3358	0.263	0.261	0.561	0.572	0.2015
Action Time-sec (t_a)	2.911	2.786	2.339	2.380	2.499	2.470	2.405	2.429	2.531
Burn Time - sec (t_b)	2.755	2.640	2.199	2.276	2.275	2.327	2.299	2.266	2.327
Ignition Interval - sec (t_i)	0.178	0.151	0.106	0.158	0.161	0.184	0.088	0.118	0.281
Ignition Delay - sec (t_d)	0.041	0.051	0.044	0.078	0.052	0.071	0.026	0.038	0.101
Average Burning Rate in/sec (\dot{r}) _{ave}	0.595	0.621	0.746	0.721	0.721	0.704	0.714	0.724	0.705
Propellant Straw Rate at 1000 psi - in/sec	0.857	0.857	0.963	0.968	0.968	0.988	0.932	0.932	0.988
Max. Head-End Pressure - Psia (P_1) _{max}	513.6	523.6	674.9	608.5	646.5	621.1	617.4	601.3	607.0
Pressure Time Integral - Psia - sec (PTi)	1309	1320	1383	1287	1309	1328	1271	1269	1309
Average Action Pressure - Psia (P_1) _a	449.8	473.7	591.2	540.9	543.2	537.8	528.4	528.4	517.2
Average Burning Pressure - Psia (Pb)	460.9	484.5	608.1	552.0	556.4	551.6	538.9	538.1	540.1
Maximum Thrust Lb (F_{Tmax})	16,934	18,950	25,201	22,868	25,469	23,098	20,997	21,341	21,369
Total Impulse - lb-sec (I_T)	41,807	45,948	50,688	45,519	47,330	43,331	43,331	44,301	44,722
Average Action Thrust lb (F_a)	14,362	16,492	21,671	19,126	19,451	19,162	18,017	18,238	17,670
Average Burn Thrust lb (F_b)	14,785	16,931	22,352	19,579	19,982	19,725	18,438	18,881	18,551
Thrust Time Integral lb-sec (0-0)	41,901	46,048	50,825	45,602	46,991	47,507	43,440	44,482	44,984
Pressure Time Integral Psi-sec (0-0)	1,316	1,326	1,390	1,292	1,316	1,338	1,278	1,280	1,339
Total Operating Time-sec (0-0)	3,092	2,936	2,494	2,514	2,610	2,700	2,586	2,649	3,909
Average Thrust During Igniter - lb	15,631	18,399	24,060	20,778	21,030	20,928	18,940	19,619	19,270
Average Thrust After Igniter - lb	14,372	15,772	21,015	18,845	19,308	19,559	17,810	18,132	19,317
Average Pressure During Igniter - Psia	474.1	516.8	653.3	574.1	578.8	576.5	538.3	546.8	554.1
Average Pressure After Igniter - Psia	464.0	463.3	571.5	552.0	549.5	559.9	540.9	539.5	567.2
Pre-Fire Throat Area - in ² (A_{tm})	19.64	19.64	19.64	19.50	19.57	19.47	19.67	19.66	19.67
Post-Fire Throat Area - in ² (A_{tm})	19.39	19.31	19.41	19.63	19.46	19.49	19.58	19.66	19.72
Propellant Weight - lb	164.0	164.0*	161.0	157.0	158.0	160.5	164.5	155.0	165.0

* Propellant weight estimated - actual weight data suspect

TABLE D-1

	1	2	3	4	5	6	7	8	9
Igniter Motor									
Burning Time - sec (10 - 50%)	*	1.245	1.346	1.421	1.373	1.351	1.185	1.146	1.209
Ignition Interval - sec (t_i)	0.033	0.044	0.034	0.017	0.029	0.029	0.026	0.039	0.056
Ignition Delay - sec (t_d)	0.004	0.013	0.002	0.004	0.003	0.004	0.002	0.015	0.008
Maximum Pressure - psi (P_{max})	1756	1652	1731	1653	1293	1260	2759	2819	2246
Pressure Time Integral (Psia - sec)	--	1678	1820	1829	1501	1465	2234	2158	2713
Average Burning Pressure Psia	*	1348	1352	1287	1093	1085	1885	1883	2244
Pre-Fire Throat Area - in ² (A_f)	0.612	0.612	0.609	0.610	0.610	0.610	0.611	0.611	0.269
Post-Fire Throat Area - in ² (A_t)	--	--	0.605	0.595	0.595	0.586	0.589	0.605	0.235
Grain Length - in	18.6	18.6	18.6	18.6	16.1	16.1	23.4	23.4	11.3
Propellant Weight - lb	8.5	8.5	8.52	8.53	7.53	7.41	10.6	10.6	5.185

* Igniter instrumentation lost on first test prior to tail-off.

TABLE D-2

Test 2

Test 2 was conducted with the igniter placed at an ϵ^* location of 1.36 and with a maximum igniter mass flow parameter of 0.337 lbm/sec-in². The maximum igniter chamber pressure of 1652 psia occurred at 100 ms and continuously decayed to a steady state value of 1200 psia just before tailoff. Motor nozzle blockage by the igniter jet, as evidenced by the motor throat and exit cone pressure oscillations, was indicated until after igniter tail-off. Intermittent blocked and unblocked operation was noted (P_8/P_7) until approximately 1400 ms at an igniter to motor pressure ratio of 1.57. This corresponded quite closely with termination of throat P_7 and motor chamber (P_1) pressure oscillations which occurred at about 1320 ms. Using average values of the throat pressure (P_7), the throat to motor pressure ratio was recorded at a nearly constant value of 0.54 as early as 800 ms indicating theoretical subsonic pressure ratios had been reached; however, the oscillations in the nozzle and throat measurements indicate that some type of blockage was occurring and that the critical pressure ratio criteria does not provide a good method of determination of unblockage in the absence of throat oscillations. Effective motor throat area vs time calculations indicated an initial large blockage value which decreased with decreasing igniter chamber pressure. The motor throat and chamber pressure oscillations also seemed to agree with this as the amplitude of oscillations were quite high at the beginning of the run decaying with decrease in igniter chamber pressure. The decay in amplitude of the oscillations corresponded to the reduction in blockage as determined by the A_t vs time calculations.

Test 3

Test 3 was run at an ϵ^* location of 1.21 and a maximum igniter-mass flow parameter of 0.352 lbm/sec-in².

The most severe motor and nozzle pressure oscillations as well as actual chamber overpressurizations were noted on this run. Except for the two tests with higher igniter mass flow parameters on test three, full ignition was achieved in the shortest time interval.

The time of first ignition was approximately 49 ms and burning of the total grain surface area was achieved at 113 ms as determined from tripwire data. Steady state chamber pressure was achieved at approximately 120 ms. Severe nozzle pressure oscillations began at 85 ms and persisted, although decaying gradually, until 1400 ms.

Pressure oscillations, A_t vs time calculations and pressure ratio tests indicated that the motor unblocked at approximately 1.390 seconds at a igniter to motor pressure ratio (P_{21}/P_1) of 2.28. From that point the motor head-end pressure gradually decayed until it reached a value of 670 psia at 1020 ms and at a igniter to motor pressure of 1.92.

A maximum average thrust value of 25,600 lbs was recorded at 1020 ms. The average thrust level at 170 ms was 23,900 lbs. Maximum thrust oscillations with a peak-to-peak value of approximately 6000 lb and a frequency of one cycle every 20 milliseconds was recorded at about 900 ms. These oscillations dampened out to about a tenth of this amplitude after the completion of igniter action.

Test 4

Test 4 was run at an igniter ϵ^* location of 1.45 and a maximum igniter mass flux parameter of 0.337 lbm/sec-in². A maximum igniter pressure of 2637 psia was recorded at 80 ms. The time of initial ignition of the grain surface was 55 ms and the flame propagation was complete by 153 ms. Steady state motor operating pressure was achieved by 160 ms.

High frequency pressure oscillations were noted in the motor throat and chamber pressure measurements from about 140 to 900 ms. The severity of these oscillations was considerably less than on test 3. Beginning around 450 ms motor throat and chamber oscillations were observed to intermittently cease for periods of up to 20 ms. During these periods motor nozzle measurements indicated sonic conditions at the throat i.e., $p_7/p_8 < 1$. At 880 ms the throat and motor oscillations ceased altogether indicating no further blockage of the main motor throat. Pressure measurements in the exit cone (P_8 thru P_{17}) appeared to be highly unstable until about 750 ms. From 750 ms to about 1050 ms, they were steadier and seemed to exhibit a bi-stable operating mode--one mode for the blocked condition and the other in the unblocked condition. From 1050 to igniter tail-off at about 1500 ms, they exhibited a fairly stable average value with intermittent pressure oscillations. After igniter tail-off the nozzle exit cone pressure oscillations died out completely.

The interaction of nozzle flow with motor pressure oscillations (P_7, P_8 , etc.) was illustrated very well on P_{18} during this test. The data seemed to indicate that for the blocked condition a shock was induced by the back pressure at a low igniter expansion ratio. For the

non-blocking case P_{18} indicated a much lower pressure corresponding to a shock location at a higher expansion ratio.

A maximum motor chamber overpressure of approximately 11 percent was noted at 206 ms. This compares with maximum overpressures of 36 percent ($\epsilon^* = 1.2$) and 21 percent ($\epsilon^* = 1.34$) recorded on tests 2 and 3, respectively.

Test 5

Test 5 was conducted with the igniter located at $\epsilon^* = 1.28$ and a maximum igniter mass flux parameter of $0.263 \text{ lb/sec-in}^2$. Complete ignition of the main motor was observed at about 160 ms. Tests 5 and 6 were conducted at lower igniter chamber pressures to study the effects of lower igniter mass flow and lower igniter to motor total pressure ratios. Maximum igniter chamber pressures for both tests were approximately 1300 psia and steady state design conditions were 1100 psia. In test 5 a maximum igniter pressure of 1288 psia was reached at about 900 ms.

The severity of the motor chamber and nozzle oscillations were both qualitatively and quantitatively similar to those noted in test 4. Again, intermittent throat unblocking was observed to occur about halfway through igniter action time. However, pressure oscillation at P_7 and the ratio of P_8 to P_7 indicated that intermittent blockage occurred until about 1300 ms, by which time final unblocking occurred. At approximately 300 ms, P_8 indicated pressures above P_7 (i.e., subsonic flow and hence blockage) about half of the time. This percentage dropped to about 20% by 800 ms and 95% by 1000 ms, indicating intermittent blockage condition which decreased with decreasing igniter to main motor pressure ratio. The last P_8 pressure peak above P_7 pressure was noted at approximately 1300 ms by which time motor pressure oscillations had decayed to the level where they were indistinguishable from normal instrumentation noise. From 1300 to 1400 a few spurious pressure disturbances were recorded at one of the nozzle instrumentation taps.

The maximum overpressurization of approximately 10 percent was recorded around 210 ms.

Test 6

Test 6 was conducted with the igniter at an $\epsilon^* = 1.33$ and a maximum igniter flow parameter of $0.261 \text{ lb/sec-in}^2$. A maximum igniter chamber pressure of 1269 was recorded at 69 ms. The chamber pressure decayed to an average steady state value of 1050 psia at approximately 1000 ms. Steady state operating conditions were achieved in the main motor at approximately 200 ms.

The characteristic motor and nozzle pressure oscillation were almost identical to those recorded in test 5.

A maximum overpressure in the neighborhood of 10 percent was recorded at 270 ms. After 650 ms throat and nozzle pressure oscillations became intermittent and did not die out completely until about 1350 ms during igniter tail-off.

Test 7

Test 7 was run at an ϵ^* location of 1.65 and maximum igniter mass flow parameter of $0.561 \text{ lb/sec-in}^2$. Tests 7 and 8 were run at higher igniter chamber pressures and mass flow rates to study the effects of the higher igniter motor total pressure ratios and igniter mass flow parameters on blockage and ignition. The igniter chamber pressure reached a peaked value of 2770 psia at 70 ms and decayed to 1700 psia at 1020 ms.

The motor ignition transient on test 7 was the fastest recorded on any test in the program. First ignition as determined by tripwire data was observed at 38 ms and the entire surface had ignited by 66 ms. Steady state chamber pressure was reached at about 110 ms. For test seven and test eight there was a greater time lag between ignition of the entire burning surface and attainment of steady state pressure in the motor. This would seem to indicate that the chamber filling rate was limiting rather than flame propagation into the motor head-end.

Initially, the motor nozzle and chamber pressure operating characteristics were similar to those noted in test 1 in which no overpressurizations were noted. The nozzle pressure data indicated that igniter jet blockage of the main motor throat ceased during the ignition transient before steady state motor operating conditions were reached. Shortly after steady state conditions were reached, a major pressure disturbance was noted in the nozzle and motor chamber pressure measurements. This disturbance which was later found to be caused by ejection

of an object from the motor, did not appear to significantly affect the steady state operating conditions of the motor which continued to operate in a stable unblocked mode until approximately 530 ms. At this time, intermittent pressure disturbances began to be recorded in the motor nozzle and chamber. As time progressed they became more continuous and severe until approximately 1100 ms when the igniter began to tail-off. Simultaneous with the nozzle exit cone pressure disturbances, similar disturbances were seen in the igniter exit cone pressure measurement (P_{18}). The timing and general character of P_{18} pressure perturbations closely resembled data recorded at nozzle measurement P_{10} which because of its position relative to the igniter lip on this test best approximates the pressure at the igniter exit plane. It is postulated that the pressure disturbances were the result of pulsations or an unstable operation of the igniter jet. However, because the time of onset of the pressure disturbances at P_{18} and P_{10} were nearly simultaneous, it was difficult to establish whether the nozzle pressure disturbances were being caused by an inherent instability in the igniter jet or whether they were the result of a jet instability caused by changes in the back-pressure seen by the igniter.

These nozzle and motor pressure disturbances at first appeared to be momentary deviations or perturbations from a stable mode of operation. As the igniter chamber pressure decayed further, they became characteristic of the pressure disturbances previously noted which were more oscillatory in nature and seemed at times to exhibit a bi-stable character.

Although the pressure disturbances in the nozzle were at times quite severe, little affect was displayed by the motor chamber data, except at times corresponding to the worst nozzle pressure disturbances when pressure oscillations were observed on the motor chamber data. There did not appear to be any increase in chamber pressure level and except for the intermittent oscillations, the motor chamber data was completely normal.

Test 8

Test 8 was run at an igniter $\epsilon^*=1.54$ and a maximum igniter mass flow parameter of $0.572 \text{ lbm/sec-in}^2$. The peak igniter chamber pressure of 2840 psi occurred at approximately 50 ms and decayed with a saddle backed trace to 1700 psi at 800 ms.

As in test 7, the ignition transient was significantly faster than that recorded on the previous tests. First, ignition was observed at 37 ms and steady state pressure was attained in the motor by 115 ms. The

flame propagation as evidenced by tripwire data was slightly slower on this test than test 7. Theoretically the ignition interval should have been shorter by virtue of the lower ϵ^* and higher maximum igniter mass flow parameter. No apparent reason for this theoretical inconsistency could be found.

Pressure disturbances in the nozzle and motor chamber pressures similar to those noted in test 7 were again observed. The onset of these disturbances were sooner and the severity greater. Main motor head end pressure and throat pressure were similar to igniter pressure until about 100 ms at which time the motor flow appeared to choke at the throat. Beginning at 267 ms, approximately 147 ms after the main motor achieved steady state pressure, intermittent pressure disturbances were noted, the first seemed to record at pressure tap p_{10} near the igniter exit. These pressure disturbances seemed to propagate both up and down stream and persisted until 1200 ms when the igniter began to tail off.

Unlike test 7, some of the initial pressure disturbances brought about momentary increases in the motor chamber pressure. These disturbances endured at most from 20 to 30 ms. The maximum main motor overpressurization was approximately 50 psia at P_1 . These momentary overpressures diminished as the run progressed until the overpressures were small and, in general, discernable primarily by the inducted oscillations.

Test 9

Test 9 was run at an $\epsilon^* = 1.45$ and an igniter design pressure of 2250 psi. The igniter throat area was reduced for this run to accommodate a decrease in w/A to about 0.200 at the design point. The ignition interval was considerably longer for this test than for any previous test, the time to 100% P_c being about 300 ms. The first tripwires at the aft-end broke at about 80 ms and the last one at the grain head-end at approximately 300 ms. Flame propagation as indicated by the tripwires was slow and fairly linear.

Except for the longer ignition interval, the test appeared to be in character like the earlier tests in the low-to-moderate ϵ^* range. Motor nozzle pressure oscillations similar to those on tests 2 thru 6 but of less severity began before steady state operating pressure was reached and were observed to die-out about midway through igniter action (700 ms). Unblocking according to motor throat to chamber pressure ratio (P_7/P_1) occurred about 300 ms at a igniter to booster

pressure ratio of approximately 4.3. This, however, did not correspond to the cessation of throat pressure oscillations which did not completely dampen out until about 700 ms at an igniter to booster chamber pressure ratio of 3.60. Slight oscillations were noted in the chamber pressure measurement during the period of nozzle pressure perturbations; however, they were not as large as those noted on previous tests. Any increase in motor chamber pressure during these times of slight blockage was of such a small magnitude as to be indeterminate.

APPENDIX E

THROAT AREA AND OVERPRESSURIZATION CALCULATIONS

A. SUMMARY

Throat areas and overpressurization were calculated for all runs except 1 and 7 for times from complete ignition to the beginning of main motor tail-off.

The formula used for the effective throat area calculation was:

$$A_m^* = \frac{c^* a \bar{P}^n \rho A_b}{P_{5_0} g_c} \quad (1)$$

where:

a = burn rate coefficient

\bar{P} = average chamber pressure = $\frac{P_1 + P_2}{2}$

P_{5_0} = total pressure at sensor 5

ρ = propellant density

A_b = burn area as a function of web burn back.

n = propellant burn rate exponent

c^* = 95% of theoretical motor characteristic exhaust velocity.

Overpressures were calculated using the ratio of A_m^* to the actual throat area:

$$\Delta P/P_{1,0} = (A_{tm}/A_m^*)^{\frac{1}{1-n}} - 1.0 \quad (2)$$

It was found from these calculations that runs 8, 9 were unblocked over the time duration from full ignition to tail-off. Runs 2 thru 6 showed blocking.

Results for a typical run (figure III-73) show that blocking is greatest initially when the igniter is at peak pressure. As the igniter reduces in pressure and tails-off, the effect motor throat area increases gradually, goes through a slight dip, and then reaches its unblocked value. Overpressurization begins at a high value (approximately 0.3), decreases to a plateau value, makes a slight hump corresponding to the dip in A_t , then decreases to 0. The plot of $\Delta P_m/P_{m,0}$ versus P_{21}/P_1 (figure III-76) is similar to those of Salmi⁽⁵⁾ for the same value of ϵ^* . However, the large dip in the curves reported by Salmi at about $P_{21}/P_1 = 3$ was generally reduced and in one instance (Test 2) was not evident.

B. CALCULATION OF THROAT AREA & OVERPRESSURIZATION

The throat area was calculated for each run using equation (1). In this equation, c^* , ρ , a , g_c were constant for each calculation and $P_1(t)$, $P_5(t)$ were time dependent values obtained from the firing data for a given test. $A_b(r)$, or the burn area versus burn-back curve, and P_5 (total pressure at tap 5) were calculated as explained below.

First, a computation for the burn rate coefficient "a" was made. This was done by taking an average of \bar{p} . Using the burn time, Δt_b , and the total web thickness r_t , "a" was obtained from the formula:

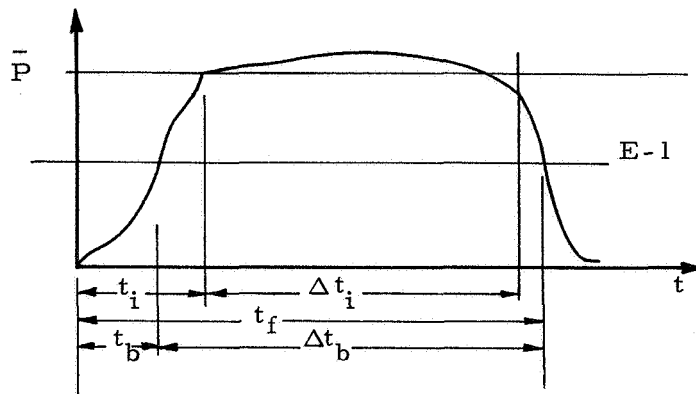
$$a = \frac{r_t}{(\Delta t_b) \bar{p}^n} \quad (3)$$

A diagram which shows the meaning of t_b as well as other time constants used in the calculation is illustrated in figure E-1.

To obtain A_b at a point in time, t , the instantaneous web-burn back distance r was calculated by the formula:

$$r = \int_{t_i}^t a \bar{p}^n dt + r_i \quad (4)$$

where r_i was the initial web burn back after completion of ignition.



t_b = time to 1/2 average pressure

t_f = time to 1/2 average pressure at tail-off.

t_i = time to complete ignition

Figure E-1

The value for r_i was:

$$r_i = a(t_i - t_b) \overline{p}^n \quad (5)$$

Using the calculated value of r , the value of A_b was obtained by interpolation from burn area vs. web burn-back data from tests 1 and 7.

The total pressure at tap 5 (P_5) was calculated by use of the instantaneous static pressure at station 5, the web burn back distance and the mass flow past tap 5. These data were used to determine the Mach number compressibility effect at tap 5. The cross-sectional area at station 5 was calculated using r and the initial port diameter, R , to be:

$$A_5 = \pi(R + r)^2 \quad (6)$$

The flow past station 5 was

$$w_5 = \rho A_c \bar{a}^n \quad (7)$$

where A_c , the burn area forward of station 5, was given by:

$$A_c = A_b - 2\pi(R+r)(8-r) + \pi(R+r_t)^2 - \pi(R+r)^2 \quad (8)$$

The Mach number at station 5 was obtained by solving the following equation for M_5 :

$$\frac{w_5}{A_s p_5} \cdot \sqrt{\frac{RT}{g_c}} = M_5 \sqrt{1 + \left(\frac{\gamma-1}{2}\right) M_5^2} \sqrt{\gamma} \quad (9)$$

With M_5 , P_5 was calculated from:

$$P_{5_0} = P_5 \left(1 + \left(\frac{\gamma-1}{2}\right) M_5^2\right)^{\frac{\gamma}{\gamma-1}} \quad (10)$$

With these calculations all the quantities necessary in formula (1) to calculate A_m^* have been found.

With the assumed values of the constants c^* , ρ , and g , the plateau value for A_m^* did not always come out to be 19.6 the design value. In order that the plateau value level off at 19.6 the calculations were redone by setting a new ρ value by the equation

$$\rho_{\text{new}} = \rho_{\text{old}} \cdot (19.6/A_m^*)_{\text{plateau}} \quad (11)$$

Here $(A_m^*)_{\text{plateau}}$ = the leveling off value of A_m^* for the initial calculations.

While a change in the propellant density value is not justifiable from a physical point of view it should be noted that in the calculations this is the same as making changes to "a", the propellant burn rate coefficient.

C. CALCULATION OF THE BURN AREA VERSUS BURN BACK

Both run 7 and 1 were used to obtain A_b . Although differing methods were used for both calculations, the results obtained for the A_b were almost identical. Run 3 which was used to verify that calculations of $A_b(r)$ by both methods would give similar results, indicated agreement to within 2% in the calculation of A_m^* . The formula used for the calculation of A_b in run 1 was

$$A_b = \frac{P_{50} A_{tm} g_c}{c^* a p^{-n} \rho} \quad (12)$$

The constants A_m^* , and ρ were set at 19.6 in^2 and 0.064 lbm/in^3 , respectively.

The pressure traces used to make the calculations were $P_1(t)$, $P_4(t)$ and $P_7(t)$. To obtain $P_5(t)$ in formula (1), one uses the value of p^*/P_{50} for $\gamma = 1.14$ which is 0.576. Hence

$$P_{50} = p^*/0.576 = P_7/0.576$$

The value for \bar{p} was obtained from:

$$\bar{p} = (0.222)P_1 + (0.778)P_4$$

which assumes linear distribution of pressure down the port from the head end of the rocket. The value for "a" was obtained as described in section B.

Formula (1) was used to calculate, for some given t, a value for A_b . Equation (4) was used to obtain the corresponding value for r at this given t.

The method used for calculation of A_b in run 7 was similar to the procedure used in the calculation of A_m^* in section B. A calculation of A_m^* based upon the $A_b(r)$ was obtained for run 1. Note that in equation (1) that A_m^* is linearly related to A_b . A new A_b was then selected for trial in equation (1) by the use of the formula:

$$A_b)_{\text{new}} = A_b)_{\text{old}} \cdot 19.6/A_m^*)_{\text{old}} \quad (13)$$

Since A_c is functionally dependent on A_b , this new value for A_b (A_b)_{new}, may have been slightly in error, however, by iteration in A_b it will come out to a value such that A_m^* assumes 19.60 in². after the cessation of igniter action.

DISTRIBUTION LIST

NASA Lewis Research Center		NASA George C. Marshall	
2100 Brookpark Road		Space Flight Center	
Cleveland, Ohio 44135		Redstone Arsenal	
Attn: Contracting Officer	(1)	Huntsville, Alabama 35812	
Mail Stop 500-313		Attn: Technical Library	(1)
Solid Rocket Technology Branch	(8)	R-P&VE-PA/K. Chandler	(1)
Mail Stop 500-205			
Technical Library	(2)	Jet Propulsion Laboratory	
Mail Stop 60-3		California Inst. of Technology	
Tech. Rpt Control Office	(1)	4800 Oak Grove Drive	
Mail Stop 505		Pasadena, California 91103	
J. Kennard	(1)	Attn: Richard Bailey	(1)
Mail Stop 3-14		Technical Library	(1)
Tech. Utilization Office	(1)		
Mail Stop 3-19		Scientific and Technical	
Patent Counsel	(1)	Information Facility	
Mail Stop 501-3		NASA Representative	
		P. O. Box 33	
National Aeronautics and		College Park, Maryland 20740	
Space Administration		Attn: CRT	(6)
Washington, D.C. 20546			
Attn: RPM/William Cohen	(3)	<u>Government Installations</u>	
RPS/Robert W. Ziem	(1)		
ATSS-AL/Technical Library	(2)	AF Space System Division	
		Air Force Unit Post Office	
NASA Ames Research Center		Los Angeles, Calif. 90045	
Moffett Field, California 94035		Attn: Col. E. Fink	(1)
Attn: Technical Library	(1)		
		AF Research & Technology Div.	
NASA Langley Research Center		Bolling AFB, D. C. 20332	
Langley Station		Attn: Dr. Leon Green, Jr.	(1)
Hampton, Virginia 23365			
Attn: Robert L. Swain	(1)	AF Rocket Propulsion Lab	
Technical Library	(1)	Edwards AFB, Calif. 93523	
		Attn: RPM/Mr. C. Cook	(2)
NASA Goddard Space Flight Center			
Greenbelt, Maryland 20771		AF Ballistic Missile Division	
Attn: Technical Library	(1)	P. O. Box 262	
		San Bernardino, California	
NASA Manned Spacecraft Center		Attn: WDSOT	(1)
2101 Webster Seabrook Road			
Houston, Texas 77058	(1)		

Army Missile Command Redstone Scientific Information Ctr. Redstone Arsenal, Alabama 35809 Attn: Chief, Document Section (1)	Defense Materials Info Center Battelle Memorial Inst. 505 King Avenue Columbus, O. 43201 (1)
Picatinny Arsenal Dover, New Jersey 07801 Attn: Technical Library (1)	Materials Advisory Board Nat'l Academy of Science 2101 Constitution Ave., N. W. Washington, D. C. 20418 Attn: Capt. A.M. Blamphin (1)
Navy Special Projects Office Washington, D. C. 20360 Attn: H. Bernstein (1)	Institute for Defense Analysis 1666 Connecticut Ave., N. W. Washington, D. C. Attn: Technical Library (1)
Naval Air Systems Command Washington, D. C. 20360 Attn: AIR-330/Dr. O. H. Johnson (1)	Advanced Research Proj. Agcy Pentagon, Room 3D154 Washington, D. C. 20301 Attn: Tech Info Office (1)
Naval Propellant Plant Indian Head, Maryland 20640 Attn: Technical Library (1)	<u>Industry Contractors</u>
Naval Ordnance Laboratory White Oak Silver Spring, Maryland 20910 Attn: Technical Library (1)	Aerojet-General Corporation P O Box 1168 Solid Rocket Plant Sacramento, Calif. 94086 Attn: Dr. B. Simmons (1) Tech. Info Center (1)
Naval Ordnance Test Station China Lake, Calif. 93557 Attn: Technical Library (1) C. J. Thelen (1)	Aerojet-General Corporation P O Box 296 Azusa, California 91702 Attn: Technical Library (1)
Naval Research Laboratory Washington, D. C. 20390 Attn: Technical Library (1)	Aerospace Corporation 2400 East El Segundo Blvd El Segundo, Calif. 90245 Attn: Technical Library (1) Solid Motor Dev. Off. (1)
Chemical Propulsion Info Agcy Applied Physics Laboratory 8621 Georgia Avenue Silver Spring, Maryland 20910 (1)	
Defense Documentation Center Cameron Station 5010 Duke Street Alexandria, Virginia 22314 (1)	

Aerospace Corporation
P. O. Box 95805
Los Angeles, Calif. 90045
Attn: Technical Library (1)

Atlantic Research Corporation
Shirley Highway at Edsall Rd.
Alexandria, Virginia 22314
Attn: Technical Library (1)

Boeing Company
P. O. Box 3999
Seattle, Washington 98124
Attn: Technical Library (1)

Chrysler Corporation
Space Division
Michoud Operations
New Orleans, Louisiana
Attn: Technical Library (1)

Douglas Missiles & Space
Systems
Huntington Beach, Calif.
Attn: T. J. Gordon (1)

Hercules Company
Bacchus Works
P. O. Box 98
Magna, Utah 84044
Attn: Technical Library (1)

Lockheed Missiles &
Space Company
P. O. Box 504
Sunnyvale, California
Attn: Technical Library (1)

Lockheed Propulsion Co.
P. O. Box 111
Redlands, Calif. 92373
Attn: Bud Whiteq (1)

Rocketdyne
Solid Propulsion Operations
P. O. Box 548
McGregor, Texas
Attn: Technical Library (1)

Rocketdyne
6633 Canoga Avenue
Canoga Park, Calif. 91304
Attn: Technical Library (1)

Rohm and Haas
Redstone Arsenal Res. Div.
Huntsville, Alabama 35807
Attn: Technical Library (1)

Thiokol Chemical Corporation
Wasatch Division
Brigham City, Utah 84302
Attn: Dan Hess (1)
Technical Library (1)

Thiokol Chemical Corporation
Elkton Division
Elkton, Maryland 21921
Attn: Technical Library (1)

Thiokol Chemical Corporation
Huntsville Division
Huntsville, Alabama 35807
Attn: Technical Library (1)

United Technology Center
P. O. Box 358
Sunnyvale, California 94088
Attn: Technical Library (1)